VNIVERSITAT DE VALÈNCIA

DEPARTAMENT DE FÍSICA ATÒMICA, MOLECULAR I NUCLEAR

PROGRAMA DE DOCTORAT EN FÍSICA


DOCTORAL THESIS

# Towards a precise top quark mass measurement: Improved in-situ jet response measurements and interpretation of the Monte Carlo top quark mass parameter

Naseem Bouchhar

---

Under The Supervision Of

Marcel Vos and Miguel Villaplana Pérez

Valencia, March 2024

The studies included in this doctoral thesis were conducted at the *Institut de Física Corpuscular* (IFIC), Valencia, Spain.


The Institute of Corpuscular Physics is a joint centre of the Spanish National Research Council and the University of Valencia dedicated to research in Nuclear Physics, Particle Physics, and Astroparticle Physics, as well as its applications in Medical Physics and other fields of Science and Technology.

What can be considered the recent stage of the Institute of Corpuscular Physics began in July 1985, when the University of Valencia and the Spanish National Research Council signed a specific collaboration agreement creating an institute of mixed character and shared ownership under the umbrella of a framework agreement of collaboration between both institutions that had been signed at the end of 1983. This new joint centre retained its previous name to honour the tradition of Valencia in the field of Particle and Nuclear Physics, which by then had more than 30 years of history. In the new institute, experimental and theoretical physicists converged, and in addition to the professors of the University of Valencia, other Spanish and foreign researchers working in various foreign institutions joined in the following years.


# Acknowledgements

This thesis is dedicated to my younger brother and sister, Taha and Basmala. I hope seeing this proves to you that you can do whatever you choose to do. Dream big.

I'd like to first and foremost thank my mum and dad for their support throughout my whole life. To have parents that I can truly look up to is a blessing and a privilege. Thank you. I hope I make you proud.

I would also like to thank my supervisors, Marcel Vos and Miguel Villaplana, for... well... giving me a job and allowing me this opportunity. But also for guiding and supporting me throughout this PhD, with respect and kindness. It has been a foundation of my scientific and personal development during this time and I deeply appreciate it.

On top of this, I would like to extend my gratitude to the members of my thesis defense committee — Reina, Veronica, Matteo, Daniel, Emma, and Vicent - for their willingness to dedicate time reading my thesis and providing discussion that has been invaluable to this process.

Lastly, I would like to thank my friends, especially those that I have made in this period in Valencia. To Mariam, David, Adrian, Marcos, Marta, Lorenzo, Paolo, Fabio, Sergio, Juan, Josep, Francesco, Quique, Andrej, Javier, Daniel, Emilio ... oof it's a lot of names ... Alicia, Maria, Androniki, Triin, Omar, Emanuela, JP, Aurelio, Drona, Chitra, Baibhab, Miguel. These have been some of the best times of my life and I'm so honoured and grateful that you have allowed me to spend them with you. This experience would genuinely have been impossible without you guys. Thank you, thank you, thank you.

Okay, enough of the sentimental talk. Let's talk Physics.

J.M.W Turner, '*Snow Storm: Hannibal and his Army Crossing the Alps*'.

إِذَا غَامَرتَ في شَرَف مَرُومٍ فلَا تَقنَع بِمَا دُونَ النُجُومِ

(If you venture in pursuit of noble honour, then be not satisfied with less than the stars.)

*Al-Mutanabbi*

# Contents

# Brief History of Particle Physics

Humanity's quest to understand and master the fundamental forces of the universe is a tale as old as time. The discovery of fire, around 1.5 to 2 million years ago, stands as a landmark in this journey, sparking wonder and questions about the mysteries and depths of nature. While we now see fire as a commonplace tool, its initial discovery likely enveloped early humans in awe and mystique.

Similarly, each generation encounters its own 'fire'—a groundbreaking discovery that initially baffles but eventually revolutionises our understanding and existence. These discoveries are the heartbeats of physics, echoing the essence of particle physics and the broader field.

The idea of the four classical elements—earth, fire, air, and water—as the basic components of everything in the universe was first proposed by the Greek philosopher Empedocles in the 5th century BC. Empedocles' concept significantly influenced later Greek thinkers, including Plato, who further developed these ideas, associating each element with a specific geometric shape, and integrating them into his philosophical system [1]. This early philosophical exploration set the stage for future scientific exploration.

Around 400 BC, philosophers Leucippus and Democritus began contemplating the divisibility of matter, which led to the early atomic theory. They proposed that there 'exists a point beyond which a stone cannot be further divided', leading to the concept of a fundamental unit — eventually discovered as the atom [2].

The understanding and classification of elements have significantly evolved over time. Antoine Lavoisier, a pivotal figure in this development, discovered the law of conservation of mass. He found that the total mass of reactants and products in a chemical reaction remains constant, thus supporting the idea that atoms are neither created nor destroyed during reactions [3]. This breakthrough was furthered in the 18th Century by John Dalton, who studied the ratios in which

different elements combine to form compounds and examined the relationships between their masses [4]. Dalton proposed that each chemical element is made of unique types of atoms and they cannot be altered or destroyed but can be combined. He further theorised that atoms differ in size and mass and that chemical compounds are formed from whole number ratios of these atoms.

This laid the groundwork for Dmitri Mendeleev's periodic table in 1869 [5], which was further refined by Henry Moseley in 1913, resulting in the modern periodic table [6].

However, Dalton's theory was later revised as scientists discovered that atoms were not the smallest particles, leading to a deeper understanding of atomic structure and the discovery of subatomic particles.

In 1897, English physicist J.J. Thomson made a groundbreaking discovery while studying cathode rays [7]. He identified minuscule, negatively charged subatomic particles, which we now know as electrons. This discovery marked him as the pioneer in identifying a subatomic particle. Thomson proposed a model where these electrons were embedded in a positively charged medium, a significant departure from the then-prevailing notion of atoms as indivisible units.

In the early 1900s, Ernest Rutherford conducted his famous gold foil experiment [8]. He bombarded a thin gold foil with alpha particles (each consisting of 2 protons and 2 neutrons). While most alpha particles passed through the foil, a few deflected at large angles, and about 1 in 20,000 even rebounded. This surprising result suggested that an atom's positive charge and most of its mass were concentrated in a small, dense nucleus, challenging Thomson's model. Rutherford's experiment laid the groundwork for the nuclear model of the atom, with a central nucleus surrounded by electrons in varying energy levels.

However, Rutherford's model faced a significant challenge: it predicted that electrons in circular motion should continuously emit energy, leading to unstable atoms, which contradicted observed behaviours. Hydrogen, for example, displayed distinct line spectra rather than the continuous spectrum predicted by this model.

Niels Bohr, in 1913, addressed this inconsistency by introducing a revolutionary model in which electrons orbit the nucleus in specific, quantised orbits, each corresponding to a fixed energy level [9]. This model successfully explained the discrete emission spectrum of hydrogen. Bohr suggested that light emission occurs when an electron transitions from a higher to a lower energy level, a concept

foundational to quantum mechanics.

Finally, in 1932, James Chadwick conducted experiments involving radiation and beryllium and discovered the neutron [10]. His observation of particles with a mass similar to protons but without any charge led to the identification of neutrons. This discovery completed the picture of the atom's basic constituents: protons, neutrons, and electrons.

As atomic models evolved through groundbreaking discoveries, parallel debates about the nature of light also unfolded. From ancient Greece, where Aristotle conceived light as a disturbance in the air [11], to the 17th century when René Descartes revived this notion, suggesting light travelled as a wave-like disturbance [12]. Descartes' theory set the stage for a significant philosophical debate, as his contemporary Pierre Gassendi proposed a contrasting view that light consisted of discrete particles [13].

This philosophical divide reached a new height with Isaac Newton in 1672. Newton, after experimentation such as prism experiments and interference patterns involving thin films (aptly known as Newton's Rings), supported the particle theory of light [14]. His stance on light as particles led to a scientific rivalry with Robert Hooke, who advocated the wave theory, based on phenomena like reflection and refraction [15].

In the early 1800s, Thomas Young's double-slit experiment provided pivotal evidence for the wave nature of light [16]. When a beam of light passed through two closely spaced slits and reached a screen, an interference pattern of bright and dark bands appeared instead of two distinct bands. This experiment strongly supported the wave theory of light.

The resolution to this debate seemed clear until the early 20th century when quantum mechanics emerged. Max Planck, addressing the black-body radiation problem, proposed that energy is emitted or absorbed in distinct increments, or "quanta" [17]. This concept explained the observed radiation spectrum across all wavelengths. Building on this, Albert Einstein proposed that light is composed of discrete energy packets, or "photons", drawing on observations from the photoelectric effect [18]. The Planck-Einstein relationship, $E = h\nu$, linked the energy and frequency of light, bridging Planck's quantisation of energy and the particle nature of light.

Louis de Broglie then extended the wave-particle duality concept beyond light,

suggesting that all particles exhibit this duality [19]. He formulated the de Broglie equation, $\lambda = h/p$, relating a particle's wavelength to its momentum. This theory was later validated through experiments like cathode ray diffraction.

Erwin Schrödinger contributed with the Schrödinger equation, which describes the behaviour of a particle's wavefunction, $\psi$, in terms of its kinetic and potential energies [20]. $i\hbar\frac{\partial}{\partial t}\psi(x,t) = -\frac{\hbar^2}{2m}\frac{\partial^2}{\partial x^2}\psi(x,t) + V(x,t)\psi(x,t)$ encompasses the total energy of a system in terms of its wavefunction.

Werner Heisenberg's focus on the observable properties of electrons led to the Heisenberg uncertainty principle, $\Delta x \Delta p \geq \hbar/2$, highlighting the inherent limitations in simultaneously determining a particle's position and momentum [21].

Finally, Max Born's interpretation of the Schrödinger equation in terms of probability amplitudes marked a significant advancement [22]. He posited that particles exist in a superposition, being simultaneously present at various positions, with the wave equation providing the probability of finding a particle at a particular location.

**The immense evolution of these theories has provided the foundational pillars for this thesis.**

# Part I

# INTRODUCTION

# Chapter 1

# The Standard Model

During the 1960s, an ambitious two-mile accelerator situated at the *Stanford Linear Accelerator Center* (SLAC) embarked on pioneering experiments involving *Deep Inelastic Scattering* (DIS) with electrons. This approach aimed to investigate the internal structure of nucleons by measuring the deflection and kinetic properties of electrons scattering off target particles within the nucleons. The energy of the electron beam reached levels of up to 21 GeV, a remarkable achievement for that era [23]. The outcomes of these experiments unveiled a game-changing revelation: **particles possessed constituents with point-like characteristics**. This breakthrough heralded the experimental inception of *The Standard Model of Particle Physics* (SM), an idea that found its origins with Steven Weinberg in his publication titled *'A Model of Leptons'* [24]. While Weinberg's work focused on the behaviour of *leptons*, it paved the way for a deeper understanding of the fundamental constituents of all matter, including not only leptons but also the building blocks of protons, neutrons, and other hadrons: *quarks*.

The particles in the SM are divided into two distinct categories: *fermions* and *bosons*, which are displayed in Figure 1.1 with each related particle's attributes.

Fermions comprise all the matter in the Universe. They possess a half-integer spin quantum number and, depending on their charges, participate in interactions related to all the fundamental forces: ***gravity, electromagnetism (EM), the weak force, and the strong force***. Fermions are categorised into two distinct groups: quarks and leptons. Both groups are structured into three generations. The initial generation of quarks and leptons constitutes everyday

matter, consisting of up ($u$) and down ($d$) quarks, the electron ($e$), and the electron neutrino ($\nu_e$). The second generation includes the strange ($s$) and charm ($c$) quarks, the muon ($\mu$), and the muon neutrino ($\nu_\mu$). The third generation encompasses the top ($t$) and bottom ($b$) quarks, the tau ($\tau$) lepton, and the tau neutrino ($\nu_\tau$).[1] As generations progress, particles exhibit greater mass relative to their predecessors, with the potential exception of neutrinos, whose small yet non-zero masses remain under precise determination. The heaviest quark in the Standard Model, the top quark, is of particular interest for this thesis and will be discussed in detail in Chapter III.

In contrast to fermions, bosons correspond to each force, possessing an integer spin quantum number, and serving as intermediaries for the interplay between fermions. Specifically, the electromagnetic interaction is overseen by the photon ($\gamma$), the weak interaction is governed by the $W^\pm$ and $Z$ bosons, and the strong force interaction is dictated by the gluon ($g$). Additionally, one of the most important predictions of the Standard Model is the Higgs mechanism, which explains how particles acquire mass. According to this mechanism, all particles acquire mass by interacting with the Higgs field that is associated with the Higgs boson ($H$).

All of the particles of the Standard Model have been experimentally verified, with the most recent being the Higgs boson that was discovered by ATLAS and CMS in 2012 [26] and led to the 2013 Nobel Prize in Physics being awarded to Peter Higgs and François Englert.

The behaviour and interactions of the particles in the Standard Model are theoretically described with a single *Quantum Field Theory* (QFT). The concept of particles in QFT is rooted in the notion that they emerge as excitations of fields, encapsulating packets of energy according to the principles of quantum mechanics. A fundamental aspect of this framework is the position-space operator, represented as $\hat{\phi}(x)$, serving as an operator within the position-space of particle states and dependent on spacetime coordinates. Complementary to this is another essential element: the associated fields denoted as $\psi$ and $\bar{\psi}$. An illustrative example of this concept is depicted in Figure 1.2, where the oscillation of the $\phi$ field leads to the excitation of the $\psi$ and $\bar{\psi}$ fields. Essentially, one can interpret this as the interaction involving the decay of a particle associated to the $\phi$ field into two particles linked to the $\psi$ and $\bar{\psi}$ fields. In the realm of particle interactions, the Lagrangian plays a crucial role in describing the dynamics of the particles.

[1] Every quark and lepton has a corresponding antiparticle with an opposing electric charge and a reversed associated quantum number.

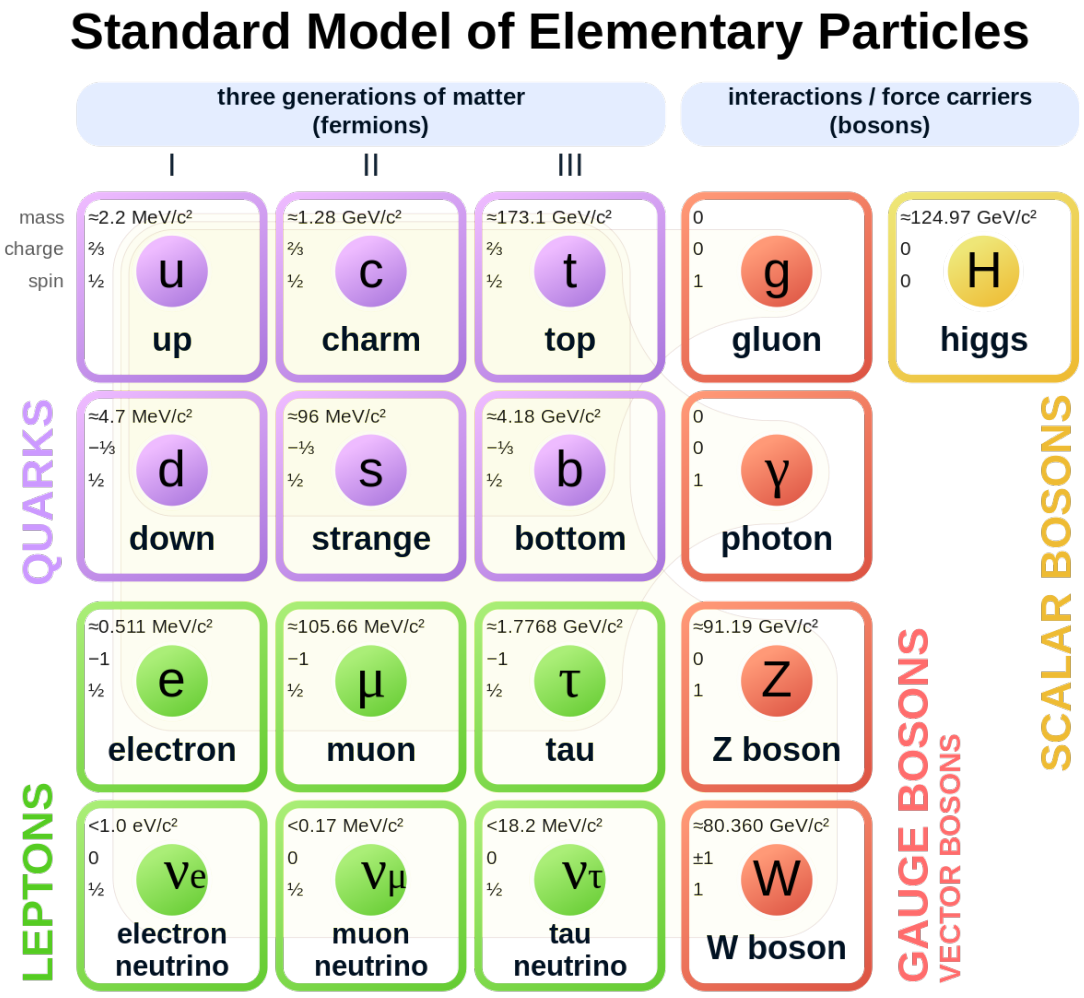


Figure 1.1: Standard Model of Elementary Particles [25].

Through these fields, it becomes evident that a subset of the Lagrangian governing these interactions takes the form $y\phi(x)\bar{\psi}(x)\psi(x)$, where $y$ represents the coupling strength associated with the field. Notably, the mass of the initiating particle, $m_\phi$, must exceed the mass of both resulting particles, $2m_\psi$, to ensure the viability of the interaction.

An important characteristic of the Standard Model is that it is a gauge theory, wherein the SM Lagrangian remains invariant through local transformations referred to as gauge transformations. The matrices that depict these unaltered transformations serve as the generators for a symmetry group. The foundation of the Standard Model relies on the symmetry group $SU(3)_C \otimes SU(2)_L \otimes$

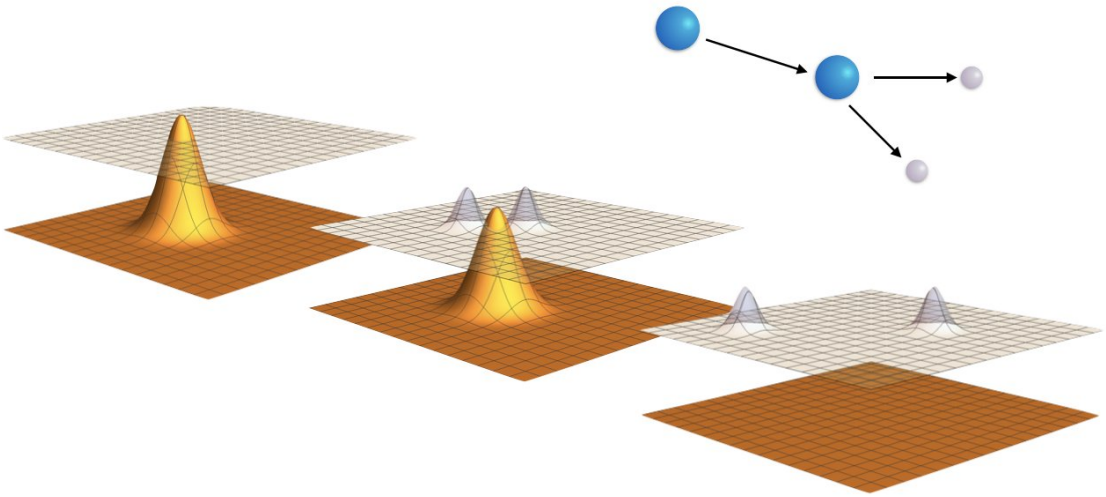

Figure 1.2: Illustration depicting the decay of a particle interpolated by a $\phi$ field, shown in the lower orange segment. The oscillation of the $\phi$ field triggers the excitation of the $\psi$ and $\bar{\psi}$ fields, as illustrated in the upper white portion. Figure courtesy of Martin Bauer.

$U(1)_Y$, which encapsulates its essential symmetrical structure.[2] $SU(2)_L \otimes U(1)_Y$ characterises fermion interactions through the *electroweak* (EW) force, which describes both the electromagnetic and weak forces and $SU(3)_C$ represents fermion interactions through the strong force. These forces are discussed in more detail throughout the introduction of this thesis; the electromagnetic force in Section 1.1, electroweak in 1.2, and the strong force in 1.4.

As previously mentioned, the Standard Model provides a unified description of three fundamental forces of nature. However, gravity, while unmistakably present in our macroscopic world, is not encompassed within the descriptions provided by the Standard Model. At the small scales, within QFT, where the Standard Model is applicable, gravity exerts a notably weak influence, which becomes truly consequential only at the Planck scale, denoted as $E_{Planck} = 1.2 \times 10^{19}$ GeV, which is far beyond the capabilities of any existing technology to probe, making it an elusive domain of exploration. However, it is important to clarify that the exclusion of gravity from the Standard Model is not solely due to its weakness at small scales. It is also due to the unresolved issue of reconciling the principles of

[2]The subscripts C,L and Y indicate colour, weak isospin, and hypercharge respectively.

quantum mechanics with the principles of general relativity to create a coherent and mathematically consistent framework for quantum gravity. This challenge remains one of the most profound questions in theoretical physics.

## 1.1 Quantum Electrodynamics

*Quantum Electrodynamics (QED)* is a theoretical framework that successfully combines quantum mechanics and special relativity to describe electromagnetic interactions between charged particles. QED is based on Dirac's theory of the electron, which provides a relativistic description of these particles. Within the QED framework, the electromagnetic field is quantised, resulting in the concept of photons as the exchange particles mediating electromagnetic interactions. The main proponents of QED are Paul Dirac [27], Richard Feynman [28], Julian Schwinger [29], and Tomonaga Shinchiro [30]; for which the latter three won a Nobel Prize in Physics in 1965.

To begin building the Lagrangian of EM interactions within QED, the Dirac equation for a fermion must first be used:[3]

$$\mathcal{L} = \bar{\psi}(i\gamma^\mu \partial_\mu - m)\psi \tag{1.1}$$

Here $\psi$ is the fermion field and $\bar{\psi}$ is the Dirac conjugate of the fermion field. $\gamma^\mu$ are the Dirac gamma matrices, $\partial_\mu$ is the partial derivate with respect to the spacetime coordinate $x^\mu$, and $m$ represents the mass of the fermion. $\bar{\psi}\psi$ and $\bar{\psi}\gamma\psi$ can be described as the physical quantities of charge density and current respectively. These quantities are invariant when adding a local phase $\Lambda(x)$ and this is the local $U(1)$ gauge transformation:

$$\psi(x) \to e^{iq\Lambda(x)}\psi \tag{1.2}$$

$$\bar{\psi}(x) \to \bar{\psi}(x)e^{-iq\Lambda(x)} \tag{1.3}$$

In these equations, the parameter $q$ represents the strength of the phase transformation. In the context of the QED Lagrangian, $q$ can be interpreted as a charge. It is worth noting that $q$ does not have a specific, fixed value in this transformation but rather represents the charge associated with the particle

[3]Note that we are using natural units for ease and clearer demonstration. Units are chosen such that the speed of light, $c$, and the Planck constant, $\hbar$, are both set to 1.

being described. This charge may vary depending on the type of particle involved, such as electrons having a charge of −1, while protons have a charge of +1. Thus, the parameter $q$ serves as a way to account for the charge of the particle in the transformation without specifying a particular value.

The Lagrangian in Equation 1.1 is also required to be invariant; however, the derivative doesn't transform covariantly under local gauge transformation. In order for the derivative to transform covariantly (and thus the Lagrangian be gauge invariant) a gauge field must be introduced. The vector field $A_\mu(x)$ introduced can be described in terms of a covariant derivative which means it is invariant under local gauge transformations:

$$D_\mu = \partial_\mu - iqA_\mu, \tag{1.4}$$

and $A_\mu$ must transform as:

$$A_\mu \xrightarrow{U(1)} A_\mu - \partial_\mu \Lambda(x), \tag{1.5}$$

which leads to a new Lagrangian:

$$\mathcal{L} = \bar{\psi}(i\gamma^\mu(\partial_\mu - iqA_\mu) - m)\psi \tag{1.6}$$

When applying the gauge transformations outlined in Equations 1.2 and 1.3 to the fermion fields within the Lagrangian depicted in Equation 1.6, it becomes evident that the Lagrangian remains unaltered, thereby establishing its newfound gauge invariance.

The introduction of the vector field, $A_\mu$, requires a kinetic term in order to make it a true propagating field:

$$-\frac{1}{4}F_{\mu\nu}F^{\mu\nu}, \tag{1.7}$$

where $F_{\mu\nu} = \partial_\mu A_\nu - \partial_\nu A_\mu$ is the standard EM field strength. Usually a mass term, $\frac{1}{2}m^2 A_\mu A^\mu$, would also be included but this would break gauge invariance, and so the photon must remain massless.[4] This finally leads us to the QED EM

[4]While the photon is theoretically regarded as a massless particle, its behaviour experimentally can deviate from this ideal in the presence of the matter it interacts with. For instance, in studies conducted on the surface of matter, the photon has been observed to exhibit an "effective" mass, which has been experimentally measured to be $m_\gamma = 5.6 \times 10^{-25}$ MeV [31].

Lagrangian for a charged Dirac fermion (electron, muon, etc.) and massless vector boson (photon) of spin 1 that is invariant under $U(1)$ transformations:

$$\mathcal{L}_{QED} = \bar{\psi}(x)(i\gamma^\mu\partial_\mu - m)\psi(x) + q\bar{\psi}\gamma^\mu\psi A_\mu(x) - \frac{1}{4}F_{\mu\nu}(x)F^{\mu\nu}(x) \tag{1.8}$$

Here $eJ^{EM}_\mu = eq\bar{\psi}\gamma^\mu\psi$ can be introduced as the EM current where e is the $U(1)$ coupling. In practice the addition of the Dirac fermion and the gauge field leads to the well-known QED vertex, when allowing $q$ to be interpreted as the electromagnetic charge operator of a fermion, $Q_f$. This vertex is shown in the Feynman diagram in Figure 1.3.

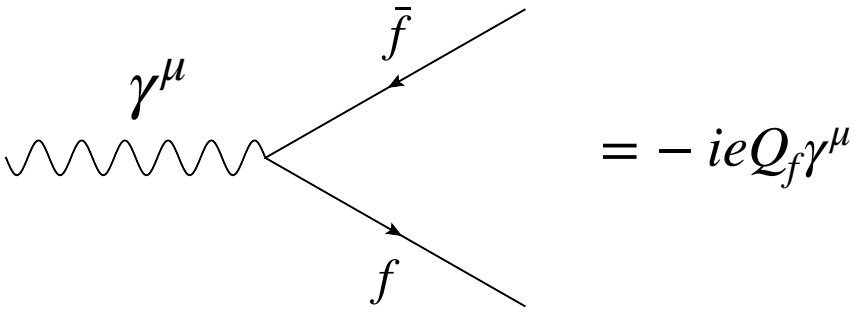


Figure 1.3: Feynman diagram for QED vertex of an interaction between two fermions and a photon.

## 1.2 Electroweak Theory

The Lagrangian for QED, as shown in Equation 1.8, solely incorporates electromagnetic interactions and does not account for weak interactions. In 1979, Sheldon Glashow [32], Abdus Salam [33], and Steven Weinberg [24] were awarded the Nobel Prize for their development of the electroweak theory, which unifies electromagnetic and weak interactions. This theoretical framework introduces massive gauge bosons — namely, the charged $W^\pm$, neutral Z — and the massless photon to describe the unified force. A pivotal aspect of this theory is that three of the four gauge bosons exhibit mass. However, the mechanism for this mass generation was not initially clarified until later when the Higgs boson was introduced, which became an integral part of the theory afterward. Detailed discussion of this development can be found in Section 1.3.

Another inclusion of electroweak interactions is neutrinos. When studying $\beta^-$ decay and assuming a two-body final state ($n \to p + e^-$) it was expected that monoenergetic electrons would arise ($p_e \approx m_n - m_p$). However, it turned out the electron spectrum was continuous, as demonstrated in Figure 1.4a. In an attempt to describe this, Enrico Fermi suggested the theoretical use of a massless particle, which he coined the neutrino, that carried part of the decay energy [34].[5] This lead to the decay process being summarised as $n \to p + e^- + \bar{\nu}_e$ as shown in Figure 1.4b, with a corresponding Fermi amplitude defined as:

$$\mathcal{M} = \frac{G_F}{\sqrt{2}}(\bar{\psi}_p \gamma^\mu \psi_n)(\bar{\psi}_e \gamma_\mu \bar{\psi}_\nu), \tag{1.9}$$

with the Fermi constant $G_F$.

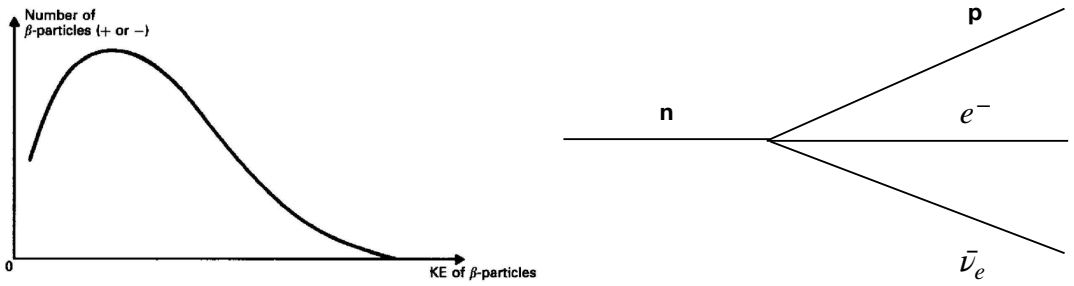


(a) (b)

Figure 1.4: (a) The $\beta^\pm$ decay spectrum [35]. (b) A basic interaction diagram for $\beta$ decay.

In the context of the electroweak regime, fermion fields exhibit a property known as chirality, which can be divided into two distinct forms: left-handed ($L$) and right-handed ($R$). These designations describe the relationship between the spin direction and the linear momentum of massless fermions. In the case of $L$ chirality, the spin is oriented in a direction opposite to the linear momentum, while for $R$ chirality, the spin is aligned in the same direction as the linear momentum.

Another aspect of particle interactions is *parity*. Parity refers to the behaviour of a physical system under spatial reflection, i.e. whether a system appears the same when viewed in a mirror. In an experiment known as the Wu experiment, focusing on the beta decay of Cobalt-60, electrons emitted during the decay were mostly ejected in a direction opposite to the spin of the cobalt nuclei [36].

[5] Originally, however, the idea of a neutrino was first introduced in an open letter by Wolfgang Pauli in 1930, four years before Fermi used this in his beta decay studies.

This discovery suggested that the conservation of parity was violated in weak interactions. The introduction of parity violation leads to the QED vector $\bar{\psi}\gamma^{\mu}\psi$ being replaced with the V - A (vector minus axialvector) combination, given as $\bar{\psi}\gamma^{\mu}\psi - \bar{\psi}\gamma^{\mu}\gamma_5\psi$. This leads the relation:

$$\bar{u}_L\gamma^{\mu}u_L = \bar{\psi}P_R\gamma^{\mu}P_L\psi = \frac{1}{2}\bar{\psi}\gamma^{\mu}(\mathbb{1} - \gamma^5)\psi, \tag{1.10}$$

where right- and left- handed fermion fields and their charge conjugates are defined as $u_{R,L} = P_{R,L}\psi$ and $\bar{u}_{R,L} = \bar{\psi}P_{L,R}$ .

The Fermi Amplitude defined in 1.9 can be adjusted using the relation from Equation 1.10 to give a current-current interaction structure of the form:

$$\mathcal{M} = \frac{4}{\sqrt{2}}G_F J_i^{\mu}J_{j,\mu}^{\dagger}, \tag{1.11}$$

where $J_i^{\mu} = \bar{u}_L\gamma^{\mu}\frac{1}{2}(\mathbb{1} - \gamma_5)u_R$ and $J_{j,\mu}^{\dagger} = \bar{u}_R\gamma^{\mu}\frac{1}{2}(\mathbb{1} - \gamma_5)u_L$.

These amplitudes suggest the following properties for electroweak interactions:

- The expression $\gamma^{\mu}(\mathbb{1} - \gamma_5)$ serves as a tool for distinguishing between left-handed and right-handed fermions, as well as their corresponding anti-fermions as expected. This is illustrated by the equation:

$$\gamma_5 u_L = \gamma_5 P_L u = \gamma_5\frac{1}{2}(\mathbb{1} - \gamma_5)u = -\frac{1}{2}(\mathbb{1} - \gamma_5)u = -u_L \tag{1.12}$$

  Notably, this differentiation highlights the absence of right-handed neutrinos, a characteristic feature of the Standard Model, described in detail in Ref. [37].

- The consistency in applicability of $G_F$ as the strength of an interaction across electroweak interactions highlights its fundamental importance.

- While both parity and charge conjugation can influence experimental outcomes, the symmetry known as *Charge Parity (CP)* remains conserved. This is illustrated with an example of pion decay:

$$\Gamma(\pi^+ \to \mu_R^+ + \nu_L) \neq \Gamma(\pi^+ \to \mu_L^+ + \nu_R) \Longrightarrow \text{P not conserved.}$$
$$\Gamma(\pi^+ \to \mu_R^+ + \nu_L) \neq \Gamma(\pi^- \to \mu_R^- + \bar{\nu}_L) \Longrightarrow \text{C not conserved.}$$
$$\Gamma(\pi^+ \to \mu_R^+ + \nu_L) = \Gamma(\pi^- \to \mu_L^- + \bar{\nu}_R) \Longrightarrow \text{CP is conserved.}$$

### 1.2.1 Construction of $SU(2)_L \otimes U(1)_Y$ EW Lagrangian

The currents related the weak interaction are *charged currents (CC)* and *neutral currents (NC)*. CCs correspond to transitions between pairs of fermions whose charge differs by one unit. These currents can be considered by following the V-A interaction described with Equation 1.10 and written as:

$$j_\mu = j_\mu^+ = \bar{u}_L^0 \gamma_\mu u_L \tag{1.13}$$

$$j_\mu^\dagger = j_\mu^- = \bar{u}_L \gamma_\mu u_L^0 \tag{1.14}$$

Here, $u$ ($\bar{u}$) typically describes a lepton (anti-lepton), which is negatively charged (positively charged). $u^0$ and $\bar{u^0}$ generally refer to a neutrino and anti-neutrino respectively, which are both neutrally charged.

The concept of isospin, denoted as $T$,is an abstract quantum number, analogous to spin. It is used to describe the similarity in properties of protons and neutrons, which are considered as two different states of the same particle, the nucleon, forming an isospin doublet with $T = \frac{1}{2}$.

Extending this concept to the realm of the electroweak interaction, a similar doublet structure can be postulated for leptons, in terms of weak isospin. In this framework, a lepton doublet consists of a neutrino and its associated charged lepton, represented as:[6]

$$\chi_L = \begin{pmatrix} \nu \\ l \end{pmatrix}_L \qquad T_3 = +\frac{1}{2} \text{ for } \nu,\ T_3 = -\frac{1}{2} \text{ for } l \tag{1.15}$$

In this doublet, the weak isospin component, $T_3$, is $+\frac{1}{2}$ for the neutrino and $-\frac{1}{2}$ for the charged lepton.

For weak interactions, the transitions within these doublets are described using raising ($\tau_+$) and lowering ($\tau_-$) operators, defined as $\tau_\pm = \frac{\tau_1 \pm i\tau_2}{2}$. Using these operators, the charged currents from Equations 1.13 and 1.14 can be expressed as:

$$J_\mu^+ = \bar{\chi}_L \gamma_\mu \tau_- \chi_L \tag{1.16}$$

[6] Alternatively, the isospin doublet structure also applies to quarks, i.e. $\begin{pmatrix} u \\ d \end{pmatrix}_L$. However, the treatment is more complex due to the interaction with the strong force and the presence of colour charge, which will be described in Section 1.4.

$$J_\mu^- = \bar{\chi}_L \gamma_\mu \tau_+ \chi_L \tag{1.17}$$

This leads to the prediction of three currents; the third existing current doesn't change charge and is what is called the neutral current. It is associated with a weak isospin singlet, $T_3(u_R) = 0$, and can be defined as:

$$J_\mu^3 = \bar{\chi}_L \gamma_\mu \frac{1}{2} \tau_3 \chi_L = \bar{u}_L^0 \gamma_\mu \frac{1}{2} u_L^0 - \bar{u}_L \gamma_\mu \frac{1}{2} u_L \tag{1.18}$$

Finally, combining the CCs and NCs, a weak isospin triplet of weak currents is obtained:

$$J_\mu^i = \bar{\chi}_L \gamma_\mu \frac{1}{2} \tau_i \chi_L \tag{1.19}$$

where $i = 1, 2, 3$ and the commutation relation for Pauli matrices applies: $[\tau_i, \tau_j] = i\epsilon_{ijk}\tau_k$.

One of the central objectives of the electroweak theory is to unify the EM and weak interactions. However, the EM current, $J_\mu^{EM}$, must be invariant not only under $U(1)$ but also under $SU(2)_L$. To address this, an $SU(2)_L$-invariant $U(1)$ current is introduced, and hyper-charges $Y_R$ and $Y_L$ are introduced as conserved charged operators to the $U(1)_Y$ symmetry. This leads to the expression:

$$J_\mu^Y = \bar{u} \gamma_\mu Y_R u_R + \bar{\chi}_L \gamma_\mu Y_L \chi_L \tag{1.20}$$

To derive a relationship for the newly-introduced hyper-charges, the electromagnetic QED current can be written as a linear combination of the neutral current and half of the newly-defined hyper-charge current:

$$\begin{aligned} J_\mu^{EM} = J_\mu^3 + \frac{1}{2} J_\mu^Y = \bar{u}_R \gamma_\mu Q u_R + \bar{u}_L \gamma_\mu Q u_L \\ = \bar{u}_L^0 \gamma_\mu \frac{1}{2} u_L^0 - \bar{u}_L \gamma_\mu \frac{1}{2} u_L + \frac{1}{2} \bar{u}_R \gamma_\mu Y_R u_R + \frac{1}{2} \bar{\chi}_L \gamma_\mu Y_L \chi_L, \end{aligned} \tag{1.21}$$

giving rise to the relation:

$$Y_R = 2Q \qquad Y_L = 2Q + 1 \tag{1.22}$$

Furthermore, by incorporating the three weak isospin components, the

relationship can be extended to:

$$Y = 2Q - 2T_3 \tag{1.23}$$

The related quantum numbers for quarks and leptons can be found in the Table 1.1

| Particle | T | $T_3$ | Q | Y |
|---|---|---|---|---|
| $\nu_L$ | 1/2 | 1/2 | 0 | -1 |
| $\nu_R$ | 0 | 0 | 0 | 0 |
| $l_L$ | 1/2 | -1/2 | -1 | -1 |
| $l_R$ | 0 | 0 | -1 | -2 |
| $q_{u,L}$ | 1/2 | 1/2 | 2/3 | 1/3 |
| $q_{u,R}$ | 0 | 0 | 2/3 | 4/3 |
| $q_{d,L}$ | 1/2 | -1/2 | -1/3 | 1/3 |
| $q_{d,R}$ | 0 | 0 | -1/3 | -2/3 |

Table 1.1: Quantum numbers for leptons and quarks involved in weak interactions. The right-handed neutrino does not carry charges in $SU(2)_L$ nor $U(1)_\gamma$ and is thus decoupled from EW interactions.

Similar to the gauge field in the Lagrangian of QED shown in Equation 1.8, there is the introduction of a new $SU(2)_L$-gauge field triplet, $\tilde{W}_\mu = \frac{\tau_i}{2} W^i_\mu$, and a singlet, $B_\mu$, associated with weak isospin and weak hyper-charge, respectively. These fields give rise to a massless Lagrangian for EW interactions:

$$\mathcal{L}^{EW} = -i g_W J^i_\mu W^{i\mu} - i \frac{g_Y}{2} J^Y_\mu B^\mu \tag{1.24}$$

Here, $g_W$ is the coupling constant for the triplet field, and $g_Y$ is the coupling constant for the singlet field, representing the strength of the electroweak interactions. Just as in the kinetic term of Equation 1.7, the EW gauge fields require gauge-invariant kinetic terms, given by:

$$\mathcal{L}^{EW}_{Kin.} = -\frac{1}{4} B_{\mu\nu} B^{\mu\nu} - \frac{1}{4} W^i_{\mu\nu} W^{\mu\nu}_i, \tag{1.25}$$

where $B_{\mu\nu} = \partial_\mu B_\nu - \partial_\nu B_\mu$ and $W^i_{\mu\nu} = \partial_\mu W^i_\nu - \partial_\nu W^i_\mu - g \epsilon_{ijk} W^j_\mu W^k_\nu$.

From these fields, the charged vector bosons can be constructed:

$$W^{\pm\mu} = \frac{1}{\sqrt{2}} (W^{1\mu} \mp i W^{2\mu}), \tag{1.26}$$

and the neutral vector bosons are a linear combination of $W^{3\mu}$ and $B^{\mu}$ through the transformation matrix:

$$\begin{pmatrix} W^{3\mu} \\ B^{\mu} \end{pmatrix} = \begin{pmatrix} \cos\theta_W & \sin\theta_W \\ -\sin\theta_W & \cos\theta_W \end{pmatrix} \begin{pmatrix} Z^{\mu} \\ A^{\mu} \end{pmatrix}$$

$$\begin{aligned} \Longrightarrow A^{\mu} &= B^{\mu}\cos\theta_W + W^{3\mu}\sin\theta_W \quad \text{massless} \rightarrow \gamma, \\ \Longrightarrow Z^{\mu} &= -B^{\mu}\sin\theta_W + W^{3\mu}\cos\theta_W \quad \text{massive} \rightarrow Z^0 \end{aligned}$$

where $\theta_W$ is known as the weak mixing angle or Weinberg angle.

Substituting these quantities into the interaction Lagrangian of the neutral electroweak current:

$$\begin{aligned} -igj_3W^{3\mu} - i\frac{g}{2}j_{\mu}^{Y}B^{\mu} = &-i\left(g\sin\theta_W j_3 W^{3\mu} + \frac{g}{2}\cos\theta_W j_{\mu}^{Y}A^{\mu}\right) \\ &- i\left(g\cos\theta_W j_3 W^{3^{\mu}} - \frac{g}{2}\sin\theta_W j_{\mu}^{Y}Z^{\mu}\right) \end{aligned} \tag{1.27}$$

The first term in Equation 1.27, related to $A^{\mu}$, corresponds to the electromagnetic current when considering $J_{\mu}^{EM} = J_{\mu}^{3} + \frac{1}{2}J_{\mu}^{Y}$ from Equation 1.21. This leads to a relation linking the three couplings together:

$$g_W \sin\theta_W = g_Y \cos\theta_W = e \tag{1.28}$$

The second term corresponds to the weak neutral current mediated by the $Z^{\mu}$ field when rearranging the relation from Equation 1.21 to $J_{\mu}^{Y} = 2(J_{\mu}^{EM} - J_{\mu}^{3})$:

$$J_{\mu}^{NC} = \frac{g}{\cos\theta_W}(J_{\mu}^{3} - \sin^2\theta_W J_{\mu}^{EM}) \tag{1.29}$$

The Lagrangians of each interaction give rise to three new gauge bosons: the charged $W^{\pm}$ bosons related to the CCs and the neutral Z boson linked to the NC. These Langrangians and their associated Feynman vertices can each be described as:

$$\begin{aligned} \mathcal{L}_{int}^{CC} &= -i\frac{g}{\sqrt{2}}(\overline{\chi}_L\gamma_{\mu}\tau_{+}\chi_L)W^{+\mu} - i\frac{g}{\sqrt{2}}(\overline{\chi}_L\gamma_{\mu}\tau_{-}\chi_L)W^{-\mu} \\ &= -i\frac{g}{\sqrt{2}}\bar{\nu}_l\gamma_{\mu}\left(1-\frac{\gamma_5}{2}\right)lW^{+\mu} - i\frac{g}{\sqrt{2}}\bar{l}\gamma_{\mu}\left(1-\frac{\gamma_5}{2}\right)\nu_l W^{-\mu} \end{aligned} \tag{1.30}$$

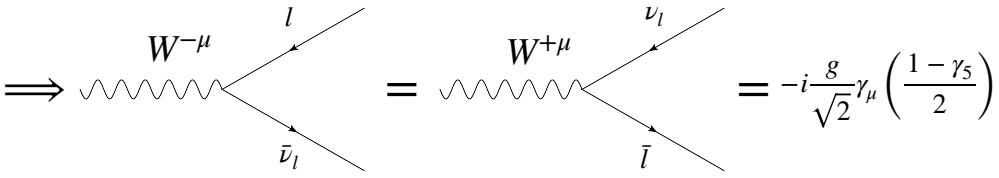


Figure 1.5: Feynman diagram for EW vertex of an interaction between two fermions and a W boson.

$$\begin{aligned}\mathcal{L}_{int}^{NC} &= -i\frac{g}{\cos\theta_w}\bar{\psi}_f\gamma_\mu\left[\left(\frac{1-\gamma_5}{2}\right)T_3 - \sin^2\theta_w Q\right]\psi_f Z^\mu \\ &= -i\frac{g}{\cos\theta_w}\bar{\psi}_f\gamma_\mu\frac{1}{2}(c_V^f - c_A^f\gamma_5)\psi_f Z^\mu,\end{aligned} \tag{1.31}$$

where $c_V^f$ and $c_A^f$are the vector and axial vector couplings of the fermion type f.

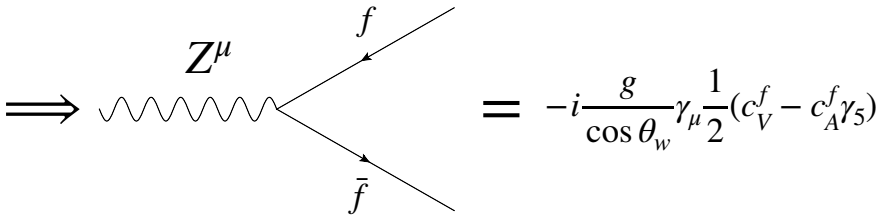


Figure 1.6: Feynman diagram for EW vertex of an interaction between two fermions and a Z boson.

A simple calculation yields:

$$c_f^V = T_3^f - 2\sin^2\theta_w Q^f \tag{1.32}$$

$$c_f^A = T_3^f \tag{1.33}$$

Finally, the electroweak Lagrangian is obtained as the combination of all the previous Lagrangians mentioned:

$$\mathcal{L}_{EW} = \mathcal{L}_0 + \mathcal{L}_{QED} + \mathcal{L}_{CC} + \mathcal{L}_{NC} + \mathcal{L}_{Kin.}^{EM+QED} + h.c. \tag{1.34}$$

### 1.2.2 Quark mixing in electroweak interactions

Although electroweak interactions in the context of leptons have been discussed, it is important to note that quarks also play a significant role in electroweak interactions. The weak isospin doublet structure from Equation 1.15 can be arranged with an up quark and down quark as opposed to a lepton-neutrino pairing. Another aspect with regards to quarks in EW interactions is that quark mixing between different generations is allowed in the CC weak interactions due to the fact that quarks are massive particles in the SM.

The physical eigenstates of quarks ($d$, $s$, $b$) do not directly correspond to the flavour eigenstates ($d'$, $s'$, $b'$) as a result of the mixing that occurs between different quark generations. The relationship between these eigenstates is described by the *Cabibbo-Kobayashi-Maskawa (CKM)* matrix which quantifies the mixing angles and phases that govern the transitions between different quark flavours during weak interactions:

$$\begin{pmatrix} d' \\ s' \\ b' \end{pmatrix} = \begin{pmatrix} V_{ud} & V_{us} & V_{ub} \\ V_{cd} & V_{cs} & V_{cb} \\ V_{td} & V_{ts} & V_{tb} \end{pmatrix} \begin{pmatrix} d \\ s \\ b \end{pmatrix}, \tag{1.35}$$

and the CKM matrix is often parametrised by three mixing angles and the complex CP-violating KM phase [38]:

$$V_{CKM} = \begin{pmatrix} c_{12}c_{13} & s_{12}c_{13} & s_{13}e^{-i\delta} \\ -s_{12}c_{23} - c_{12}s_{23}s_{13}e^{i\delta} & c_{12}c_{23} - s_{12}s_{23}s_{13}e^{i\delta} & s_{23}c_{13} \\ s_{12}s_{23} - c_{12}c_{23}s_{13}e^{i\delta} & -c_{12}s_{23} - s_{12}c_{23}s_{13}e^{i\delta} & c_{23}c_{13} \end{pmatrix}, \tag{1.36}$$

where $c_{ij} = cos\theta_{ij}$, $s_{ij} = sin\theta_{ij}$, and $\delta$ is the aforementioned complex phase.

Because of the fundamental significance of the CKM matrix, its elements are subject to meticulous measurement through numerous experiments, as shown in Table 1.2. The strengths of the couplings exhibit considerable variations depending on the specific pair of quarks involved. Notably, the element $V_{tb}$ is remarkably close to 1, indicating a very strong coupling between the top and bottom quarks. Another phenomenon to mention with regards to quark mixing in EW interactions are neutral currents. When applied to quarks they are called *flavour-changing neutral currents (FCNC)*, where a quark and an antiquark of different flavours exchange a chargeless boson and leads to changes in quark

| CKM element | Global fit value |
|---|---|
| $\lvert V_{ud}\rvert$ | $0.97435 \pm 0.00016$ |
| $\lvert V_{us}\rvert$ | $0.22500 \pm 0.00067$ |
| $\lvert V_{ub}\rvert$ | $0.00369 \pm 0.00011$ |
| $\lvert V_{cd}\rvert$ | $0.22486 \pm 0.00067$ |
| $\lvert V_{cs}\rvert$ | $0.97349 \pm 0.00016$ |
| $\lvert V_{cb}\rvert$ | $0.04182^{+0.00085}_{-0.00074}$ |
| $\lvert V_{td}\rvert$ | $0.00857^{+0.00020}_{-0.00018}$ |
| $\lvert V_{ts}\rvert$ | $0.04110^{+0.00083}_{-0.00072}$ |
| $\lvert V_{tb}\rvert$ | $0.999118^{+0.000031}_{-0.000036}$ |

Table 1.2: The absolute values of the nine CKM matrix elements are determined through a comprehensive global fitting procedure that considers all accessible measurements [39].

flavour during the interaction. Due to the interplay of the W and Z bosons and the properties of the CKM matrix, at tree level (the simplest interactions), FCNC processes are forbidden, and at higher orders they require a loop process involving virtual W exchange but are highly suppressed. This is described by the Glashow-Iliopoulos-Maiani (GIM) mechanism [40].

## 1.3 Spontaneous Symmetry Breaking

The electroweak Lagrangian, as depicted in Equation 1.34, encompasses interactions between the electromagnetic and weak fields, yet it initially omits the consideration of masses for the associated bosons. This was first experimentally observed in 1983 with the SPS matter-antimatter collider, where evidence was detected for massive W and Z bosons [41–43]. Specifically, the W bosons exhibit a mass of $80.4 \pm 0.012$ GeV and the Z boson has a mass of $91.2 \pm 0.002$ GeV [39].

To account for these masses, the concept of *Spontaneous Symmetry Breaking (SSB)* within the electroweak model was introduced. It involves the Higgs field acquiring a non-zero *Vacuum Expectation Value (VEV)*, which breaks the symmetry and generates masses for the W and Z bosons. As a result, the weak force transitions to a short-ranged interaction, the W and Z bosons attain mass, and the photon remains massless.

The concept of spontaneous symmetry breaking was initially developed by Jeffrey Goldstone in 1961 for global symmetries, leading to the prediction of massless

Goldstone bosons [44]. The application of symmetry breaking to local gauge symmetries was later influenced in 1962 by Philip W. Anderson's work in condensed matter physics, specifically in the context of superconductivity [45]. Then in 1964, a comprehensive theory of spontaneous gauge symmetry breaking was developed by Peter Higgs, François Englert, Robert Brout, Gerald Guralnik, C.R. Hagen, and Tom Kibble, in which the scalar field doublet known as the Higgs doublet, denoted here as $\phi(x)$, was formulated [46–48]. The Lagrangian for the Higgs field in the context of $SU(2)_L \times U(1)_Y$ symmetry is expressed as follows:

$$\mathcal{L}^{Higgs}_{SU(2)_L \times U(1)_Y} = D_\mu(x)^\dagger D^\mu \phi(x) - V(x) \tag{1.37}$$

where the covariant derivate $D^\mu$ is constructed with respect to the electroweak gauge fields $B^\mu$ and $W^\mu$. The Higgs doublet $\phi(x)$ is defined as:

$$\phi(x) = \begin{pmatrix} \phi^+(x) \\ \phi^0(x) \end{pmatrix}, \tag{1.38}$$

The potential $V(x)$ encompasses terms in the scalar field relating to its mass and self-interactions:

$$V(x) = \mu^2 \phi^\dagger(x)\phi(x) + \lambda(\phi^\dagger(x)\phi(x))^2 \tag{1.39}$$

The parameters $\lambda$ and $\mu$ determine the shape of the Higgs potential and, consequently, the symmetry. A representation of this can be seen in Figure 1.7. To ensure the potential is bounded from below, it is necessary that $\lambda > 0$. However, $\mu$ can be either positive or negative. If $\mu > 0$, a vacuum state occurs where $\phi^\dagger\phi = 0$. Alternatively, if $\mu < 0$, a ring of local minima form at:

$$\phi = \left| \sqrt{\frac{-\mu^2}{\lambda}} \right| = |v| \tag{1.40}$$

Here, $v$ signifies the vacuum expectation value of the Higgs field, giving rise to a range of distinct vacuum states with equal energy. This spontaneous symmetry breaking, where $\phi \to e^{-i\phi}$, breaks the $SU(2)_L(1)_Y$ symmetry yet retains the gauge invariance of the Lagrangian. As a result, this mechanism imparts mass to the $W^\pm$ and $Z$ bosons, and also gives rise to the physical Higgs boson.

The natural question arising from the presence of gauge boson masses is: what of the fermions? Within the framework of Higgs-induced spontaneous symmetry

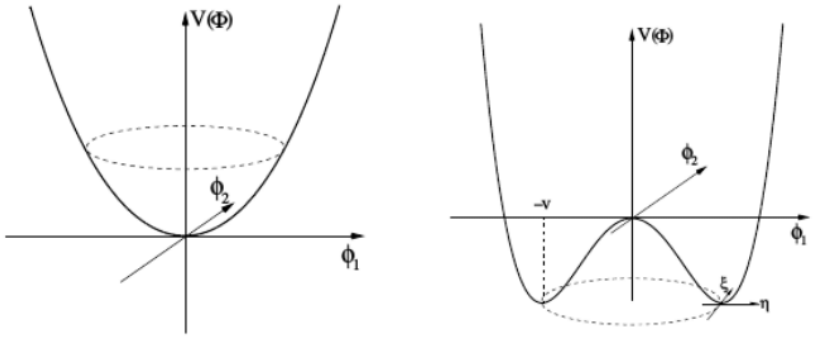


Figure 1.7: Higgs potential for $\mu^2$ (left) and $-\mu^2$ (right) [49].

breaking, fermions can also acquire mass. This is achieved by incorporating Yukawa interactions into a Lagrangian that combines fermions:

$$\mathcal{L}_{Yukawa} = -\zeta_f[\bar{f}_L \phi f_R + \bar{f}_R \phi^\dagger f_L], \tag{1.41}$$

where $\zeta_f$ denotes the Yukawa coupling associated with a specific fermion $f$. When the electroweak symmetry is broken, the Yukawa term becomes:

$$\mathcal{L}_{Yukawa} = -\frac{\zeta_f v}{\sqrt{2}} f\bar{f} - \frac{\zeta_f H}{\sqrt{2}} f\bar{f} \tag{1.42}$$

This implies that the coupling of the Higgs to fermions is proportional to the Yukawa coupling $\zeta_f$ and to the Higgs field $H$ as $-\frac{\zeta_f}{\sqrt{2}} H f \bar{f}$ and this is illustrated with a Feynman diagram in Figure 1.8. The fermion acquires mass through the interaction with the Higgs field, and the mass is given by $m_f = \frac{\zeta_f v}{\sqrt{2}}$. The first

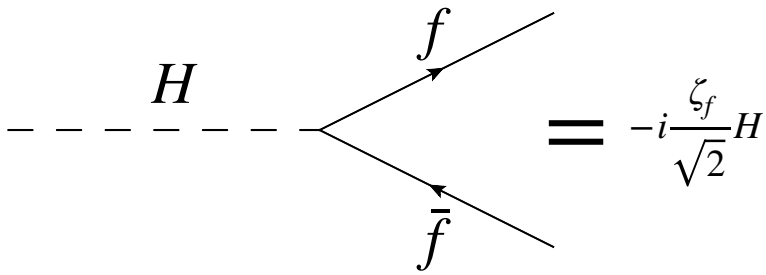


Figure 1.8: Feynman diagram for vertex of an interaction between two fermions and a Higgs boson.

observation of the top Yukawa coupling was directly measured in 2018 in the $t\bar{t}H$ production channel at the LHC [50].

## 1.4 Quantum Chromodynamics

The appropriately named strong force stands as the most powerful natural known force. *Quantum Chromodynamics (QCD)* provides the theoretical foundation for describing this strong interaction. Within the realm of QCD, quarks and gluons engage in interactions governed by the $SU(3)_C$ symmetry group, where the subscript $C$ indicates the colour charge, and quarks exist in three distinct colours.

Due to the nature of the triplet of colours, and that gauge transformations act differently on quarks and antiquarks ($3 \neq 3^*$), all $SU(3)$ transformations must be gauged. This suggests that $q\bar{q}$ pairs and $qqq$ triplets form colour singlets called hadrons. Individual quarks and gluons must be bound inside such colour-neutral objects: a property of the theory that is called confinement, described in Section 1.4.1.

Particles composed of a quark-antiquark pair are referred to as mesons. There are nine possible $q\bar{q}$ combinations involving the light $u$, $d$, and $s$ quarks, which are classified into an octet and a singlet of light quark mesons: $\bar{3}\otimes 3 = 1\oplus 8$. The singlet is a unique combination of quark-antiquark pairs, whereas the octet consists of eight combinations with different properties. Particles made up of 3-quark ($qqq$) configurations are termed baryons, and their arrangements are encapsulated as $3 \otimes 3 \otimes 3 = 1_A \oplus 8_M \oplus 8_M \oplus 10_S$. In this expression, $1_A$ represents a unique antisymmetric combination, often symbolised as $\Lambda_1$ which involves one of each quark type $(u, d, s)$. The $8_M$ terms denote two sets of octets, each with mixed symmetry properties, while $10_S$ represents a decuplet of symmetric states. The subscripts $A$, $M$, and $S$ indicate the symmetry properties of these states under the exchange of any two quarks. An interesting phenomenon in the quark model is the possibility of state mixing. This occurs when two or more states have the same quantum numbers (such as spin and parity) and can therefore mix to form physical particles. A notable example of this is the mixing of the $\eta$ and $\eta'$ mesons. The $\eta$ meson is primarily a mixture of up, down, and strange quark-antiquark pairs, often represented at $\frac{1}{\sqrt{6}}(u\bar{u} + d\bar{d} - 2s\bar{s})$. On the other hand, $\eta'$ mesons also contains a mixture of these same quark-antiquark pairs but in a different

combination, usually expressed as $\frac{1}{\sqrt{3}}(u\bar{u} + d\bar{d} + s\bar{s})$. The mixing in the $\eta$ and $\eta'$ mesons is influenced by the breaking of $SU(3)$ flavour symmetry, primarily due to the mass difference between the strange and the lighter up and down quark, and leads to superpositions of these quark-antiquark states.

Until relatively recently, only 3-quark baryons had been experimentally verified. However, in 2003 the Belle experiment first reported observations of exotic 4-quark hadrons, tetraquarks [51]. Also in 2015, the first measurements of 5-quark hadrons, pentaquarks, were reported at the LHCb experiment [52].

$SU(3)$ is a non-abelian group, thus its transformation laws are more intricate than those of its electromagnetic counterpart. In contrast to the previously discussed $U(1)$ scenario, the $SU(3)$ case introduces eight independent transformations. These stem from the $SU(3)$ group, which contains eight parameters according to Lie theory [53]. Similar to the photon in the $U(1)$ case, maintaining gauge invariance necessitates massless gluons. However, photons are electrically neutral, while the gluon has colour charge, meaning that the self-interaction of gauge bosons is possible within the framework of QCD, unlike QED.

Any three-dimensional unitary matrix with a determinant of 1 can be expressed as $U(\epsilon_a) = \exp\left(-i\sum_{a=1}^{8}\epsilon_a\frac{\lambda_a}{2}\right)$, where $\epsilon_a$ corresponds to eight parameters and $\lambda_a$ refers to eight hermitian, traceless Gell-Mann matrices. These matrices satisfy commutation relations characterising the Lie algebra of $SU(3)$:

$$[\lambda_a, \lambda_b] = 2if_{abc}\lambda_c, \tag{1.43}$$

described by real, completely anti-symmetric structure constants $f_{abc}$.

The gauge principle necessitates invariance of the theory concerning arbitrary space-time dependent functions $\epsilon_a(x)$. Instead of a singular gauge field, $A^\mu$, as we introduced in Section 1.1, we now incorporate eight vector fields $G_a^\mu(x)$ into the covariant derivative:

$$(D^\mu q)_i = \partial^\mu\delta_{ij}q_j + ig_s\sum_{a=1}^{8}\frac{G_a^\mu\lambda_{a,ij}}{2}q_j = \left(\partial^\mu + ig_sG^\mu\right)q_i \tag{1.44}$$

Here, the real coupling constant $g_s$ gauges the strength of the quark-gluon interaction, analogous to how the electromagnetic coupling, $e$, quantifies

electromagnetic interaction. In matrix notation:

$$G^{\mu}_{ij} = G^{\mu}_{a}\frac{\lambda_{a,ij}}{2}, \tag{1.45}$$

resulting in the covariant derivative's transformation as:

$$G^{\mu} \to G'^{\mu} = U(\epsilon)G^{\mu}U^{\dagger}(\epsilon) + ig_s\partial^{\mu}U(\epsilon)U^{\dagger}(\epsilon), \tag{1.46}$$

ensuring that $(D^{\mu}q)_i$ transforms analogously to $q_i$ itself.

For propagating gluon fields, an analogous version of the electromagnetic field strength tensor $F^{\mu\nu}$ is needed. This can be achieved by calculating the commutator of two covariant derivatives:

$$[D^{\mu}, D^{\nu}] = [\partial^{\mu} + ig_sG^{\mu}, \partial^{\nu} + ig_sG^{\nu}] = ig_sG^{\mu\nu}. \tag{1.47}$$

The non-abelian field strength tensor $G^{\mu\nu} = G^{\mu}_{a}\frac{\lambda_a}{2}$ adopts the following explicit form:

$$G^{\mu\nu} = \partial^{\mu}G^{\nu} - \partial^{\nu}G^{\mu} + ig_s[G^{\mu}, G^{\nu}]. \tag{1.48}$$

The gauge invariant colour trace:

$$\mathrm{tr}(G^{\mu\nu}G_{\mu\nu}) = \frac{1}{2}G^{\mu\nu}_{a}G^{a}_{\mu\nu} \tag{1.49}$$

possesses the suitable structure for a gluon kinetic term, where $G^{a}_{\mu\nu} = \partial_{\mu}G^{a}_{\nu} - \partial_{\nu}G^{a}_{\mu} + g_sf_{abc}G^{b}_{\mu}G^{c}_{\nu}$ represents the strong strength tensor. This establishes the $SU(3)_c$ invariant QCD Lagrangian, which accommodates $f = 1, ..., N_F$ quark flavours, leading to the QCD Lagrangian:

$$\mathcal{L}_{\mathrm{QCD}} = \sum_{f=1}^{N_F}\bar{q}_{f,i}\left(i\gamma^{\mu}(D_{\mu})_{ij} - m_f\delta_{ij}\right)q_{f,j} - \frac{1}{2}\mathrm{tr}(G^{\mu\nu}G_{\mu\nu}) \tag{1.50}$$

With the last term of Equation 1.50 being the kinetic term plus the self-interactions.

An example of one of the QCD vertices is displayed in Figure 1.9.

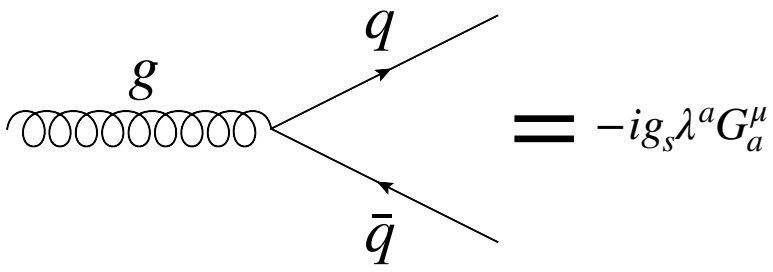


Figure 1.9: Feynman diagram for a QCD vertex of an interaction between two quarks and a gluon.

### 1.4.1 Running Coupling Constant and Renormalisation

In previous sections, we have provided illustrations of Feynman diagrams representing interaction vertices as examples. The strength of these interactions between particles and gauge bosons are governed by what is called a *coupling constant*; given as $\alpha$ in EM interactions, $\alpha_W$ for weak interactions, and $\alpha_s$ with strong interactions. Although known as coupling constants, these values actually depend on the interaction energy scale $Q^2$ and so are also known as *running* coupling constants. The relationship between the running coupling constants and the interaction energy scale is illustrated in Figure 1.10.

At low energies, the electromagnetic coupling constant assumes the well-known value of the fine-structure constant, denoted as $\alpha \approx 1/137$ [55], and experiences a slight increase at higher energy scales. Meanwhile, the weak force's coupling constant, $\alpha_W$, is significantly weaker than $\alpha$ at low energies. The primary reason for the weak force's reduced strength at low energies is due to the massive nature of its force carriers, the W and Z bosons. These masses that result from the Higgs mechanism, make the weak force short-ranged and weaker compared to the long-range electromagnetic force mediated by massless photons. While $\alpha_W$ is weaker than $\alpha$ at low energies, it becomes more comparable at higher energies, particularly near the electroweak symmetry breaking scale.

Strong interactions exhibit a similar behaviour in terms of running coupling constants as the weak force, however there are some differences, as shown in Figure 1.11. In QCD, quantum fluctuations lead to a loop correction (or cloud) of virtual $q\bar{q}$ pairs, and gluon self-interactions lead to a loop correction of virtual

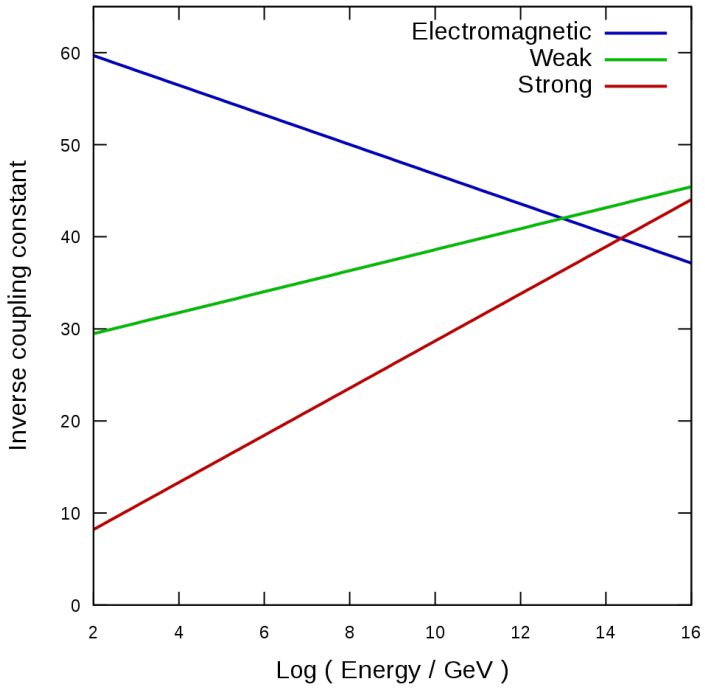


Figure 1.10: Running coupling constants as a function of interaction energy scale in the different force regimes [54].

gluons.[7] Due to gluon self-interactions, as particles are probed at larger distances the exchange of gluons between themselves creates a complex environment of colour charges; this is called *colour screening*. The effective colour increases at larger distance (low energy) meaning $\alpha_s$ is large, making it impossible for the quarks to be separated into isolated particles; this is *quark confinement*. At high energies (small distance), $\alpha_s$ is small and quarks can be treated as free particles; this is *asymptotic freedom*.

Due to the coupling assuming modest values when dealing with large energy scales, observables linked to quarks and gluons, such as their production rates, can be computed using perturbative methodologies. An example of the $\alpha_s$ measurements as a function of energy scale for different perturbative regimes is displayed in Figure 1.12.

[7]Virtual corrections are corrections that enter a calculation but do not produce any new particles.

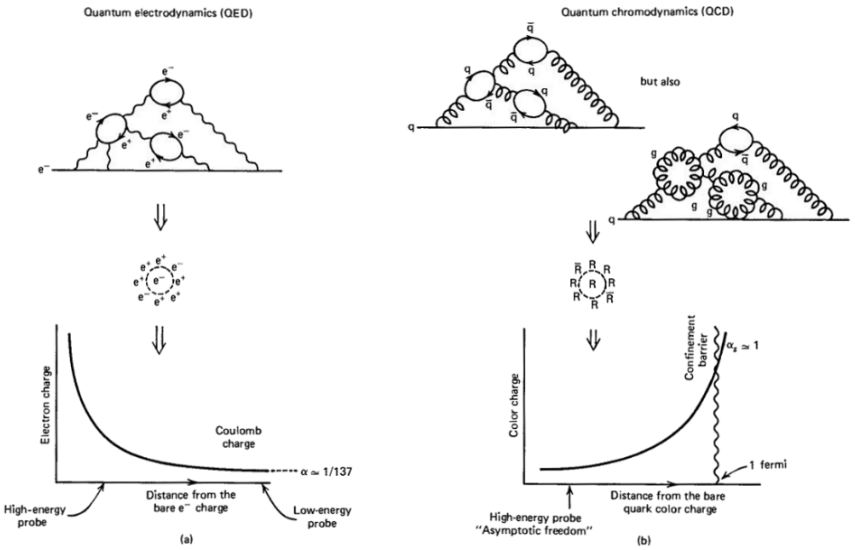


Figure 1.11: Screening in the electric (left) and colour (right) charge in QFT [56].

### 1.4.2 Perturbative QCD

Perturbative QCD employs a series expansion in terms of $\alpha_s$ to describe QCD processes at higher energies where the interactions become weaker. This expansion is typically represented as a power series, where each term corresponds to a higher-order interaction between quarks and gluons. The expansion can be expressed in terms of an observable $\mathcal{O}$ as follows:

$$\mathcal{O} = \mathcal{O}_0 + \alpha_s \mathcal{O}_1 + \alpha_s^2 \mathcal{O}_2 + \ldots + \alpha_s^n \mathcal{O}_n \tag{1.51}$$

In this context, $\mathcal{O}_0$ represents the *leading-order (LO)* term, which accounts for particles in the initial and final states as well as virtual propagating particles. The *next-to-leading-order (NLO)* term, denoted as $\mathcal{O}_1$, includes radiative corrections and higher-order effects, typically of the order $\alpha_s$. These corrections are depicted, for instance, by closed loops or real emissions in Feynman diagrams as shown in Figure 1.13.

At the next level of precision, the *next-to-next-to-leading-order (NNLO)* term, represented by $\mathcal{O}_2$, achieves an order of $\alpha_s^2$ and incorporates additional corrections and effects beyond NLO. This hierarchy of terms can theoretically extend infinitely to $\mathcal{O}_n$, but practical limitations arise due to the increasing

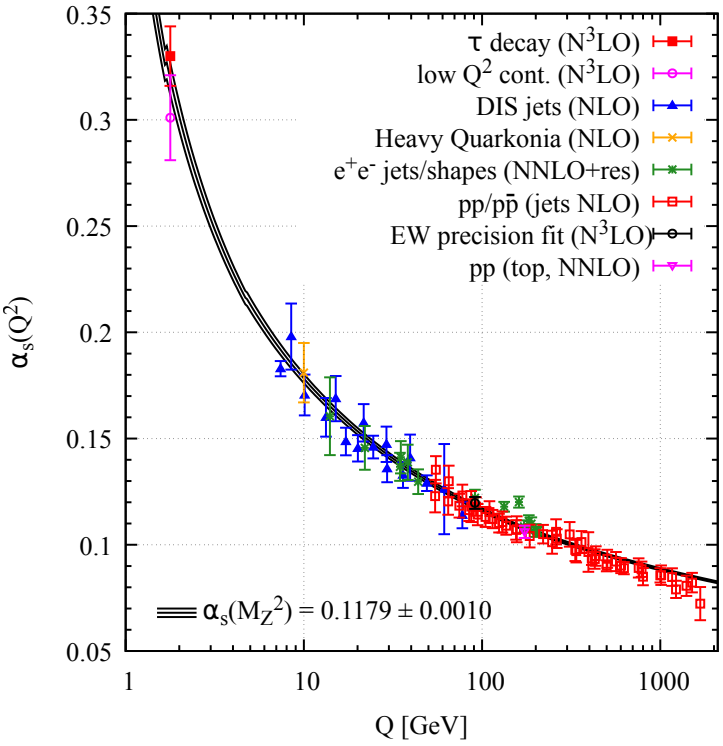


Figure 1.12: A synopsis of $\alpha_s$ measurements across various energy scales Q. The level of QCD perturbation theory employed in deriving $\alpha_s$ is denoted within brackets. These annotations signify the degree of perturbation theory used for the extraction of $\alpha_s$, including NLO (next-to-leading order), NNLO (next-to-next-to-leading order), NNLO +res. (NNLO matched with a resummed calculation), and N3LO (next-to-NNLO) [57].

computational demands of higher-order calculations. Although each term in the series corresponds to interactions at lower energies, the precision of many processes depend on higher-order calculations.

When performing calculations using perturbation theory, often times non-interacting theories are used as a starting point because they are more manageable. Interaction effects are then treated as perturbations on top of this non-interacting theory. However, predictions of such a theory need to be expressed in terms of modified, physical properties, such as masses and couplings of particles due to interactions modifying these properties.

When, however, confronted with confinement at low energy scales, where $\alpha_s > 1$, the perturbative expansions break down and processes must be described by non-perturbative QCD. When the binding energy exceeds the threshold for quark-antiquark generation, the formation of new quark and gluon pairs begins, which

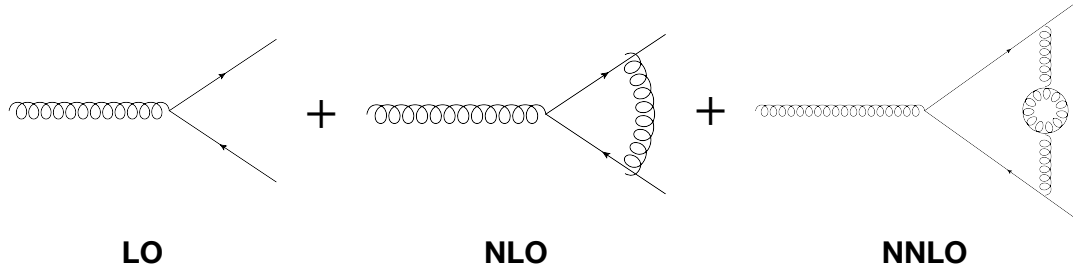


Figure 1.13: Examples of Feynman diagrams for gluon-to-quark interactions for the different virtual corrections in perturbative QCD.

is a process referred to as *hadronisation*. After this, these newly formed particles undergo *fragmentation*, interacting with each other and the initial pair to generate an array of colour-neutral hadrons. Each of these hadrons inherits a fraction of the original particle's momentum. These clusters of hadrons, termed jets, represent the experimentally observable remnants of quarks or gluons generated during high-energy interactions. These jets play a very important role in hadron colliders, such as the LHC.

Due to confinement, quarks are not directly observable as free particles; thus quarks must be measured from jet reconstruction. Another result of this is that quark masses are not observable, and must be re-defined through theoretical prescriptions in QFT called renormalisation schemes.

The LHC is discussed in detail in Chapter 2, jet phenomenology is described in depth in Part II, and the hadronisation of particles within the realm of particle detectors is explained in Section 3.3.

### 1.4.3 Divergences and Renormalisation

At higher order in perturbation theory, closed loops associated with unconstrained momenta that can approach infinity are encountered, leading to the occurrence of Ultraviolet (UV) divergences. To combat divergences such as this, two procedures are introduced: *regularisation* and *renormalisation*.

Regularisation renders infinite integrals finite and is required to preserve the theoretical local symmetry. The simplest regularisation scheme is cutoff regularisation, which requires a momentum cutoff, denoted by $\Lambda_{UV}$, preventing integrals from reaching infinite values. Physically, this mimics the idea that certain

processes are only valid up to a certain energy scale, beyond which new physics might emerge.

In practice, a more widely used scheme is dimensional regularisation, which treats dimensions as a continuous parameter $d$. This satisfies the idea that Feynman integrals would exhibit finiteness if the spacetime dimension were below 4, and their results would manifest as analytic functions with respect to the dimension. The integral dimension is therefore defined as $d = 4 \rightarrow d' = d - 2\epsilon$ [58]. Here $\epsilon$ is a parameter that defines how divergences are considered when a term contains a $1/\epsilon$ factor. A renormalisation parameter $\mu_R$ must be included to keep the coupling constant dimensionless when considering $\epsilon \rightarrow 0$.

The divergent parameters that arise in loop calculations are absorbed by allowing the the renormalised parameters in the Lagrangian to depend on $\mu_R$. When applying the regularisation scheme such as dimensional regularisation, it cancels out the divergent terms in the loop integrals leaving the divergences effectively removed and giving rise to physically meaningful results.

Different choices of how to absorb the divergences lead to different schemes known as *Renormalisation Schemes (RS)*. Each RS has its own set of renormalised parameters that depend on the renormalisation scale. This dependence reflects the fact that the theory's predictions can vary depending on the scale at which renormalisation is performed.

The physical observables must remain invariant under changes of the renormalisation scale. This can be ensured by taking the *Renormalisation Group Equation (RGE)*:

$$\begin{aligned} &\mu_R^2 \frac{d}{d\mu_R^2} \mathcal{O}\left(\frac{Q^2}{\mu_R^2}, \alpha(\mu_R^2), m(\mu_R^2)\right) \\ &= \left(\mu_R^2 \frac{\partial}{\partial \mu_R^2} + \beta(\alpha)\frac{\partial}{\partial \alpha} - \gamma(\alpha) m \frac{\partial}{\partial m}\right)\mathcal{O} \\ &= 0 \end{aligned} \tag{1.52}$$

This ensures the invariance of an observable $\mathcal{O}$ with respect to the coupling constant, $\alpha$, and mass term, $m$.

Two extra dimensionless terms are introduced. The first is the beta function describing how the coupling constant evolves with changes in the renormalisation

scale:

$$\beta(\alpha) = \mu^2 \frac{\partial \alpha}{\partial \mu_R^2} = -\sum_{i=0} (\beta_i \alpha^{i+2}) \tag{1.53}$$

The second is the anomalous mass dimension describing how the mass parameter evolves with changes in the scale:

$$\gamma(\alpha) = -\mu_R \frac{1}{m} \frac{\partial m}{\partial \mu_R^2} = \sum_{k=0} (\gamma_k \alpha^{k+1}) \tag{1.54}$$

These solutions of the RG equations describe how parameters evolve with changes in the renormalisation scale. This running behaviour can be expressed as a power series in terms of $\alpha$. The parameters are often renormalised to a reference scale ($\mu_0$) where accurate measurements can be made, ensuring consistency between theoretical predictions and experimental measurements. An example of this is the running of $\alpha$ at LO being evaluated at a reference scale $\alpha(\mu_0)$, where $\mu_0 << \mu_R$:

$$\alpha(\mu_R^2) = \frac{\alpha(\mu_0^2)}{1 + \beta_0 \alpha(\mu_0^2) log(\frac{\mu_R^2}{\mu_0^2})} \tag{1.55}$$

In QED, where the coupling constant is expressed as $\alpha = \frac{\alpha_{QED}}{\pi}$, the LO beta function is $\frac{2}{3}\alpha^2$. Conversely, in the case of QCD, where the coupling constant is defined as $\alpha = \frac{\alpha_s}{\pi}$, the beta function becomes $\beta_0 = \frac{11N_c - 2N_f}{12}$, where $N_c$ represents the number of quark colours and $N_f$ corresponds to the number of active quark flavours.

There are a number of renormalisation schemes, namely the $\overline{\text{MS}}$ and MSR scheme, which will be discussed in detailed in Part III in terms of their utilisation for top quark mass measurements.

## 1.5 Problems of the Standard Model

The Standard Model is considered to be one of the most successful scientific models of all time due to the sheer number of experimentally proven predictions it contains. However, we know that it is not complete and fails to explain a number of phenomena. A few examples of this are as follows:

- Hierarchy Problem - The hierarchy problem arises from the apparent

disparity between the strength of the gravitational force and the electromagnetic, weak, and strong forces. It is evident from the Higgs boson's mass. The Higgs mass is several orders of magnitude smaller than the mass that would naturally arise in theoretical calculations involving fundamental constants. This stark difference in predicted and observed mass values is due to quantum corrections.

When integrating over virtual particles' contributions, certain terms exhibit quadratic divergences. These divergences can lead to mass corrections for the Higgs boson that are exceedingly large. To obtain the observed Higgs mass while avoiding enormous quantum corrections, the parameters of the SM need to be precisely fine-tuned which is effective but not elegant. This involves cancelling out large contributions from virtual particles.

- Dark Matter - Observations of galaxies' rotational speeds, the behaviour of galaxy clusters, and the gravitational lensing of light around massive cosmic structures indicate that there exists more matter in the Universe than the mass described by the SM. In fact, it is widely accepted through observational methods, that the matter from the SM only accounts for 10-20% of the matter in the entire Universe [59]. This shortfall suggests the existence of additional matter that is not involved in EM interactions and cannot be directly observed through light-based methods, known as 'dark matter'.

  Several candidate particles for dark matter have been proposed beyond the Standard Model, including *Weakly Interacting Massive Particles (WIMPs)*, axions, and sterile neutrinos. The most widely accepted dark matter theory is named the *Lambda Cold Dark Matter ($\Lambda_{CDM}$)* model [60], which describes relations between high-level quantities such as dark matter density and the large-scale structure of the Universe. However, it does not offer a microscopic description of dark matter, and so does does not propose a specific candidate for the identity of a dark matter particle.

  Experimental efforts to detect and understand dark matter are ongoing, involving many different experiments. There are three main approaches to detect dark matter, as displayed in Figure 1.14. The detection methods include: collider detection with experiments such as detectors within the LHC [61], direct detection with underground detectors such as the LUX-ZEPLIN Dark Matter Experiment (LZ) [62] and

XENONnt experiments [63], and lastly indirect detection with astrophysical observations from detectors such as the Cherenkov Telescope Array (CTA) [64].

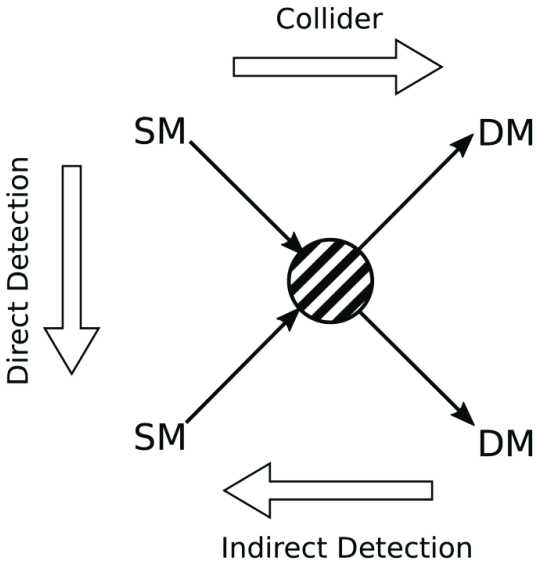


Figure 1.14: Schematic showing possible dark matter detection channels [65].

- Dark Energy - This is based on observations of distant galaxies, supernovae, and the large-scale structure of the Universe. In the late 1990s, it was observed that the Universe's expansion is not slowing down due to gravitational attraction, as one might expect, but is actually accelerating [66, 67]. Instead, the expansion is accelerating, meaning galaxies are moving away from each other at an increasing rate over time which is not described by the SM. On the contrary, SM interactions should predict a decelerating Universe.

  The concept of an energy called 'dark energy' that fills space uniformly is introduced to explain this. Dark energy has negative pressure, which would cause a repulsive gravitational effect, pushing the accelerated expansion of the Universe. Dark energy dominates the energy content of the Universe, roughly 67% [60].

  The prevailing theory of dark energy is from the cosmological constant, $\Lambda$, originally developed by Einstein as a concept to maintain a static Universe [68]. However, when it was proven through red-shift measurements

that the Universe was expanding, this idea was transferred to dark energy to describe an accelerating Universe [69].

- Unification of Forces - The idea of a *Grand Unified Theory (GUT)* aims to unify the three non-gravitational forces (EM, weak, and strong) into a single, more fundamental force at very high energies. While the electroweak theory successfully combines the electromagnetic and weak forces, the strong nuclear force is not included within this combination. Moreover, gravity remains outside the scope of GUTs and the SM, as it is described by the theory of general relativity in the realm of classical physics.

Consequently, various theories have emerged in an attempt to address these challenges, collectively known as *Beyond the Standard Model (BSM)* theories. These include parametrisations such as *Effective Field Theory (EFT)* that allows for operators to be included to the SM, *Supersymmetry (SUSY)* which is a proposal for an extension of the SM, or *String Theory*, which is a mathematical framework speculating what BSM physics could look like.

Within this thesis, we have explored and will continue to delve into facets of EFT. Specifically, we will address processes like renormalisation aimed at mitigating divergences in QCD and restoring perturbation theory, as elaborated upon in Section 1.4.3.

The LHC programme attempts to address some of these questions in several ways, for example by testing solutions to the hierarchy problem and looking for dark matter. The foundation of this thesis, which is a measurement of the top quark mass, is part of the 'precision measurement' method that aims to test the SM with precision measurements of parameters in the SM and relations predicted by the theory.

# Chapter 2

# The Large Hadron Collider

*The European Organization for Nuclear Research (CERN)*, situated in Geneva, Switzerland, hosts an impressive array of accelerator-based experiments. As depicted in Figure 2.1, the map of the CERN accelerator complex illustrates the vast scale of the organisation. At the heart of CERN lies the *Large Hadron Collider (LHC)*, renowned as the world's largest and most powerful particle accelerator. The LHC plays a pivotal role in advancing our understanding of particle physics, probing into the fundamental properties of particles. A significant achievement of the LHC, as discussed in Section 1.3, was the experimental observation of the Higgs boson in 2012 [26].

## 2.1 The LHC Complex

The LHC is based in a 26.7 kilometer circular tunnel that lies 100 meters underground, spanning the border between France and Switzerland. Inside the tunnel, two beams of protons are bended and accelerated to extremely high velocities, ~ 99.9999991% the speed of light, with energies currently up to 6.8 TeV, using a series of superconducting magnets. The beams are then made to collide at four different points around the ring, where detectors are placed to study the resulting particles. Prior to entering the LHC, protons undergo a journey through a chain of injectors that are shown in Figure 2.1. These stages progressively increase the energy of the protons before they are injected into the LHC:

1. The process begins with negatively ionised hydrogen gas ($H$ ions) that are extracted and accelerated to a momentum of 160 MeV through the

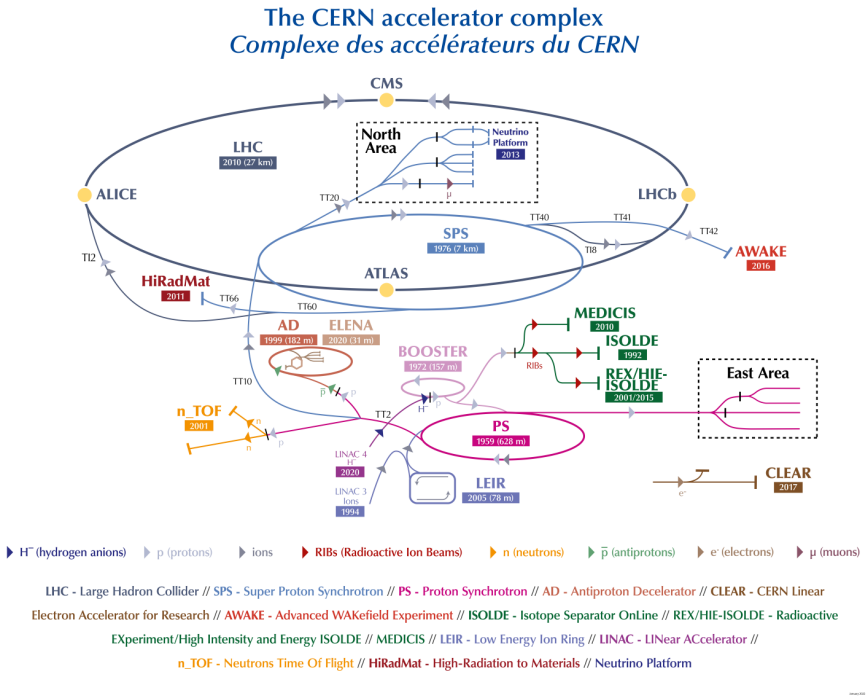


Figure 2.1: Schematic of CERN accelerator complex [70].

Linear Accelerator-4 (LINAC-4), being pulsed through the accelerator for 400 microseconds at a time.[1] At the exit of the LINAC-4, these ions are stripped of their electrons, to leave only protons.

2. They then enter the first circular accelerator, the Proton Synchrotron Booster (BOOSTER), where the protons that are accelerated to reach an energy of 2 GeV.

3. The proton beams then progress to the second circular accelerator, the Proton Synchrotron (PS), with a circumference of 628 m and consisting of 277 electromagnets, the proton beams are further accelerated to up to 26 GeV.

4. Subsequently, they enter the third circular accelerator, the Super Proton Synchrotron (SPS), which reaches a circumference of 7 km and contains 1317 electromagnets, where the protons' energy is increased to 450 GeV. As mentioned in Chapter 1, the SPS acted in the past as a matter-antimatter

[1]The reason to begin with $H^-$ ions as opposed to bare protons is the negative charge enhances the ion's interaction with the magnetic and electric fields used for acceleration and focusing. This allows for more efficient beam control.

collider and was instrumental in the discovery of the W and Z bosons in 1983 [41–43].

5. Finally, the proton beams are injected into the LHC that contains 1232 dipole magnets each of 15 m length and 392 quadrupole magnets that reach 5-7 metres in length. Here is where the protons collide into one another and data is taken for the various experiments [71].

In Figure 2.2 the plan of the LHC is depicted, showing the different runs,[2] upgrade phases, and expected improvements during specific timelines. The LHC was successfully comissioned in 2010, where protons were each accelerated up to an energy of 3.5 TeV, giving a total collision energy (or centre-of-mass energy, $\sqrt{s}$) of 7 TeV and in 2012, the LHC increased the centre of mass energy to 8 TeV. The period of 2010 to 2012 of data taken by the LHC is referred to as Run 1. In this 3-year span, the LHC achieved a total integrated luminosity — a measure indicating the volume of data gathered — of nearly 30 fb$^{-1}$ [72].[3] Luminosity, denoted as $\mathcal{L}$, in $pp$ collisions serves as a significant metric for quantifying the number of collisions taking place per unit area and time interval:

$$\frac{dN}{dt} = \mathcal{L}\sigma \tag{2.1}$$

In this equation, $\sigma$ represents the production cross section of the $pp$ interactions. As the production cross section remains constant, Equation 2.1 underscores the importance of increasing the luminosity to amplify the number of collisions.

The total integrated luminosity in Run 2 data, taken between the years of 2015 to 2018, increased dramatically from Run 1, and reached a value of 160 fb$^{-1}$ [73]. This was also matched with a very large increase in the total collision energy which reached 13 TeV.

At the time of the writing of this thesis, the LHC is currently collecting data in its Run 3 phase until 2025, with an energy of 13.6 TeV and expected to reach a luminosity of 350 fb$^{-1}$ [74]. In the near future a *High-Luminosity (HL)* upgrade to the LHC is expected to be installed to substantially increase the luminosity to 3000 fb$^{-1}$ [74]. For the LHC-based results in this paper, we will be considering the data taken from Run 2, with the corresponding centre-of-mass energy of $\sqrt{s} = 13$ TeV.

[2]The periods during which the collider operates and collects data are typically referred to as 'runs'.

[3]The values for these metrics depend on the LHC-based experiments. The numbers quotes apply to the two general-purpose experiments: ATLAS and CMS

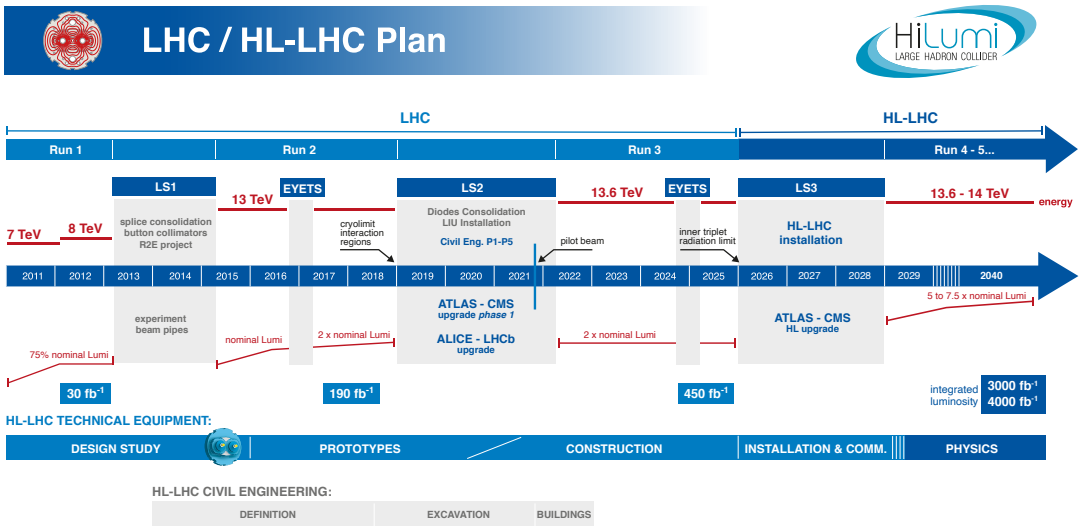


Figure 2.2: LHC and HL-LHC plan [75].

The LHC facility hosts a number of experiments that are used to study the particles produced in $pp$ collisions. The two main detectors are the *A Toroidal LHC ApparatuS* (ATLAS) and the *Compact Muon Solenoid* (CMS). They are made up of many layers of different types of detectors, such as calorimeters, muon chambers, and tracking detectors, which are used to measure the energy, momentum, and position of the particles.

Other detectors include:

- A Large Ion Collider Experiment (ALICE) - This experiment primarily studies heavy ions and the properties of quark-gluon plasma (QGP). Naturally, this also extends to research in QCD-related observables and the strong interaction [76].

- Large Hadron Collider Beauty Experiment (LHCb) - This experiment is mainly focused on the properties of $b$ quarks, primarily to probe CP violation and rare $b$ decays. However, it is also used to study the characteristics of $c$ quarks [77].

- Total, Elastic and Diffractive Cross-Section Measurement Experiment (TOTEM) - This experiment delves into the characteristics of the colliding protons, primarily aimed at precise examinations of the invariant mass

of these collisions. It is the longest-running experiment conducted at CERN [78].

This thesis focuses on the ATLAS detector, which will be discussed in Section 2.3.

By 2017, CERN boasted a community of over 12,200 scientists hailing from 110 different nationalities and affiliated with institutes spanning across more than 70 countries [79]. The LHC stands as one of the most remarkable and impactful scientific and engineering accomplishments ever accomplished, while it holds the distinction of being the world's largest scientific collaboration.

## 2.2 Proton-Proton Collisions

Protons are composite particles, made up of valence quarks, comprising two up quarks and one down quark. Integral to their structure are the gluons that are responsible for the interactions between quarks. Through a phenomenon known as gluon-splitting, gluons can temporarily transform into a quark-antiquark pair. This process results in the generation of additional quark-antiquark pairs inside the proton, known as sea quarks.

Two types of interactions apply to $pp$ collisions: elastic scattering and inelastic scattering. Elastic scattering predominantly occurs at lower energies, while inelastic scattering becomes more prevalent at higher energies. At extremely high energies, such as those reached at the LHC, hard scattering takes place, allowing access to the quark content of the proton.[4] During a collision between two protons at the LHC, a parton from each proton participates in the hard scattering process. This interaction can be treated as independent of the other partons within the protons. The remaining partons contribute to the final state of the event through low-energy hadronic activity. The hard processes are explained in Sections 2.2.1 and 3.1, while the description of the soft processes can be found in Section 3.4.

[4]Technically, the protons in the LHC undergo deep inelastic scattering (DIS), however this term is historically reserved for lepton-hadron interactions.

### 2.2.1 Parton Distribution Function and Factorisation Theorem

The interaction between partons involved in collision processes is described using *Parton Distribution Functions (PDFs)* for non-perturbative processes. PDFs provide the probability, denoted as $f_i(x, Q^2)$, of finding a specific parton within a proton carrying a fraction, $x$, of the proton's total momentum. The PDFs are also dependent on the energy scale, represented as $Q^2$, as well as the flavour of parton, $i$.

The production cross section for any given hard-scatting process can be calculated using the QCD factorisation theorem [80]. This theorem establishes a clear separation between short-distance (perturbative) and long-distance (non-perturbative) physics. The scale that delineates the boundary between these two regimes is referred to as the factorisation scale, denoted as $\mu_f$. A typical choice for $\mu_f$ is approximately the same as the hard scattering scale $Q^2$, such that $\mu_f = \mu_R = Q^2$, where $\mu_R$ is the renormalisation scale discussed in Section 1.4.3 [81].

According to the factorisation theorem, the cross section for a $pp$ interaction can be expressed as the combination of the partonic cross section $\hat{\sigma}_{ij\to ab}$ for the process $pp \to ab + X$, and the proton's PDFs, resulting in:

$$\sigma_{pp\to ab+X} = \sum_{i,j} \int_0^1 dx_1 dx_2 f_i(x_1, \mu_f^2) f_j(x_2, \mu_f^2) \hat{\sigma}_{ij\to ab}(x_1, x_2, s, \mu_f^2, \mu_r^2, \alpha_s) \qquad (2.2)$$

Here, $f_n(x_n, \mu_f^2)$ represents the PDF for parton type $n$, carrying a momentum fraction, $x_n$, of the proton's momentum when probed at the scale $\mu_f$. The centre-of-mass energy of the collision is denoted by $\sqrt{s}$. The $\hat{\sigma}_{ij\to ab}$ term signifies the interaction cross-section between particles, which is calculated in the perturbative regime as a series expansion involving the strong coupling constant, $\alpha_s(\mu_R)$:

$$\hat{\sigma}_{ab} = \hat{\sigma}_{ab,\mathrm{LO}} + \alpha_s(\mu_R)\hat{\sigma}_{ab,\mathrm{NLO}} + \alpha_s(\mu_R)^2\hat{\sigma}_{ab,\mathrm{NNLO}} + \ldots$$

Although PDFs are descriptors of non-perturbative processes, it is possible to perturbatively determine their evolution with respect to $\mu_f$. This is known as PDF evolution. The PDFs are extracted from global fits to experimental data and then extrapolated to new energy scales in QCD. This can be achieved with a set of differential equations known as the *Dokshitzer-Gribov-Lipatov-Altarelli-*

*Parisi (DGLAP)* Equations [82–84]:

$$\mu^2 \frac{d}{d\mu^2} f_a(x, \mu^2) = \sum_b P_{ab}(x, \alpha_s(\mu)) \otimes f_b(x, \mu^2) \tag{2.3}$$

Here, $P_{ab}(x)$ represents the splitting functions, encapsulating the probability of a parton $a$ emitting another parton $b$ while carrying a fraction $x$ of its longitudinal momentum.

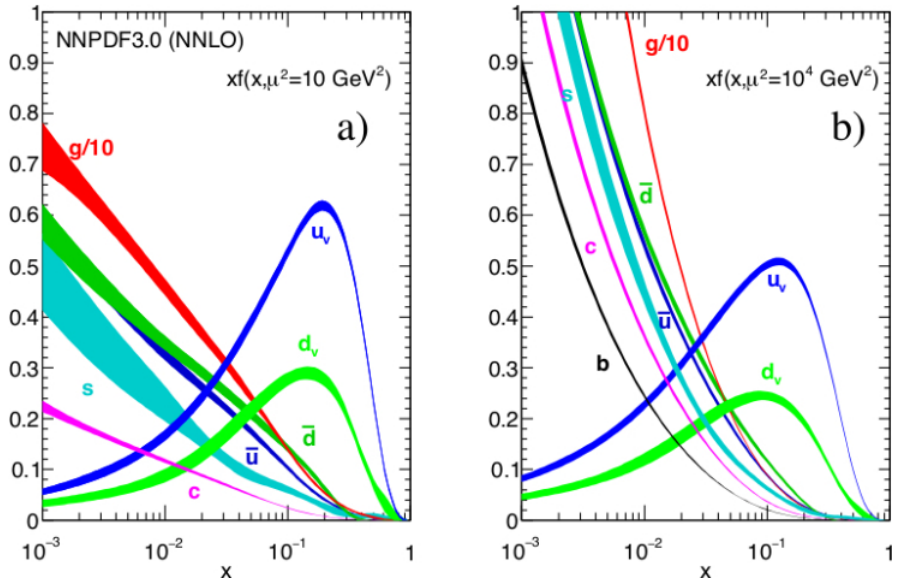


Figure 2.3: The NNPDF 3.1 NNLO PDFs, evaluated at low energies $\mu_f^2$ = 10 GeV$^2$(left) and higher energies $\mu_f^2 = 10^4$ GeV$^2$ (right) [85].

Figure 2.3 shows an example of the PDFs associated to unpolarised protons fitted by the NNPDF collaboration [86] at two different factorisation scales: $\mu_f^2$ = 10 GeV$^2$ and $10^4$ GeV$^2$. The valence quarks, especially $u_v$, tend to have the largest probability of being found at higher momentum fractions for both factorisation cases. However, at lower momentum fraction, the non-valence quarks and gluons have a lot larger probabilities; especially for the higher factorisation scale regime.

Since PDFs are independent of specific processes they can be universally tested by a number of different experiments that study different types of interactions. This is illustrated in Figure 2.4, where the kinematic coverage of the energy scale against momentum fraction is displayed for different interaction processes. These datasets correspond to a number of types of interactions:

- Fixed-target DIS: Involves electrons colliding with a stationary target such as a proton. These experiments have historically been important for probing the structure of protons at various scales of $x$ and $Q^2$ [87].

- Collider DIS: Similar to fixed-target DIS but conducted in collider settings, which enables probing different kinematic regions due to both target and beam particles being in motion.

- Fixed-target Drell-Yan processn : Encompasses quark-antiquark annihilation in fixed target experiments. This results in lepton pairs, offering a window into the sea of quark-antiquark pairs within hadrons [88].

- LHC Data: The rest of the data sets include data from a variety of processes observed at the LHC, crucial for exploring the high-energy behaviour of quarks and gluons.

The associated experiments for each process are outlined in Table 2.1.

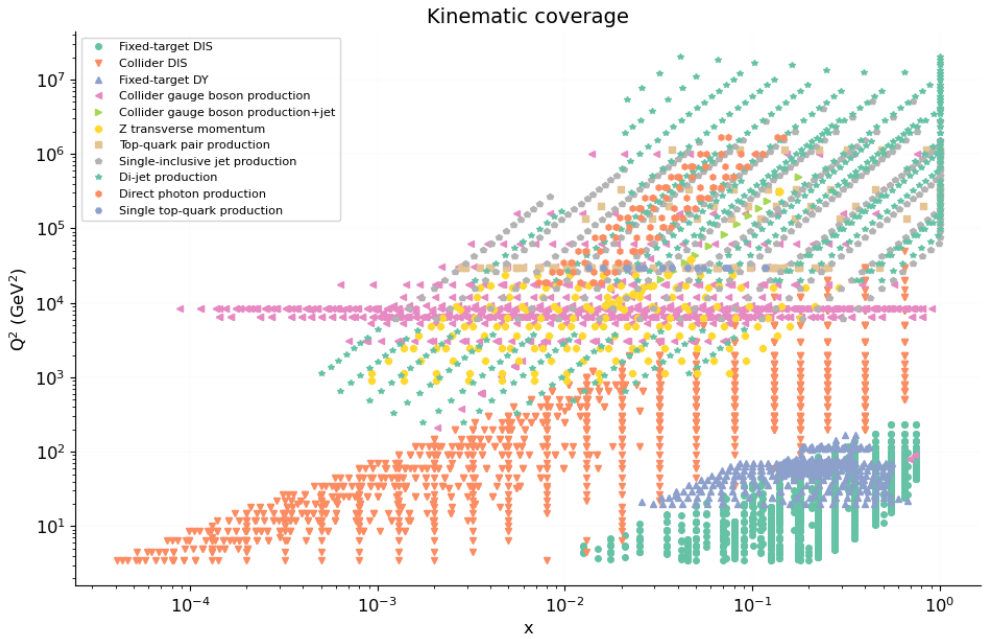


Figure 2.4: Kinematic coverage of NNPDF 3.0 [89].

The NNPDF 3.0 NLO PDF set is the current default for the parametrisation of PDFs in ATLAS MC simulations, with $\alpha_s = 0.118$ [90].

| Process | Experiments |
|---|---|
| Fixed-target neutral-current deep-inelastic scattering (NC DIS) | NMC, SLAC and BCDMS |
| Fixed-target charged-current deep-inelastic scattering (CC DIS) | CHORUS, NuTeV and NOMAD |
| Collider neutral- and charged-current DIS | HERA |
| Fixed-target Drell-Yan (DY) | E866 (NuSea), E605 and E906 (SeaQuest) |
| Collider gauge boson production | CDF, D0, ATLAS, CMS, LHCb |
| Collider gauge boson production with jets | ATLAS, CMS |
| Z boson transverse momentum production | ATLAS, CMS |
| Single-inclusive jet and dijet production | ATLAS, CMS |
| Direct photon production | ATLAS |
| Top-quark pair production | ATLAS, CMS |
| Single top-quark production | ATLAS, CMS |

Table 2.1: List of processes shown in Figure 2.4 and their related experiments [89].

## 2.3 The ATLAS Detector

The ATLAS detector is the largest detector at CERN, having been completed in 2008 after 10 years of construction. It is currently the largest detector for a particle collider, weighing 7,000 tonnes with dimensions of 46 metres in length and 25 metres in diameter.

The coordinate system describing the ATLAS detectors and particles that come from the *pp* collisions considers the positive x-axis to be defined as pointing towards the centre of the LHC ring from the interaction point (origin of the coordinate system), the positive y-axis pointing upwards and the positive z-axis in the direction of the beam. This coordinate framework is used to define the *rapidity* and *pseudo-rapidity* of particles. These are two variables that are essential for characterising the angular distribution of collision products with respect to the beam axis. The rapidity is defined by the equation:

$$y = \frac{1}{2} ln \left( \frac{E + p_z}{E - p_z} \right), \tag{2.4}$$

where $E$ is the energy of the particle and $p_z$ is the component of the particle's momentum along the beam axis.

However, pseudo-rapidity is used widely in LHC analyses as it does not require the measurement of the particle's energy but only of the angle of its trajectory:

$$\eta = -ln \left[ tan \left( \frac{\theta}{2} \right) \right], \tag{2.5}$$

where $\theta$ is the polar angle between the particle's momentum and the beam axis. These measures are useful within the coordinate system of collider experiments

due to the fact that the difference between two different rapidities is Lorentz invariant along the direction of the beam.

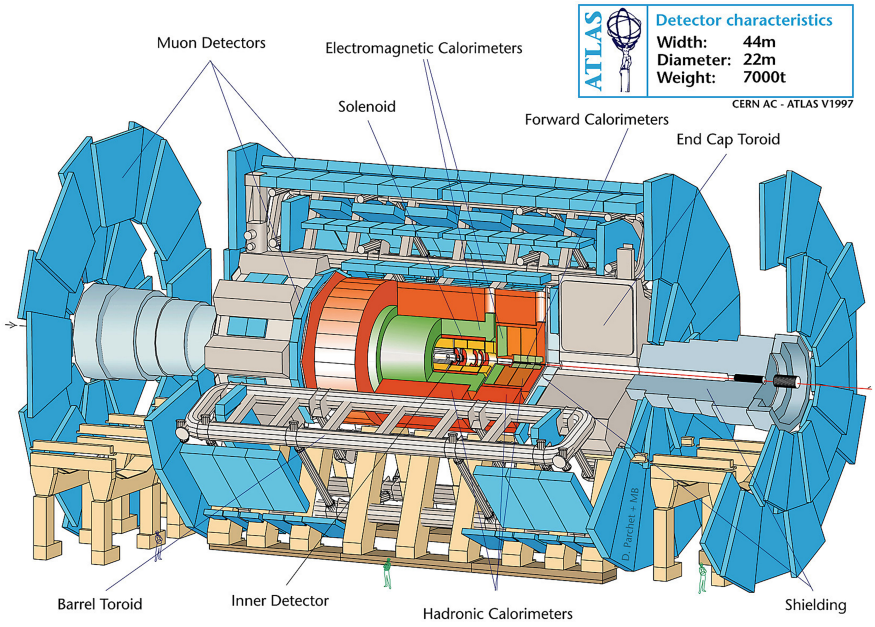


Figure 2.5: Diagram of the ATLAS detector [91].

The ATLAS detector acts as a multi-purpose system consisting of multiple sub-detectors, which each comprise of a cylindrical barrel and two end-caps, as shown in Figure 2.5.

Each of the sub-detectors play a crucial role within the detector, and are required for not only detecting signals from particles but also differentiating which type of particles are being detected. Figure 2.6 illustrates the types of particle signals identified within the ATLAS detector and indicates the specific regions within the detector where they are observed. One notable particle absent from this list is the neutrino, which remains undiscoverable within the ATLAS detector owing to its exceedingly weak interactions with matter. Despite their elusiveness, neutrinos are indeed factored into analyses, often being treated as components of missing energy.

Each of the parts of the ATLAS experiment are described in detail in the following subsections.

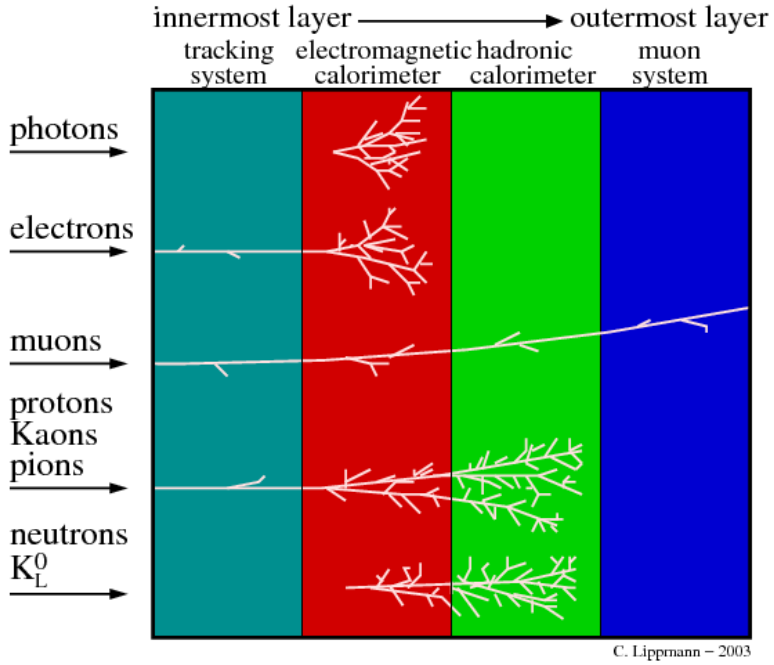


Figure 2.6: Representation of signatures left by different types of particles in the ATLAS detector [92].

### 2.3.1 Inner Detector

The *Inner Detector (ID)* of the ATLAS detector provides high-precision tracking and vertexing capabilities. It is located closest to the collision point and is immersed in a 2 T magnetic field provided by a superconducting solenoid. When charged particles produced in $pp$ pass through this magnetic field, they are deflected. The degree of this deflection depends on the charge and momentum of the particles. By observing the curvature of the particle tracks in the magnetic field, the properties of the particles can be determined. The ID is designed to measure the trajectories of the charged particles produced in the collisions (tracks), as well as their momenta and charges. It is also used to reconstruct vertices (points of origin) of particles. It is designed for an acceptance in pseudorapdity of $|\eta| < 2.5$ for particles coming from the beam-interaction region. Tracks and vertices are discussed in greater detail in Section 4.1.

The ID is composed of three sub-detectors:

- The Pixel Detector is the innermost sub-detector of the ID, being only 3.3 cm away from the beamline, making it the ATLAS detector's first point of detection. It is made up of 92 million individual pixels that are located

closest to the collision point. It contains 4-barrel layers with 1736 sensor modules, and 3 disks in each end-cap with 288 modules. These sensors detect the position of charged particles as they pass through the detector, providing precise position information with a resolution of about 10 microns [93].

  - The *Insertable B-Layer (IBL)* is an additional innermost pixel layer of the Pixel Detector, introduced in Run 2 to cope with the challenges posed by the increased luminosity at the LHC. The IBL was designed to improve the resolution and identification of tracks to improve vertex and track reconstruction while also enhancing the performance of flavour tagging [94].

- The Semiconductor Tracker (SCT) is located outside the Pixel Detector. It is composed of more than 4,000 silicon strip sensor modules, each containing around 6 million "micro-strips" of silicon sensors, that provide high-precision tracking of charged particles. The silicon is distributed over 4 cylindrical barrel layers and 18 endcap disks providing coverage over the full pseudorapidity range of the detector and a spatial resolution of around 25 microns [95].

- The Transition Radiation Tracker (TRT) is the final layer of the ID, located just outside the SCT. It is comprised of 300,000 slender drift tubes possessing a mere 4 mm diameter and housing 31 $\mu m$ gold-plated tungsten wire in its centre. Filled with a gas mixture of primarily xenon, these drift tubes induce ionisation within the gas as charged particles traverse through, generating a discernible electric signal. This signal is harnessed to reconstruct the particles tracks and, due to transition radiation, is used to provide information of the particle type; i.e. electrons or pions [96].

All of these subdetectors work in conjunction with one another to provide high-precision tracking and vertexing of charged particles. The ID is able to reconstruct tracks with a high degree of accuracy, even for particles that have a low transverse momentum, $p_T$ (perpendicular to the beamline). This is crucial for the identification of particles and the reconstruction of physics objects such as jets, electrons, photons and muons.

### 2.3.2 Calorimeter

The calorimeters of the ATLAS detector are crafted with the purpose of measuring incoming particles' energies. This is achieved by absorbing the majority of particles resulting from collisions, ensuring particles lose and deposit their energy within the confines of the detector. ATLAS calorimeters are constructed through a combination of absorbing high-density materials intended to stop incoming particles, with layers of an active medium that quantifies their energy. The calorimeters are located outside the ID and cover a pseudorapidity range of $|\eta| < 4.9$. They are designed to identify and measure the energy of electrons, photons, and hadrons produced in the collisions.

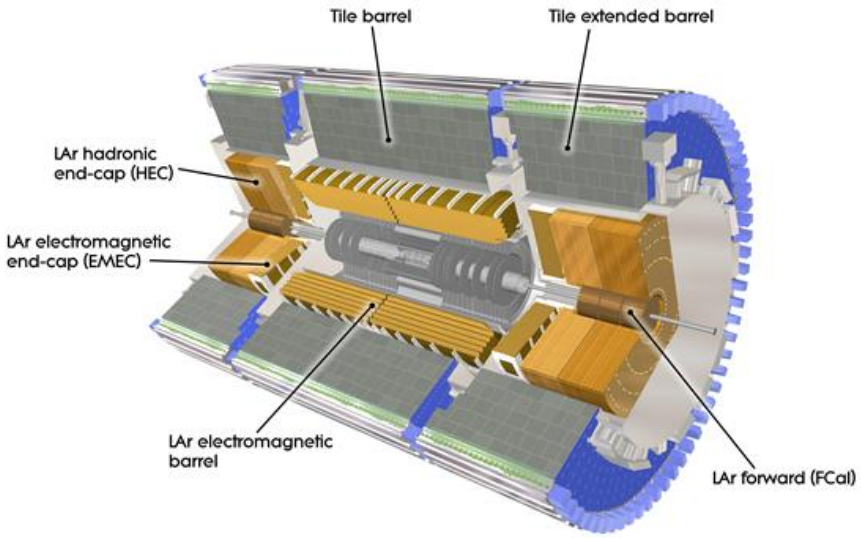


Figure 2.7: Computer generated image of the ATLAS calorimeter system [97].

The ATLAS calorimeters are the *Electromagnetic Calorimeter (ECAL)* (also known as *The Liquid Argon Calorimeter (LAr)*) and *Hadronic Calorimeter (HCAL)* (also known as *The Tile Hadronic Calorimeter (TILE)*). These are shown in Figure 2.7 with their related parts.

The ECAL envelopes the inner detector and measures the energy of primarily electromagnetic particles, such as electrons and photons. It is composed of tiers of metallic materials, including tungsten, copper, or lead, which intercept incoming particles and transforms them into a "shower" of lower energy particles. Charged particles formed in the shower then ionise the liquid argon that is interlaced between these metal layers, generating an electric current that is subsequently

measured. The calorimeter is kept at -184°C to keep the argon in liquid form and is 6.4 m long and 53 cm thick. There is also the ECAL endcap, which contains the forward calorimeter and EM endcap [98]. These endcaps are designed to measure the energy of particles that move close to the direction of the colliding proton beams, i.e. at small angles relative to the beam axis. Although the ECAL is mainly designed for the measurements of EM particles, it can be used to reconstruct the energy of hadrons if the hadronic shower begins in the ECAL.

The ECAL is divided into two sections: the barrel and the endcaps. The barrel is cylindrical in shape and covers the region between the pseudorapidity values of $|\eta| < 1.475$. The endcaps cover the region $1.375 < |\eta| < 3.2$.

However, most hadronic activity is measured by the HCAL, which encloses the ECAL. The HCAL is made up of layers of steel and about 420,000 plastic scintillator tiles. Upon colliding with the steel layers, particles initiate a shower of new particles. After which, the plastic scintillators emit photons, which are converted into an electric current. The intensity of the current corresponds directly to the energy of the initial particle. The HCAL is the heaviest part of the ATLAS detector, coming in with a total weight of 2900 tonnes, and contains 9,500 Photomultiplier Tubes (PMT) that read out the intensity of the produced current to measure the energy deposited by a particle [99].

The HCAL is divided into three parts: the barrel, the hadronic endcaps, and *The Forward Calorimeter (FCAL)*. The barrel and endcaps cover the region $|\eta| < 3.2$, and the FCAL covers the region $3.1 < |\eta| < 4.9$.

### 2.3.3 The Muon Spectrometer

Similar to electrons, muons are a part of the lepton family, but are roughly 200 times heavier than electrons. Due to the fact that they are minimum ionising particles, they are able to pass through the layers of the EM calorimeter. Thus, a separate part of the detector is needed for the identification and measurement of muons that are produced in LHC $pp$ collisions: The *Muon Spectrometer* (MS) [100]. The MS is made up of both precision detectors and fast-response detectors, and covers a pseudorapidity range of $|\eta| < 2.7$.

The precision detectors consist of 3 cm wide aluminium Monitored Drift Tubes (MDTs) filled with a gas mixture of primarily argon. As muons traverse the tubes, they knock electrons from the gas, which subsequently drift towards a wire

located at the tube's centre, inducing a signal. Over 380,000 aluminium tubes with a resolution of 80 microns are stacked in multiple layers to be able to trace the muon's trajectory and determine the position of a muon to one tenth of a millimeter.

The fast-response detectors are placed all throughout the ATLAS detector, with the first being Resistive Plate Chambers (RPCs) that cover the central region of the detector. These detectors are composed of sets of parallel plastic plates maintained at differing electric potentials with gas in between.

At the ends of the ATLAS detector are Thin Gap Chambers (TGCs). Both of these chambers contain 30 $\mu m$ parallel wires in a gas mixture, which when ionised generates a signal to be able to detect muons.

Two extra detector technologies are Micromegas and Small-Strip Thin-Gap Chambers (sTGCs), which are implemented close to the LHC beam pipe to track muons in high-intensity interactions with a high precision.

These detectors all combine to rapidly choose potentially interesting collision events, with decisions being made within 400,000th of a second.

### 2.3.4 ATLAS Trigger, Data Acquisition, and Computing

Within the ATLAS experiment, all of the combined detectors contain tens of millions of individual 'channels', which are distinct regions on the detector's surface where particle interactions generate signals. The LHC, in its relentless cascade of one billion interactions per second, generates a substantial amount of data to analyse, with each event being up to 2.2MB of unprocessed data. Naturally, the task of recording all this data is nigh-impossible. This is where the pivotal role of the *ATLAS Trigger and Data Acquisition* (TDAQ) system comes into play.

The trigger system is a two-tiered system responsible for real-time (online) selection of the subset of events to be recorded. The first level of the trigger system is known as the Level-1 trigger, designed to make a quick decision on whether an event is interesting or not. It processes the data from the ATLAS sub-detectors in real-time by making its decision based on a set of pre-defined criteria, such as the presence of high energy particles or the presence of specific types of particles. The Level-1 trigger reduces the nominal $pp$ interaction rates of 40 MHz to manageable data rate of 100 kHz and has an average processing time

of 2.5 $\mu s$ [101]. This selection is based on broad criteria that identify potentially interesting events. It includes detecting leptons, photons, and jets with sufficient $p_T$, as well as specific combinations of these elements. Specialised triggers are also applied to capture events of particular interest for specific analyses. During the latency period of the Level-1 trigger, the tracker data is temporarily stored in the detector. This data is only read out and further processed if an L1 trigger is issued which ensures efficiency in the data management and prioritises significant events.

The second level of the trigger system, also known as the *High-Level Trigger* (HLT), is designed to make a more detailed decision on whether an event is significant enough. The HLT operates from a farm of roughly 40,000 CPU cores and makes its decision based on a more complex set of criteria based on types of particle interactions. The HLT reduces the data rate from 100 kHz to about 1-1.5 kHz, with an average processing time of the order 400 $ms$.

The data that passes through the trigger system is then passed on to the data acquisition (DAQ) system, which is responsible for collecting and storing the data for further offline analysis. The DAQ system is made up of several components, including data concentrators, data multiplexers, and data storage systems. The data concentrators are responsible for collecting the data from the ATLAS sub-detectors and sending it to the data multiplexers. The data multiplexers are responsible for merging the data from the different sub-detectors into a single stream of data. The data storage systems are responsible for storing the data for further analysis.

Due to the large volume of data that needs to be stored and processed, the Worldwide LHC Computing Grid (WLGC) was created [102]. The WLCG is a global network of computing resources combining about 1.4 million computer cores and 1.5 exabytes of storage from over 170 sites in 42 countries, which allow researches around the world to collaboratively analyse LHC data.

The ATLAS data management system involves multiple tiers, each with specific functions in handling data:

- Tier 0: This is the initial data processing stage, directly connected to the LHC detectors. It receives raw data from the detectors and performs basic data reconstruction and initial processing. The primary goal is to quickly identify and flag interesting events. After this initial processing, the data is distributed to Tier 1 centres.

- Tier 1: These are large computing centres located around the world. They store a copy of the raw and processed data from the Tier 0 centres. Tier 1 centres are responsible for further processing and reprocessing of data, as well as providing data distribution to Tier 2 centres and scientists for analysis. They also play a role in long-term data storage and data preservation.

- Tier 2: Tier 2 centres are typically university or research institution clusters that handle more specific analysis tasks. They receive processed data from Tier 1 centres and distribute it to individual researchers and analysis groups. Scientists perform detailed data analysis and simulations on Tier 2 resources.

- Tier 3: Tier 3 resources are often located at individual research institutions or even on the personal computers of researchers. These resources are used for specific analysis tasks by individual researchers or small groups. Tier 3 resources access data from Tier 2 centres when needed.

The WLGC runs over 2 million tasks per day and global transfer rates can exceed 260 GB/s.

# Chapter 3

# Monte Carlo Simulation

A *Monte Carlo (MC)* Simulation is a computational technique used to model the behaviour of complex systems or processes through random sampling and statistical analysis. The term 'Monte Carlo' originates from the famous casino in Monaco and was coined due to the reliance on random numbers. Within the realm of particle physics Monte Carlo simulations describe everything from the interaction of incoming beam particles in colliders all the way to detector signals by generating large numbers of statistically random events. They are crucial in correcting measurements to a level where they can be compared to theory.

Monte Carlo event generators follow a number of steps to simulate each stage of particle interactions, as displayed in Figure 3.1:

- Hard Scatter Matrix Element Calculation: This step involves formal perturbative calculations to determine the initial hard scatter event. This is where the fundamental interaction that leads to the particle collision or decay is simulated. The calculation is based on solutions of the Lagrangian at a given order in perturbation theory, and takes into account various factors such as energy, momentum, and the types of particles involved. This process is the focus of Section 3.1.

- Parton Shower, Fragmentation, and Hadronisation: After the initial hard scatter, the simulation proceeds to model the subsequent stages of the event. This includes the parton shower, where the quarks and gluons emitted in the hard scatter evolve, and fragmentation and hadronisation, where these partons transform into hadrons. Sections 3.2 and 3.3 discuss these stages in more detail.

- Interactions with the Detector (GEANT4): The final stage of the simulation involves modelling how the generated particles interact with the detector. This is performed using software such as GEANT4 [103], which simulates the passage of particles through matter. This step accounts for various effects such as particle energy loss, scattering, and the detector's resolution, allowing the simulation to accurately represent how particles would be detected in a real experiment.

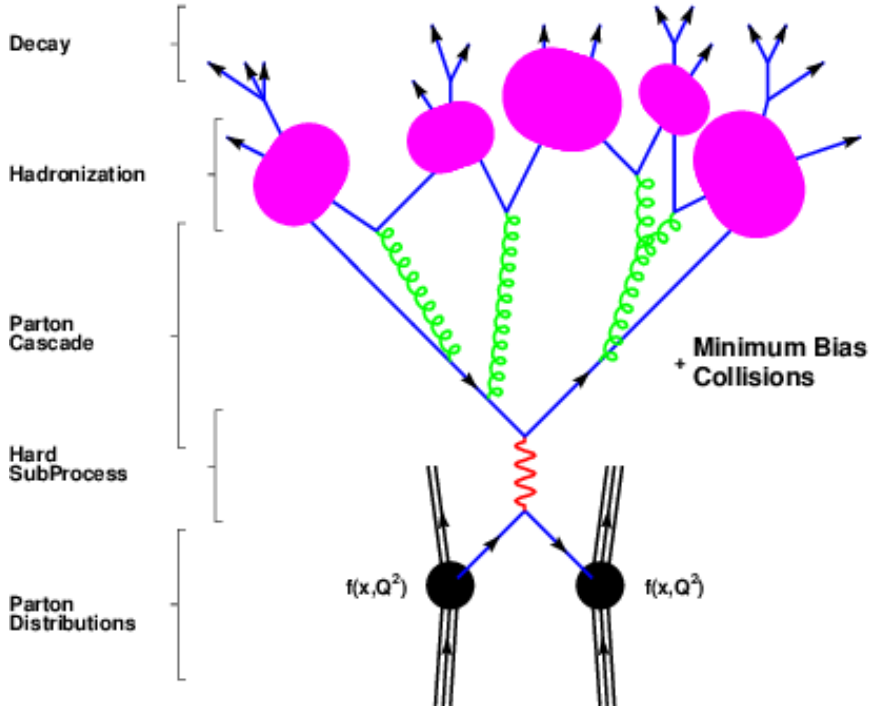


Figure 3.1: The basic structure of a particle collision and its following processes [104].

MC simulations are vital in enabling physicists to predict experimental outcomes, optimise experimental setups, estimate backgrounds from various sources, and possibly discover new physics phenomena by identifying deviations between simulated predictions and actual experimental data. These simulations involve a substantial amount of computational resources and require careful calibration and validation to ensure their accuracy and reliability.

## 3.1 Matrix Element

In the case of the LHC, the *Matrix Element (ME)* in MC simulations defines the perturbative component of the hard scattering cross section for $pp$ interactions, as discussed in Section 2.2.1. In essence, the matrix element is a rigorous perturbative calculation that describes the scattering processes involving partons.

Considering the factorisation theorem presented in Equation 2.2, which combines perturbative and non-perturbative descriptions of the hard scatter, the ME is viewed as the perturbative term within this equation, denoted as $\hat{\sigma}_{ab\to X}$. This term quantifies the probability amplitude $\mathcal{M}$ for the transition from the initial state to the final state $X$, i.e, $t\bar{t}$. It can be expanded and written with regard to a final state for different order corrections denoted as $F$:

$$\hat{\sigma}_F = \sum_{k=0}^{N_{legs}} d\Phi_{X+k} \left| \sum_{l=0}^{N_{loops}} \mathcal{M}_{X+k}^{(l)} \right| \tag{3.1}$$

Here $d\Phi_{X+k}$ is the phase space for the final state, $X$, along with 'legs', k, which are the real additional outgoing partons. $\mathcal{M}_{X+k}^{(l)}$ is the matrix element for the final state including additional partons, with an additional number of virtual corrections (loops), $l$.

The composition of the full final states depends on the specific values assigned to $k$ and $l$. When both variables are set to 0, the final state consists of only $X$ at LO. If $k = n$, where $n$ is a positive integer, it results in the final state $X$ with $n$ extra quarks and gluons. The variable $l$ in Equation 3.1 plays the role of determining the order of precision for the final state production. Specifically, the higher the value of $l$, the more accurate the theoretical prediction becomes, because increasing $l$ involves incorporating more complex loop corrections, which account for higher-order quantum effects. So, as $l$ increases, the calculation progresses from LO to NLO to NNLO, and so on.

## 3.2 Parton Shower

A *Parton Shower* (PS) is defined in the context of higher-order real emission corrections from hard scattering events. This remains a valid approximation up to the energy scale of $Q \approx 1$ GeV. Parton showers consists of the emission of gluons from a particle produced in the matrix element (either quarks or gluons).

These subsequent gluons can emit further gluons or split into $q\bar{q}$ pairs.

The dynamics of parton showers can be mathematically described using the DGLAP equations defined in Equation 2.3. However, instead of as a function of $\mu$ they can be reformulated as a function of energy scale, $Q^2$, to help understand the change of the quark, antiquark, and gluon densities with regards to the QCD splittings:

$$\frac{\partial}{\partial ln Q^2}\begin{pmatrix} q_i(x,Q^2) \\ g(x,Q^2) \end{pmatrix} = \frac{\alpha_s(Q^2)}{2\pi}\sum_j \int_x^1 \frac{dy}{y} \\ \begin{pmatrix} P_{q_iq_j}(\frac{x}{y},\alpha_s(Q^2)) & P_{q_ig}(\frac{x}{y},\alpha_s(Q^2)) \\ P_{gq_j}(\frac{x}{y},\alpha_s(Q^2)) & P_{gg}(\frac{x}{y},\alpha_s(Q^2)) \end{pmatrix}\begin{pmatrix} q_j(y,Q^2) \\ g(y,Q^2) \end{pmatrix} \tag{3.2}$$

Here, $y$ represents the momentum fraction of the parton entering the hard process, and this fraction decreases due to gluon radiation. The symbols $q_i$, $q_j$, and $g$ denote the quark, antiquark, and gluon distributions, respectively, with the flavour indices $i$ and $j$.

There are four possible QCD splittings at LO, $q \to qg$, $q \to gq$, $g \to q\bar{q}$, and $g \to gg$. The Altarelli-Parisi splitting kernels, $P_{i,j}$, describe the probability of such splittings. These splitting functions are visually represented in Feynman diagrams in Figure 3.2, where $z = \frac{x}{y}$.

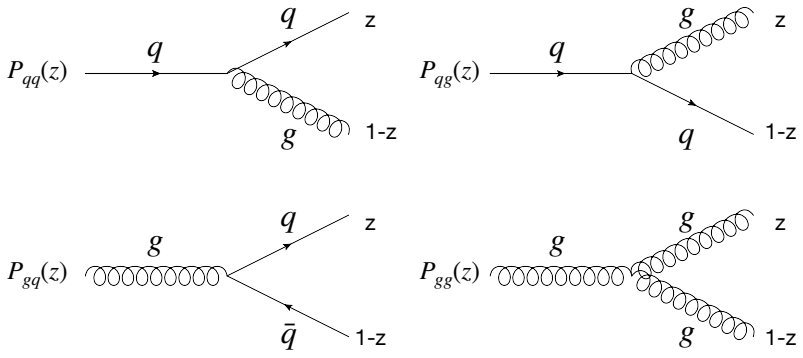


Figure 3.2: The splitting functions of the $q \to qg$, $q \to gq$, $g \to q\bar{q}$, and $g \to gg$ splittings.

There are instances when a parton remains unaltered and does not split into

further partons. This is characterised by the probability a parton does not undergo further splittings between two distinct energy scales or momentum transfer scales, denoted as $P_a(t)$:

$$P_a(Q) = \Gamma_a(Q) \exp\left(-\int_{q_0}^{Q} dQ' \Sigma_a(Q')\right) \tag{3.3}$$

Here, $\Gamma_a(Q)$, represents the branching rate for a specific parton $a$ as a function of the energy scale $Q$. It quantifies how likely it is for this parton to undergo further branchings within the energy range between the initial scale, $q_0$, and final scale, $Q$. The integral $\int_{q_0}^{t} dt' \Sigma_a(Q')$ involves summing up the branching probabilities over the entire range from $q_0$ to $Q$ and accounts for all possible branchings that could have occurred during the parton's evolution. The Sudakov form factor, represented as $\exp\left(-\int_{q_0}^{Q} dQ' \Sigma_a(Q')\right)$, reflects the likelihood of not observing further branchings between $q_0$ and $Q$. This factor increases as the likelihood of additional branching decreases, reflecting an exponential decrease in the probability of observing further splittings. This suppression arises from QCD, in which, while the probability of gluon radiation increases with the energy of a parton, a phenomenon known as *Colour Coherence* causes an interference effect that can suppress emissions at certain angles, especially in dense partonic environments [105].

Additional radiation is not limited to occurring solely after the primary hard-scatter event; it can also manifest before it. Radiation produced prior to the primary hard-scatter interaction is termed *Initial-State Radiation (ISR)*, while radiation arising after the hard-scatter is known as *Final-State Radiation (FSR)*. ISR and FSR primarily consist of soft collinear particles, yet they can encompass hard emissions that have the potential to impact the final state, including the formation of high-energy jets.

## 3.3 Hadronisation

After the PS completes its role, all remaining coloured partons in the final state undergo a process known as *hadronisation*, where they combine to form colour-neutral hadrons. The transition from the perturbative parton shower to the non-perturbative hadronisation algorithm happens at the parton shower cut-off scale. The cut-off is usually set to approximately 1 GeV where the strong

coupling constant becomes large, perturbation theory becomes ineffective. On the other hand, *fragmentation* refers to the concept of fragmentation functions, which are used in MC simulations to describe the probability distribution of how the energy of a quark or gluon is shared among the produced hadrons. An example of fragmentation is a $b$–quark forming $B$–hadrons. The terms hadronisation and fragmentation are sometimes used interchangeably, but technically describe different aspects of the process by which quarks and gluons transition to hadrons.

In the non-perturbative domain of hadronisation, the conventional tools of perturbative QCD are no longer applicable, meaning the understanding and modelling of hadronisation are predominantly based on phenomenological approaches which serve as approximations to describe hadronisation. There are two main methods of this: *Lund string fragmentation* [106] and *cluster fragmentation* [107]. These methods are used in different MC generators that will be discussed later in this chapter.

The concept of the Lund string model is that the strong force between quarks is represented by 'strings' of colour charge, as is portrayed in Figure 3.3, which is motivated by the confinement properties of QCD. The strong force is represented by an elastic string-like connection and, as the quarks move apart and the strong force increases, the energy in the string increases. When the energy surpasses the limit of tension of the string, it snaps, which is analagous to the creation of a new quark-antiquark pair. This process continues until there are no more high-energy strings left and the newly formed quarks and anti-quarks combine, forming colour-neutral hadrons. MC simulations use probabilistic methods to model the formation of strings, their breaking, and the creation of hadrons.

As opposed to the string-like behaviour of the colour charge with regards to quarks and gluons in the Lund string model, the cluster fragmentation model proposes that quarks and gluons combine into smaller colour-neutral clusters. This is motivated by the observation that cluster properties are invariant under energy. These high-energy clusters are formed spontaneously and can be composed of combinations of quarks and gluons; as long as their colour charge cancels out, ensuring colour neutrality. These clusters are considered precursors to the colour-neutral hadrons and decay into these hadrons once formed, without the need for continuous string breaking. The specific processes by which clusters decay and the types of hadrons (i.e. baryons or mesons) they produce can depend on the energy, momentum, and other kinematic properties of the initial partons.

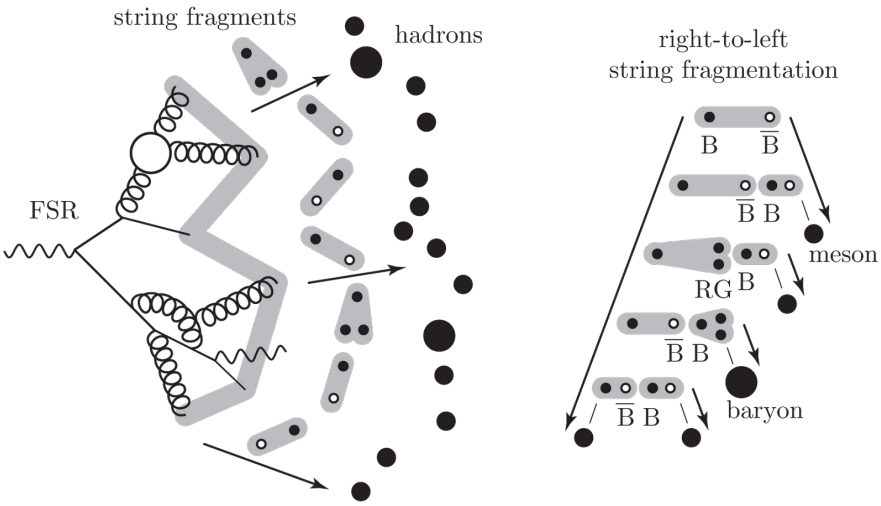


Figure 3.3: String hadronisation of a parton shower [108].

The typical timescale for hadronisation in *pp* collisions at the energies of the LHC is of the order of $10^{-24}$ seconds. The newly formed hadrons often have a short lifetime and decay further soon after hadronisation has occurred. The particle that is at the forefront of this thesis, the top quark, is the only known quark that does not undergo hadronisation due to its substantial mass, leading to its very short lifetime, on the order of $10^{-25}$ seconds, which is an order of magnitude smaller than the hadronisation timescale in the LHC.

## 3.4 Underlying Event

The *Underlying Event (UE)* encompasses all additional activity that occurs in conjunction with hard scattering processes at low energy. Typically these gluon scattering processes, $gg \rightarrow gg$. The UE comprises of various components, including *Multiple Parton Interactions (MPI)*, *Beam-Beam Remnants (BBRs)*.

MPIs can be thought of as additional interactions that occur simultaneously within the same *pp* collision event, visualising this as if multiple mini-collisions are happening within the main collision. As the collision energy is increased, MPIs become more prevalent. This trend arises from the heightened probability of interactions as energy levels increase, resulting in a greater number of partons with lower momentum fractions.

In the aftermath of the MPIs, the coloured partons involved are modelled

as being connected by colour strings, as described with the Lund string model. These strings can intertwine with colour strings originating from the primary hard scattering interaction, and they can even overlap with colour fields from other MPIs. To make sense of this intricate web of strings, the *Colour Reconnection (CR)* mechanism is introduced. This mechanism manages how the colour strings are formed and can even rearrange the colour configuration of the event before hadronisation.

These processes generate numerous coloured partons, akin to those originating from the hard scattering, which eventually transform into colour-neutral hadrons through the hadronisation process explained in Section 3.3. The low-energy activity that constitutes the UE are called 'soft' particles, and tend to have a much higher multiplicity (number of particles) than the particles from the hard-scattering [109].

Within the realm of MCs, it is essential to adequately understand and incorporate the UE. UE models are not constructed from first principles and their parameters need to be fit by measurements. This is encapsulated within what are termed *tunes*. Tunes are essentially collections of parameter settings for each process of the particle interaction, specifically selected to match observational data from various sources. These parameters are not fundamental constants of nature, nor are they predicted by any particular theory, but represent adjustable elements within the simulation model that can be fine-tuned to ensure the simulation accurately reflects a wide range of collider data.

It is also worth emphasising the continuing relevance of data not just from current experiments but also earlier experiments, such as those conducted at the *Large Electron-Positron Collider (LEP)*. LEP data is particularly valuable due to its less complex nature, absence of ISR and UE. This simpler experimental context makes LEP data an essential reference point for calibrating and validating simulations, especially in areas where theoretical predictions are less certain.

The complex structure of MC simulations of the $pp$ collision activity described in this chapter is represented in Figure 3.4.

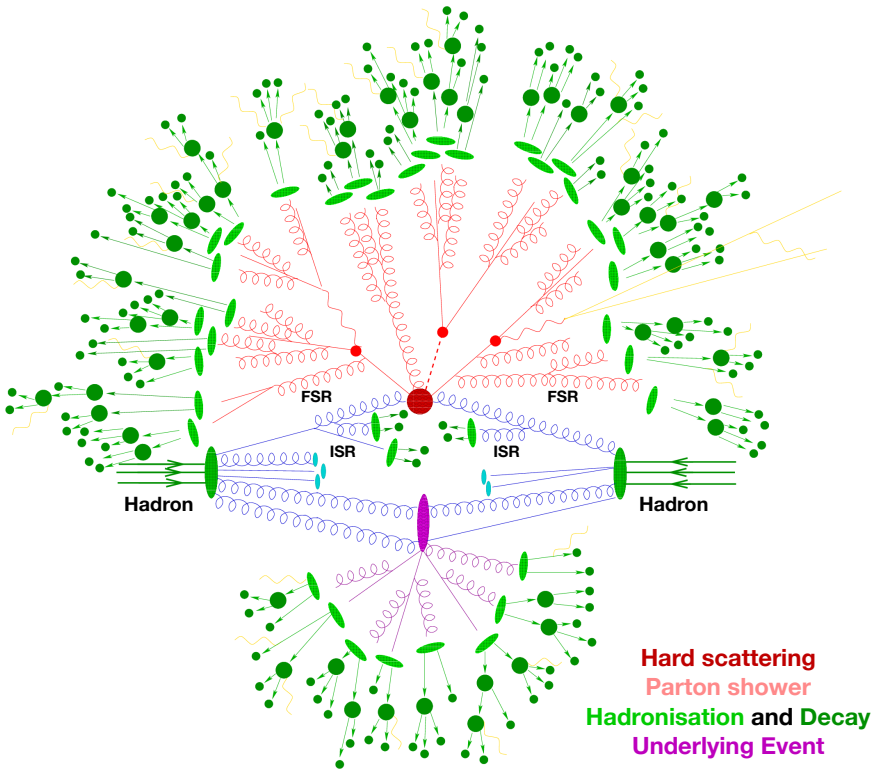


Figure 3.4: Particle collision and the subsequent processes as simulated in Monte Carlo generators. Modified figure from Ref. [110].

## 3.5 MC Event Generators

Several Monte Carlo event generators are available, each offering its unique approach to simulating the various stages of $pp$ collisions, from the initial hard scattering to particle decay processes. In this thesis, the primary focus will be on Pythia and Sherpa, which are the most extensively discussed generators. However, other generators will also be mentioned for completeness.

### 3.5.1 Matrix Element Generators

The MC generators discussed in this section will focus on those that created specifically for simulating the matrix element. This is best for simulating hard, wide-angle gluons.

- MadGraph [111] is primarily designed for LO calculations of $2 \to n$ scattering processes. It introduces FEYNRULES, a Mathematica

package aimed at streamlining the implementation of new particle physics models [112]. The latest version of this software is MadGraph 5 [113]. MadGraph has the ability to interface with the NLO MC generator MC@NLO [114] which leads to the program MadGraph5_aMC@NLO [115]. This program can produce up to 4 coloured partons at NLO and 5 coloured partons at LO. Additionally, MadGraph provides a dedicated matrix element output format compatible with Pythia 8.

- Powheg [116–118] is tailored for NLO calculations and is commonly associated with $2 \rightarrow 2$ processes. It can be seamlessly interfaced with PS generators such as Pythia, enhancing the modelling of processes to allow for more accurate representation of physics phenomena. Powheg is not an automatic tool like MadGraph, the processes involved in this generator are introduced by hand by theorists and optimised accordingly. The latest iteration of Powheg is Powheg V2.

### 3.5.2 Parton Shower and Hadronisation Generators

In this section, the MC generators discussed have a specific focus on the parton shower and hadronisation that follows the hard scatter. This is best for simulating soft, collinear radation.

**Pythia**

The MC program based on the Pythia 8 event generator, uses LO matrix elements and parton showers to simulate the hard scattering process. The Lund string fragmentation model is used to simulate the hadronisation process and the PS are *Leading-Log (LL)* accurate. Pythia focuses on simulating the parton showering and hadronisation stages in detail, making it particularly well-suited for studies involving softer emissions and final-state hadrons. It also includes a number of additional features and models, such as the aforementioned multiple parton interactions, beam remnants, and the simulation of underlying event activity. This can all be seen with an example of a $pp \rightarrow t\bar{t}$ interaction displayed in Figure 3.5, which shows exactly where each feature applies in the structure of the process. At the time of writing this thesis, the most current version is Pythia 8.3 [119].

Pythia primarily employs the so-called *MLM* matching scheme [120] to merge

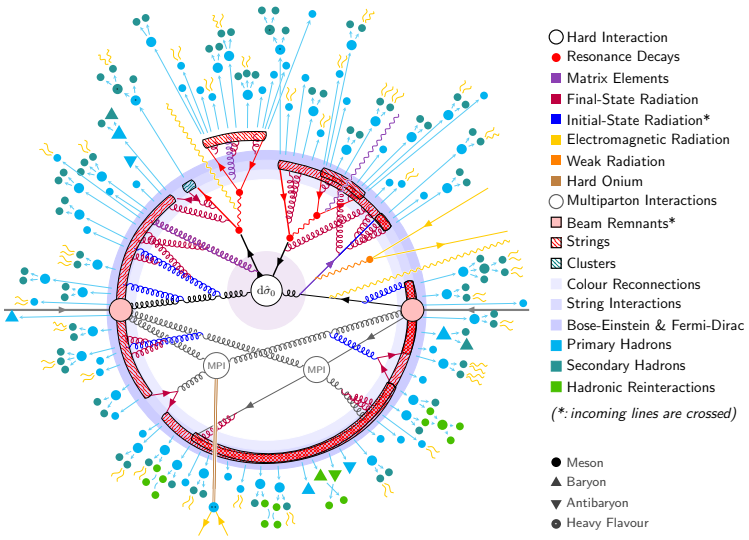


Figure 3.5: Schematic of the structure for an example $pp \to t\bar{t}$ process, modelled in PYTHIA [119].

ME calculations, particularly from ME event generators such as POWHEG, with parton showers. This approach divides the phase space into distinct regions based on the number of emitted partons or jets. For instance, there are regions with no additional parton emissions (LO), regions with one extra parton emission (NLO), and so forth. In regions of the phase space where only LO matrix element calculations are reliable, PYTHIA exclusively relies on these calculations to ensure accurate descriptions of hard scattering processes. The MLM matching scheme maintains consistency across different phase space regions, preserving the precision of matrix element calculations where they are most critical, such as for hard processes. Simultaneously, it incorporates parton showers and higher-multiplicity emissions in softer phase space regions. This integration results in more dependable and precise event simulations for complex multi-parton processes. The key steps involved in the MLM matching scheme are as follows [121]:

- Parton-level events are defined applying minimum transverse energy ($E_T^{min}$) and separation ($R_{min}$) criteria to the produced partons. The $E_T$ threshold ensures that only sufficiently energetic partons are considered for further analysis, focusing on those most likely to contribute significantly to the final state of the collision. The separation criteria determine how far apart the

partons must be before they are treated as distinct entities within the event.

- A jet cone algorithm is employed to match partons to jets, ensuring that each parton has a corresponding matched jet. More on jet clustering can be found in Section 4.3. Events are considered fully matched only when all partons have matched jets.

- Beyond the matched parton-jet pairs, any additional jets that may emerge in the event are systematically suppressed and not included in the final simulation. This suppression mechanism serves as an alternative to Sudakov reweighting, which is a technique used to account for the probability of the emission of additional partons, due to missing higher order corrections in the calculations [122]. Instead of modifying the event's weights,[1] extra jets are rejected if they do not correspond to matched partons.

**Herwig**

HERWIG (or HERWIG++) [123, 124], like PYTHIA, is a LO general-purpose event generator primarily used to simulate parton showers, hadronisation, and the subsequent processes that follow after the hard scatter, with the hadronisation being performed using the cluster model. The latest release of HERWIG software is referred to as HERWIG 7. This version incorporates the POWHEG framework and includes an internal implementation of MADGRAPH 5. This integration enables HERWIG 7 as a standalone tool capable of generating predictions that combine NLO calculations with PS predictions.

### 3.5.3 Generalised Event Generator

**Sherpa**

SHERPA is a comprehensive event generator for $2 \to n$ processes that combines matrix element calculations with parton showers, providing ME calculations up to NLO accuracy. At the time of writing of this thesis, the most recent version is SHERPA 2.2 [125], reaching up to version SHERPA 2.2.15.

SHERPA uses the cluster algorithm to simulate hadronisation processes. It also uses the *Cacciari-Krauss-Kuhn-Willis-Lavesson (CKKW-L)* [126] merging scheme

[1] Weights refer to numerical factors that are applied to events in order to adjust their significance to account for differences in theoretical predictions, experimental conditions, and statistical representations of events.

to combine matrix elements of different multiplicity with parton showers. This allows it to accurately simulate the full range of final states, from a few hard jets to many soft jets. CKKW-L uses matrix element calculations up to a certain order of accuracy (e.g. NLO) across the entire phase space. In contrast, MLM often uses matrix elements up to LO accuracy but with fixed multiplicity, meaning it accounts for a fixed number of partons. In regions where NLO matrix elements are necessary to provide accurate predictions, SHERPA smoothly transitions from LO to NLO calculations. This transition incorporates higher-multiplicity emissions and parton showers, which are important in the softer and collinear regions.

The main steps involved in the CKKW-L merging scheme are as follows [127]:

- The scheme begins by calculating matrix elements to determine possible jet configurations, considering various numbers of jets. The acceptance or rejection of these jet configurations is determined based on specific criteria described below, to ensure the inclusion of relevant jet configurations while maintaining computational efficiency.
- In the CKKW prescription, the separation of phase space for different multi-jet processes uses a $k_\perp$ algorithm [128–130] to separate jets based on their relative transverse momenta. A 'shower history' is reconstructed by applying the $k_\perp$-algorithm to cluster the initial and final state partons.
- Sudakov weights are applied to matrix elements to mimic the evolution of parton showers, where these weights account for the likelihood of emitting additional partons during the showering process. Coupling weights are also applied to represent $\alpha_s$ at different energy scales in the process respectively. This allows accurate simulation of emission probabilities and strong force interactions in the parton shower evolution.

CKKW-L often performs better in regions with multiple soft emissions, while MLM excels in processes with a few hard jets [121]. Although interpolation methods used to merge matrix elements and parton showers differ between CKKW-L and MLM, both aim for a smooth and consistent transition which is crucial to maintain accuracy across the entire phase space.

SHERPA also includes the possibility to include simulation of photon-induced processes and a built-in NLO calculation framework; this allows SHERPA to be a versatile tool for both LO and NLO particle interaction simulations.

# Part II

# Jet Physics and Object Reconstruction

# Chapter 4

# Event Reconstruction in ATLAS

Event reconstruction in the LHC is designed to accurately identify and measure the properties of particles resulting from $pp$ collisions. This process begins with the detection of low-level signals: hits in the particle tracker and energy deposits in the calorimeter. These detections are not direct observations of particles themselves, but rather the interactions or traces they leave behind in the detector. From these initial signals, intermediate-level objects are constructed, such as tracks from the series of hits in the tracker which indicates the path of charged particles, and spatially related clusters of energy deposits in the calorimeter. The process finalises with the identification of high-level objects such as photons, b-jets, and top quark candidates. These objects correspond more directly to the particles produced in the collisions. For example, jets reconstructed in the ATLAS detector can be interpreted as a spray of hadrons resulting from the hadronisation of quarks or gluons. Once these objects are reconstructed, their four-momenta must be calibrated to fine-tune the measured energy or transverse momentum that matches as closely as possible with the true properties of the particles.

## 4.1 Tracks and Vertices

*Tracks* refer to the path of charged particles as they pass through the detector, and *vertices* refer to the point of origin of a particle or group of particles.

Tracks are reconstructed from the curved trajectories of charged particles travelling through the inner detector and muon spectrometer. This curvature, induced by the magnetic field in the ID, is a key measure of the particles' transverse

momentum. Due to the $\eta$ coverage of the tracking system in the inner detector, these particles can only be measured up to $|\eta| = 2.5$. There are three steps to reconstructing these curved tracks through the ID [131]:

1. Clusters are formed from individual cells in the pixel and strip detectors. A *Neural Network (NN)*-based cluster splitter is used, which is trained using machine learning to effectively distinguish and separate overlapping clusters.

2. Track seeds are generated when three hits are detected in the pixel and/or strip detector. Afterwards, a number of selection criteria, referred to as 'cuts' are applied, designed to exclude false signals and reduce noise, ensuring that only likely particle tracks are considered. Simultaneously, an iterative algorithm known as a Kalman filter [132] is applied. This filter enhances the accuracy of the reconstructed particle paths by iteratively refining the tracks with each new hit. Tracks that are identified in the initial layers of the detector extend into subsequent layers, where the tracks are projected into the new layer and compatible hits are searched for. In cases where multiple compatible hits emerge, separate cloned track candidates are created for each possibility. These clones explore various potential paths, and incorrect paths, that deviate from the expected physical trajectory of the particles in the ID, are eliminated either in the later layers or during the process of ambiguity resolution.

3. An ambiguity solver is applied to remove fake track possibilities or duplicates. Then the final tracks extend into the TRT to improve the momentum resolution.

After the identification of these tracks, they are combined with data of the strength of the magnetic field to measure precisely what momentum is associated to each track. To understand track trajectories and physics properties, several key track parameters are examined. The curvature of the track indicates the $p_T$, and the track's orientation is characterised by two angles: the azimuthal angle, $\phi$ and the polar angle, $\theta$. Additionally, impact parameters, $z_0$ and $d_0$, are crucial as they reflect the point of closest approach to the interaction point where the proton collisions occur.

Vertices, on the other hand, are the points of origin of the particles or groups of particles. The primary vertex is the interaction point where the $pp$ collisions

occur, and is where the majority of particles originate. Additionally, there are secondary vertices, distinct from the primary vertex, where subsequent particle interactions or decays occur, following the initial collision. Secondary vertices are particularly important in the study of certain processes, such as the decay of hadrons containing a bottom quark, $B-$hadrons. These hadrons have a relatively long lifetime, which allows them to travel a measurable distance from the primary vertex before decaying. The decay of $B-$hadrons therefore results in secondary vertices, which can be physically separated from the primary collision point, and is instrumental in identifying and tagging $b-$jets, which are jets of particles that arise from the fragmentation of bottom quarks. The research of $b$-jets is of significant importance in the study discussed in Section 5.5.

The vertex reconstruction algorithm matches intersecting tracks to identify the point of origin of a particle or group of particles. There are three stages to vertex reconstruction [133]; vertex finding and vertex fitting:

1. After applying a vertex selection criteria, reconstructed tracks that follow these criteria are chosen for analysis. The impact parameter, $z_0$, of these tracks represents the distance between the trajectory of a charged particle and primary vertex within the detector, specifically along the z-axis. The primary vertex is one well-defined point in each collision, but differs from one collision to the next. Calculations of the impact parameter are then performed with reference to the reconstructed centre of the beam spot, which represents the average position where the particle beams intersect.

2. From this a seed is then generated, which is grouped with the tracks. A vertex fitting algorithm is applied to estimate the best vertex position and uncertainty.

3. Once the vertex position is decided, the incompatible tracks are removed and used for the calculation of another vertex. This is repeated with all remaining tracks in the event.

The vertex that contains the largest sum of transverse momenta squared of associated tracks is considered as the hard-scatter vertex (primary vertex).

## 4.2 Objects

In the ATLAS detector, different particles yield different signatures. This is used to reconstruct and identify each object:

- Electrons - The reconstruction of electrons from showers in the ECAL involves matching them to tracks in the inner detector. The primary sources of electron misidentification are photons that undergo electron-positron pair decay and energy deposits in the ECAL resulting from charged hadrons. The reduction of these backgrounds can be achieved by implementing cuts based on the shower shape, correlation of calorimeter and track energies, and the minimum number of hits in the B-Layer and TRT [134].

- Photons - The identification of photons is based on energy deposits in the ECAL. There are two categories of photons based on their interaction with the inner detector: unconverted and converted. Unconverted photons are identified by their characteristic energy deposit in the EM calorimeter without an associated track in the inner detector. However, a significant fraction of photons in ATLAS convert into electron-positron pairs. This conversion is shown by a pair of tracks appearing in the tracker. At high energies, these tracks do not sufficiently separate enough to create individual EM calorimeter clusters, resulting in a single, merged energy deposit in the ECAL, these are converted photons. The primary background in the identification of photons is contamination from hadronic jets, which can be reduced by implementing isolation cuts and applying restrictions on the properties of the EM shower shape in the ECAL [135]. The identification and isolation of photons are discussed in more detail further in this section.

- Hadronic Jets - In hard-scattering collisions, the outgoing quarks and gluons undergo hadronisation, forming tightly grouped, collimated sprays of stable particles - these are jets. In the reconstruction process, jets are identified using clusters of energy in the calorimeters and tracks in the inner detector. These are then combined in the *Particle-Flow (PFlow)* algorithm [136], which serves as a proxy for stable particles. The anti-$k_t$ algorithm [137], a component of the FastJet software [138], is used for clustering these elements. A key parameter in this process is the radius $R = \sqrt{\Delta\eta^2 + \Delta\phi^2}$, dictating the size of the jet. ATLAS typically uses two radii: small-$R$ jets with $R = 0.4$ and large-$R$ jets with $R = 1.0$. More details on jet clustering is

available in Section 4.3, and additional information on large-$R$ jets can be found in Chapter 6.

- Muons - These are detected through their tracks in both the inner detector and muon spectrometer, which are independently measured by each system. The compatibility of the two muon tracks is verified and the four-momentum is reconstructed through a global track fit [139].

- Missing Transverse Energy $E_T^{miss}$ - Very weakly interacting particles such as neutrinos, which do not leave detectable tracks in particle detectors, contribute to an imbalance in the vector sum of the $p_T$ of the observable particles in a collision's final state. This missing energy is also influenced by residual soft transverse energy, often originating from pile-up, a term described in Chapter 5, which may not be fully captured in jet reconstruction. To address this, a Soft Term Vertex Fraction algorithm has been developed, improving the accuracy of $E_T^{miss}$ calculations. However, as there are no detectors along the beam axis, the missing energy in this direction cannot be directly measured. Therefore additional analyses, based on momentum conservation of the particles in a jet required to infer the four-momentum of the neutrinos [140].

### 4.2.1 Photon Isolation and Identification

In this thesis, photons hold an important significance, requiring a comprehensive discussion that is elaborated on more in Section 5.5. Specifically, the focus is on photons that emerge directly from parton interactions, that are termed "prompt photons" [141]. The generation of prompt photons occurs through two distinct mechanisms, illustrated in Figure 4.1: direct-photon processes, when a photon is produced in the hard interaction, and fragmentation processes, where a parton is fragmented into a photon. Non-prompt photons are those that are produced as a secondary product of the hadronisation and decay processes within a jet.

**Photon Identification**

Photon identification with ATLAS exploits the fine granularity of the electromagnetic calorimeter by utilising what is known as Shower Shape Variables (SSVs) that describe the lateral and longitudinal development of photon-initiated cascades in the ECAL. To streamline the process of photon identification, ATLAS uses several identification working points. Each of these working points is defined

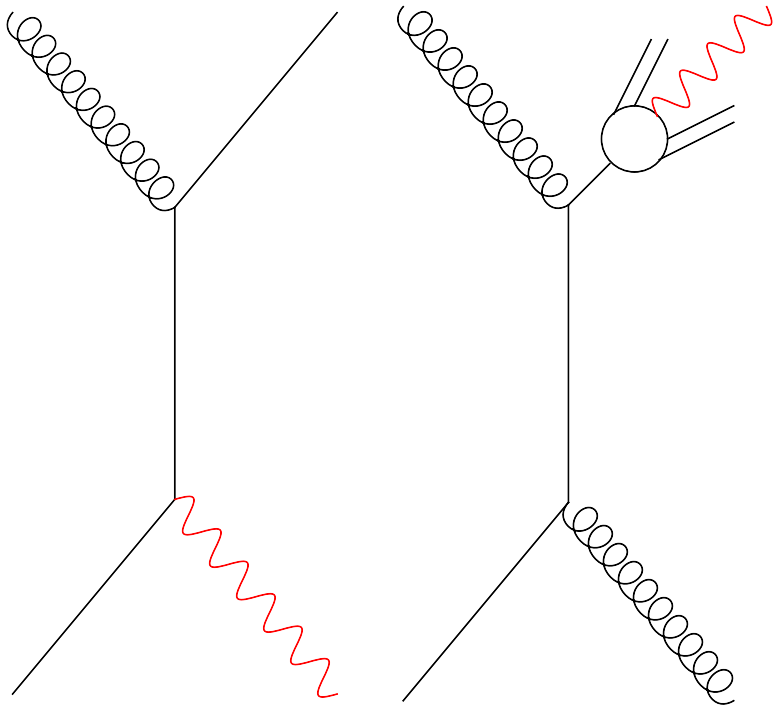


Figure 4.1: Example Feynman diagrams of (a) direct photon, and (b) photon fragmentation processes.

by a unique set of requirements, that are detailed in Table 4.1. These criteria are designed based on several aspects of the photon's interaction in the ECAL, such as:

- Cuts in $\eta$: This involves selecting events based on the pseudorapidity of the particles, which helps in differentiating the photon signals.
- Hadronic Leakage: This term is used to describe instances where hadrons partially deposit their energy in the ECAL before continuing to the HCAL. Hadronic leakage is a measure of the energy in the hadronic calorimeter behind the EM cluster. A lot of leakage means the object is likely a hadron.
- Cuts on the EM strip layer: This is the first layer of the ECAL which maps the early development of the EM shower to provide high-resolution measurements.
- EM middle layer cuts: This is the second layer of the ECAL, where the majority of the shower development occurs, and is designed to capture the

maximum energy from the EM showers.

| Category | Description | Name | loose | tight |
|---|---|---|---|---|
| Acceptance | $\|\eta\| < 2.37$, with $1.37 \leq \|\eta\| < 1.52$ excluded | - | ✓ | ✓ |
| Hadronic leakage | Ratio of $E_T$ in the first sampling layer of the hadronic calorimeter to $E_T$ of the EM cluster (used over the range $\|\eta\| < 0.8$ or $\|\eta\| > 1.52$) | $R_{had1}$ | ✓ | ✓ |
| | Ratio of $E_T$ in the hadronic calorimeter to $E_T$ of the EM cluster (used over the range $0.8 < \|\eta\| < 1.37$) | $R_{had}$ | ✓ | ✓ |
| EM middle layer | Ratio of the energy in $3 \times 7$ $\eta \times \phi$ cells over the energy in $7 \times 7$ cells centered around the photon cluster position | $R_\eta$ | ✓ | ✓ |
| | The lateral shower width, $\sqrt{(\sum E_i \eta_i^2)/(\sum E_i) - ((\sum E_i \eta_i)/(\sum E_i))^2}$, where $E_i$ is the energy and $\eta_i$ is the pseudorapidity of cell $i$ and the sum is calculated within a window of $3 \times 5$ cells | $w_{\eta 2}$ | ✓ | ✓ |
| | Ratio of the energy in $3 \times 3$ $\eta \times \phi$ cells over the energy of $3 \times 7$ cells centered around the photon cluster position | $R_\phi$ | | ✓ |
| EM strip layer | Lateral shower width, $\sqrt{(\sum E_i (i - i_{max})^2)/(\sum E_i)}$, where $i$ runs over all strips in a window of $3 \times 2$ $\eta \times \phi$ strips, and $i_{max}$ is the index of the highest-energy strip calculated from three strips around the strip with maximum energy deposit | $w_{s3}$ | | ✓ |
| | Total lateral shower width, $\sqrt{(\sum E_i (i - i_{max})^2)/(\sum E_i)}$, where $i$ runs over all strips in a window of $20 \times 2$ $\eta \times \phi$ strips, and $i_{max}$ is the index of the highest-energy strip measured in the strip layer | $w_{stot}$ | | ✓ |
| | Energy outside the core of the three central strips but within seven strips divided by energy within the three central strips | $f_{side}$ | | ✓ |
| | Difference between the energy associated with the second maximum in the strip layer and the energy reconstructed in the strip with the minimum value found between the first and second maxima | $\Delta E_s$ | | ✓ |
| | Ratio of the energy difference between the maximum energy deposit and the energy deposit in the secondary maximum in the cluster to the sum of these energies | $E_{ratio}$ | | ✓ |
| | Ratio of the energy in the first layer to the to the total energy of the EM cluster | $f_1$ | | ✓ |

Table 4.1: Discriminating variables used for loose and tight photon identification [142].

The first working point, known as the loose cut, utilises four key shower-shape variables, namely $R_{had1}$, $R_{had}$, $R_{\eta}$, and $w_{\eta 2}$. In contrast, the tight cut incorporates a more comprehensive set of criteria, encompassing all 11 variables shown in Table 4.1. Additionally, a subset of criteria, termed the loose' selection, is established to offer a more relaxed approach compared to the tight cut. This loose category includes several variations, each with distinct levels of strictness:

- LoosePrime4: This is the nominal loose' cut, which omits all variables from the tight cuts except for $w_{s3}$, $f_{side}$, $\Delta E_s$, and $E_{ratio}$.

- LoosePrime5: Further relaxes the criteria from LoosePrime4 by also removing the cut on $w_{stot}$.

- LoosePrime3: Retains the tight cut on $E_{ratio}$ but the other cuts are relaxed.

- LoosePrime2: Preserves the $E_{ratio}$ and $\Delta E_s$ cuts but relaxes the remaining variables, making it the tightest cut among the loose' definitions.

Non-tight photon candidates refer to photons that satisfy the loose' criteria but fail at least one of the tight requirements. More on this in section 5.5.4.

**Photon Isolation**

Within the LHC not only are prompt photons produced, but photons are also generated inside jets, such as through the decay of $\pi^0$ particles and other neutral mesons. To effectively study prompt photons and differentiate them from photons originating within jets, an isolation requirement is imposed:

$$E_T^{iso} = \sum_i E_T^i < E_T^{max} \tag{4.1}$$

This isolation requirement is based on evaluating the energy deposited within a circular region of radius R, centered on the photon's position in the $\eta - \phi$ plane. The goal is to examine the energy surrounding the photon while excluding energy contributions from the photon itself. By doing so, it becomes possible to suppress the majority of photon contributions originating inside jets, as well as the contribution from fragmentation processes.

## 4.3 Jet Reconstruction

Jets are important in high-energy physics as they provide a handle on the properties of the original quarks or gluons that produced them and can be used to study the properties of these fundamental particles, such as their energy, momentum, or flavour. Due to many theories of new physics predicting the production of new particles that can decay into jets from quarks and gluons, they are also an important tool for the search of new particles and new interactions that are not predicted by the Standard Model.

Jets are reconstructed using a clustering algorithm run on a set of input four-vectors, typically obtained from topologically associated energy deposits in the calorimeter, charged-particle tracks, or simulated particles.

The jet clustering algorithms used in this thesis are sequential recombination algorithms. They begin by treating each particle in the event as a "pseudojet". The distance between the pseudojet and the beam is defined as $d_{iB}$, and the distance between two pseudojets is calculated using the $d_{ij}$ variable, which is determined by the transverse momenta of the pseudojets, their angular separation in the angle-energy space, and a parameter called R, which controls the size of the jet:

$$d_{iB} = p_{Ti}^{2P} \tag{4.2}$$

$$d_{ij} = \min(p_{Ti}^{2P}, p_{Tj}^{2P}) \frac{\Delta R_{ij}^2}{R^2} \tag{4.3}$$

During each iteration, the algorithm selects pseudojets with the smallest distance value; if this is $d_{ij}$, then the pseudojets $i$ and $j$ are removed and a new pseudojet takes their place, with the momentum of the new pseudojet calculated as the vector sum of the momenta of the original pseudojets $i$ and $j$. However, if the smallest distance value corresponds to $d_{iB}$, then the pseudojet $i$ is not mergeable and is removed from the list and considered as a jet. This merging process continues until there are no remaining pseudojets.

What defines a jet depends on what type of algorithm is used [143], which depends on the value of the parameter $P$: Several common jet algorithms [143] correspond to the following choices for the value of $P$ in Equations 4.2 and 4.3:

- $P = 0$ is the **Cambridge/Aachen (C/A)** algorithm, which relies only on angular ordering when grouping the constituents of a jet. Due to the independence on the momentum, this algorithm can de-cluster very well and so is best suited to the studying of jet substructure. However, the area varies and can be susceptible to the effects of pile-up and underlying event.
- $P = 1$ corresponds to the $\mathbf{k_t}$ algorithm, which initially groups the softest pseudojets into harder ones and then combines the hardest pseudojets together. The prioritisation of clustering soft particles first implies a predominance of low $p_{\mathrm{T}}$ characteristics, which enhances the method's capability to resolve subjets effectively. However, this approach also renders the algorithm more susceptible to pile-up and underlying event effects. This algorithm can also lead to the production of jets that possess non-uniform shapes, which can, in turn, lead to challenges in calibration.
- $P = -1$ corresponds to the **anti-$\mathbf{k_t}$** jet-clustering algorithm which follows an inverted power law dependence on the $p_T$ of pseudojets, resulting in the clustering of the hardest constituents first, followed by the inclusion of soft radiation in later stages of the process. The resulting jets exhibit a circular shape and are typically centered around hard radiation deposits [137]. It has a parameter, R, that controls the size of the jet, which can be adjusted to optimise the performance of the algorithm for different physics analyses.

An important characteristic of these algorithms is that they are infrared- and collinear-safe (IRC-safe), meaning they remain well-defined and consistent even when dealing with very low-energy particles or particles closely aligned in angle. The significance of IRC-safety extends beyond just experimental robustness; it's also crucial for theoretical physics, particularly in the calculation of cross sections. Theoreticians rely on IRC-safe algorithms to ensure that their calculations are accurate and consistent across different energy scales and particle configurations, making these algorithms fundamental in both experimental and theoretical aspects of particle physics.

The different topologies of each of these algorithms are displayed in Figure 4.2. The most obvious observation is that the anti-$k_t$ jets (bottom right of the figure) all have circular shapes, while the rest of the algorithms' shapes are a lot more complex. Currently, for the majority of jets deployed in the LHC, and for the jets that are to be discussed in Chapter 5, the anti-$k_t$ algorithm is used for the jet treatment, along with its implementation in the FastJet software package [144].

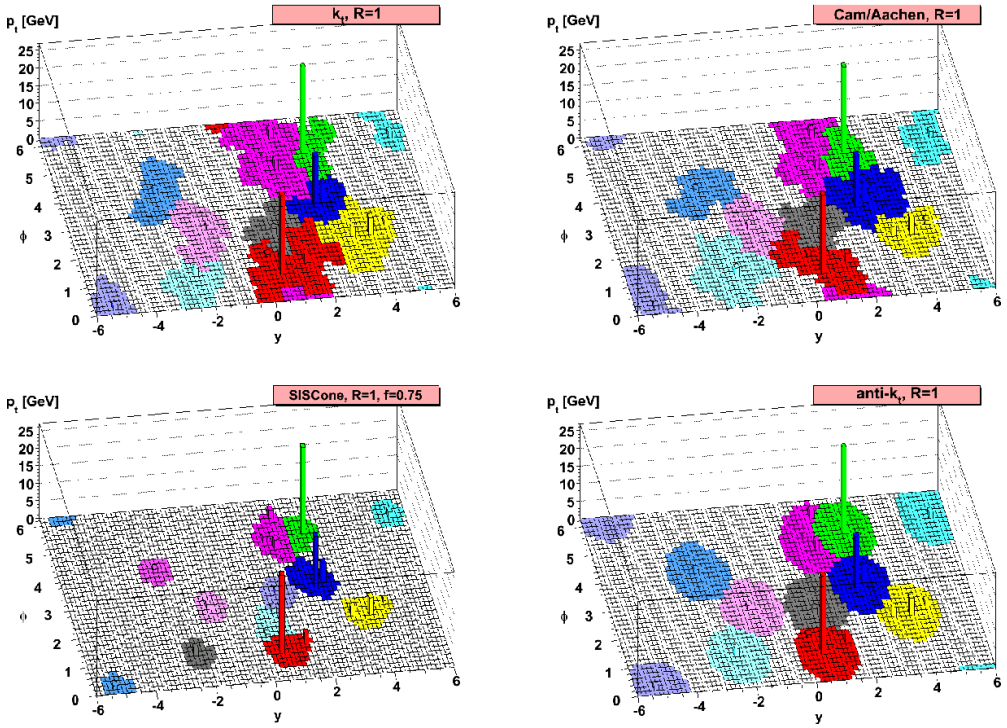


Figure 4.2: A parton-level event produced using Herwig, combined with numerous random soft artificial particles referred to as "ghosts" and then subjected to clustering using four distinct jet algorithms, showcasing the "active" regions encompassed by the resulting hard jets. The shapes of these jets, particularly in the case of $k_t$ and Cam/Aachen algorithms, are partially influenced by the characteristics of the ghost particles used, and their configurations may vary with modifications to the ghost inputs [137].

### 4.3.1 Jet $b$-tagging in ATLAS

The term $b$–tagging, also known as $b$–jet identification, is a technique used in high-energy physics experiments to identify jets of particles that are likely to have originated from the decay of a bottom quark ($b$–quark). It is important because bottom quarks are relatively heavy and have a relatively long lifetime, which is key for the ability to tag them. They are also a key signature of many physics processes such as being the primary quark in the decays of the top quark and the Higgs boson.

It is performed in ATLAS using a multivariate algorithm, which combines information from several different sources to form a discriminant variable. The main sources for $b$–jet identification are ID tracks, primary vertex reconstruction, jets, and track-jet matching [145].

Tracks from bottom quarks tend to have a larger impact parameter than tracks from other quarks or gluons, due to the longer lifetime of bottom hadrons. Additionally, the reconstruction of the secondary vertex is a powerful method to identify $b$–jets, since the $B$–hadrons produced in the $b$–quark decays tend to have a longer lifetime. This means that a secondary vertex is formed further away from the primary vertex than for quarks with shorter lifetimes. Lifetime-based variables that can be associated to the secondary vertex for use in $b$–tagging include decay length significance, the flight distance and the vertex mass. These variables are based on the distance between the primary and secondary vertex and the invariant mass of the tracks associated with the secondary vertex. The combination of these variables is used to construct a multivariate discriminant, which separates $b$–jets from other types of jets. The discriminant is trained using a sample of jets that are known to contain a high fraction of $b$–jets, such as jets from $t\bar{t}$ events. The performance of the $b$–tagging algorithm is then evaluated using a sample of jets that are known to contain a low fraction of $b$–jets, such as jets from QCD multi-jet events.

The performance of $b$-tagging algorithms is characterised not only by the $b$-tagging efficiency (the fraction of $b$-jets correctly identified) but also by the light-flavour jet rejection (the fraction of light-flavour jets correctly rejected) and the mis-tag rate (the rate at which non-$b$-jets are incorrectly tagged as $b$-jets). We can estimate $b$-tagging efficiencies using Monte Carlo simulations for events with real $b$-jets and measure it in data using di-lepton $t\bar{t}$ events, assessing light-jet rejection presents challenges. However, the presence of a non-negligible fraction of real $b$-jets in the multi-jet sample complicates this estimation. The best performance is achieved when the $b$–tagging efficiency is high and the light-flavour jet rejection is low. To effectively manage the trade-off between tagging efficiency and rejection rates, different Working Points (WPs) are established. These WPs are set by applying varying thresholds on the $b$-tagging discriminant's output. For instance, a looser WP might tag 85% of $b$-jets correctly but with lower rejection of light-flavour jets, whereas a tighter WP might have a higher rejection rate but only tag 60% of $b$-jets correctly.

The IBL mentioned in Section 2.3.1 significantly improved the $b$–tagging capability of the ATLAS detector. This improvement was quantified as a 10% increase in $b$–tagging efficiency at a fixed rejection rate [146].[1]

[1]The rejection rate here refers to the detector's ability to correctly reject particles that do not contain a bottom quark.

# Chapter 5

# Jet Energy Scale Calibration in ATLAS

In the process of jet reconstruction, several potential sources of uncertainty can impact the accuracy of measurements in analyses that involve jets. To mitigate these issues and accurately determine the energy of the jets, a specialised calibration process is applied to jets reconstructed from energy deposits in the ATLAS detector. This process is known as the *Jet Energy Scale (JES)* calibration. It consists of a sequence of steps, each contributing to the precision of the jet energy determination before jets can be propagated to use in analyses. A visual overview for each stage of the JES calibration procedure is provided in Figure 5.1.

In this chapter, we will explore each stage of the JES calibration process, along with some new techniques developed to improve the accuracy of these calibrations. A more detailed look at this can be found in Ref. [147]. The main contribution to the JES calibration in regards to this thesis is that of the dedicated in-situ bJES correction, described in Section 5.5.

## 5.1 Pile-up Corrections

The first step in the JES calibration process focuses on addressing the challenge of *pile-up*, a phenomenon considered as one of the largest problems faced in jet reconstruction. Pile-up occurs during instances when multiple $pp$ collisions take place simultaneously within the same bunch crossing. This leads to an overlap of signals within the detector, complicating the task of the jet reconstruction

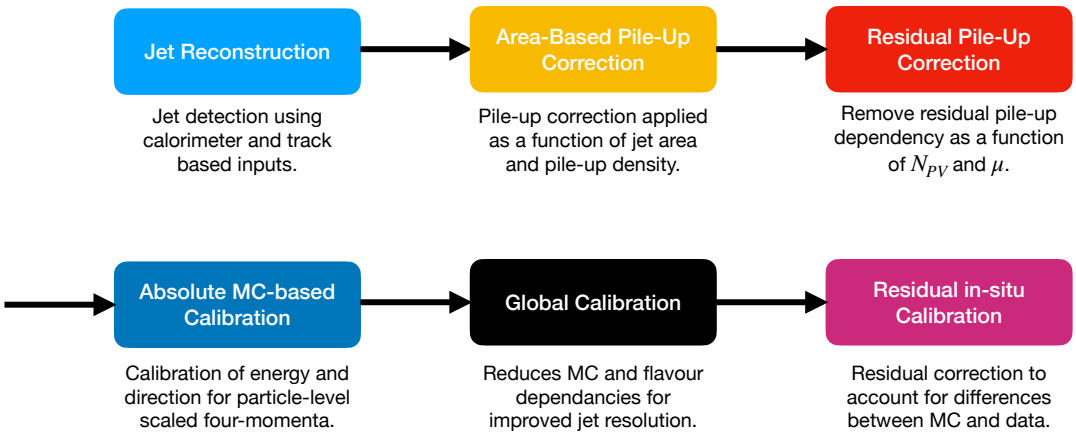


Figure 5.1: JES calibration chain stages.

algorithm, and causing possible distortions in the accuracy of jet properties as proxies for their originating particles. During Run 2, the LHC experienced up to 40-60 $pp$ collisions every bunch crossing. These mostly produce soft 'minimum-bias' interactions, but that still adds up to a lot of background activity that can get clustered into jets. The result is a decline in jet energy resolution and an increase in jet energy scale uncertainty, which can adversely affect the precision of measurements and the ability to distinguish between signal and background events. Therefore, it is crucial to minimise the impact on the response and accurately correct for the additional energy. As the LHC progresses into Run 3 and beyond, with increasing luminosity, effectively managing pile-up becomes more important than ever for reliable jet reconstruction.

### 5.1.1 Area-Based Pile-up Correction

The area-based pile-up correction approach is based on the assumption that the energy deposited in the detectors due to pile-up behaves like a uniform, diffuse, and randomly distributed background. This method requires calculating the pile-up density, $\rho$, which involves a measurement of numerous low $p_T$ jets that collectively span the entire detector. This ensures a whole representation of pile-up activity, extending beyond the vicinity of just high-energy jets. The approach involves calculating the area, $A^{jet}$, of each jet. This is achieved by determining whether

a 'ghost particle' would be clustered in the jet's area [148].[1] If it is, the ghost particle's location contributes to the area of the jet. Afterwards, the median energy per unit area of all the jets is calculated across the detector to establish the pile-up density, expressed as:

$$\rho = \text{median}\left(\frac{p_{T,i}^{jet}}{A_i^{jet}}\right), \tag{5.1}$$

where $p_{T,i}^{jet}$ represents the transverse momentum of the $i$-th jet and $A_i^{jet}$ is its area. For this calculation, only jets with $|\eta < 2|$ are used, as $\rho$ has a steep fall off beyond this region, due to a combination of physics and detector effects.

Following this, the jet's $p_T$ is adjusted to account for the pile-up density, defining a new term, $p_T^{area}$:

$$p_T^{area} = p_T - \rho \times A \tag{5.2}$$

Here, $p_T$ is the original transverse momentum of the jet and $A$ is its area. This correction is applied as a scaling factor to the four-momentum of the uncorrected jet, compensating for the extra energy due to pile-up, without affecting the jet's direction.

### 5.1.2 Residual Pile-up Correction

An additional residual correction is implemented to consider the impact of both in-time and out-of-time pile-up collisions. This correction takes into account two main factors: the number of reconstructed vertices in the event, $N_{PV}$, and the average number of interactions per bunch crossing, $\langle\mu\rangle$. $N_{PV}$ provides sensitivity to in-time pile-up, as vertex reconstruction is dependent on pile-up collisions leaving tracks in the tracker within one or two bunch crossings, while $\langle\mu\rangle$ is more indicative of the general pile-up environment. Out-of-time pile-up affects the calorimeter readings, especially the Liquid Argon system, which accumulates energy deposits from several bunch crossings before and after the actual collision. This energy from out-of-time pile-up is still integrated into topoclusters and subsequently into jets, contributing to an overall increase in measured jet energy. This correction also addresses the effects of pile-up on the reconstructed jet $p_T$, $p_T^{reco}$, and the reconstructed jet pseudorapidity, $\eta_{reco}$.

[1] A ghost particle is a hypothetical, inifinitesimally low energy particle, uniformally distributed in the $\eta \times \phi$ plane and overlaid on top of signals in the event [149].

The jet $p_T$ scale is shifted to match the truth[2] jet scale in bins of $\eta_{reco}$ as a function of ($N_{PV}$,$\langle\mu\rangle$,$p_T^{area}$), which corrects for pile-up and detector effects while also accounting for correlations in $N_{PV}$ and $\mu$. The corrected $p_T$ is defined as

$$p_T^{corrected} = p_T^{area} - \Delta p_T^{area-truth}(N_{PV}, \langle\mu\rangle, p_T^{area}), \tag{5.3}$$

where $\Delta p_T^{area-truth} = p_T^{area} - p_T^{truth}$ is fit as a function of $p_T^{area}$ using a linear plus logarithmic function for jets in the range $20 < p_T^{truth} < 200$ GeV, in bins of $N_{PV}$, $\langle\mu\rangle$, and $p_T^{reco}$.

## 5.2 Absolute MC-based correction

The absolute MC-based jet energy scale (MCJES) and $\eta$ calibration is the next step in this chain and aims to adjusts the reconstructed four-momentum of a jet to the energy scale of particle-level jets. It accounts for factors such as calorimeter responses, energy losses in dead material, out-of-cone radiation effects, and biases in the jet $\eta$ reconstruction due to the transition between different calorimeter technologies and changes in calorimeter granularity.

The average jet energy response $\mathcal{R}$ is characterised as the mean of a Gaussian fit to $\frac{E_{reco}}{E_{truth}}$ in bins of $E_{true}$ and $\eta_{det}$. $E_{reco}$ is defined as the energy of the reconstructed jet, $E_{true}$ is the energy of the particle-level jet, and $\eta_{det}$ is the jet $\eta$ which is oriented from the geometric centre of the detector. The rationale for applying this correction in terms of energy and not $p_T$ is due to that fact that, by design, calorimeters measure the energy of a particle, not of the $p_T$.

As displayed in Figure 5.2, there are obvious disparities in the jet energy response as a function of $\eta_{det}$ ($E_{true}$) for different values of $E_{true}$ ($\eta_{det}$). This is most prominent in jets that cover two separate calorimeter regions due to the differences in technology and inherent biases present between the distinct regions. A numerical inversion technique is utilised for the calibration, wherein the jet energy response at each $\eta$ bin is modelled against $E_{true}$, and the calibration factor for the jet is determined as a function of $E_{reco}$ by inverting this model. This calibration is applied to the jet $p_T$. A similar approach is also applied for the calibration of

[2]Truth (also known as particle-level) jets are theoretical representations of how jets should ideally appear without any experimental limitations.

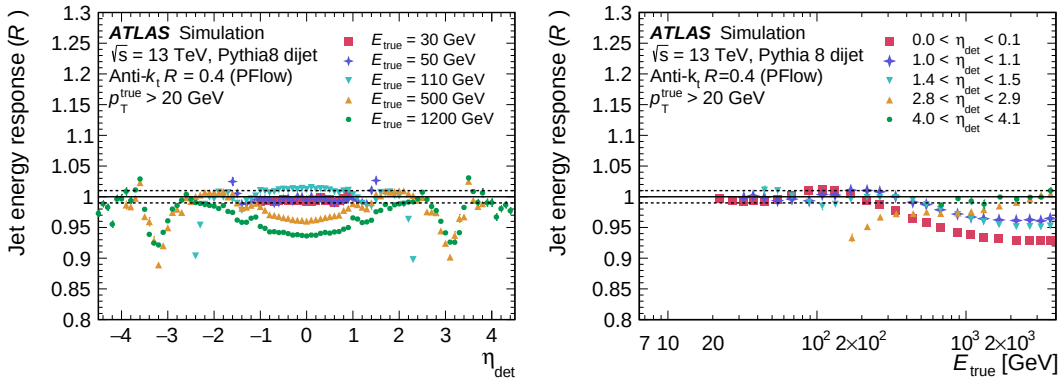


(a) (b)

Figure 5.2: The jet energy response prior to the MCJES calibration (a) at fixed energies as a function of $\eta_{det}$, and (b) at fixed $\eta_{det}$ as a function of truth jet energy. (a) The square shows the response for $E_{true} = 30$ GeV, the plus-sign shows the response for $E_{true} = 50$ GeV, the down-triangle shows the response for $E_{true} = 110$ GeV, the up-triangle shows the response for $E_{true} = 500$ GeV, and the circle shows the response for $E_{true} = 1200$ GeV. (b) The square shows the response for $0.0 < \eta_{det} < 0.1$, the plus-sign shows the response for $1.0 < \eta_{det} < 1.1$, the down-triangle shows the response for $1.4 < \eta_{det} < 1.5$, the up-triangle shows the response for $2.8 < \eta_{det} < 2.9$, and the circle shows the response for $4.0 < \eta_{det} < 4.1$ [147].

the jet pseudorapidity, $\eta$.

## 5.3 Global Calibration

Although the previous stages of the calibration correct the JES for bins of jet energy and pseudorapidity, there are other variables that the response is dependent on. For example, the energy and flavour distribution within the jet, and the distribution of energy across the different layers of the calorimeter.

A significant effect on the characteristics of a jet is attributed to the initiating particles of the jet, specifically whether the jet is quark- or gluon-initiated. Quark-initiated jets typically contain fewer hadrons, with each hadron bearing a larger fraction of the jet's $p_T$, which leads to a more extensive distribution of the jet's energy deeper within the calorimeter layers. On the other hand, jets initiated by gluons typically contain a greater number of hadrons with lower $p_T$, which causes a wider transverse profile and a lower response in the calorimeter.

This is illustrated in Figure 5.3, which shows how the jet response distribution

changes depending on the initiating parton, and also how the behaviour of the jet response distribution with different initiating partons depends on $p_T^{true}$. The response of the jet $p_T$ also depends on the MC modelling due to differences in the way the MC generators model soft radiation and jet constituent distributions.

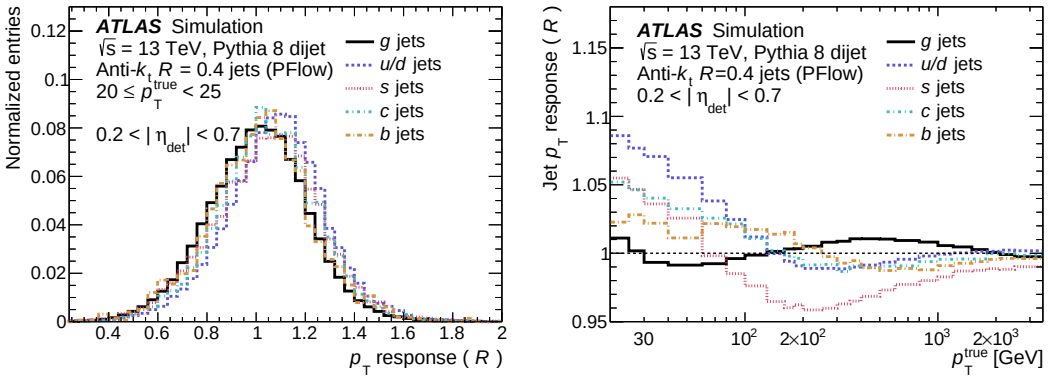


(a) (b)

Figure 5.3: The (a) distribution of the jet $p_T$ response of jets with different flavours is shown for jets between $20 < p_T^{true} < 25$ GeV, (b) the jet $p_T$ response with various flavours as a function of their $p_T^{true}$ is depicted. Gluon jets are represented by a solid line, light quark jets by a long dashed line, strange jets by a short dashed line, charm jets by an alternating medium and short dashed line, and bottom jets by an alternating long and short dashed line [147].

The global calibration aims to apply further corrections to jets depending on certain individual characteristics, reducing MC prediction disparities in the JES, and improving the *Jet Energy Resolution (JER)*. The definition of the JER is the variability in jet energy measurements, typically represented as the standard deviation of the ratio of momenta or energy between the reconstructed jet and particle-level jet.

Previously, the global calibration was achieved by implementing a technique called the *Global Sequential Calibration (GSC)* [150]. This is a multiplicative series of corrections relying on global jet measurements, including the energy distribution along calorimeters, tracking data linked to the jet, and details concerning the muon chambers positioned behind the jet. With the GSC, six observable inputs are used to improve the JER without affecting the average JES, while reducing MC modelling uncertainties. Each factor provides an independent correction on the four-momentum as a function of $p_T^{true}$ and $\eta_{det}$.

Since the GSC is implemented step-by-step, it is beneficial in processes such

as validating each applied correction and testing the mismodelling of inputs. However, due to this iterative procedure, the observables used as inputs must be uncorrelated so as not to affect the observable in the next step. Therefore, a simultaneous correction would be much more useful, in order to include more inputs while accounting for the correlations between them. This is where a new calibration technique called the *Global Neural Network Calibration (GNNC)* is introduced [147]. The GNNC utilises the training of a deep neural network (DNN) that is able to apply a simultaneous correction while accounting for observable correlations.[3]

The list of the input variables handled by the GNNC is shown in Table 5.1, where the observables that were also used by the GSC are displayed with an asterisk next to their name. We can see that this calibration step depends on information based on the energy deposited in the calorimeter, information about jet kinematics, data on energy deposits in the tracking and muon calorimeter layers, and pile-up information.[4]

Figure 5.4 compares the jet $p_T$ response and resolution between the MCJES, GSC, and GNNC for $0.2 < |\eta_{det}| < 0.7$. Figure 5.4a displays the $p_T$ closure, and shows that, in general, the GNNC has a better closure than the GSC; the reasoning for this is because the GNNC is designed to change the jet $p_T$ scale to match that of the truth $p_T$, wherea the GSC is designed not to change the energy response of the jets.

Figure 5.4b shows that the jet resolution is greatly improved with the inclusion of the GNNC compared to the GSC, with improvements of up to 25%.

## 5.4 In-situ Calibration

The previous MCJES+GSC steps are designed to standardise the jet response to a value of 1, ensuring that the reconstructed jet $p_T$ is equal to the truth jet $p_T$. However, these adjustments are purely MC based. When comparing the simulated jets to those of reconstructed jets from actual experimental data, differences in the responses are often observed. These discrepancies can be due

[3]The jets used for the subsequent calibration steps in this chapter will have the GSC applied.

[4]Although a pile-up correction has already been applied, the previous MCJES step reintroduces some of these pile-up dependencies and so pile-up is still slightly present in the global calibration.

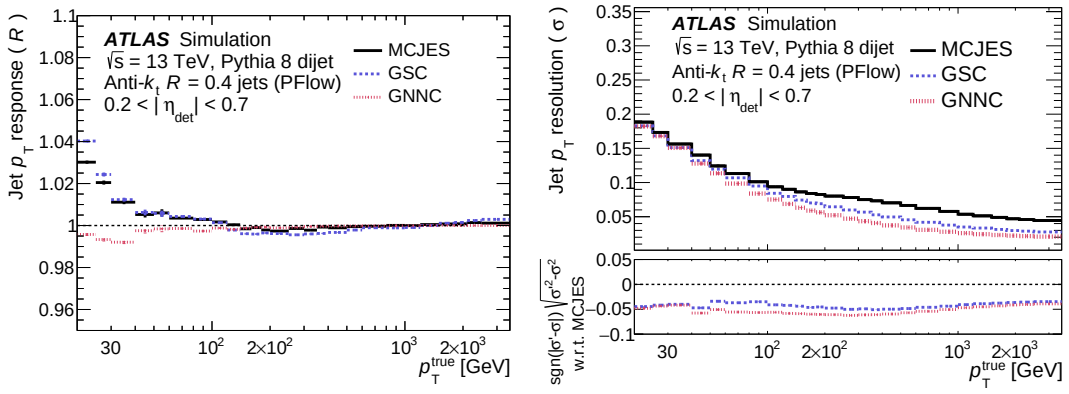


(a) (b)

Figure 5.4: The (a) jet $p_T$ closure and (b) jet $p_T$ resolution for $0.2 < |\eta_{det}| < 0.7$. The MCJES is shown with a solid line, GSC by a long dashed line, and GNNC by a short dashed line [147].

| | | |
|---|---|---|
| Calorimeter | $f_{\mathrm{LAr},0-3}$* | The $E_{\mathrm{frac}}$ measured in the 0th-3rd layer of the EM LAr calorimeter |
| | $f_{\mathrm{TILE}0*-2}$ | The $E_{\mathrm{frac}}$ measured in the 0th-2nd layer of the hadronic tile calorimeter |
| | $f_{\mathrm{HEC},0-3}$ | The $E_{\mathrm{frac}}$ measured in the 0th-3rd layer of the hadronic end cap calorimeter |
| | $f_{\mathrm{FCAL},0-2}$ | The $E_{\mathrm{frac}}$ measured in the 0th-2nd layer of the forward calorimeter |
| | $N_{90\%}$ | The minimum number of clusters containing 90% of the jet energy. |
| Jet kinematics | $p_{\mathrm{T}}^{JES}$* | The jet $p_{\mathrm{T}}$ after the MCJES calibration |
| | $\eta_{\mathrm{det}}$ | The detector $\eta$ |
| Tracking | $w_{\mathrm{track}}$* | The average $p_{\mathrm{T}}$-weighted transverse distance in the $\eta$-$\phi$ plane between the jet axis and all tracks of $p_{\mathrm{T}} > 1$ GeV ghost-associated with the jet |
| | $N_{\mathrm{track}}$* | The number of tracks with $p_{\mathrm{T}} > 1$ GeV ghost-associated with the jet |
| | $f_{\mathrm{charged}}$* | The fraction of the jet $p_{\mathrm{T}}$ measured from ghost-associated tracks |
| Muon segments | $N_{\mathrm{segments}}$* | The number of muon track segments ghost-associated with the jet |
| Pile-up | $\mu$ | The average number of interactions per bunch crossing |
| | $N_{PV}$ | The number of reconstructed primary vertices |

Table 5.1: List of input variables for the GNNC. Observables with a * correspond to those that are also used by the GSC.

to inaccuracies or limitations in MC simulation modelling for certain physics processes, or imperfections in the detector. The *in-situ calibration* accounts for these residual differences between data and simulation after all the previous steps of the calibration chain have been carried out.

To correct for this, a data-based correction is derived from collision data for

processes where a jet is balanced against an object with a well-known energy scale.[5] The processes used in the in-situ calibration are di-jets (for $\eta$-intercalibration), photon+jet, Z+jet, and multi-jet; which are illustrated in Figure 5.5. This balance

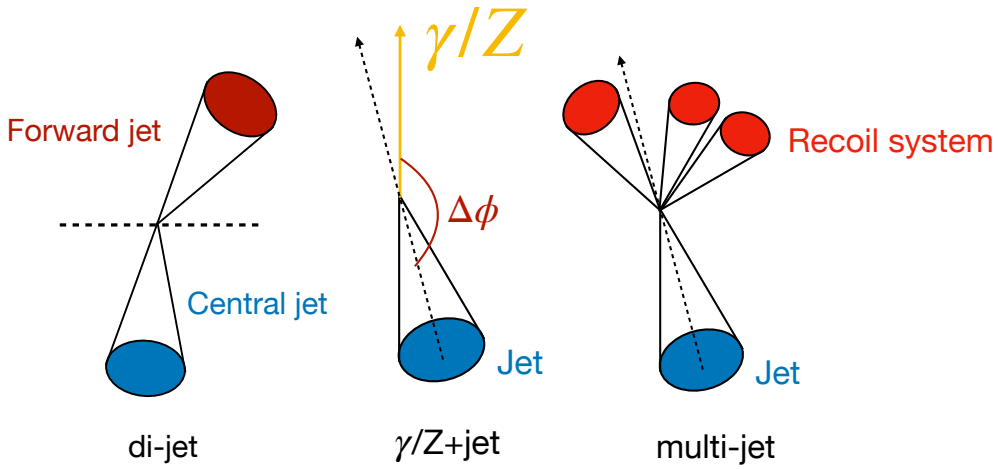


Figure 5.5: Balance diagrams for (a) di-jet, (b) $\gamma$/Z+jet, and (c) multi-jet events, that are used in the in-situ calibration

provides a direct way to assess the jet's energy, so if the reference object's $p_T$ is assumed to be well-calibrated, any deviation in the jet's $p_T$ balance can highlight a discrepancy in the jet measurement that can be corrected. The $p_T$ responses are fitted in bins of the reference object with a Gaussian function and the correction is applied to data to harmonise the scale of experimental observations and MC simulations. This correction factor is given as a double ratio between data and MC:

$$\frac{1}{c} = \frac{R^{MC}_{in-situ}}{R^{Data}_{in-situ}} \tag{5.4}$$

A statistical combination of data-to-MC ratios of the response measurements for all the different processes is used to apply a correction exclusively to the data. The combined results from the 2015-2017 data collection period are shown in Figure 5.6 . This visual representation clearly indicates the need for an in-situ correction, while also demonstrating an agreement of this requirement among all the methods used.

[5]Corrections are applied to data rather than simulation to ensure that experimental outcomes align with theoretical predictions, for which MC serves as a reliable approximation.

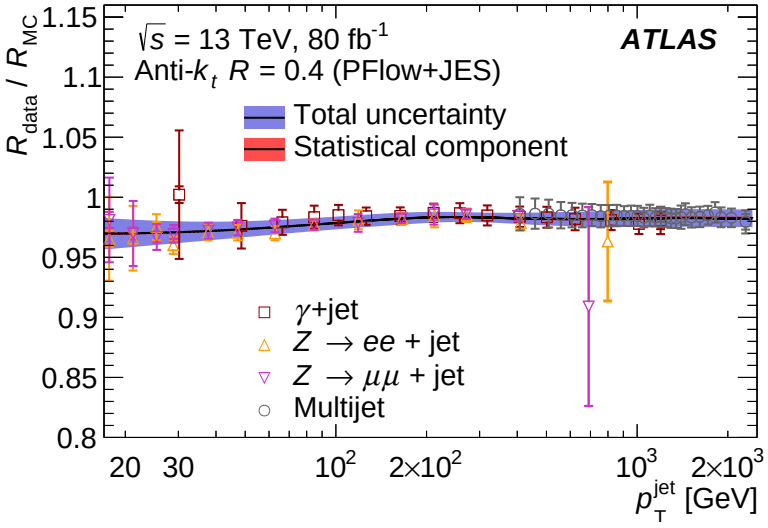


Figure 5.6: Comparison of the PFlow+JES jet balance response ratio between data and nominal MC event generators, as a function of $p_T^{jet}$ for data taking in 2015-2017. This comparison is for three different in-situ calibration processes: Z+jet, $\gamma$+jet, and multijet. The inner horizontal markers represent the statistical uncertainty. The outer horizontal markers indicate the combination of both statistical and systematic uncertainties, added in quadrature. The final correction applied is also shown, with its associated uncertainty bands for both statistical and total uncertainties [151].

### 5.4.1 $\eta$-intercalibration

The $\eta$-intercalibration is a correction that uses di-jet topologies for calibrating the energy scale of forward jets in the detector, that are between the ranges of $0.8 \leq |\eta| \leq 4.5$. These jets are-calibrated to match the energy scale of central jets in the detector, which are in the range of $|\eta| < 0.8$. Due to the MCJES calibration stage mentioned in section 5.2, the central region is assumed to be better understood than the forward region of the detector where the structure is more complicated. This means that the forward jets energy scales can be corrected relative to the central jets. Di-jet events are exactly two jets recoiling against one another, and can be considered even within different regions of $\eta$ to each other. This means that all of the different regions can be calibrated relative to one another.

As shown in Figure 5.5a, the two leading jets in the di-jet topoplogy are back-to-back. Thus, an asymmetry in the jet $p_T$ is considered between two separate

detector regions, which are given the names of left and right regions:

$$\mathcal{A} = \frac{p_T^{left} - p_T^{right}}{p_T^{avg}},\ p_T^{avg} = \frac{p_T^{left} + p_T^{right}}{2} \tag{5.5}$$

A relative jet response ratio based on the correction factor, $c = \frac{c^{right}}{c^{left}}$, is then defined, calculated in terms of the average value of $\mathcal{A}$ in bins of $p_T^{avg}$ and $\eta_{det}$:

$$\frac{1}{c} = \frac{2+ < \mathcal{A} >}{2- < \mathcal{A} >} \approx \frac{p_T^{left}}{p_T^{right}} \tag{5.6}$$

This relative jet response is shown in Figure 5.7 for the 2017 dataset, comparing data and two MC samples, Powheg+Pythia 8 and Powheg+Herwig 7 as a function of $|\eta_{det}|$ for a range of $25 \leq p_T^{avg} < 40$ GeV (Figure 5.7a), and jet $p_T$ for a range of $1.2 \leq \eta_{det} < 40$ GeV (Figure 5.7b). The MC simulation approximately matches the features shown in data, but the data is, on average, slightly higher than the MC for both as a function of jet $p_T$ and of $\eta_{det}$.

In Figure 5.7a, the largest deviation of MC/data is roughly 1.5% within the region of $2.5 < \eta_{det} < 3.5$. This is due to the outer hadronic endcap being within the range of $2.5 < |\eta| < 3.2$ as explained in Section 2.3.2. As the calorimeter changes technologies, the response can be influenced and this effect is increased as the jets enter deeper and deeper the endcap region, until they move back into the forward calorimeter and the response drops back off again [152].

### 5.4.2 $p_T$ response calibration with Z+jet and $\gamma$+jet events

The next stage of the in-situ calibration uses $p_T$-based responses for processes involving well-measured photons, Z bosons and multi-jets to bring the absolute JES in data to the same as in simulation. In this thesis the focus will be on $\gamma$/Z+jet in-situ calibrations.

Due to the fact that electrons and muons resulting from Z boson decays, along with photons, are well measured in the ATLAS detector and all have low energy scale uncertainties, they are good references for the calibration of the JES [153]. The other benefit of using multiple different reference objects is the phase space of $p_T$ that can be covered; with Z+jet measurements offering high statistics at low $p_T$, while $\gamma$+jet measurements being more statistically reliable at higher $p_T$.

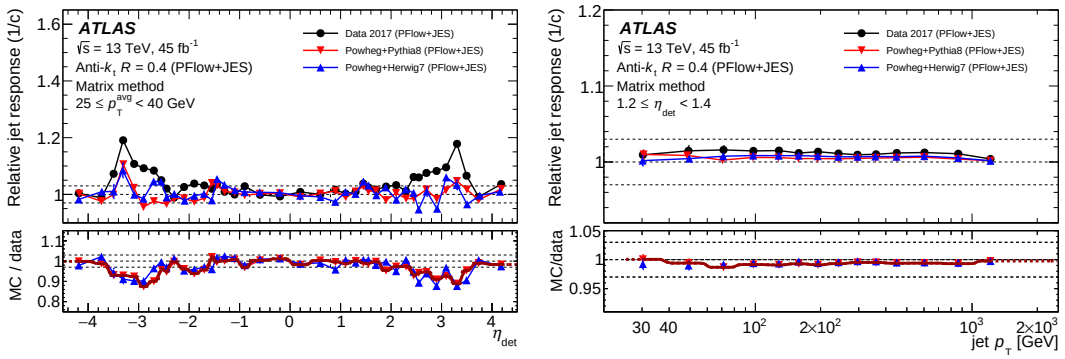


(a) (b)

Figure 5.7: Relative jet response, $\frac{1}{c}$, calibrated with PFlow+JES as (a) a function of $\eta_{det}$ for the range $25 \leq p_T^{avg} < 40$ GeV and (b) for the range $1.2 \leq \eta_{det} < 40$ GeV. The top panels show the relative response for data (black dots), Powheg+Pythia 8 (red triangles), and Powheg+Herwig 7 (black triangles). The bottom panels show the MC-to-data response ratios and smoothed in-situ calibration factor which is used to perform the calibration correction [147].

For these calibrations, the *Missing-$E_T$ Projection Fraction (MPF)* technique is used. This approach takes the balance between the full hadronic recoil of an event against the well-measured reference object momentum to obtain a correction factor for the differences between data and MC simulation.

At particle level, the $p_T$ of the hadronic recoil activity should be equal and opposite to the $p_T$ of the reference object, as per the conservation of momentum:

$$\overrightarrow{p}^{ref}_{T,truth} + \overrightarrow{p}^{recoil}_{T,truth} = 0 \tag{5.7}$$

Well-calibrated objects are considered to have a response of 1 at detector level while the hadronic recoil response, $r_{\mathrm{MPF}}$, is below unity. Assuming the reason for this value being lower than unity is due to missing energy, $E_T^{miss}$, the previous equation can then be defined as the following at detector level:

$$\overrightarrow{p}^{ref}_{T} + r_{\mathrm{MPF}}\,\overrightarrow{p}^{recoil}_{T} = -\overrightarrow{E}^{miss}_{T} \tag{5.8}$$

When projecting to the direction of the reference object, we can conclude that the hadronic recoil response depends only on the event's missing energy and reference

$p_T$, leading to a definition of the average MPF response, $\mathcal{R}_{\text{MPF}}$:

$$\mathcal{R}_{\text{MPF}} = \left\langle 1 + \frac{\hat{n}_{ref} E_T^{miss}}{p_T^{ref}} \right\rangle \tag{5.9}$$

An example of the most recent in-situ calibration results using MPF for Z/$\gamma$+jet events in Run 2 is shown in Figure 5.8.[6] The correction factors for in-situ measurements are calculated from the ratio of MC/data as shown in the bottom panel of both plots in the figure. We can see that the data has a lower jet energy relative to the MC, meaning a correction gets applied to jets in data to account for these differences. This correction factor uses the nominal MC, which is MadGraph5+Pythia 8 for the Z+jet events and Pythia 8 for the $\gamma$+jet events. The secondary MC, Sherpa 2.2.11 in Z+jet and Sherpa 2.2.2 in $\gamma$+jet events, is used to account for the difference in the two MC samples, which is considered as the Monte Carlo modelling uncertainty in the in-situ measurement. This is discussed in more detail in Section 5.5.5.

The in-situ measurements of $\gamma$+jet and Z+jet events are combined with the aforementioned multi-jet events measurement which can probe a much higher $p_T$ range. A smooth in-situ correction is derived based on the nominal MC-to-data ratios as a function of $p_T$, with a complete set of uncertainties, similar to what was shown in Figure 5.6. A detailed view of the in-situ combination can be found in Ref. [154].

## 5.5 In-situ bJES

This thesis introduces a new aspect to the in-situ calibration process by incorporating a *b–jet energy scale (bJES)* calibration for $\gamma$+jet events. This work represents the first instance of applying a bJES specific in-situ calibration to PFlow jets in this context. The motivation for this study is to assess the effectiveness of the ATLAS JES calibration for $b$-jets. Given the critical role of $b$-jets in precision measurements involving top quarks and the Higgs boson, where the $b$ quark exhibits the strongest coupling, determining the suitability of the ATLAS JES calibration chain for these jets is key. This calibration tests the modelling of $b$-fragmentation and $B$-decays in the ATLAS Monte Carlo simulation,

[6]Note that the MPF response for the Z→ $\mu\mu$+jet channel and the related uncertainties for all the MPF results can be found in Appendix A.

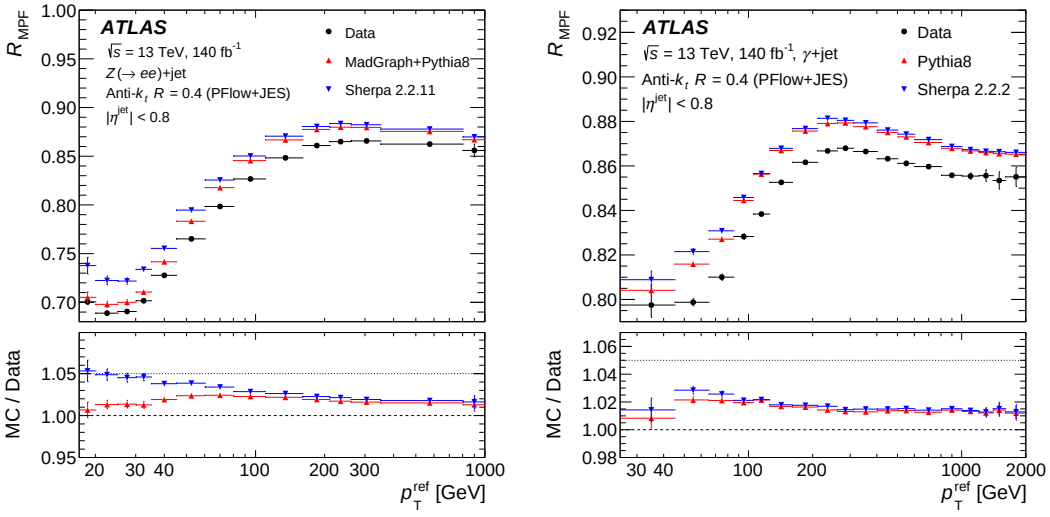


(a) (b)

Figure 5.8: MPF calibrated with PFlow+JES for ?? $Z \rightarrow ee$(+jets) and (b) $\gamma$+jet events as a function of $p_T^{ref}$ in the range $17 \leq p_T^{ref} \leq 1000$ GeV. The black circles represent data, the red triangles represent PYTHIA 8, and the blue triangles represent SHERPA. The bottom panel shows the MC-to-data response ratios. The error bars correspond to statistical uncertainties.

while providing an in-situ measurement of the response of $b$-jets.

This JES measurement for processes involving photons, is similar to the procedure shown in Section 5.4.2, but using the *Direct Balance (DB)* technique as opposed to the aforementioned MPF technique. The DB method takes the balance of a single $b$–jet recoiling against a single well-calibrated photon. This method utilises the reference momentum, $p_T^{ref}$, that multiplies the photon $p_T$ with the cosine of the azimuthal angle, $\phi$, between the jet and the photon: $p_T^{ref} = p_T^{\gamma} \times |cos(\Delta\phi)|$. The direct balance is defined as the average of the average ratio of the jet transverse momentum, $p_T^{jet}$, and the reference $p_T$:

$$R_{DB} = \left\langle \frac{p_T^{jet}}{p_T^{ref}} \right\rangle \tag{5.10}$$

In this section, the average direct balance, $R_{DB}$, will be determined for an inclusive sample of $\gamma$+jet events, that is dominated by light quark jets, and a sample where the jets are $b$-tagged using several working points of the DL1r tagger. Fits to the balance distribution, described in Section 5.5.3, will use full Run 2 data, and MC

samples generated with PYTHIA 8.2 and SHERPA 2.2.2. The selection follows that described in Section 5.5.1, with the addition of a $b$-tagging requirement.

Firstly in this section we will describe the treatment of measuring the JES of inclusive jets step-by-step, and then move onto $b-$tagged jets which involve the same treatments as the inclusive jet JES measurement. A result is then derived relating to the compatibility of the energy scale between the inclusive and $b-$tagged samples. This result can be measured very precisely since the systematic uncertainties tend to cancel each other out when comparing the ratio between the two regimes.

### 5.5.1 Data Selection

The data used in this measurement was collected with the ATLAS detector between 2015 and 2018, when the LHC delivered $pp$ collisions at a center-of-mass energy of 13 TeV. The total integrated luminosity of the collected sample is 140 $fb^{-1}$ and the average number of $pp$ interactions per bunch crossing is 33.7 [155]. There are roughly 17 billion events available from data during this data taking period, before any selection criteria is applied.

A number of single-photon triggers are used to select $\gamma$+jet data events using different photon $E_T$ thresholds and loose identifications. Events with low $p_T$ photons, all the way down to 15 GeV, were collected using prescaled triggers [156], whose thresholds and prescale factors are displayed in Table 5.2, while only the highest-level trigger is not prescaled. Prescaled triggers are a method to reduce the rate of events selected by a specficic trigger. The prescale factor is essentially a skip factor that tells the trigger system to only record one event out of every $N$ events that fulfill the trigger conditions and is used for processes that are abundant, where recording every event is unnecessary for the physics analyses. Unprescaled triggers select all events that meet the specified criteria without any intentional reduction in the rate. These triggers are typically used for processes of particular interest, where it's important to analyze as many qualifying events as possible.

Anti-$k_t$ PFlow jets were employed in this measurement, with radius R = 0.4; calibrated with the previous steps of this chapter up to the $\eta$-intercalibration step.

Jets found in the central detector, following the criteria of $|\eta^{jet}| < 0.8$, are used

| $E_T^\gamma$ range ( GeV) | HLT trigger |
|---|---|
| 15-100 | HLT_g10_loose |
| 20-100 | HLT_g15_loose |
| 25-100 | HLT_g20_loose |
| 30-110 | HLT_g25_loose |
| 40-110 | HLT_g35_loose |
| 45-120 | HLT_g40_loose |
| 50-120 | HLT_g45_loose |
| 55-130 | HLT_g50_loose |
| 65-130 | HLT_g60_loose |
| 75-140 | HLT_g70_loose |
| 85-140 | HLT_g80_loose |
| 105-150 | HLT_g100_loose |
| 125-160 | HLT_g120_loose |
| 145-inf | HLT_g140_loose |

Table 5.2: List of prescaled photon triggers used for $\gamma$+jet events.

as these are better reconstructed than those in the forward regions, and the energy scale is well understood. The leading jet is required to have a $p_T > 20$ GeV to ensure that b-tagging calibrations are available. A sub-leading jet cut $p_T^{sub-jet} <$ max(0.10×$p_T^{ref}$, 15) GeV and azimuthal angle cut between the leading jet and photon $\Delta\phi_{\gamma,jet} > 2.8$ are required to suppress additional parton radiation effects from the events and allow the leading jet and photon to be relatively back-to-back. A tight JVT cut is required to suppress contamination from pile-up; where the JVT was required to be > 0.5 for jets in the range $20 < p_T^{jet} < 60$ GeV. The jets are required to be $\Delta R(\gamma, j) > 0.4$ away from the photon to avoid double counting of energy deposits. Photons entering the analysis are required to have $E_T^\gamma > 45$ GeV, although the photon bins studied will change depending on statistics, as explained in Section 5.5.6, and to fall in $|\eta^\gamma| < 1.37$, while also passing the tight isolation and identification selection criteria [135]. A discussion of isolation and identification can be found in Section 4.2.1. On top of this, specifically for the $b$–tagged jets, the DL1r $b$–tagging algorithm was used, which is a multidimensional output neural network (NN) tagger [157]. The sample is sufficient to calibrate jets with $p_T > 150$ GeV with good statistics, while the prescaled triggers extend the range down into the important jet $p_T$ interval of about 50-150 GeV, with lesser statistics.

After applying all the selections, the dataset for the $\gamma$+jet calibration is narrowed down to 1.5 million events. When the $b$-tagging tool is used, this value is further reduced to between 8.5% and 2%, depending on the strictness of the efficiency

criteria used in the tagger.

### 5.5.2 Monte Carlo Samples

MC events from Pythia 8.2 [158] and Sherpa 2.2.2 [159] are generated for this in-situ study to determine the JES and related uncertainties. The Monte Carlo campaigns a, d, and e - which correspond to the data luminosity and data taking conditions of 2015-2016, 2017, and 2018, respectively - are produced individually in $\gamma$+jet events. They are then normalised before being combined. These samples are produced separately to ensure that they match the experimental conditions for each data-taking period during Run 2. To normalise each sample within their respective MC campaigns, the luminosity is scaled by the ratio of the cross section multiplied by the filter efficiency to the total number of events in each sample. Information for the different MC generator campaigns used can be found in tables in Appendix B; including the event counts, cross sections, and filter efficiencies for each $E_T^\gamma$ range bin.

Typically in ATLAS simulations primarily describe light-quark processes, but also describe those with heavy flavour jets in the final state. Before cuts are applied, Pythia has roughly 600 million $\gamma$+jet events in the full $p_T$ range, while Sherpa has approximately 110 million. According to the truth labels in MC, a small fraction of about 2% correspond to $b$–jets, and 15% to charm jets. After implementing the selections described in Section 5.5.1, the count decreases to approximately 11.8 million events for Pythia and 7 million event for Sherpa. Further application of the $b$-tagging tool further reduces these numbers to a range of 10% to 1.5%, varying with the stringency of the efficiency criteria used.

As described in Section 3, the fragmentation is modelled through the Lund string model in Pythia, while Sherpa employs the cluster fragmentation model. Both generators use the EvtGen particle decay simulation package to simulate the B hadron decays [160].

### 5.5.3 Fitting of direct balance

The DB technique employs a binning scheme based on the reference object transverse momentum, $p_T^{ref}$; in this case the reference object is a photon. It must be noted that due to the naming schemes chosen there are two versions of $p_T^{ref}$,

one of which was defined earlier in Equation 5.10 for the DB and one that we have defined here as being the reference object (the photon). For future reference when $p_T^{ref}$ is shown in a plot or mentioned, it is considered the latter unless mentioned otherwise.

The response of the system under study is initially determined within each bin of $p_T^{ref}$ using a maximum likelihood estimation method with a Gaussian distribution. To minimise the impact of potential discrepancies from extreme events in the simulation, the fitting range is restricted to twice the root mean square (RMS) of the response distribution around its mean. This ensures that the tails of the distribution, which may be subject to inaccuracies in the MC modelling, have a reduced influence on the final result.

### 5.5.4 Background estimation and signal purity

After applying the selections detailed in Section 5.5.1, particularly the identification and isolation cuts on the photons, a non-negligible amount of background still remains in the sample. This background predominantly originates from multi-jet processes, in which a jet is misidentified as a photon. These jets usually consist of a single light neutral meson, such as a $\pi^0$ or $\eta$ meson, which fakes the photon signature.

To combat this, a background estimation method has been developed, aptly named the ABCD method [161, 162]. Within this method the observed number of events in four control regions are defined using the variables photon identification, $\gamma_{ID}$, and photon isolation $E_T^{iso}$. Region A is considered the signal region, and three additional regions: B, C, D, are considered to be relatively abundant in background produced events.

As displayed in Figure 5.9, the 4 regions are separated, with each following a set of criteria:

- Signal region A contains a cut for tight and isolated ($E_T^{iso} < 2.2 \times 10^{-2} \times E_T^{\gamma} + 2.45$ GeV) photon candidates.
- Control region B contains a cut for tight and non-isolated ($E_T^{iso} > 2.2 \times 10^{-2} \times E_T^{\gamma} + 2.45$ GeV) photon candidates.
- Control region C contains a cut for non-tight and isolated ($E_T^{iso} < 2.2 \times 10^{-2} \times E_T^{\gamma} + 2.45$ GeV) photon candidates.

- Control region D contains a cut for non-tight and non-isolated ($E_T^{iso} > 2.2 \times 10^{-2} \times E_T^{\gamma} + 2.45$ GeV) photon candidates.

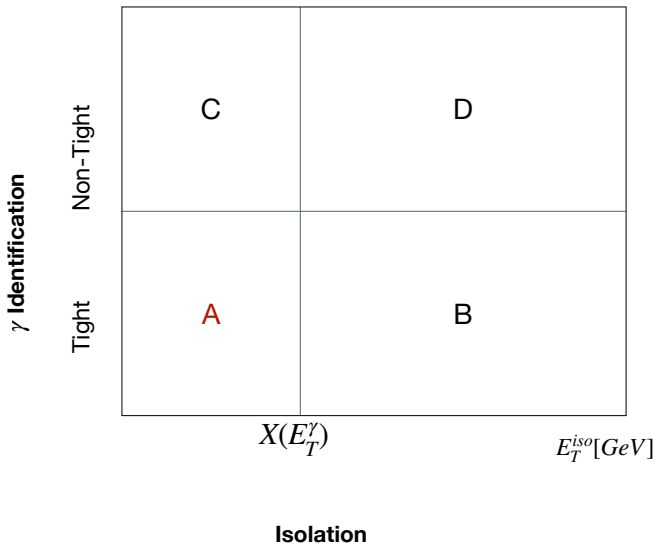


Figure 5.9: 2-D plane of photon identification cuts vs isolation cuts used to estimate the background in the signal region, A, from the three control regions B, C, and D.

The assumption of this method is that the fractions of background events that pass isolation and identification factorise, such that $N_A$ can be predicted from $N_B$, $N_C$ and $N_D$:

$$\frac{N_C^{bkg}}{N_D^{bkg}} = \frac{N_A^{bkg}}{N_B^{bkg}} \tag{5.11}$$

This holds true if the two observables are sufficiently uncorrelated, thus the reason for the use of the $\gamma_{ID}$ and $E_T^{iso}$ variables. However, this assumption is not quite correct as the two variables are slightly correlated. This requires the use of the background correlation variable, $R^{bg}$, to account for this. Another assumption is that the contamination of background in the signal region is small enough, which, again, is not entirely correct and must be considered by removing the background contamination from the signal region.

This leads to the number of signal events observed in region A being defined by the equation:

$$N_A^{sig} = N_A - R^{bg} \frac{(N_B - \epsilon_B N_A^{sig})(N_C - \epsilon_C N_A^{sig})}{(N_D - \epsilon_D N_A^{sig})}, \tag{5.12}$$

where $N_k$ is the number of events in region k, and $N_A^{sig}$ is the number of expected signal events. The background correlation can then be defined as:

$$R^{bg} = \frac{N_A^{bg} N_D^{bg}}{N_B^{bg} N_C^{bg}}, \tag{5.13}$$

where $N_K^{bg}$ is the number of background events in region k. Here $R_{bg}$ is the measure of correlation between the isolation and identification variables and ideally would be given a value of 1 if there was no correlation.

The *Signal Leakage Fraction (SLF)* is denoted by $\epsilon_K$ for each control region k. These fractions represent the estimated number of signal events into the control regions and are, thus, calculated as $\epsilon_K = \frac{N_K}{N_A}$. As presented in Figure 5.10a, the SLFs are calculated from Pythia and Sherpa for the nominal inclusive sample, with the event selection described in Section 5.5.1. The assumption of the number of signal events in the control regions is evaluated by applying a background estimation uncertainty, explained in Section 5.5.5.

The signal leakage fractions in region B, represented as $\epsilon_B$, exhibit an initial value of approximately 0.5 in the lower $p_T^\gamma$ bins and gradually decrease to around 0.1 in the higher bins. The agreement between the MC generators remains good until approximately 200 GeV, after which they start to deviate. Regarding $\epsilon_C$, which denotes the fractions in control region C, it fluctuates within the range of 0.07 to 0.1. The MC generators remain consistent with each other throughout this region. At lower $p_T^\gamma$ bins, $\epsilon_D$, which considers the fractions in region D, lies between 0.05 and 0.01, with Sherpa and Pythia showing reasonable agreement until about 150 GeV. Beyond this point, Sherpa's values decrease relative to Pythia, primarily due to pronounced differences in bremsstrahlung effects.

The signal purity, $P$, which is computed as the ratio of $N_A^{sig}/N_A$ is displayed in Figure 5.10b. In the lowest $p_T^\gamma$ bin, the purity is approximately 0.75. As the $p_T^\gamma$ bins increase, the purity consistently rises, surpassing 0.95 for the majority of the higher $p_T^\gamma$ bins.

To ensure accuracy in the response measurements and account for the signal region estimation, these purities are what are used in the purity-corrected responses:

$$R_A^{corr} = \frac{1}{P} R_A + R_C \left(1 - \frac{1}{P}\right), \tag{5.14}$$

where $R_A$ is the response of signal region A and $R_C$ is the response of control region

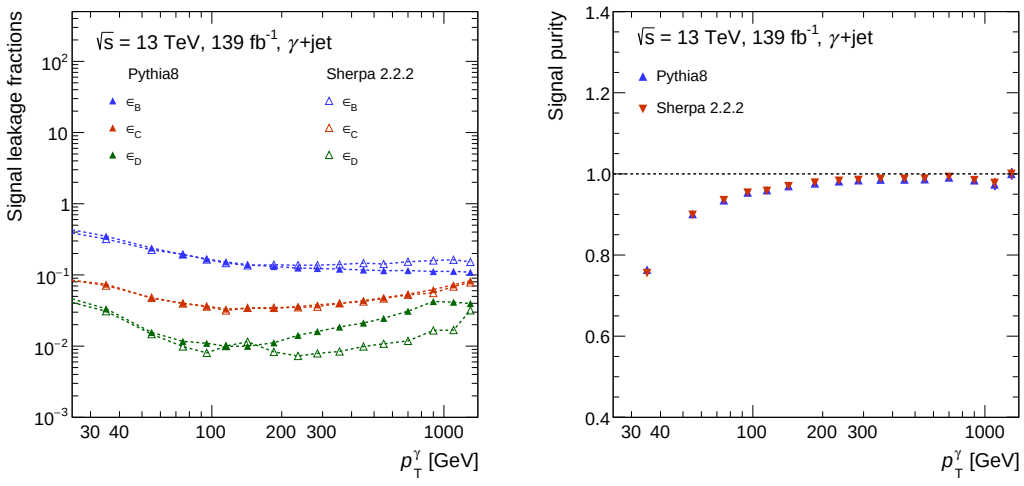


(a) (b)

Figure 5.10: (a) The SLFs for PYTHIA (SHERPA) displayed by solid markers (see-through markers) for the control regions B (blue), C (red), and D(green) as a function of $p_T^\gamma$. (b) The signal purities estimated using the SLFs in PYTHIA (SHERPA) in blue (red) as a function of $p_T^\gamma$.

C. The purity correction $R_A^{corr}/R_A$ is then applied to the response measurements in the $\gamma$+jet measurements. This is shown in Figure 5.11, where the largest correction is about 1% in the lowest $p_T^\gamma$ and becomes negligible for the higher bins.

The reason that region C is chosen as the control for the purity correction and not the other background regions is due to the importance in reducing effects due to imbalanced topologies. For example, a leading-jet in an imbalanced topology can be mis-constructed as a fake photon passing the $\gamma_{ID}$ criteria, contributing to larger/lower response. Requiring isolation (that is required in region C) reduces these kind of configurations and ensures that, if the fake photon passes isolation, it carries most of the energy of the jet and leads to more balanced topologies.

As mentioned earlier, the ABCD technique relies on the assumption that the two variables being used are uncorrelated, resulting in an ideal $R_{bg}$ value of 1, but the photon ID and isolation exhibit some degree of correlation. To quantify this correlation, the background regions B and D are split into four subsets (B´, B´´, D´, D´´) by applying an isolation cut (C) at various testing values above the lower limit ($X(E_T^\gamma)$). The isolation cut is defined as $X = 2.2 \times 10^{-2} \times E_T^\gamma + 2.45$ GeV $+ Y$,

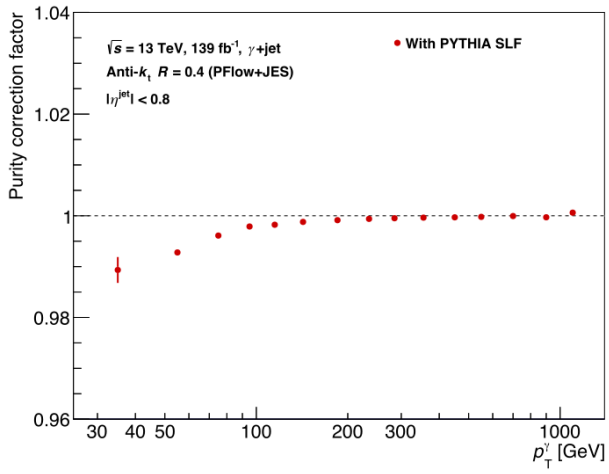


Figure 5.11: The purity correction factor with the use of PYTHIA signal leakage fractions as a function of $p_T^\gamma$

where Y is a testing value. To compute the new background correlation ($R_{bg}$), the following formula is used:

$$R_{bg} = \frac{(N_{B'} - \epsilon_{B'} N_A^{sig})(N_{D''} - \epsilon_{D''} N_A^{sig})}{(N_{B''} - \epsilon_{B''} N_A^{sig})(N_{D'} - \epsilon_{D'} N_A^{sig})} \tag{5.15}$$

The obtained $R_{bg}$ value is then compared with an ideal value of 1, using different threshold inputs. The threshold that yields the largest difference between $R_{bg}$ and 1 is considered as the correlation uncertainty in the purity corrected response estimation. The analysis of this correlation uncertainty is presented in Figure 5.12, where five thresholds were tested, and the study is limited up to 6.45 GeV. The dashed red line represents the correlation uncertainty used, corresponding to the highest difference. Observations reveal that in the lowest $p_T^\gamma$ bins, the value is approximately 1.15, while beyond 100 GeV, the highest marker value is 1.5, using the 6.45 GeV threshold. It is noted that the uncertainty is overestimated in the higher $p_T^\gamma$ region for ease of uncertainty calculation, but it has a negligible impact on the corrected response.

### 5.5.5 Inclusive response

The DB response defined in Equation 5.10 is measured as a function of $p_T^{\text{ref}}$ in 13 bins, $p_T^{\text{ref}} \in \{45, 65, 85, 105, 125, 160, 210, 260, 310, 400, 500, 600, 800, 1000\}$ GeV.

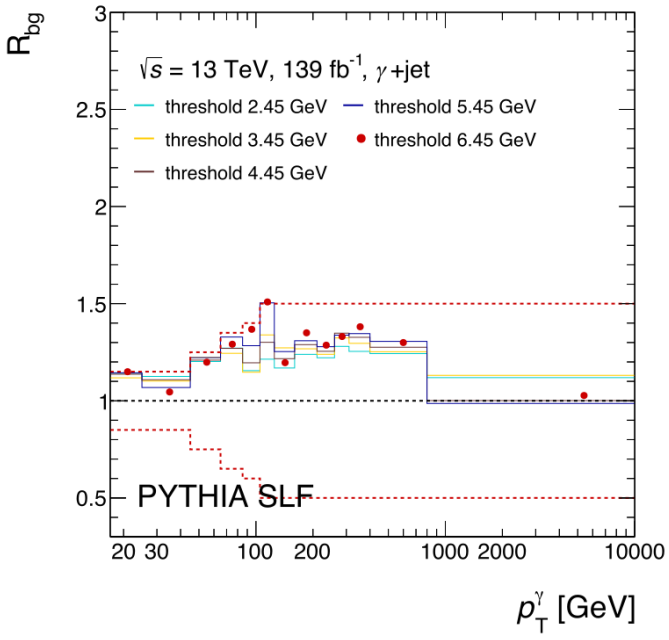


Figure 5.12: The background correlation, as a function of $p_T^\gamma$, using the PYTHIA signal leakage fractions. The different threshold values are 2.45 GeV (blue line), 3.45 GeV (yellow line), 4.45 GeV (purple line), 5.45 GeV (blue line), and 6.45 GeV (red marker). The dashed black line is marks unity and the dashed red line marks the uncertainty region used in the corrected response.

The upper part of Figure 5.13 shows the average responses against the full inclusive $p_T^{ref}$ range. We can see that the response in both the PYTHIA and SHERPA is always overestimated relative to the response in data, where $R_{DB}$ is lowest for small $p_T$ bins and tends closer to 1 as the $p_T$ increases. The lower part of the figure displays the MC to data ratio for both the MC generators; with the deviation of the ratio being about 1-4% higher than in MC than in data. This gets fixed when applying the in-situ correction to data, ensuring that data and MC have the same response. However, the two generators are in good agreement with each other when it comes to the prediction of the DB response for Run 2 in $\gamma$+jet events for small-$R$ PFlow jets.

The error bars in the balance distribution relate to the statistical uncertainty on the JES. This uncertainty is estimated in each $p_T^{ref}$ bin by calculating the error of the mean value obtained from fitting the Gaussian distribution to the data. The statistical errors are relatively small, with the largest being in the lowest $p_T^{ref}$ bins where the fitting of the Gaussian shape to data is slightly more difficult due to the cut on photon $p_T$ being around this range.

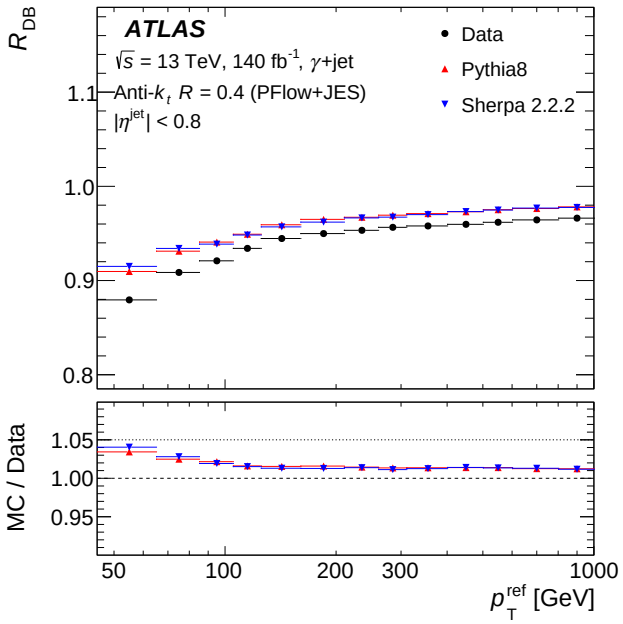


Figure 5.13: Direct balance calibrated with PFlow+JES for $\gamma$ + jet in the range $45 \leq p_T^{ref} \leq 1000$ GeV in data and MC simulation full Run 2 [147].

Systematic uncertainties also arise from the JES measurement that must be included in the calibration. Figure 5.14 illustrates these specific uncertainties, alongside the total systematic uncertainty obtained by summing each variable in quadrature. This cumulative value represents the error that is incorporated into the JES correction factor.

To address certain systematic uncertainties, a rebinning procedure is implemented to ensure that the observed features in the final outcome hold statistical significance and are not solely attributable to fluctuations arising from a small number of simulated or observed events. This rebinning procedure follows a bootstrapping approach, where pseudo-experiment datasets are generated by sampling from a Poisson distribution with a mean of 1 for each event in the data or MC simulation. As a result, these pseudo-experiments possess statistical correlations while remaining distinct from one another. By examining the RMS of the response distribution across the pseudo-experiments, a measure of the statistical uncertainty inherent to the analysis is obtained [163].

### Photon Energy Scale and Resolution

When photons are reconstructed, they undergo an energy calibration somewhat

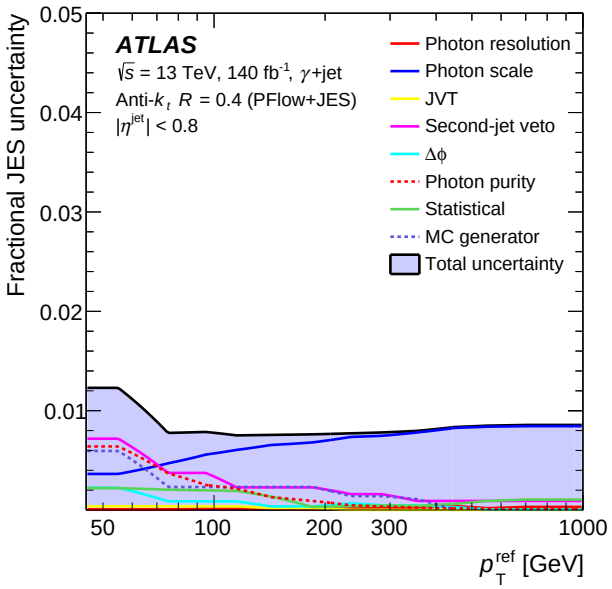


Figure 5.14: Uncertainties associated with the direct balance JES uncertainty with PFlow+JES for $\gamma$+jet in the range $45 \leq p_T^{ref} \leq 1000$ GeV in data and MC simulation full Run 2 [147].

similar to that of the in-situ jet reconstruction. For the photon calibration, the difference in energy scale between data and simulation is affected by various systematic uncertainties that are dependent on their $E_T$ and $\eta$ [164]. When examining most of the considered uncertainty variations, their influence on photon energy is evaluated separately for reconstructed converted and unconverted photons. Converted photons tend to have a shower development more similar to that of electrons, resulting in typically smaller systematic uncertainties in terms of energy scale compared to unconverted photons. The different sources of systematic uncertainties for the energy scale are the energy shift caused by pile-up events, the effects stemming from the calibration of detector layers, the calibration associated with the $E_4$ scintillator, influences arising from the material located in front of the calorimeter, the non-linear behaviour in the cell energy measurement, the modelling of the lateral shower shape, and the modelling of the photon reconstruction classification.

An analogous prescription to that employed for the photon energy scale uncertainty can be utilised to characterise the photon resolution uncertainty. The energy resolution has a number of sources of systematic uncertainties; these

include the fluctuations arising from showering and sampling in the calorimeter, variations in energy loss prior to reaching the calorimeter, the impact of electronics and noise from pile-up events, as well as the effects of remaining non-uniformities that affect the energy measurement in the collected data.

To assess the impact of uncertainties in the photon energy scale on the in-situ calibration, each source of uncertainty was independently varied by $\pm 1\sigma$ in the MC simulation to assess the photon energy scale and resolution in the data-to-MC ratio. This process allows for the determination of the impact of each individual source on the ratio between the data and the MC simulation. As shown in Figure 5.14 the photon energy scale is the dominant uncertainty past a $p_T^{ref}$ value of $\approx 80$ GeV, starting at roughly 0.4% and reaching nearly 0.9% for the JES uncertainty in the $\gamma$+jet calibration. On the other hand, the photon energy resolution is seen to be negligible in the full $p_T^{ref}$ range.

**Background estimation**

To evaluate the systematic uncertainty arising from the impact of the multi-jet background on the measured DB responses, there are three sources of uncertainties to consider. The first is the uncertainty on the purity of the samples, the second is the uncertainty related to the isolation-based background correlation which is discussed in Section 5.5.4, and the third is an uncertainty related to the definition of the identification cuts used.

The purity of the $\gamma$+jet sample was determined using the ABCD subtraction method mentioned in Section 5.5.4, making use of signal leakage fractions from the Pythia MC sample. The uncertainty on the purity is given by the expression $\Delta P(i)$, which is calculated as:

$$\Delta P(i) = (1 - P(i)) \times \frac{R_{in-situ}^{LNT}(i) - R_{in-situ}(i)}{R_{in-situ}(i)} \tag{5.16}$$

Here $P(i)$ represents the signal purity in the $p_t^{ref}$ bin $i$, $R_{in-situ}(i)$ denotes the DB data response measured with nominal selections in bin $i$, and $R_{in-situ}^{LNT}(i)$ stands for the measured response in-situ in data for photons that pass the loose' (LoosePrime4) but fail at least one of the tight identification requirements. This uncertainty is significantly dependent on the purity discussed in Section 5.5.4.

Lastly, an additional uncertainty is taken into account, known as the "loose" variation uncertainty. Since we use the LoosePrime4 identification cut to decide

what is tight and non-tight in the regions of the ABCD method, an uncertainty must be placed on this choice of cut by varying the criteria for the tight identification. This involves removing some of the shower shape cuts. The resulting modified control regions are denoted as LoosePrime2, LoosePrime3, LoosePrime4, and LoosePrime5. Here, "LoosePrimeX" indicates that X cuts have been removed from the identification requirements. For further details on LoosePrime, refer to Section 4.2.1. The variation in purity observed using the LoosePrime control region serves as part of the purity systematic variation.

The purity uncertainty is most significant in the lowest $p_T^{ref}$ bins, where the purity is at its lowest. In this region, the uncertainty reaches its maximum value of 0.6% on the overall JES uncertainties and becomes the second-largest source of uncertainty. However, with the progression to higher $p_T^{ref}$ bins, where the purity achieves its highest values, the uncertainty gradually diminishes.

**MC modelling**

The difference in the MC/data ratio between the two MC generators used in the DB response predictions is taken as the MC modelling uncertainty. As explained in Chapter 3, Pythia and Sherpa have different methods in how they model jet hadronisation, parton shower, and multiple parton interactions. The MC modelling uncertainty is $\approx 0.5\%$ in the first bin and, while moving towards the high end of the $p_T^{ref}$ range, it becomes a negligible uncertainty.

**Additional pile-up**

An additional uncertainty is applied for jets that can be produced in residual pile-up interactions for both data and MC as a check that these events do not affect the DB response. The nominal JVT requirement is set to 0.5, whereas a loose cut is varied to 0.2, allowing more pile-up-heavy jets to see the impact of this on the response. Since these jets should primarily affect the tails in the balance distributions they should have negligible impact on the response. The JVT systematic uncertainty was taken by measuring the MC-to-Data ratio with these two cuts and comparing to the nominal ratio. This uncertainty is negligible for the full $p_T^{ref}$ range, as expected.

**Suppression of further radiation**

As mentioned in section 5.5.1 a cut is applied on the sub-leading jet, and a cut is applied to the $\phi$ between the jet and photon in order to suppress additional QCD effects on the momentum between the leading jet and photon. Variations

are applied to the two cuts mentioned, in order to impose an uncertainty related to them. For the $\Delta\phi_{\gamma,jet}$ cut, there is a variation of ±0.1 relative to the nominal cut of $\Delta\phi_{\gamma,jet} > 2.8$, so the tight (loose) cut is 2.9 (2.7). The sub-leading $p_T$ cut is varied by ±0.05 for the relative $p_T$ and ±5 GeV for the absolute $p_T$ relative to the nominal cut of $P_T^{sub-jet} < \max(0.10\times p_T^{ref}, 15)$ GeV; thus the tight cut is set to $\max(0.05\times p_T^{ref}, 10)$ GeV and loose cut is $\max(0.15\times p_T^{ref}, 20)$ GeV. The MC-to-Data ratio is obtained with varied these cuts and compared to the nominal ratio to obtain the measurement these uncertainties. The $\Delta\phi$ uncertainty begins at ≈ 0.2% and, towards the higher end of the $p_T^{ref}$ spectrum, becomes negligible. The sub-leading jet $p_T$ cut is the second most dominant uncertainty in the first $p_T^{ref}$ bin, having a maximum value of ≈ 0.7% and quickly becomes negligible towards a higher $p_T^{ref}$. This indicates that, especially in the lowest $p_T$ bins, the radiation we are vetoing is not too well modelled by the MC.

### 5.5.6 $b$–tagged response

The next step of this study is the direct balance measurement for events where a leading $b$–jet is recoiling against a well-calibrated photon. This is achieved with an algorithm-based tool used within ATLAS called $b$–tagging [165].

#### $b$–tagged direct balance

As explained in section 4.3.1, the ATLAS $b$–tagging tool is separated into different efficiencies, specifically defined as working points at 60%, 70%, 77%, and 85%. The $b$–jet and $c$–jet content of the inclusive and $b$–tagged $\gamma$+jet samples are estimated with MC truth labels. Truth labels are are tags assigned to simulated particles in MC event samples to indicate a type of particle with its related information. Through $\Delta R$ matching, a truth-level particle can be matched to its corresponding reconstructed particle from the detector.

The quark compositions of jets in both the Pythia and Sherpa MC generators are shown in Table 5.3 for their full $p_T$ range.[7] In the inclusive jet sample, light quark and gluon flavoured jets dominate, while $c$–jets account for approximately 10-15% of the sample, and $b$–jets only represent roughly 2%. Although $b$–jets constitute a small number of the jets in the samples, they are still

[7]From examination of these values in different $p_T$ bins, it seems the jet content is constant for each bin of $p_T$, and so it seems there is no strong $p_T$ dependence for the jet quark compositions.

| Hadron Label | Inclusive jet | | WP 60% | | WP 70% | | WP 77% | | WP 85% | |
|---|---|---|---|---|---|---|---|---|---|---|
| | Pythia 8 | Sherpa | Pythia 8 | Sherpa | Pythia 8 | Sherpa | Pythia 8 | Sherpa | Pythia 8 | Sherpa |
| $b$ | 1.9% | 2.0% | 92.1% | 85.8% | 81.3% | 79.2% | 59.2% | 61.7% | 36.3% | 39.2% |
| $c$ | 14.2% | 10.6% | 2.3% | 1.6% | 13.4% | 9.2% | 35.4% | 27.0% | 57.4% | 49.7% |
| light $q$ or gluon | 83.9% | 87.4% | 5.6% | 12.6% | 5.3% | 11.6% | 5.4% | 11.3% | 6.3% | 11.1% |

Table 5.3: The average fractions of jet flavours for various $b$–tagging working points and inclusive jet.

enough to determine the bJES, due to the large number of events in the samples that we given in Section 5.5.2.

$b$–tagging enriches the samples in charm and bottom jets, drastically changing the quark content of the samples. To start with, the lightest $b$–tagging requirement is the one connected to the 85% WP. This is the only $b$–tagged sample where $c$–jets constitute the majority instead of $b$–jets. Specifically, in this working point, $b$–jets account for 57% (50%) in the case of Pythia (Sherpa). Consequently, the 85% efficiency working point can be viewed as a "cJES" measurement due to its significant prevalence of $c$–jets.

In the case of the 77% WP, the percentage of $b$–jets increases to about 60%, whereas $c$–jets decrease to around 30% of the sample. Moving on to the 70% WP, the proportion of $b$–jets increases slightly to approximately 79.2% of the sample. There is also a decrease in $c$–jets, making up roughly 10%, while light quark and gluon jets remain similar to the previous sample and show a consistent distribution across all the $b$–tagged samples. Consequently, $c$–jets lose their dominance as $b$–jets start to take a much more prominent role.

Lastly, The 60% WP exhibits the lowest efficiency and is primarily dominated by $b$–jets, comprising around 90% of the sample. Light quark and gluon jets follow with a relatively significant discrepancy between MC generators; Pythia accounting for 5.6%, and Sherpa for 12.6%. On the other hand, $c$–jets constitute the smallest percentage, making up only about 2% of the sample.

For the $b$–tagging tool there is a balance that must be maintained; that is to say that the lower value working points contain a higher purity of the sample (more $b$–jets), but lower statistics. Therefore, due to the lack of statistics in the last $p_T^{ref}$ bins of data in the 60% and 70% WP regimes, these two WPs will only have 12

$p_T^{ref}$ bins, $p_{\mathrm{T}}^{ref} \in \{45, 65, 85, 105, 125, 160, 210, 260, 310, 400, 500, 600, 800\}$ GeV.

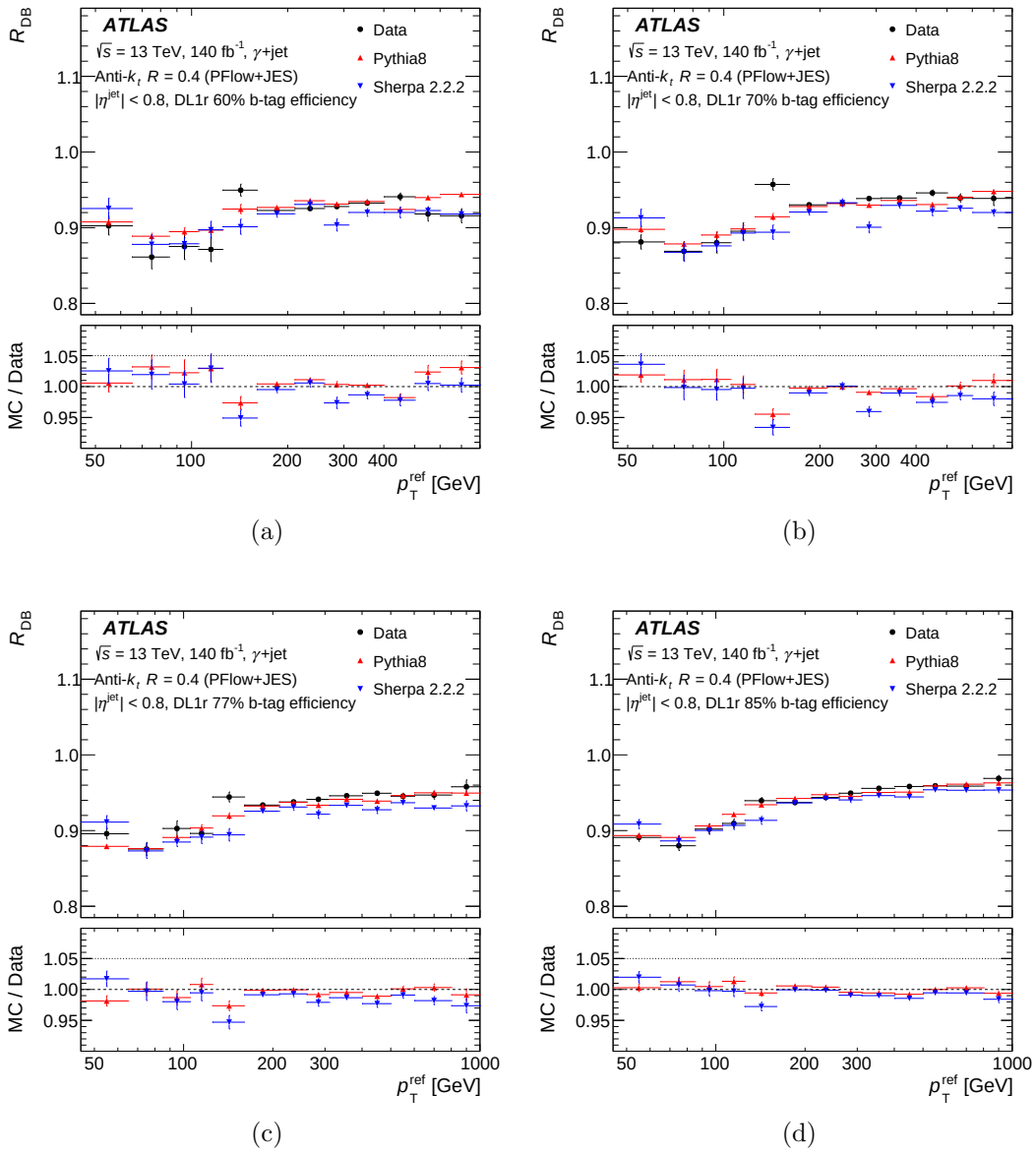


Figure 5.15: b-jet direct balance calibrated with PFlow+JES for $\gamma$ + jet in the range $45 \leq p_T^{ref} \leq 800$ GeV in data and MC simulation for (a) 60% and (b) 70% b-tagged working points and in the range $45 \leq p_T^{ref} \leq 1000$ GeV in data and MC simulation for (c) 77% and (d) 85% b-tagged working points [147].

For each working point, the $b$–jet direct balance is performed on both MC and data; these measurements can be seen in Figure 5.15. One thing to note, for all four distributions, is an obvious outlier in the fifth $p_T^{ref}$ bin between the values 125-160 GeV in both the balance response and MC/data. This discrepancy was

investigated; the balance distribution, fit quality and chi-squared, and the flavour composition were all studied and found to be in line with what we would expect and with the other bins in the samples. Additional checks were performed, including varying the jet veto and looking at the contributions from different triggers with which no clear explanation was found. Within this bin is where the lowest prescaled trigger HLT_g140_loose indicated in Table 5.2 begins. The most plausible explanation for this is a statistical fluctuation, possibly amplified by the substantial weights of events entering through the prescaled trigger. For future investigations, it may be beneficial to consider rebinning or conduct a more comprehensive study on the triggers to ascertain the underlying cause of this discrepancy. Nevertheless, for the current measurement, the discrepancy will remain as part of the analysis.

The DB distributions for working points 60% and 70% are shown in the Figures 5.15a and 5.15b, respectively, for the range $45 < p_T^{ref} < 800$ GeV, and the working points 77% and 85% are shown in Figures 5.15c and 5.15d, respectively, for the range of $45 < p_T^{ref} < 1000$ GeV. Overall, the ratios comparing simulation to data are consistent with 1 in most cases. The most noticeable statistical fluctuations are observed in the lower 5 $p_T$ bins, primarily attributed to limited statistics in these ranges due to the applied unprescaled triggers. Additionally, the WP 60% distribution exhibits the greatest variation in MC/data values per $p_T$ bin due to lack of statistics. This variability gradually stabilises when moving towards WP 85%, where there is an increase in statistical robustness.

The uncertainties related to the direct balance response for the $b$–tagged 77% working point are displayed in Figure 5.16. The systematic uncertainties for the other working points can be found in Appendix C, which exhibit similar uncertainty patterns, except the statistical uncertainty, which is greater overall in the 60% and 70% WPs, and lower in the 85% WP. The approach to handling uncertainties and the specific individual uncertainties utilised are identical to those described in Section 5.5.5, with the exception of incorporating the $b$-tagging uncertainty. This comes from the imperfect knowledge of the efficiency and misidentification rate of $b$–jets by the $b$–tagging algorithms. It accounts for the uncertainties in tagging true $b$–jets as non-$b$–tagged and misidentifying non-$b$–jets as $b$–tagged.

Regarding the uncertainties presented in Figure 5.16, the dominant source over the complete $p_T$ range of systematic uncertainties is the MC modelling, likely due

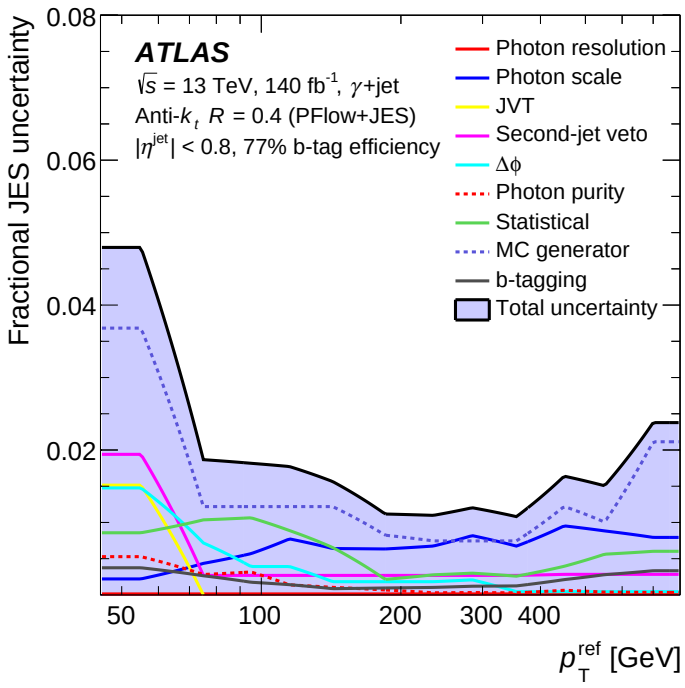


Figure 5.16: Uncertainties associated with the $b$–jet direct balance JES uncertainty with PFlow+JES for $\gamma$ + jet in the range $45 \leq p_T^{ref} \leq 1000$ GeV in data and MC simulation for the 77% $b$–tagged working point [147].

to the difference in how both MC generators model the fragmentation of $b$–quarks and $D$–hadrons (a hadron that contains a $c$–quark). The photon energy scale is as important as it is in the inclusive case and is not affected too much by the use of the $b$–tagging. Overall, the bJES has a minimum minimum of 1%, with the best results around the 200-400 GeV $p_T^{ref}$ bins, while the largest is roughly 4%, with these largest uncertainties typically in the lowest $p_T^{ref}$ bins where statistics are the lowest.

### Results

The primary objective of the in-situ bJES measurement is to quantify the compatibility between the JES of $b$–jets and inclusive jets. This involves comparing the energy scale of these two categories and determining the magnitude of their differences. To achieve this, the MC/Data ratio is computed for each category, and a new observable called $\tilde{R}_{bJES}$ is introduced to characterise the energy scale variation between $b$–tagged and inclusive jets:

$$\tilde{R}_{bJES} = \frac{\mathbf{R}^{MC}_{b-tagged}/\mathbf{R}^{data}_{b-tagged}}{\mathbf{R}^{MC}_{inclusive}/\mathbf{R}^{data}_{inclusive}} \tag{5.17}$$

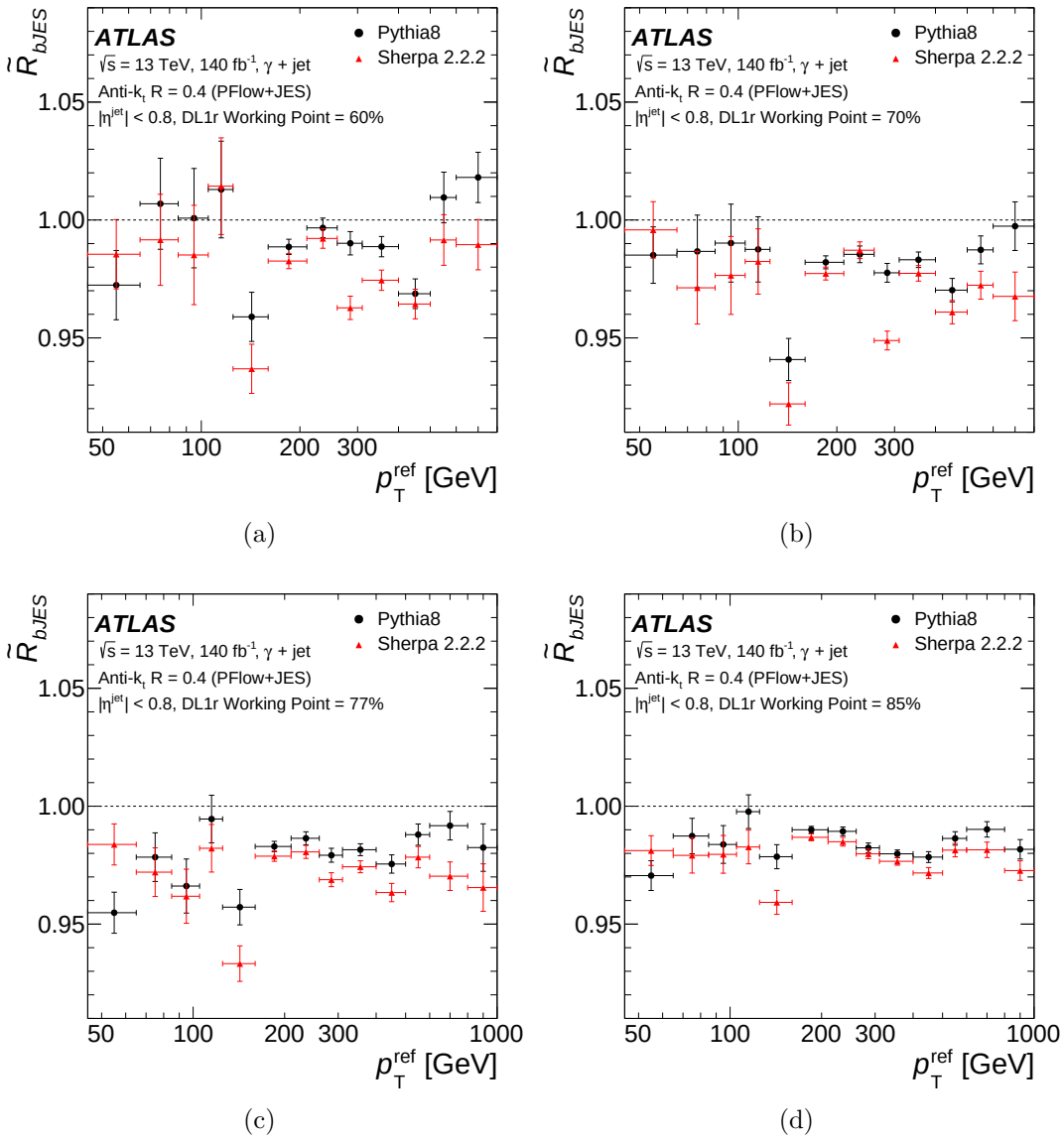


Figure 5.17: $\tilde{R}_{\mathrm{bJES}}$ as a function of reference photon $p_{\mathrm{T}}$ determined using either Pythia 8 or Sherpa for $b$–tagging working point with an efficiency of (a) 60%, (b) 70%, (c) 77% and (d) 85%. The error bars correspond to the statistical uncertainties.

The newly defined observable, $\tilde{R}_{bJES}$, is showcased in Figure 5.17 using the Pythia 8 and Sherpa 2.2.2 MC samples for each working point as a function of $p_{\mathrm{T}}^{ref}$. In general, the $\tilde{R}_{bJES}$ is lower than 1 for the majority of points; this means

the $b$–tagged JES is underestimated relative to the inclusive JES. Some outliers remain, mainly in the WP's 60% and 70% but this is to be expected due to the aforementioned statistical fluctuations from these samples. The statistical uncertainties associated with these values are calculated using the Clopper-Pearson method [166].

The systematic uncertainties associated with each experimental condition are determined by calculating the average direct balance value for both the nominal and systematically adjusted cases in the $b$–tagged and inclusive scenarios. The $R_{bJES}$ uncertainty is derived by adding a fraction of the systematic uncertainties to the nominal response values for the $b$–tagged scenario relative to the inclusive scenario. Mathematically, it is expressed as follows:

$$\begin{aligned} \tilde{R}_{bJES}^{Syst} &= \frac{\tilde{R}_{bJES} + \Delta\tilde{R}_{bJES}}{R_{DB} + \Delta R_{DB}} \\ \Delta\tilde{R}_{bJES}^{Syst} &= |\tilde{R}_{bJES}^{nominal} - \tilde{R}_{bJES}^{Syst}| \end{aligned} \tag{5.18}$$

Presented in Table 5.4 are the averaged $R_{bJES}$ values within the range $85 < p_{\mathrm{T}}^{ref} < 800$ GeV for the $b$–tagging working points of 60% and 70%, and within the range $85 < p_{\mathrm{T}}^{ref} < 1000$ GeV for the 77% and 85% working points. The table includes results for each MC generator, along with their associated statistical and systematic uncertainties. To mitigate the impact of statistical fluctuations on the final result from low statistics in the lower $p_{\mathrm{T}}^{ref}$ bins, a minimum $p_{\mathrm{T}}^{ref}$ value of 85 GeV is chosen.

The table reveals a pattern of underestimation of the jet energy scale for $b$–tagged jets, which varies depending on the $b$–tagging efficiency and MC generator used. Regarding $b$–jet saturated measurements, the highest purity samples exhibit values closest to unity. Specifically, for WP 60%, the $b$–tagged JES is underestimated by 1% (1.6%) for Pythia (Sherpa); for WP 70%, it is underestimated by 1.6% (2.6%); and for WP 77%, it is underestimated by 2.2% (3.4%). In the case of the predominantly $c$–jet measurement, the $b$–tagged JES is underestimated by 1.1% (2.1%) for Pythia (Sherpa) [147].

The deviation from unit ratio revealed by this study can likely be attributed to differences in the hadronisation or fragmentation models employed by the MC generators, but deserves more investigation. It is possible that this arises from mis-modelling of the neutrino momentum, which is influenced by the

| WP | PYTHIA 8 | SHERPA |
|---|---|---|
| 60% | $0.990 \pm 0.010$ (stat.) $\pm 0.013$ (syst.) | $0.984 \pm 0.010$ (stat.) $\pm 0.013$ (syst.) |
| 70% | $0.984 \pm 0.010$ (stat.) $\pm 0.011$ (syst.) | $0.974 \pm 0.010$ (stat.) $\pm 0.012$ (syst.) |
| 77% | $0.978 \pm 0.006$ (stat.) $\pm 0.011$ (syst.) | $0.966 \pm 0.006$ (stat.) $\pm 0.011$ (syst.) |
| 85% | $0.989 \pm 0.004$ (stat.) $\pm 0.007$ (syst.) | $0.979 \pm 0.004$ (stat.) $\pm 0.007$ (syst.) |

Table 5.4: $\tilde{R}_{\text{bJES}}$ obtained for various $b$–tagging working points using PYTHIA 8 and SHERPA 2.2.2 separately for $85 < p_{\text{T}} < 800$ GeV for working points 60% and 70%, and $85 < p_{\text{T}} < 1000$ GeV for Working points 77% and 85% [147].

fragmentation function and decay modelling of $B$– and $D$–hadrons. The balance distributions versus the number of entries for both data and PYTHIA between $85 < p_T^{ref} < 1000$ GeV are presented in Figure 5.18. A comparison of these distributions for inclusive jets (Figure D.1a) and $b$–tagged jets at the 77% working point (Figure D.1d) reveals a noticeable shift in the left tail in PYTHIA. This is characterised by a greater number of $b$–tagged jets with significantly lower $p_T$ relative to the photon in the balance topology, indicating the presence of more neutrinos that are formed in $B$– and $D$– decays as opposed to light jets that don't contain many. This suggests that the neutrinos in the data are adequately represented in the simulated $b$–jets, and the focus should be aimed at other aspects of $b$–jet modelling in the Monte Carlo simulations. Further plots for other working points and for SHERPA are available in Appendix D.

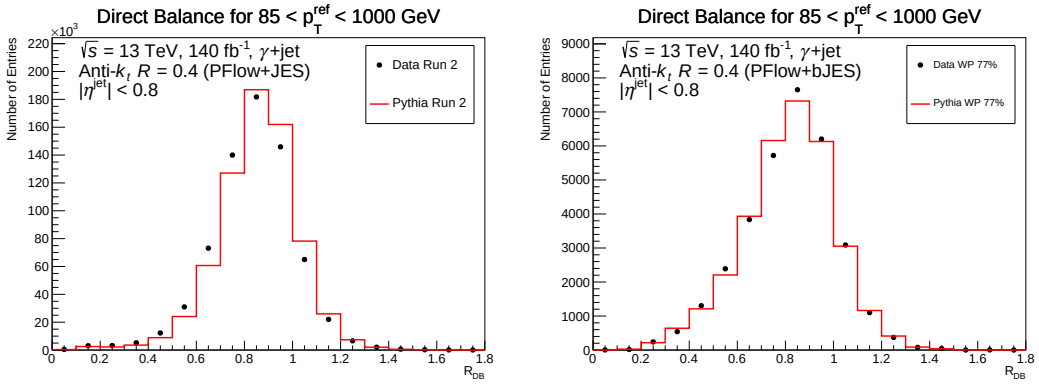


(a) (b)

Figure 5.18: The direct balance distributions of data and PYTHIA for $\gamma$+jet events in the (a) inclusive and (d) $b$–tagged working point 77% scenarios. This distribution is rebinned for all the balance response distributions in $p_T^{ref}$ bins between the range $85 < p_T^{ref} < 1000$ GeV.

The significance of these deviations can be calculated by the difference of the bJES values from unity divided by the quadratic sum of the statistical and systematic uncertainties added in quadrature. From this we can conclude that the significance of the results vary from $0.6\sigma$ to $2.7\sigma$. While this does not show a massive deviation for the bJES, it does show that the inclusive jets and $b$–jets do not seem to be compatible, and suggests that there should be a correction applied to $b$–jets at ATLAS to align the JES with that applied to inclusive jets. For future studies, it is recommended to apply an in-situ calibration of the bJES for Z+jets events. This will enable investigation of the lower $p_T$ region with a larger statistical sample, providing more robust insights. Additionally, there should be further examination of the MC generators to comprehensively understand the underlying reasons for the discrepancies highlighted in Table 5.4.

Given the significant role of the $b$-quark in ATLAS physics analyses, this study highlights the recommendation of conducting a comprehensive JES calibration specifically for $b$-jets in future work. Such a focused calibration would enhance the precision of $b$-quark related measurements and reduce bJES related uncertainties in forthcoming analyses.

# Chapter 6

# Large-$R$ Jets

When hadronically decaying heavy particles, such as W, Z, or Higgs bosons, or top quarks, are produced in LHC collisions with a large enough Lorentz boost, their decay products are collimated along the direction of the progenitor particle. When experiencing a significant Lorentz boost, the jets from these decays cannot be resolved individually and the boosted object is reconstructed as a single large-radius (large-$R$) jet. The identification of these jets as originating from a specific type of heavy particle involves examining the jet's multi-prong substructure. This refers to the spatial configuration and distribution of energy among the particles within the jet, indicative of the original particle's decay pattern, where the characteristic two-prong or three-prong patterns correspond to specific decay modes of these heavy particles. The jet's substructure along with its mass enables the tagging of jets as candidates for originating from the decaying heavy particles.

The process of large-$R$ jet reconstruction in ATLAS begins with the assembly of clusters that are then adjusted to the hadronic scale using the *Local Hadronic Cell Weighting Scheme (LCW)* [167]. In earlier approaches, these clusters were solely formed by connecting topological calorimeter cell signals, known as topo-clusters. Further development integrated tracker information with these topo-clusters to become what is known as the *Track-CaloCluster (TCC)* [168], and the aforementioned PFlow methods. Most recently, a more accurate implementation of clustering called *Unified Flow Objects (UFO)* [169] was developed which combines the TCC and PFlow algorithms, as shown in Figure 6.1. Subsequently, the Large-$R$ jets are reconstructed using the anti-$k_t$ algorithm with a radius parameter of R = 1.0. To refine the jet properties, grooming techniques are applied; a formal explanation of which can be found in Ref. [170]. These

algorithms selectively remove soft regions of the jet that make only a small relative contribution to the jet's transverse momentum. As a result, the impact from additional $pp$ interactions within the event and from the underlying event is mitigated, leading to enhanced energy and mass resolution of the jets.

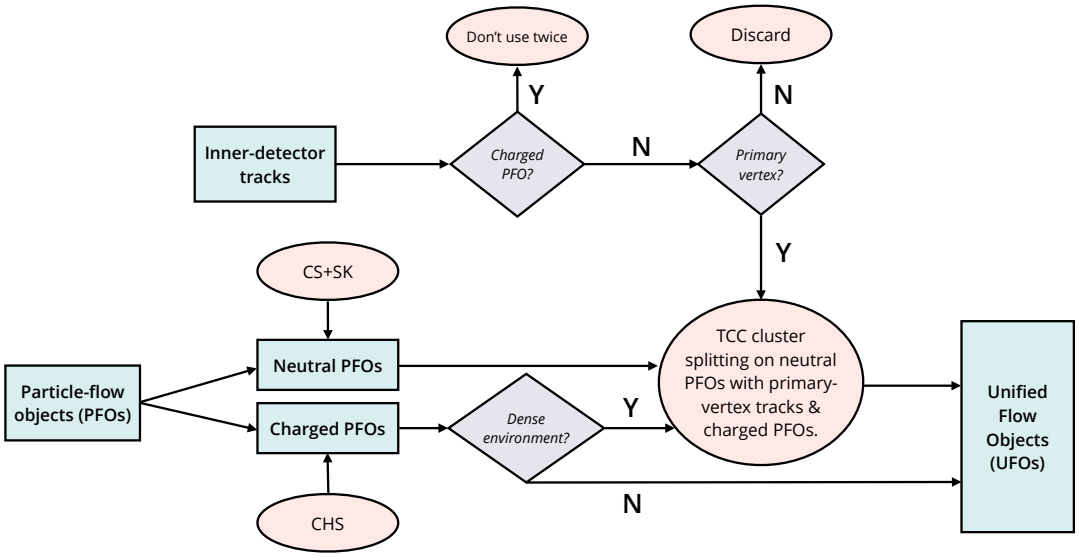


Figure 6.1: Illustration of UFO reconstruction algorithm [169].

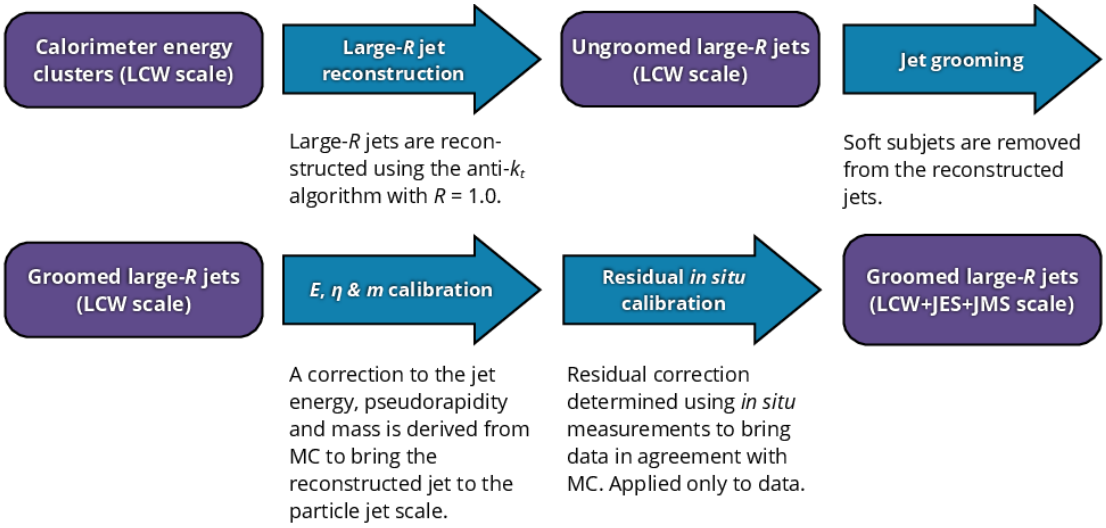


Figure 6.2: The steps of the LCW scheme [171].

The process of calibrating large-$R$ jets in the ATLAS experiment involves several stages, similar to the small-$R$ jet calibration chain, as depicted in Figure 6.2.

Initially, the groomed large-$R$ jets undergo calibration to match the energy scale of stable final-state particles. This calibration is achieved through corrections derived from MC simulations. These corrections also include adjustments to the jet mass in addition to the $\eta$ and energy corrections.

Subsequently, the jets are calibrated in-situ using response measurements obtained from $pp$ collision data. In this step, a statistical combination of data-to-simulation ratios of the response measurements is used to estimate uncertainties in the JES and *Jet Mass Scale (JMS)* and apply a correction exclusively to the data. This correction accounts for any remaining (typically 2-3% in Run 2) mismodelling in the response.

The in-situ calibration process is comprised of two distinct steps [171]. In the first step, the JES in-situ correction is determined using methods akin to those employed for the in-situ calibration of small-$R$ jets shown in Section 5.4. Again, these techniques rely on achieving $p_T$ balance in $\gamma$+jet, Z+jet, and multi-jet events as illustrated previously in Figure 5.5 and the absolute calibration is derived through a statistical combination of the three measurements. The combination of these for the 2015-2016 data taking years, at a luminosity of 36.2 $fb^{-1}$ and centre-of-mass energy, $\sqrt{s}$ = 13 TeV, is shown in Figure 6.3. There is also an $\eta$-intercalibration step based on di-jet events, similar to small-$R$, as discussed in Section 5.4.1.

A distinct contribution of this thesis is the development of an in-situ JES calibration for large-$R$ jets, derived from $\gamma$+jet events across the full Run 2 dataset. This calibration targets the direct balance technique within the central jet rapidity region ($|\eta < 0.8|$), as detailed in Figure 6.4. The direct balance was determined in 8 $p_T^{jet}$ bins, $p_{\mathrm{T}}^{jet} \in \{150, 210, 260, 310, 400, 600, 800, 1000\}$ GeV. The balance is consistently below unity for the entire jet $p_T$ range, and the data to MC ratio shows that the JES is underestimated by roughly 0.5-2.5% when considering the uncertainties. The balance is also purity-corrected, following the ABCD method defined in Section 5.5.4.

Moving to the second step of in-situ calibration, the jet mass response is studied using two distinct measurements after applying the in-situ JES correction. The first of these measurements involves evaluating the mass response in $t\bar{t}$ events. In this context, $t\bar{t}$ events are examined in two channels: one where a top quark decays into a lepton, a neutrino, and a bottom quark (lepton+jet channel). The other top quark undergoes a fully hadronic decay, which follows the decay chain

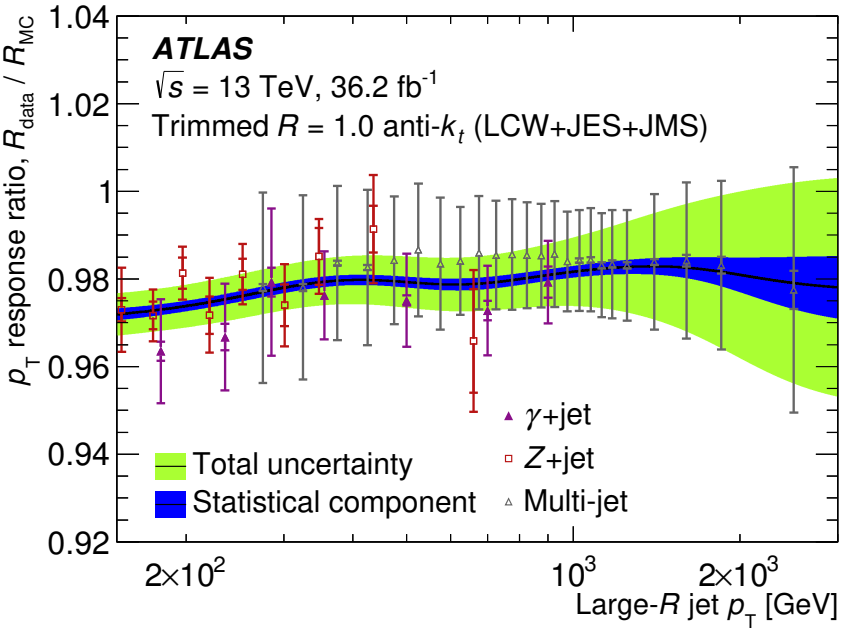


Figure 6.3: Data-to-MC ratio of the average jet $p_T$ response as a function of trimmed anti-$k_t$ large-$R$ jet $p_T$ with R=1.0. The combined result (band) is based on the in-situ direct balance for three distinct processes: Z+jet (open squares), $\gamma$+jet (closed triangles), and multi-jet (open triangles). The errors represent the statistical (inner error bars) and the total uncertainty (outer error bars). The lines are smoothed using a sliding Gaussian kernel [170].

$t \to Wb \to jjb$, resulting in a single large-$R$ jet that encapsulates all the hadronic decay products. The focus here is on fitting the jet mass distributions that emerge, particularly those that contain peaks corresponding to high-$p_{\mathrm{T}}$ W bosons and the fully hadronically decaying top quarks.

The second measurement is achieved by using the $R_{trk}$ method, which capitalises on the independent measurements from the calorimeter and the inner tracker. This method provides a calibration for the calorimeter jet mass measurement across a wide $p_{\mathrm{T}}$ range. The outcomes from both measurements are combined into a smooth $p_{\mathrm{T}}$-dependent function within two mass bins. This combined calibration can be applied to data as an in-situ correction.

Additionally, the *Jet Energy Resolution (JER)* and *Jet Mass Resolution (JMR)* are also measured in-situ and compared with MC predictions. The di-jet balance method exploits the $p_T$ balance in di-jet events to extract the JER. The JMR, on the other hand, is obtained through fits to the top quark and W boson mass peaks in high-$p_{\mathrm{T}}$ lepton+jets $t\bar{t}$ events.

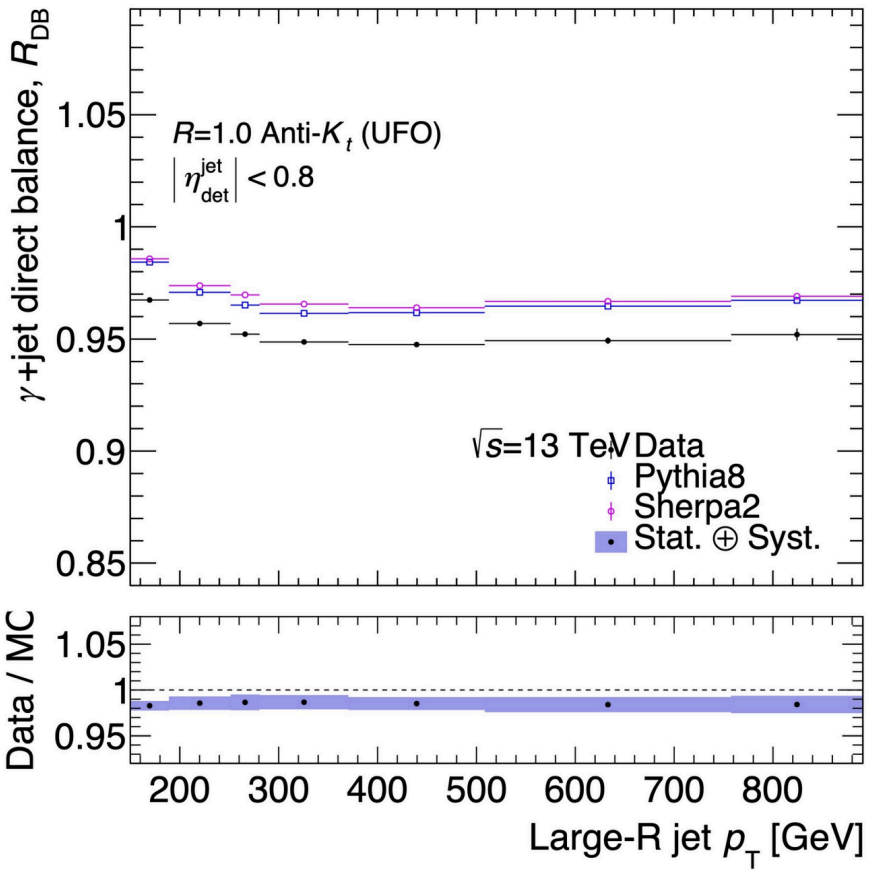


Figure 6.4: UFO large-$R$ jet direct balance as a function of large-$R$ jet $p_T$ for full Run 2 data. The uncertainties shown are due to statistics and systematics.

## 6.1 Pile-up Removal and Grooming

Contamination from phenomena such as ISR, UE, and pile-up complicates the jet finding process, especially in Large-$R$ jets, which have a large area and are therefore more susceptible to soft contamination. This contamination tends to obscure the finer details of the jet substructures, making it difficult to distinguish between relevant jet signals and background noise. Therefore, a key aspect of jet finding involves striking a balance of accounting for missing radiation that's relevant to analyses while, on the other hand, minimising the impact of soft contamination to preserve the integrity of the jet substructure.

The impact of pile-up on large-$R$ jets becomes more pronounced due to the quadratic increase in pile-up contamination with respect to the jet algorithm's distance parameter, R. To mitigate this effect, various pile-up subtraction models

have been been created. Jet grooming algorithms have also been developed, aimed at reducing the influence of pile-up on both the jet four-vector and substructure observables.

### 6.1.1 Constituents-Based Pileup Removal

- The *Constituent Subtraction (CS)* [172] method is fundamentally a local subtraction method, operating on a per-area basis, as detailed earlier in Section 5.1. However, CS goes beyond the simpler $\rho$-area subtraction techniques as it not only considers the overall pile-up density, $\rho$, within a given area but also adjusts for pile-up effects at the level of individual particle constituents. This allows for a more precise subtraction of pile-up effects.

- The *SoftKiller (SK)* [173] method is a technique used to mitigate the effects of pile-up by removing input objects with a $p_T$ below a certain cutoff, chosen to ensure that the event-wide estimate of $p_T$ flow density, $\rho$, becomes 0. ATLAS uses the SK method in conjunction with CS to yield the CS+SK combination.

- The *Pile-up Per Particle Identification (PUPPI)* technique [174] assigns a likelihood score $\alpha_i$ to each input object $i$ based on its kinematic properties and proximity to charged hard-scatter particles associated with the event's primary vertex. The likelihood score is calculated for all input objects and then the likelihood of pile-up contamination is estimated by comparing $\alpha_i$ to the mean value of $\alpha$ for all charged pile-up inputs and the root mean squared of the distribution. PUPPI then reweights the four-momentum of neutral input objects based on this along with a $p_T$ cut afterwards to account for the pile-up. PUPPI is most effective when applied to PFlow jets, as its principles rely on the matching of neutral input objects to nearby charged particles [169].

### 6.1.2 Jet Grooming

A number of different grooming techniques that are applied after the reconstruction of large-$R$ jets are displayed in Figure 6.5, giving some insight into what each does. More information is given below about these techniques: [175].

- *Jet Trimming* [176] is a traditional grooming technique used in ATLAS, which effectively removes soft radiation components from jets through clustering events using the $k_t$ jet algorithm to obtain 'seed jets' (ungroomed large-$R$ jets). Within each seed jet, the input constituents are re-clustered with a smaller distance parameter, $R_{min}$, relative to the distance in the initial construction of seed jets. The subjets that fail to meet the trimming condition $\frac{p_{\mathrm{T}}^{subjet}}{p_T^{jet}} > f_{cut}$ are discarded, and the remaining subjets are combined to form the trimmed jet. The standard parameter values employed by ATLAS were $R_{min} = 0.2$ and $f_{cut} = 0.05$ during Run 2.

- *Jet Filtering* [177] starts by re-clustering the constituents of a jet, denoted as two subjets, $j_1$ and $j_2$, using the C/A algorithm. The radius parameter for this re-clustering, $R_{\mathrm{filt}}$, is dynamically chosen based on the jet's internal structure, $R_{\mathrm{filt}} = \min[0.3, \Delta R_{j1,j2}/2]$ where $R_{\mathrm{filt}} < \Delta R_{j1,j2}$. Once the constituents are re-clustered with this tailored radius, all jet constituents that are outside the three hardest subjets are discarded. The rationale behind retaining three subjets, rather than just two, is to account for additional radiation that might be present in a two-body decay. By dynamically reclustering the jet at an angular scale that is optimally suited to resolve its internal structure, jet filtering maximises the sensitivity to decays that are highly collimated.

- *Pruning* [178] is a modification to jet clustering, using a 'pruning radius' in which hard prongs fall into separate subjets and the softer radiation outside of these prongs are discarded. When the jet is reclustered using the C/A algorithm, at each step, the softer sub-jet is discarded if it is too soft or too wide-angled. This is achieved through the conditions $\Delta R_{12} \geq R_{cut} \times 2\frac{M_{12}}{p_{T,12}}$ and $z \leq z_{cut}$. Here 12 is the subjet pair and $z = \frac{\min(p_{T,1}, p_{T,2})}{p_{T,1}+p_{T,2}}$. $R_{cut}$ and $z_{cut}$ control the amount of wide-angled and soft radiation removed by pruning, respectively.

- *Soft-Drop (SD)* [179] is also a $p_T$-based grooming technique that accounts for removing soft and wide-angle radiation from a jet. SD is very similar to pruning, using the C/A algorithm, where the clustering starts from the widest-angled radiation and moves towards the core of the jet, but with a change in the critera to drop the soft constituents. The essence of the SD technique lies in the equation $\frac{\min(p_{T,1}, p_{T,2})}{p_{T,1}+p_{T,2}} < z_{cut}(\frac{\Delta R_{12}}{R})^{\beta}$. Here, the subscripts 1 and 2 refer to the two branches resulting from the jet's

splitting, with 1 representing the harder branch and 2 representing the softer branch. This equation introduces two parameters $z_{cut}$ and $\beta$ which dictate the amount of soft and wide-angled radiation which is removed. If the specified condition is not met, the lower-$p_T$ branch of the clustering history is removed, and the de-clustering process continues with the higher-$p_T$ branch. When the condition is satisfied, the process concludes, and the remaining constituents constitute the groomed jet. A big advantage of SD grooming compared to other techniques is its ability to provide calculable results beyond leading-log accuracy [180–182]. There are also versions of SD for multi-pronged decay treatment *Recursive Soft-Drop (RSD)* and *Bottom-Up Soft-Drop (BUSD)* [183].

## 6.2 Jet Substructure Observables

### 6.2.1 Large-$R$ Jet Mass

The large-$R$ jet mass is determined by adding up the four-momenta of all its constituents, regardless of if they originate from truth particles, topological clusters, or calibrated jets created with the small-$R$ parameter. The mass of a large-$R$ jet is a fundamental feature of the jet, with many other substructure observables that probe the inner structure of the jet exhibiting substantial correlations with the jet mass.

When a large-$R$ jet contains the decay products of a top quark of high-$p_T$, the jet's mass corresponds to that of the top quark itself, and can be derived from the peak of the jet mass distribution [184]. This is the basis of the analysis detailed in Part III. In cases where jets are initiated by a single light quark or gluon they can acquire substantial mass through the emission of hard radiation at relatively large angles.

### 6.2.2 $N$–Jettiness and $N$–Subjettiness

*$N$–jettiness* [185] is a concept used to quantify how well an event can be divided into $N$ distinct jet-like regions, where $N$ represents the number of jets to identify in an event. This is due to the need to veto undesired background jets from certain processes; an example is top quarks decaying into W+$b$–jet which is a

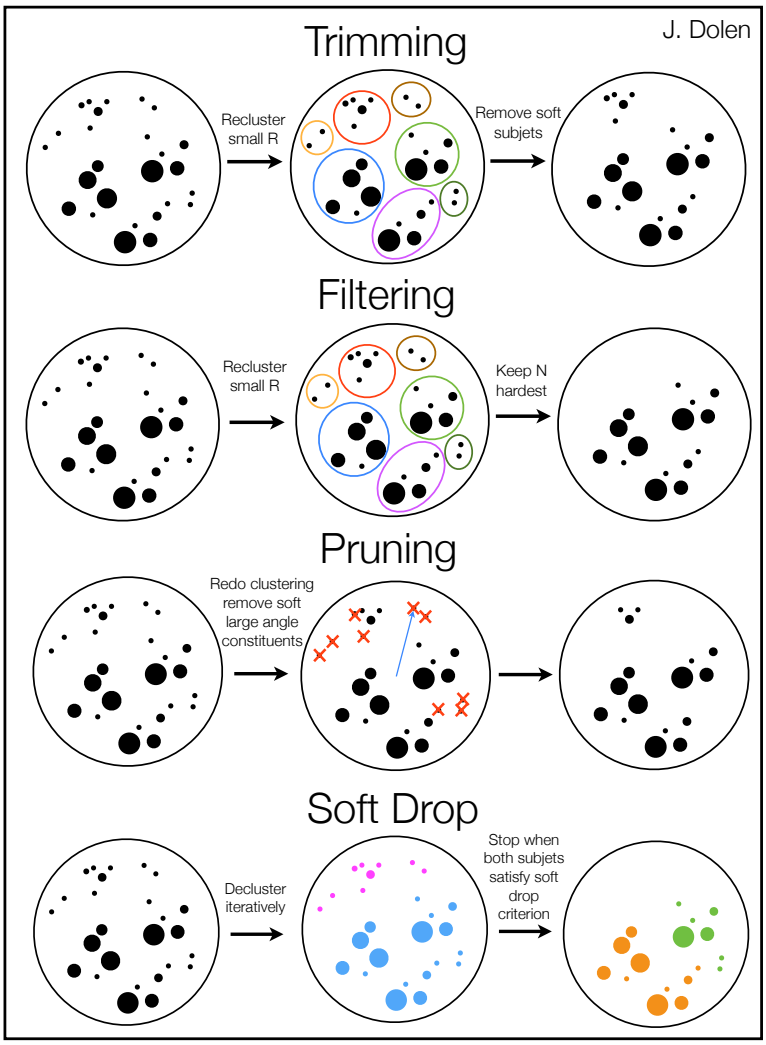


Figure 6.5: Illustration of a number of grooming techniques used with Large-$R$ jets. Figure courtesy of James Dolen.

major background for $H \to WW$ [186]. $N$-jettinness is defined as $\tau_N$, with the following equation:

$$\tau_N = \frac{2}{Q^2} \sum_k \min\{q_a \cdot p_k, q_b \cdot p_k, q_1 \cdot p_k, ..., q_N \cdot p_k\} \tag{6.1}$$

Here $p_k$ is the momenta of all measure particles in a final state that excludes hard leptons and photons (any leptons or photons from hadronic decays are included in the sum). $q_a$, $q_b$ and $q_1, ..., q_N$ are a fixed set of reference momenta of the two beams and $N$ signal jets. For simplicity, all these momenta are considered to be massless. If $\tau_N$ is small, the event's structure can be divided into $N$ distinct

subjets. If $\tau_N$ is large, it suggests many of the particles are scattered far away from the $N$ axes and do not belong to $N$ subjets.

*$N$−subjettiness* [187], on the other hand, is a specialised application of $N$-jettiness, tailored for use within a large-$R$ jet. It focuses on the constituents of the individual jet (subjets), rather than the entire event. $N$-subjettiness provides a way of examining the internal structure of the jet, and how the energy is distributed among the jet's constituents.

**XCone Jet Algorithm**

The XCone jet algorithm [188], uses the concept of $N$−jettiness to define jet boundaries within collision events. Central to its design is the minimisation of $N$−jettiness; for events featuring at least $N$ energetic jets, $N$−jettiness assesses the event's resemblance to an ideal $N$−jet configuration. This is particularly useful for filtering out unwanted jets in densely populated events, effectively distinguishing between signal and background events. In this way, XCone is suitable in scenarios where the number of jets is already predetermined. Similar to the functionality of the anti-$k_t$ algorithm discussed in Section 4.3, XCone ensures that jets are conically shaped when well-separated, making it similar in delivering geometrically coherent jet structures. A notable strength of XCone is its use in the boosted regime, where signal jets may partially overlap, making it very effective in analyses of boosted top quarks, such as the primary analysis of this thesis, found in Chapter 8.

Large-$R$ jets and taggers, are part of the standard operational toolbox of LHC experiments. They are routinely used in Run 2 searches for new physics, particularly in scenarios involving boosted W, Z, H, and top particles in the final state. The application of these methods extends beyond searches for new phenomena; they have also been utilised several precision measurements. Notably, in impactful ATLAS studies involving boosted charge asymmetry and differential cross sections using large-$R$ top jets [189]. Similarly, large-$R$ jets contributed to the CMS measurement of the boosted top quark mass [190].

# Part III

# The Top Quark

# Chapter 7

# Top Quark Physics

The top quark was then experimentally discovered at the Tevatron by the CDF [191] and D0 [192] experiments in $p\bar{p}$ collisions at 1.8 TeV. Initially, the masses of the top quarks for these experiments were measured to be $m_t = 199^{+19}_{-21}$ (stat.) $\pm 22$ (syst.) GeV for D0, and $m_t = 176 \pm 8$ (stat.) $\pm 10$ (syst.) GeV for CDF. The most recent combined result from both of these experiments has led to the Tevatron average mass value for the top quark being measured as $m_t = 174.30 \pm 0.65$ GeV [193].

## 7.1 Top Quark Production and Decay

In $pp$ collisions at the LHC, the dominant top quark pair production mechanism is gluon-gluon fusion (90%), shown in the top two Feynman diagrams in Figure 7.1. Another production mechanism is quark-antiquark fusion, which is illustrated with the bottom plot in Figure 7.1. Top quarks can also be produced individually in single-top production via the $s$, $t$, and tW channels which are depicted at LO in Figure 7.2.

The $t \rightarrow Wq$ channel is of particular interest in analyses within the LHC, where a W boson and lighter quark are produced in association with top quarks. The top quark width for this channel can be defined as adding up the partial width of all allowed channels:

$$\Gamma_t = \sum_q \Gamma(t \rightarrow Wq) \tag{7.1}$$

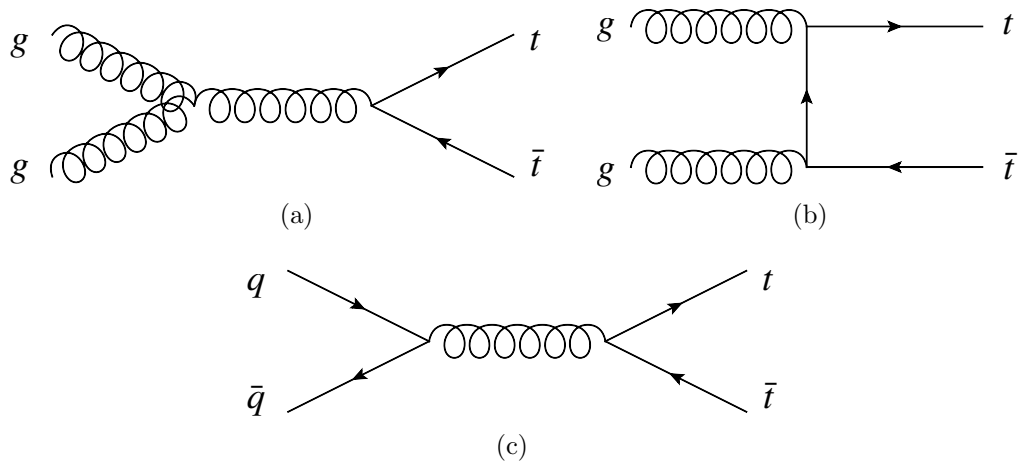


Figure 7.1: Feynman diagrams for tree-level $t\bar{t}$ production processes via (a) (b) gluon-gluon fusion, and (c) quark-antiquark fusion.

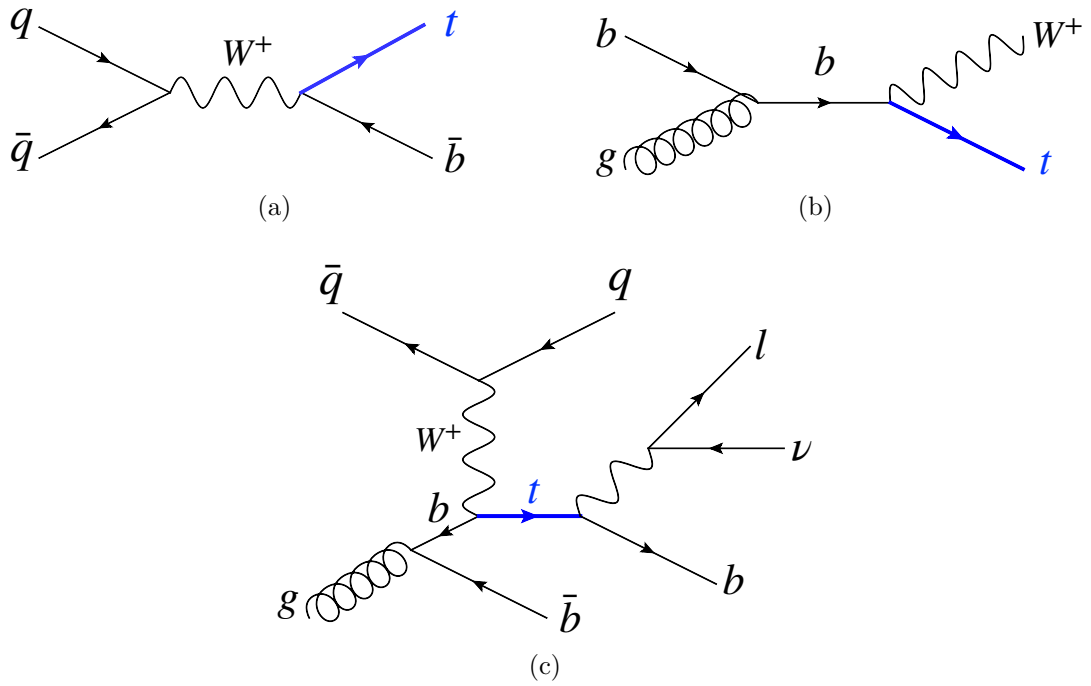


Figure 7.2: Feynman diagrams for tree-level single top production processes via the (a) s-channel, (b) tW-channel, and (c) t-channel.

Where q is the down-type quarks that the top quark is permitted to decay into ($b$,$s$,$d$). As of the writing of this thesis, the most precise top width combination measurement from the ATLAS [194], CMS [195], and D0 [196] experiments is [39]:

$$\Gamma_t = 1.42^{+0.19}_{-0.15} \text{ GeV} \tag{7.2}$$

The lifetime of the top quark, $\tau$, is related to the top width by $\tau = \frac{1}{\Gamma_t}$. This leads to a top quark lifetime of the order $10^{-25}$ seconds and, as explained in Section 3.3, this is lower than the hadronisation timescale. This causes top quarks to decay before forming hadrons, which gives us a unique opportunity to study properties of an approximately free-quark. The top quark's width is related to the top quark mass approximately by a factor of $\Gamma_t \propto m_t^3$ [197].

The top width also influences the probability of the top decaying into lighter particles, known as the top quark branching ratio. The branching ratio in the most common channel, $t \rightarrow Wq$, is defined as:

$$\mathcal{B}(t \rightarrow Wq) = \frac{\Gamma(t \rightarrow Wq)}{\Gamma_t} = \frac{|V_{tq}|^2}{|V_{tb}|^2 + |V_{ts}|^2 + |V_{td}|^2} \tag{7.3}$$

As shown in Table 1.2, earlier in the thesis when describing quark mixing, the top decays via the $|V_{tb}|$ channel with the most frequency, leading to branching ratio value of $\mathcal{B}(t \rightarrow Wb) = 0.957 \pm 0.034$ [39]. This, once again, highlights the importance of $b$−quarks and $b$−tagging - as discussed in Section 5.5 - in analyses like precision top quark measurements.

Because the top quark decays into the Wb channel almost 100% of the time, the final state formed by top quark pairs are classified according to the decay modes of the W-bosons. This consists of three categories: di-leptonic, semi-leptonic, and fully hadronic. Due to the nature of quark mixing in EW theory, as described in Section 1.2.2, the top quark can decay into all down-type quarks via charged-current interactions. The Feynman diagrams and related branching ratios for each decay mode are illustrated in Figure 7.3 Figure 7.4, respectively. Although the di-leptonic channel occurs less frequently due to its smaller branching fraction, it is experimentally the most pure due to the straightforward detection of the leptons in the final state. The fully hadronic decay mode, on the other hand, has a higher branching ratio but is heavily contaminated by QCD multi-jet background. The semi-leptonic decay channel exhibits characteristics that are midway between the other two, offering a good compromise between the purity of the di-leptonic

channel and the higher statistics of the fully hadronic channel.

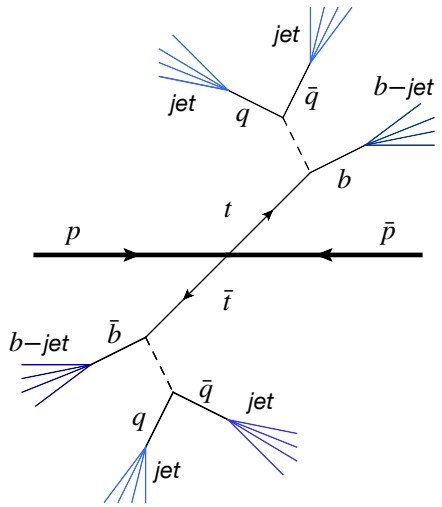


(a)

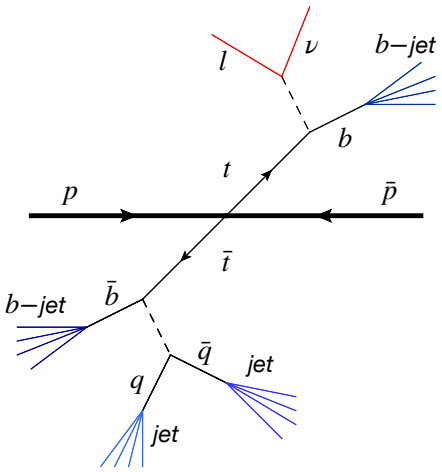


(b)

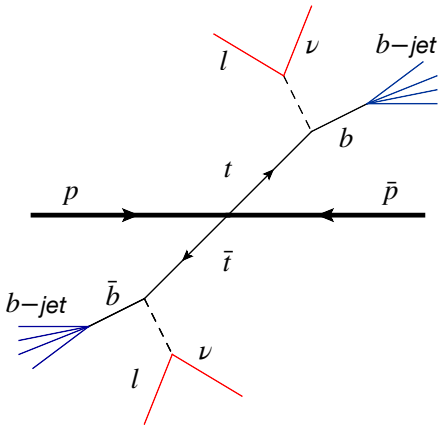


(c)

Figure 7.3: Feynman diagrams for top quark decay processes via the (a) fully hadronic, (b) semi-leptonic, and (c) di-leptonic channels.

## 7.2 Top Quark Mass Renormalisation Schemes

As discussed in Section 1.4.3, renormalisation schemes are applied to parameters of the QCD Lagrangian in order to combat divergencies that affect the validity of expanded calculations in perturbation theory. In particular, we will discuss certain

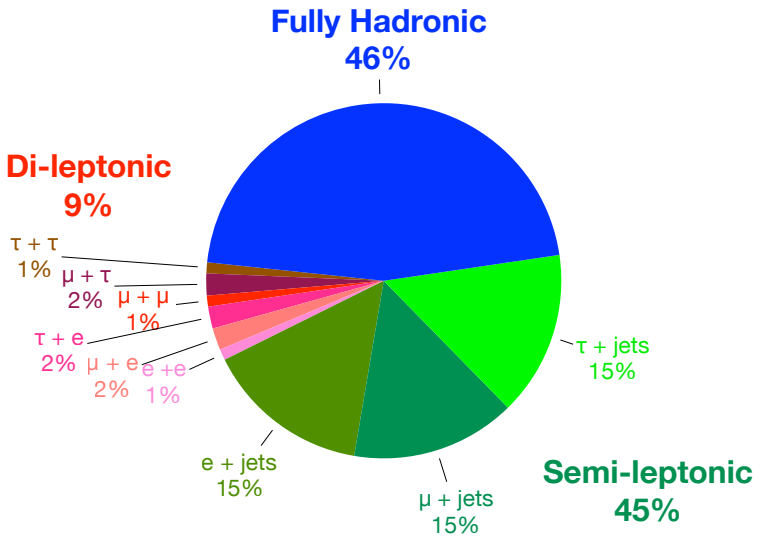


Figure 7.4: Final states and branching ratios for $t\bar{t}$ production.

renormalisation schemes that apply to the mass of the top quark. To begin with, we apply the dimensional regularisation that was described in that same section, with the calculation $d = 4 - 2\epsilon$. This means that the bare top propagator $S_t^0(p)$ without any loop corrections becomes a quark propagator $S_t(p, \mu_R)$ that includes NLO self-energy corrections that arise from gluon loops:

$$S_t^0(p) = \frac{i}{p - m_t^0} \rightarrow S_t(p, \mu_R) = \frac{i}{p - m_t^0 - \sum(p, m_t^0, \mu_R)} \tag{7.4}$$

Here, $p$ is the top four-momentum, $m_t^0$ is the bare unrenormalised top mass, and $\sum(p, m_t^0, \mu_R)$ displays the dominant contribution in the resonance limit ($p^2 \rightarrow m_t^2$) for the new dimensional calculation, defined as:

$$\sum(p, m_t^0, \mu_R) \approx m_t^0 \left(\frac{\alpha_s(\mu_R)}{\pi}\right)\left[\frac{1}{\epsilon} + ln(4\pi e^{-\gamma_E}) + A^{fin}(m_t^0/\mu_R)\right] + ... \tag{7.5}$$

The term $ln(4\pi e^{-\gamma_E})$ signifies part of the procedure for regularisation and renormalisation, with $\gamma_E$ denoting the Euler-Mascheroni constant [198]. The finite part of the self-energy correction, $A^{fin}(\frac{m_t^0}{\mu_R})$, which remains after the divergent part has been subtracted is a function of the bare mass and encodes the finite quantum corrections to the mass.

### 7.2.1 Top Quark Pole Mass

The first scheme of interest is the *Top Quark Pole Mass* ($m_t^{pole}$) [199, 200]. $m_t^{pole}$ corresponds to the mass of a free particle and can be calculated through the RGE described in Section 1.4.3. Self-energy corrections from all scales are absorbed into the mass, making it renormalisation-scale invariant:

$$m_t^{pole} = m_t^0 \left[ 1 + \left( \frac{\alpha_s(\mu_R)}{\pi} \right) \left( \frac{1}{\epsilon} + ln(4\pi e^{-\gamma E}) + A^{fin}(m_t^0/\mu_R) \right) \right] \tag{7.6}$$

By construction, in the pole mass scheme, all perturbative quantum corrections to the propagator's pole vanish. The pole mass thus corresponds to the mass of the quark as it appears in parton-level scattering amplitudes, under the assumption that quarks are real, external particles.

The pole mass presents certain challenges which can be effectively addressed by exploring alternative top quark mass schemes. Notable among these are the approaches outlined in Sections 7.2.2 and 7.2.3:

- Nonperturbative Effects: The QCD potential between colour charges does not diminish at large distances, unlike the Coulomb potential in QED. This means that the self-energy calculations that work well in QED for defining a pole mass do not converge in QCD because of the nonperturbative nature of the strong force at long distances (low energies). Thus, dealing with precision lower than 0.5 GeV, the top quarks' colour charge leads to non-perturbative effects that make the notion of a free quark unphysical, contrary to what the pole mass would imply.

- Infrared (IR) Divergences: When trying to calculate the pole mass using perturbation theory, we encounter IR divergences. These divergences indicate that the mass of the quark depends on how these IR regions of the momentum space are regulated. Even though the divergences themselves can be cancelled in theoretical computations (for example, by combining real and virtual gluon emissions), the mass still has an inherent ambiguity due to the sensitivity to these low-energy effects.

- Renormalon Ambiguity: There is also an issue known as the "renormalon problem", where the series of perturbative corrections to the quark mass in QCD is not convergent. *Renormalons* are a type of divergence in the asymptotic series that arise due to the behaviour of integrals in the

perturbative expansion that have contributions from low-momentum (long-range, or infrared) virtual particles [201]. These terms grow factorially with the order of the expansion and introduce an ambiguity into the series that is fundamentally linked to the nature of the strong force at low energies. This leads to an intrinsic ambiguity in the pole mass that is of the order of the QCD scale, $\Lambda_{QCD}$. The exact value is a matter of contention with some recent studies suggesting a value lower than 100 MeV [202] to values around 250 MeV [203]. This ambiguity can be calculated to be much larger than the precision needed for many theoretical predictions and experimental measurements, but it can vanish when considering a short distance mass (known as the running mass or $\overline{\text{MS}}$ mass).

### 7.2.2 Top $\overline{\text{MS}}$ Mass

The *Top Quark $\overline{MS}$ Mass* ($\overline{m}_t$) [199, 204, 205] is a scheme that was introduced to remain stable under perturbative corrections and be less sensitive to long-range, nonperturbative dynamics, so avoiding IR divergences. In this scheme, only the pure $1/\epsilon$ is absorbed into the mass, along with the usual $ln(4\pi e^{-\gamma_E})$ term:

$$\overline{m}_t(\mu_R) = m_t^0\left[1 + \left(\frac{\alpha_s(\mu_R)}{\pi}\right)\left(\frac{1}{\epsilon} + ln(4\pi e^{-\gamma_E})\right)\right] \tag{7.7}$$

This mass is dependent on the renormalisation scale and depends logarithmically on $\mu_R$, as shown with it satisfying the RGE:

$$\frac{d}{dln\mu}\overline{m}_t(\mu_R) = -\overline{m}_t(\mu_R)\left(\frac{\alpha_s(\mu_R)}{\pi}\right) + ... \tag{7.8}$$

This scheme absorbs only the divergent parts of quantum corrections into the mass definition, excluding low-energy quantum fluctuations. This renders the $\overline{\text{MS}}$ mass a scale-dependent, short-distance mass parameter. While it provides a more stable and calculable quantity for theoretical predictions, it is mostly applicable to high-energy processes where the energy scale $Q$ is greater than $m_t$, or in cases involving virtual top quark effects.

This mass scheme is effective for correlating with the high momentum scales that are produced by hard reactions. However, it falls short when it comes to momentum scales governed by quantum effects stemming from soft effects, where the energy scale is significantly lower than $m_t$.

### 7.2.3 Top Quark MSR Mass

Another renormalisation scheme is also introduced called the *Top Quark Modified Minimal Subtraction Renormalisation (MSR) Mass* ($m_t^{MSR}$) [206, 207], which will be the mass scheme used for the main analysis of this thesis. Unlike the $\overline{\text{MS}}$ scheme, the MSR mass provides a short-distance mass at scales below the top mass itself, with the scale allowing a smooth interpolation from $m_t(m_t)$ to the pole mass.

Within the MSR mass definition, the momentum scales are referred to as the renormalisation scale $R$. The MSR mass effectively integrates out the hard top quark quantum effects and defines the mass in a way that doesn't include the soft dynamics. The MSR mass scheme, for $R < m_t$ is defined as:

$$m_t^{MSR}(R) = m_t^0\left[1 + \left(\frac{\alpha_s(R)}{\pi}\right)\left(\frac{1}{\epsilon} + ln(4\pi e^{-\gamma_E}) + A^{fin}(m_t^0/R)\right)\right] - R\left(\frac{\alpha_s(R)}{\pi}\right)A^{fin}(1) + ... \tag{7.9}$$

This allows for the choice of $R << m_t$ and absorbing self-energy corrections from scales above $R$.

The MSR mass scheme can be considered as an extension of the $\overline{\text{MS}}$ scheme, due to them both being defined directly from the quark self-energy diagrams. As shown in Figure 7.5, the evolution of $m_t^{MSR}(R)$ and $\bar{m}_t(\mu)$ is plotted with both variables being mapped against their respective scales $\mu$ and $R$. The first note is that the two mass schemes are matched when the scales equal $m_t(m_t) = 160$ GeV, which is due to the definition of the two mass schemes together. When reaching domains where $R$ or $\mu < m_t$, the MSR mass appears to demonstrate a better stability, with a tendency to be lower than the $\overline{\text{MS}}$ mass and numerically approaching the pole mass as $R \to 0$ GeV. Additionally, the figure illustrates that the MSR mass features a linear trajectory in its evolution, a characteristic that aligns with its foundational principle as captured by taking the derivative:

$$\frac{d}{dlnR}m_t^{MSR}(R) = -\frac{4}{3}R\left(\frac{\alpha_s(R)}{\pi}\right) + ... \tag{7.10}$$

This is a fundamental trait expected of any short-distance mass framework designed to operate with a renormalisation scale $R < m_t$ [208, 209].

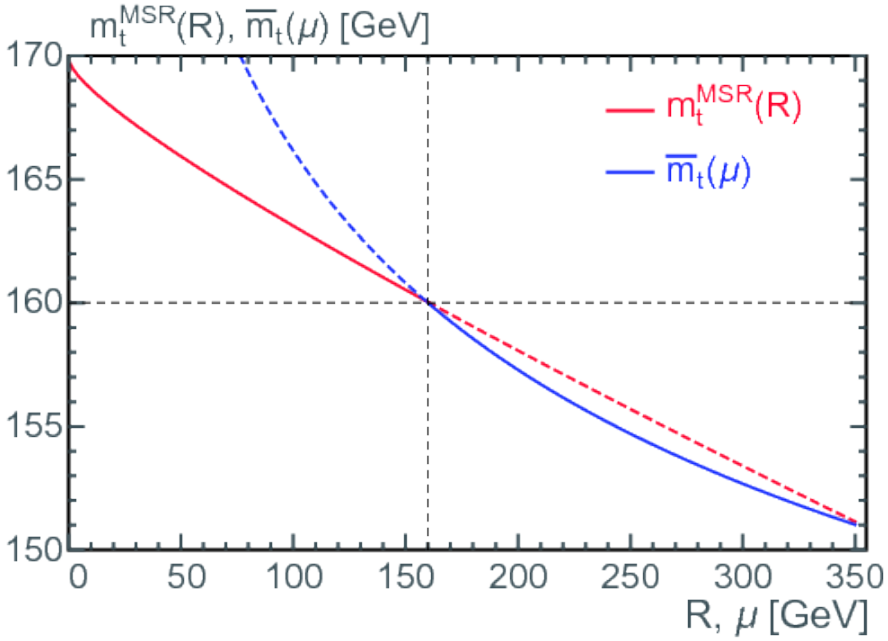


Figure 7.5: Comparison of scale dependence for $\overline{\text{MS}}$ and MSR top quark masses as a function of $\mu$ and $R$ in GeV, with $m_t = 160$ GeV [206].

## 7.3 Top Quark Mass Measurements

There are two main categories of top quark mass measurement: direct and indirect.

Direct measurements of the top quark mass use the decay products and kinematic observables of the top quark when it decays, primarily into a W boson and a $b$-quark. Such decays yield distinctive resonance patterns and endpoints in mass distributions that are inherently sensitive to the top quark's mass. The position of these resonances is most sensitive to the mass of the top quark itself, yet the nuances of their shapes and the precision of their locations are also molded by the underlying QCD and EW dynamics at energy scales lower than the top quark mass, coupled with the finite resolution capabilities of detectors.

These mass values are derived from the reconstruction of the top decay final states. Direct mass measurements rely on detector-level templates created through MC generators; first-principle predictions for these observables can not be used. This is except in specific cases like the boosted top mass, where unfolding the top jet mass to the particle level is possible, as demonstrated by efforts from CMS [210]. The reliance on MC simulations means that the measured value

reflects the MC mass parameter, $m_t^{MC}$, which requires establishing a relation between the MC mass parameter and the mass from a well-defined renormalisation scheme. The determination of $m_t^{MC}$ involves using MC simulations to identify the value of the top quark mass parameter that best fits the observed data.

The determination of the top quark mass from the analysis of decay events involves fitting collision data to a set of MC templates that vary in assumed top quark mass. These templates model the theoretical mass distributions that one would expect to see. The full reconstruction of top quark decays are used, with channels such as $t\bar{t} \rightarrow$ all jets and $t\bar{t} \rightarrow$ lepton+jets, or partial reconstruction with channels like $t\bar{t} \rightarrow$ di-lepton, and single-top quark. This method was used for the original measurement of the top quark mass in the Tevatron and is widely used in ATLAS top quark mass determinations.

Direct measurements have the lowest uncertainties of the two top quark mass determination methods. At the time of writing this thesis, the most precise direct measurements of the top quark mass with LHC-related studies are taken from a combination of Run 1 ATLAS and CMS results [211]. Figure 7.6 shows the combination of the fifteen top quark mass measurements in ATLAS and CMS, utilising semi-leptonic and hadronic decays of the top quark as well as single-top production via the EW t-channel. Overall, the full combined result gives a value of:

$$172.52 \pm 0.14 \text{ (stat.)} \pm 0.30 \text{ (syst.) GeV}$$

This precision is constrained by various sources of uncertainties, encompassing experimental aspects like detector performance and statistical considerations, as well as theoretical elements stemming from MC simulations — namely the modelling of the parton shower, hadronisation, ISR/FSR, and UE effects, and the choices of renormalisation and factorisation scales in the computations. The values of each uncertainty are displayed in Figure 7.7, where the largest systematic uncertainties affecting the measurements originate from the JES, $b$–tagging, and $t\bar{t}$ modelling. There are acknowledged limitations within the MC simulations used in direct measurements, particularly in the treatment of QCD effects. These effects are not comprehensively captured beyond LL level in the LO approach to top decay within the MC simulations. Notably, in POWHEG+PYTHIA, which is generally NLO for some processes, the description of top decay is executed only at the LO level for on-shell tops. Additionally, the top quark width in these

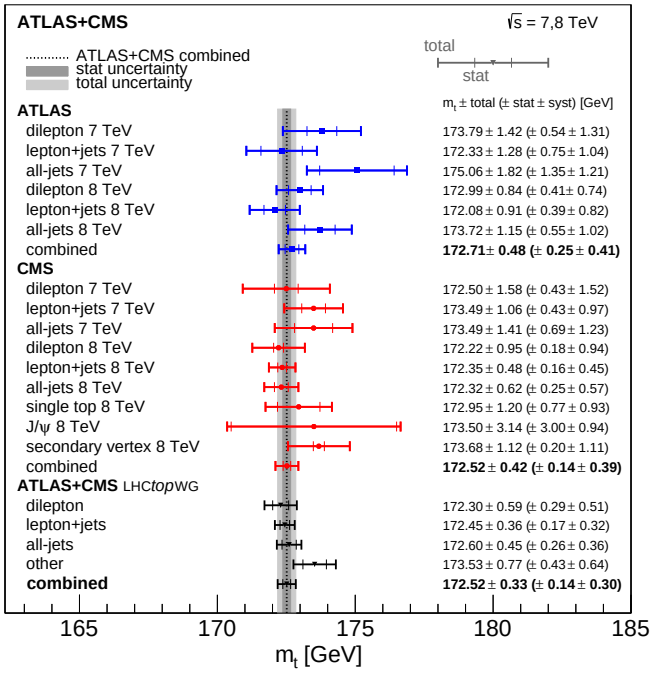


Figure 7.6: Comparison of $m_t$ measurements and overall LHC Run 1 $m_t$ combination, utilising centre of mass energies of 7 and 8 TeV [211].

simulations is only incorporated approximately. To fully account for the top quark width involves modelling off-shell effects, where the top quark's mass deviates from its resonance peak due to its finite lifetime, which requires more complex treatment that goes beyond the LO approximation, significantly increasing the computational demands for MC calculations.

The modelling uncertainties in single measurements are estimated to be in the range of 300-500 MeV, and even closer to 100 MeV when considering combined measurements [212, 213]. These discrepancies, primarily attributed to the parton shower cut-off and hadronisation processes, shift the interpretation of the MC mass parameter away from the pole mass scheme implemented in the matrix element and used in the parton shower.

These limitations, such as the treatment of specific QCD effects in MC samples, highlight that, while the mass obtained from direct measurements are numerically precise, they may not directly correspond to well-defined theoretical mass definitions used in the SM calculations, such as $m_t^{pole}$ [214]. This emphasises the need for a careful interpretation of what the measured top quark mass represents in a field-theoretic context.

| Uncertainty category | Uncertainty impact [GeV] | | |
|---|---|---|---|
| | LHC | ATLAS | CMS |
| LHC b-JES | 0.18 | 0.17 | 0.25 |
| b tagging | 0.09 | 0.16 | 0.03 |
| ME generator | 0.08 | 0.13 | 0.14 |
| LHC JES 1 | 0.08 | 0.18 | 0.06 |
| LHC JES 2 | 0.08 | 0.11 | 0.10 |
| Method | 0.07 | 0.06 | 0.09 |
| CMS B hadron BR | 0.07 | — | 0.12 |
| LHC radiation | 0.06 | 0.07 | 0.10 |
| Leptons | 0.05 | 0.08 | 0.07 |
| JER | 0.05 | 0.09 | 0.02 |
| Top quark $p_{\mathrm{T}}$ | 0.05 | — | 0.07 |
| Background (data) | 0.05 | 0.04 | 0.06 |
| Color reconnection | 0.04 | 0.08 | 0.03 |
| Underlying event | 0.04 | 0.03 | 0.05 |
| LHC g-JES | 0.03 | 0.02 | 0.04 |
| Background (MC) | 0.03 | 0.07 | 0.01 |
| Other | 0.03 | 0.06 | 0.01 |
| LHC l-JES | 0.03 | 0.01 | 0.05 |
| CMS JES 1 | 0.03 | — | 0.04 |
| Pileup | 0.03 | 0.07 | 0.03 |
| LHC JES 3 | 0.02 | 0.07 | 0.01 |
| LHC hadronization | 0.02 | 0.01 | 0.01 |
| $p_{\mathrm{T}}^{\mathrm{miss}}$ | 0.02 | 0.04 | 0.01 |
| PDF | 0.02 | 0.06 | <0.01 |
| Trigger | 0.01 | 0.01 | 0.01 |
| Total systematics | 0.30 | 0.41 | 0.39 |
| Statistical | 0.14 | 0.25 | 0.14 |
| Total | 0.33 | 0.48 | 0.42 |

Figure 7.7: Comparison of uncertainties that impact the $m_t$ measurements for LHC, ATLAS and CMS [211].

As opposed to direct methods, indirect measurements of the top quark mass use inclusive and differential cross-section measurements, $\sigma_{t\bar{t}}$, to extract the top quark mass. Indirect methods have sensitivity from the hard-scatter only, meaning the sensitivity of the mass measurements is at scales of or above the top quark mass.

Inclusive measurements are preferred for their straightforward interpretation, but differential cross section measurements are much more sensitive to the mass, as they isolate events near the pair production threshold, and can reduce the impact of systematic uncertainties by using normalised differential cross sections, where many uncertainties cancel. This approach involves the examination of the normalised cross-section for $t\bar{t}$ pair production with an additional jet, specifically varying with the invariant mass of the jets in the final state. The advantage of this method lies in its heightened sensitivity to the influence of the top quark mass on

the gluon emission from top quarks. This sensitivity is particularly pronounced in the phase-space region near the production threshold for the $t\bar{t}$ pair with one additional jet. The increase in sensitivity can be as much as five-fold compared to the inclusive cross-section method [215].

As of writing this thesis, the current most precise ATLAS and CMS determinations of the top quark mass have used NNLO+NNLL predictions for the inclusive $\sigma_{t\bar{t}}$ regime and NLO predictions for the differential regime. These mass values are displayed in Figure 7.8 for ATLAS and CMS with data using different centre-of-mass energies.

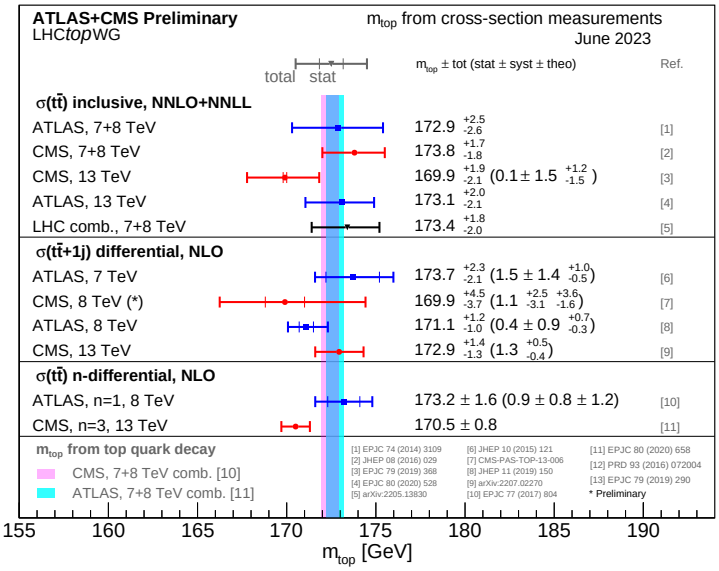


Figure 7.8: Summary of ATLAS and CMS top quark mass measurements using $t\bar{t}$ production data [216].

The ATLAS+CMS combined inclusive cross-section measurements at $\sqrt{s}$ = 7 + 8 TeV is determined to be [217]:

$$m_t^{pole} = 173.4^{+1.8}_{-2.0} \text{ GeV}$$

The most precise differential cross-section measurements for the top mass in $t\bar{t}$+1j events measured with ATLAS is at $\sqrt{s}$ = 8 TeV [212], and measured with CMS at $\sqrt{s}$ = 13 TeV [218]:

$$m_t^{pole} = 171.1^{+1.2}_{-1.1} \text{ GeV (ATLAS)}$$
$$m_t^{pole} = 172.93 \pm 1.36 \text{ GeV (CMS)}$$

## 7.4 Top Quark Mass Interpretation

In general, MC generators have achieved a high level of accuracy in describing data, particularly in the soft-collinear energy limit, around 1 GeV, typical for parton showers. This suggests that MC generators are effective enough at capturing important QCD features without needing to explicitly include high order corrections.[1] From this the question arises of whether MC generators can only be seen as good empirical models, where $m_t^{MC}$ is effective in matching experimental results but doesn't correspond directly to any fundamental QCD parameter. On the other hand, if MC generators are closely connected to the underlying theory then $m_t^{MC}$ would represent the well-defined renormalised mass, $m_t^{renorm}$, in the QCD Lagrangian, reflecting the true physical mass of the top quark after accounting for the interactions it undergoes.

The ambiguity in interpreting direct mass measurements within a field-theoretical renormalisation scheme can be reduced through dedicated 'calibration' studies. This approach tests the relation between the MC mass parameter, $m_t^{MC}$, and the mass scheme used in these calculations, as first developed in Ref. [214]. This is achieved by comparing first-principle calculations to MC predictions for observables related to boosted top quark production in $e^+e^-$ and $pp$ collisions.

The main principle of the top quark mass interpretation is the difference between the two masses, $\Delta_{t,MC}$, given by the relation:

$$m_t^{MC} = m_t^{renorm} + \Delta_{t,MC} \tag{7.11}$$

This mass relation can establish whether, and to which precision, the numerical value of the MC mass parameter can be identified with the renormalised mass. If the result is incompatible, then the mass relation can be used to convert the top quark mass parameter in the MC that is measured in direct measurements to a field-theoretical mass scheme. In either case, this study can shed light on subtle effects in Monte Carlo generators and may help to improve these important tools.

[1] The perturbative parts of Monte Carlo generators (NLO Matrix Element and parton shower) often employ the pole mass, but the non-perturbative effect (the parton-shower cut-off and hadronisation) may alter the mass scheme.

# Chapter 8

# Top Quark Mass Interpretation

The main analysis of this thesis is focused on the interpretation of the top quark mass parameter, $m_t^{MC}$ in Monte Carlo generators within a well-defined renormalisation scheme, as was discussed in Section 7.4. The relation between the MC mass parameter and the MSR mass is determined through fits of MC templates against distributions from theoretical calculations.

The relation between the MC top quark mass and the MSR mass was initially established through the calibration process detailed in Ref. [219]. The authors of Ref. [220] then performed the first analysis comparing MC predictions with a first-principle calculation at NLL and NNLL precision of the 2-jettiness observable in boosted top quark production with $e^+e^-$ collisions. The relation between the MC and MSR masses at NLL was derived as $m_t^{MC} = m_t^{MSR}(R = 1\text{ GeV}) + 180 \pm 290$ MeV, and at NNLL as $m_t^{MC} = m_t^{MSR}(R = 1\text{ GeV}) + 200 \pm 220$ MeV, using the Pythia 8.205 MC generator. These results supported the idea that the top quark mass parameter in the Pythia 8.205 generator is numerically close to the MSR mass at a low scale, and hence also to the top quark pole mass.

The authors of Ref. [221] conducted a revised analysis using an advanced theoretical approach, at NNLL+NLO precision in $e^+e^-$ collisions. In this analysis, the theoretical distributions were fitted to those of MC samples where both the top quark mass and the non-perturbative elements of the hadronisation function were considered. This approach marks a departure from the previous analyses, which primarily centered on adjusting the renormalised top quark mass parameter alone. The methodology applied in this updated framework bares close resemblance to the one we will explore in Section 8.1.2. Using Pythia version 8.305, this analysis yielded a result of $m_t^{MC} = m_t^{MSR}(R = 1\text{ GeV}) + 30 \pm 210$ MeV. The shift of the

central value with respect to the previous results was primarily due to the inclusion of power corrections absent in the previous calculation.

The theoretical basis of this analysis was also revised for use in $pp \to t\bar{t}$ processes at NLL precision, as detailed in Ref. [222]. An ATLAS-based MC top quark mass calibration utilising this theoretical approach was conducted by the authors of Ref. [223], using the 8.210 version of the Pythia MC generator. This study determined a relation of $m_t^{MC} = m_t^{MSR}(R = 1\text{ GeV}) + 80^{+350}_{-400}$ MeV, again suggesting a good agreement between the MC and MSR top quark masses.

The uncertainties in this relation are significantly higher than those in the previously discussed cases. This can be attributed to its logarithmic accuracy, which requires accounting for the larger NNLL corrections that are not included, through theoretical uncertainties. Additionally, $pp$ collisions are more complex compared to $e^+e^-$ collisions, as they also involve underlying event activity. In situations where a method for addressing UE is absent from the calculation, like in this case, it is essential to incorporate an uncertainty factor related to the UE.

In this chapter, we examine a more precise mass relation derived from $pp$ collisions, which takes advantage of an improved theoretical framework at NNLL. Additionally, this chapter introduces new findings regarding how the mass relation is influenced by the underlying event.

## 8.1 The Theoretical Framework

In this analysis, the technique for determining the top quark mass involves reconstructing the decay products of the top quark. Here, the focus is on boosted top quarks, where the decay products are collimated into a single large-$R$ jet. The key energy scales of interest here are the mass of the top quark, $m_t$, the energy scale $Q$ of the process, and the decay width, $\Gamma_t$. The jets emanating from the decay of the top quark, along with associated collinear radiation, have opening angles approximately proportional to $m_t/Q$.

The kinematic hierarchy for this method is $Q \gg m_t \gg \Gamma_t$, which allows for boosted top production to be described through factorisation. This large gap in the hierarchy establishes a clear kinematic separation between the dynamical processes related to the top quark production, decay and lower energy QCD processes. Additionally, considering the boosted state of the top quarks enables

an inclusive analysis of the top quark decay, effectively capturing all the decay products within the large-$R$ jet.

The jet is required to undergo a soft-drop (SD) grooming, as was previously described in Section 6.1.2, to effectively remove the soft contamination from the jet without significantly altering the jet's properties relevant to the top quark mass calibration [179, 222]. We make use of this technique in this analysis primarily due to its distinctive ability to be integrated into first-principles calculations for jet-related observables.

The grooming criteria are selected to ensure that major contamination is removed from the top jet, while retaining the products of boosted top decay and the associated "ultracollinear" (UC) radiation. To establish this, the soft-drop parameters $z_{cut}$ and $\beta$ must satisfy the following conditions:

$$z_{cut} \lesssim \frac{\Gamma_t}{h^{2+\beta} m_t} \left(\frac{p_T}{m_t}\right)^{\beta}, \tag{8.1}$$

$$z_{cut}^{\frac{1}{2+\beta}} >> \frac{1}{2} \left(\frac{\Gamma_t}{m_t} \frac{m_t^2}{p_T^2}\right)^{\frac{1}{2+\beta}} \tag{8.2}$$

The dimensionless function, $h$, is related to the opening angles of the subjet containing top-decay products with respect to the jet axis. The dependence of the

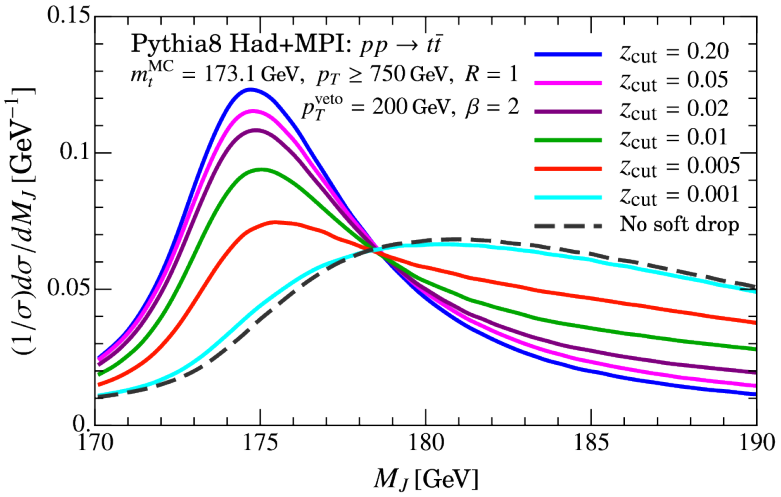


Figure 8.1: Dependence of the jet mass spectrum on the SD parameter $z_{cut}$ in Pythia 8. The MC top mass is set to 173.1 GeV and $p_T^{jet} \geq 750$ GeV [222].

jet mass on the $z_{cut}$ parameter is displayed in Figure 8.1, where the $\beta$ parameter is kept fixed at a value of 2. The grooming shifts the peak position considerably,

by about 5 GeV, with respect to the ungroomed distribution. However, for the range $0.005 < z_{cut} < 0.2$, the peak position remains approximately the same. Stronger grooming still keeps the peak position relatively unchanged as more intense grooming does not eliminate physics effects at scales much greater or equal to $m_t$. However, when the $z_{cut}$ increases to above 0.05, the light-grooming factorisation is invalidated and the more energetic collinear radiation from the top quark is also groomed away, resulting in a narrower jet mass distribution.

The boosted, groomed large-$R$ jet mass is defined by summing over the constituents that remain within the groomed jet, $\mathcal{J}_{SD}$:

$$M_J^2 = (\sum_{i \in \mathcal{J}_{SD}} p_i^\mu)^2 \cong m_t^2 + \Gamma_t m_t + ... \tag{8.3}$$

This shows that the mass of the jet is influenced by $m_t$ and $\Gamma_t$. The jet mass shape is better described by a scale, $\hat{s}_t = \frac{M_J^2 - m_t^2}{m_t}$. This scale is instrumental in defining the peak region, characterised by predominantly soft and collinear radiation from the top quark, where the jet mass $M_J^2 \approx m_t^2 + \Gamma_t m_t$. Therefore, in the peak region, we have:

$$\hat{s}_t \sim \Gamma_t \ll m_t \tag{8.4}$$

This peak region is where the sensitivity to the top quark mass arises, meaning the jet mass peak's position can serve as a probe to deduce the value of $m_t$.

The theoretical description for the perturbative and nonperturbative contributions to the peak region of the jet mass, $M_J$, and its invariant mass distribution in jets initiated by top quark decays can be derived by combining two distinct effective field theories [224, 225]. As illustrated in Figure 8.2, dynamics at scales around $m_t$ are encompassed within the *Soft-Collinear Effective Theory* (SCET) [226–232]. This EFT specialises in analysing scenarios where energetic particle emissions are either collinear with respect to the specified direction, or soft relative to the typical energy scale. For dynamics at scales much lower than $m_t$, the *Boosted Heavy Quark Effective Theory* (bHQET) [224, 233], is used, which effectively describes the dynamics of low energy radiation surrounding the top in a highly boosted regime. Together through factorisation, SCET and bHQET enable analytically resummed predictions for the jet mass distribution that are also free from leading renormalon effects in both the top mass and soft radiation. This results in a significant decrease in uncertainties associated with perturbative calculations.

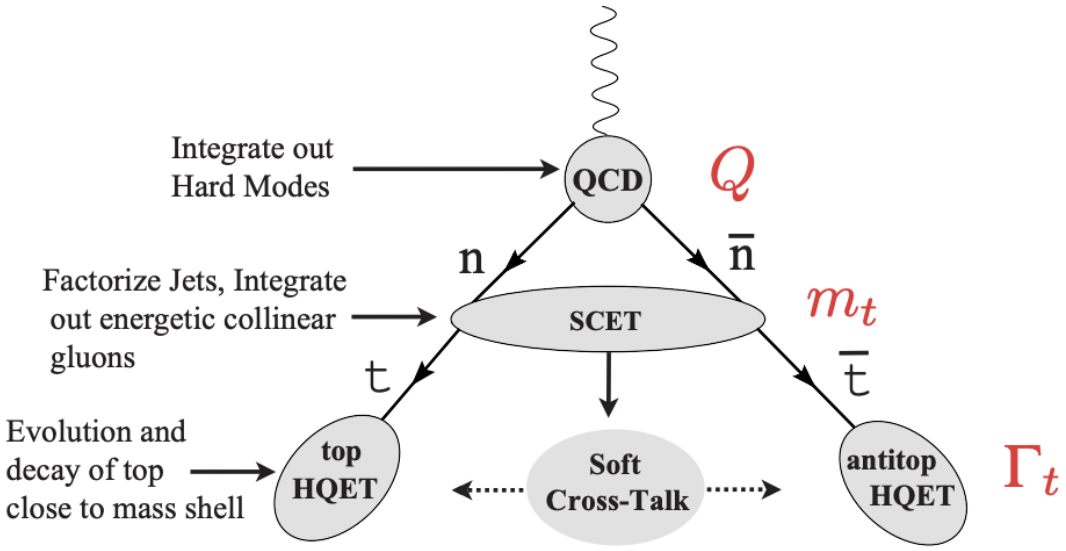


Figure 8.2: The set of effective field theories applied for calculating the invariant mass distribution of the top/antitop pair in the peak region.

This framework also enables a model independent treatment of hadronisation effects, as described further on in this chapter.

### 8.1.1 First-Principle Calculation Of The Top Jet Mass

The authors of Ref. [222] provided the calculation for the basis of a calibration procedure to relate the MC and renormalised masses in $pp$ events, focusing on the use of boosted top jets combined with light SD grooming. The differential cross section for these groomed top quark-initiated jets was derived at NLL accuracy. This derivation integrates different aspects of the top quark jet decay into a unified hadron-level factorisation formula:

$$\frac{d\sigma^{NLL}(\Phi_J)}{dM_J} = N(\Phi_J, z_{cut}, \beta, \mu) \int dr_d P(r_d, m_t/Q) \mathcal{J}_t^{had}(\hat{s}_t, \delta m, \Gamma_t, Q, Q_{cut}, r_d, \mu), \tag{8.5}$$

where $\Phi_J = \{p_T, \eta\}$ are the jet phase space variables. The normalisation factor $N(\Phi_J, z_{cut}, \beta, \mu)$ describes the hard scattering process and incorporates the hard process, PDFs, and the impact of radiation groomed away by SD.

The function $P(r_d, m_t/Q)$ in Equation 8.5 represents the distribution associated with the opening angles of the decay products of the top quark,

$r_d = h\frac{m_t}{Q}$, where $h$ was introduced above in Equation 8.1. Here, $Q = 2p_T \cosh\eta$, represents the hard scale linked to the top quark jet.

The last term, $\mathcal{J}_t^{had}(\hat{s}_t, \delta m, \Gamma_t, Q, Q_{cut}, r_d, \mu)$, describes the hadron-level jet mass distribution. This accounts for soft and collinear radiation from the top quark and its decay products, where $Q_{cut}$ denotes an energy cutoff parameter for SD grooming, $Q_{cut} \sim Q z_{cut}$ . $\delta m = m_t - m_t^{pole}$ specifies the top mass scheme used, such that $\delta m = 0$ corresponds to the pole mass scheme. $\mathcal{J}_t^{had}$ also accounts for the leading hadronisation effects in the peak, as denoted with the superscript 'had', as follows:

$$\begin{aligned}\mathcal{J}_t^{had} = \int dk^+ F_q^{\circ\circ}(k^+)\hat{\mathcal{J}}_t^{NLL}\left(\hat{s}_t - \max\{\langle r_g\rangle_{\hat{s}_t}, r_d\}\frac{Qk^+}{m_t}\delta m, \Gamma_t, Q_{cut}, \mu\right) \\ \times\left\{1 - \Theta(\langle r_g\rangle_{\hat{s}_t} - r_d)\frac{Qk^+}{m_t}\frac{d\langle r_g\rangle_{\hat{s}_t}}{d\hat{s}_t}\right\},\end{aligned} \tag{8.6}$$

with $\langle r_g\rangle_{\hat{s}_t}$ being the average groomed jet radius for a jet mass defined with the scale $\hat{s}_t$. The included decay configurations are those for which the opening angle $\hat{r}_d(\Phi_d)$ is less than one.

In the peak region of the jet mass distribution, nonperturbative hadronisation effects are significant, leading to a notable shift in the jet mass peak. On the other hand, in the tail of the distribution, these effects are smaller and can be examined through systematic expansion. The hadronisation corrections in $\mathcal{J}_t^{had}$ are incorporated by convolving the parton-level jet mass distribution, $\hat{\mathcal{J}}_t$, which is the parton-level description of the distribution that ignores hadronisation effects, with the nonperturbative shape function, $F_q^{\circ\circ}$, which describes the nonperturbative aspects of the jet formation. The leading-power nonperturbative corrections for the shape function are given by the first moment $\Omega_{1q}^{\circ\circ}$, and the next higher-order nonperturbative power corrections are captured by the parameter $x_2$:

$$\Omega_{1q}^{\circ\circ} = \int_0^\infty dk k^+ F_{1p}^q(k) \tag{8.7}$$

$$x_2 = \frac{\Omega_{2q}^{\circ\circ}}{(\Omega_{1q}^{\circ\circ})^2} - 1 \tag{8.8}$$

The theoretical predictions for the top mass distribution are compared to the corresponding MC samples and from that the mass relations can be numerically determined from a fit. In this analysis, $m_t^{MSR}$, $\Omega_{1q}^{\circ\circ}$, and $x_2$ are extracted simultaneously in a 3D grid. The impact of the three parameters is illustrated

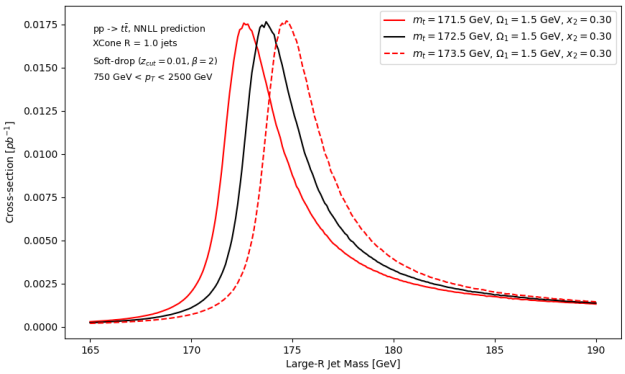


(a)

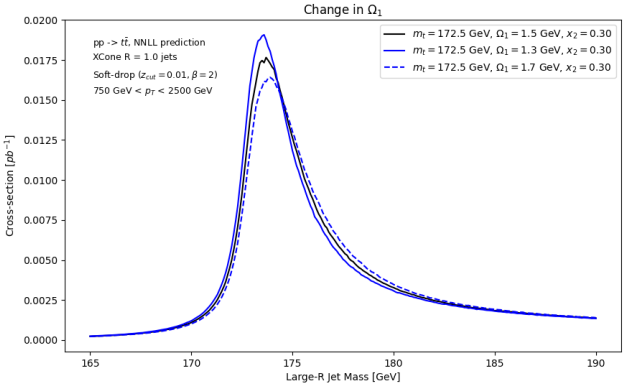


(b)

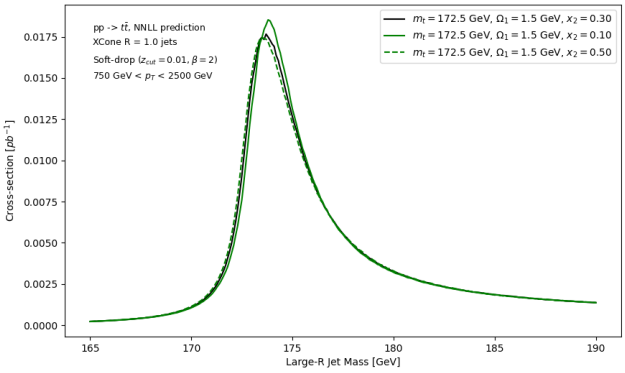


(c)

Figure 8.3: The effects of the parameters (a) $m_t^{MSR}$, (b) $\Omega_1^{\circ\circ}$, and (c) $x_2$ on large-$R$ top quark jet mass distributions . The nominal sample is taken with the values $m_t^{MSR}$ = 172.5 GeV, $\Omega_1^{\circ\circ}$ = 1.5 GeV, and $x_2$ = 0.30, as shown with the black curves. The variations are considered with ± 1 GeV for $m_t^{MSR}$, ± 0.2 GeV for $\Omega_1^{\circ\circ}$, and ± 0.20 for $x_2$.

in Figure 8.3. Specifically, Figure 8.3a demonstrates how variations in $m_t^{MSR}$ influence the distribution: while the overall shape remains consistent, the jet mass peak shifts. The effects of $\Omega_{1q}^{\circ\circ}$ and $x_2$ are depicted in Figures 8.3b and 8.3c, respectively. These parameters cause a notable shift in the peak and some pronounced variations in the distribution tails. In particular, higher values of $\Omega_{1q}^{\circ\circ}$ tend to broaden the jet mass distribution and cause a slight shift towards lower mass values, whereas lower values of $\Omega_{1q}^{\circ\circ}$ result in a narrowing of the distribution and a slight shift towards higher mass values. Similarly, variations in $x_2$ also influence the distribution's width and mass position. Lower values of $x_2$ tend to increase the mass and broaden the distribution, whereas higher values reduce the mass and narrow the distribution. However, $x_2$ is varied over a more extensive range of its allowed values so its impact is much less pronounced less significant than the other two parameters.

This calculation was compared to Monte Carlo generators for $pp \to \bar{t}t$ production at NLL precision, in collaboration with the ATLAS experiment, as documented in [223]. The analysis of this thesis will be a follow up on this publication, aiming at making the top mass relation more precise by using an improved theoretical prediction at NNLL [234].

### 8.1.2 NNLL Predictions for The Top Jet Mass

The updated theoretical framework [234], while retaining the fundamental principle of the previous factorisation method for top quark-initiated jets, brings notable improvements:

- Higher perturbative accuracy: the normalised jet mass distribution for boosted top quark jets has been calculated with light grooming at NNLL accuracy, incorporating singular corrections $\mathcal{O}(\alpha_s)$ in the parton-level jet mass distribution. The NNLL resummed results maximise the sensitivity of the peak region of the jet mass distribution to the top quark mass, and makes their predictions free from renormalon effects in both the top mass and soft radiation. This factorisation leads to significantly reduced perturbative uncertainty, better convergence, and improved stability of the peak position, which is crucial for top mass calibration and future measurements.
- An improved treatment of nonperturbative corrections by considering the dependence on the variable $r_d$ in the parton-level cross section $\hat{J}_t$.

- Non-universality of the nonperturbative parameters based on the grooming outcome: in the previous framework [222], nonperturbative parameters were assumed to be universally the same. Thus, a single universal shape function $F_q^{\circ\circ}$ with a specific first moment $\Omega_{1q}^{\circ\circ}$ was used. However, in the updated work, it was classified that the nonperturbative corrections depend on whether the soft drop grooming algorithm terminates on subjets with or without top decay products. To account for this, an additional shape function is introduced: $F_t^{\circ\circ}$ with first moment $\Omega_{1t}^{\circ\circ}$ for scenarios where each of the two stopping subjets consists of a top decay product. This distinction allows for a more accurate description of the effects in the peak region, particularly when considering the different influences of soft subjets and top decay products in the jet mass spectrum.[1] However, it was also shown that the scenario of top decay products stopping the grooming dominates, enabling us to work with a single moment, $\Omega_{1t}^{\circ\circ}$.

- Renormalon gap subtraction: The soft function, and the associated nonperturbative correction, $\Omega_{1t}^{\circ\circ}$, when renormalised in the $\overline{\text{MS}}$ scheme, contain another renormalon ambiguity. In the new calculation this renormalon has been subtracted. The renormalon subtraction has a numerically large impact on the value of the mass relation; this will be explored quantitatively in Section 8.4.

The difference in the jet mass distributions between the previous and updated calculations is illustrated in Figure 8.4. Here, the curve in representing the NNLL prescription displays a narrower uncertainty range compared to that of the NLL theory, while also seemingly exhibiting a more stable peak. A detailed comparison of these theoretical uncertainties in the context of our analysis is explored in Section 8.8. The testing of the renormalon gap subtraction is extended into the NNLL regime. Figure 8.4a illustrates the scenario without this adjustment, while Figure 8.4b demonstrates its inclusion. The incorporation of this subtraction is crucial to align the peak of the jet mass distribution in the revised NNLL prescription with that of the earlier NLL.

The theoretical prescription of the top quark mass used in this analysis is the MSR mass with a renormalisation scale value of 3 GeV, $m_t^{MSR}(R = 3\text{ GeV})$, which is chosen as the optimum value based on a thorough investigation of the dependence

[1] When considering the shape functions further in the analysis section, the symbol $F^{\circ\circ}$ will be used to describe the shape function for both cases.

of different regions of the $t\bar{t}$ invariant mass spectrum on the R scales in Refs. [235, 236]. The value choice of 3 GeV for $R$ has practical advantages compared to 1 GeV because determining the MSR mass at 1 GeV has larger perturbative uncertainties due to the larger value of $\alpha_s$ as compared to higher R values. However, 1 GeV is still suitable, at the current level of uncertainties for these analyses, and will also be studied here as a comparison to previous results.

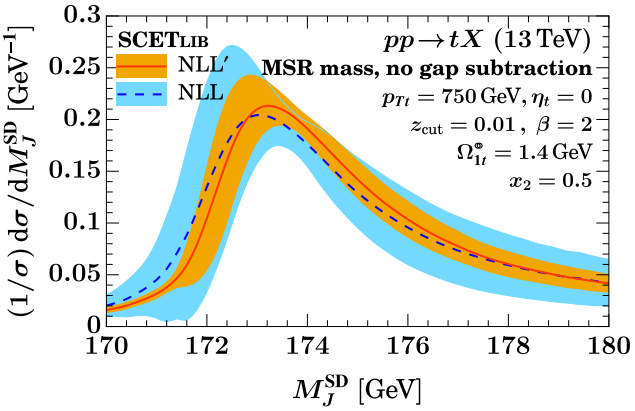


(a)

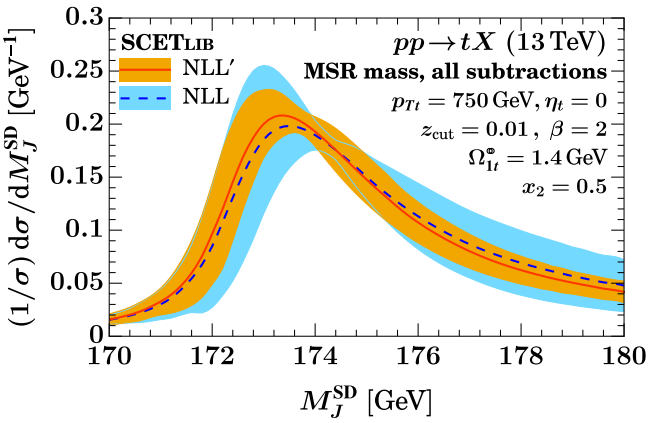


(b)

Figure 8.4: Comparison of the normalised differential jet mass spectrum for the NNLL theory (red line) and NLL theory (dashed blue line) with (a) no gap subtractions applies, and (b) all gap subtractions applied. The orange shaded area represents the theoretical uncertainty of the NNLL jet mass spectrum and the blue shaded area for the NLL distribution. In this figure NLL' represents NNLL. Figure courtesy of Aditya Pathak and Johannes Michel.

## 8.2 Methodology

### 8.2.1 Monte Carlo Samples

The top quark pair production in the Monte Carlo simulation is modelled using Pythia version 8.307 [119] with the ATLAS A14 tune [237] for parameters that govern the parton shower, hadronisation, and the underlying event models. The nominal PDF set used is NNPDF 3.0 NLO [90]. The nominal MC top quark mass, $m_t^{MC}$, is set to 172.5 GeV. The top quark width, $\Gamma_t^{MC}$, is set to match the latest combined measurements from the ATLAS, CMS, and D0 experiments, which is $1.42^{+0.19}_{-0.15}$ GeV [39].

The initial top-antitop pair is forced to decay hadronically, where the jet mass distributions at particle level are derived by clustering all stable final-state particles. These particles typically emerge from the generator's hadronisation algorithm. However, in scenarios where hadronisation is disabled (e.g., when the 'HadronLevel:all' option in Pythia 8 is turned off), the final state comprises solely of partons from the initial hard scattering and the resulting parton showers. This offers a clear contrast between the parton-level and hadron-level jet masses, as depicted in Figure 8.5. The inclusion of hadronisation notably broadens the jet mass distribution and shifts its peak to higher masses. This non-perturbative shift caused by hadronisation effects arises effectively from a splitting of the parton clusters into the lighter hadrons, which leads to a more dispersed jet and, so, to an increase in the jet mass, similarly to how parton showers increase the jet mass. Additionally, the broadening of the jet mass spectrum is partly due to the redistribution of soft radiation originating from the top quark decay post-hadronisation, contributing additional particles that influence the jet mass shape.

The impact of the underlying event is examined by changing the 'PartonLevel:MPI' switch in Pythia. One aspect of this analysis is the absence of UE in the calculation, due to no theoretical approach to UE being reliable currently. This means we must perform our fits with the UE feature disabled (PartonLevel:MPI = off), and then extrapolate the results we get to scenarios where UE is actually present. Figure 8.5 demonstrates that enabling MPI significantly modifies the jet mass distribution. Specifically, the additional UE radiation within the jet caused by MPI further broadens the distribution and elevates the tail at higher masses. However, the shift between the MPI off- and MPI on- level jet mass distributions should not be taken as a source of uncertainty

as this systematic effect can, in principle, be incorporated, and will be addressed in future work. Instead, the influence of variations in the UE-modelling on the final results is treated as source of uncertainty, discussed in detail in Section 8.3.

Furthermore, the treatment of FSR in resonance decays is governed by the 'PartonLevel:FSRinRes' switch in PYTHIA. Disabling this switch (on by default) allows us to turn off additional radiation from the decay products of the top quark. As shown in Figure 8.5, leaving FSRinRes on has a noticeable effect on the jet mass distribution compared to turning it off: while the peak position and the higher mass tails remain largely unchanged, the lower mass tail exhibits a slight increase. This effect arises from emissions from the top decay products at wider angles, which may either escape the confines of the jet or be removed through the grooming process.

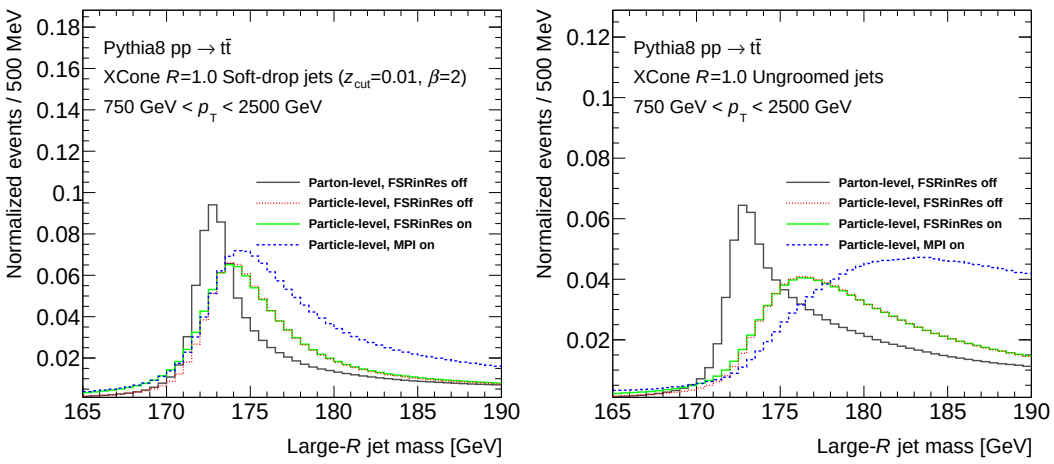


(a) (b)

Figure 8.5: The large-$R$ jet mass distributions in the PYTHIA 8 MC generator, using (b) soft-drop groomed, and (b) ungroomed jets. The distribution at the parton level is depicted by the black curve. The red dashed curve illustrates the particle-level distribution with FSRinRes turned off. The green curve signifies the particle-level distribution with FSRinRes activated. Lastly, the distribution with both FSRinRes and MPI enabled is represented by the dashed blue line.

Figure 8.5a and 8.5b compare the jet mass distributions for groomed jet and ungroomed jets, respectively. This comparison highlights the influence of jet grooming on the jet mass distributions. The most notable differences are observed in the distributions where the MPI switch is active, especially when contrasted with the curves where MPI is absent. For ungroomed jets, the deviation is

about 5 GeV, whereas it reduces to approximately 1 GeV for groomed jets, indicating that grooming effectively removes a significant portion of the UE that can greatly alter the distributions. In contrast to groomed jets, the ungroomed jet distributions exhibit more smearing, with a less distinct and effective peak, which makes fitting for the top quark mass more difficult.

### 8.2.2 Event Selection

Jet reconstruction is performed using the XCone algorithm [188], described in Section 6.2.2, with a radius parameter $R = 1$, as implemented in FastJet [138]. Soft-drop grooming [179] is applied with parameters $\beta = 2$, and $z_{\text{cut}} = 0.01$ to effectively remove soft and wide-angle contributions from the jet while not eliminating useful top quark decay products. Events are selected for analysis if they contain at least one large-$R$ jet with $p_T > 750$ GeV. Matching between the selected jet and the top or anti-top parton after the emission of FSR, but before the top quark decays, is achieved when $\Delta R_{(\text{jet,top})} < 1.0$. Additionally, to prevent overlap that could complicate the theoretical interpretation, $\Delta R$ between the leading and subleading large-$R$ jets must exceed 1.0.

### 8.2.3 Method

Reference histograms are generated with Pythia in several jet $p_T$ bins, with an equal number of events in each bin.

Theoretical templates are required in order to fit to the MC templates. These theoretical distributions are each characterised by unique parameter values. The objective is to identify the parameter set that produces a jet mass distribution most compatible with that of the observed Monte Carlo. Specifically, the MC in question is the Pythia 8 simulation for the distributions of top quark jet mass. The theoretical templates, implemented in a C++ based library, SCETlib [238], are generated through NNLL-accurate calculations, that were mentioned in Section 8.1.2.

Figure 8.6 presents an example of the comparison between theory and simulation curves, showing that Pythia and the NNLL prediction exhibit different shapes in the low tail of the jet mass distributions. This difference arises due to different treatment of certain aspects of the radiation from the top quark decay products

in the MC and analytical prediction. In the MC simulations, the ultracollinear radiation from the decay products of the top quark can be groomed away, which is a feature that is not accounted for in the theoretical calculations. To address this, the range of the fit is set between 172.5 - 180 GeV to ensure the effects of the tails have a minimum impact on the final result. This approach is deemed acceptable due to the fact that the peak of the large-$R$ jet mass distribution is what is most sensitive to the mass of the top quark. To account for this choice on the fit, an uncertainty based on the chosen fit range is incorporated into the final result, as detailed in Section 8.3.3.

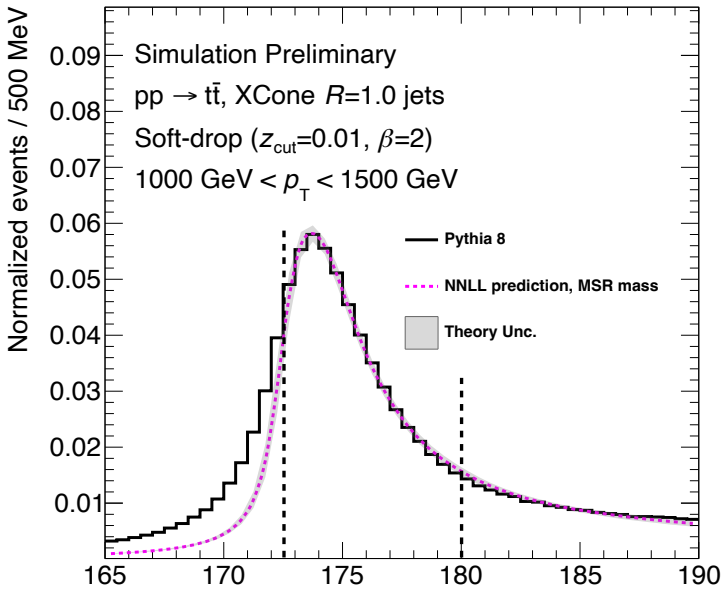


Figure 8.6: A comparison is made between the NNLL prediction for the MSR mass and the Pythia 8 simulation's distribution in the jet $p_T$ bin of 1000-1500 GeV with soft-drop grooming. MC is represented by the black curve, while the dashed purple line indicates the NNLL prediction, fitted against the MC data to obtain the nominal values for $m_t$, $\Omega_{1t}^{\circ\circ}$, and $x_2$. The jet mass values at 172.5 and 180 GeV, which represent the fit range, are marked by black vertical dashed lines.

For the nominal result, parameters include $m_t^{\mathrm{MSR}}(R = 3\ \mathrm{GeV})$ within the range 171.0 GeV and 173.0 GeV in steps of 0.02 GeV, $\Omega_{1t}^{\circ\circ}$ ranging from 1.4 GeV to 2.4 GeV with 0.05 GeV steps, and $x_2$ from 0.1 to 0.69 in increments of 0.005. A total of 1.44 million predictions were generated for use in this analysis.[2]

[2]These templates were generated using the ARTificial Environment for Machine learning and Innovation in Scientific Advanced computing (ARTEMISA) facility. This computing structure is based in IFIC-Valencia, and the core computing resources focus on the use of GPUs [239].

A $\chi^2$-minimisation process is used to match the parameters from the theoretical calculation to the Monte Carlo predictions. The calculation of $\chi^2$ for each set of distributions involves comparing the normalised NNLL predictions with the outcomes from MC simulations, factoring in statistical uncertainties inherent in the MC data. This is mathematically represented as:

$$\chi^2 = \sum_k \left( \frac{N_k^{MC} - N_k^{tmp}(\theta_1, ..., \theta_N)}{\sigma_k^{MC}(\text{stat})} \right)^2, \tag{8.9}$$

where $k$ indexes the histogram bins and $\theta_1, ..., \theta_N$ denote the $N$ parameters on which the template relies. Since there are three parameters involved in this calculation, $N = 3$.

The relationship between these parameters is shown in two-dimensional heatmap fits, visualised in Figure 8.7. The heatmap illustrates areas where different combinations of these parameters lead to the lowest values of reduced $\chi^2$ values.[3] There is a strong connection between the parameters studied but there exists an observed degeneracy when it comes to comparing them the $x_2$ parameter. This is shown by the presence of several $\chi^2$ minima along the axis of $x_2$, indicating that multiple combinations of $x_2$ and other parameters can fit the data well. Specifically, it seems that as $x_2$ increases, $m_t^{MSR}$ tends to increase, while $\Omega_{1t}^{\circ\circ}$ tends to decrease. The relationship between $\Omega_{1t}^{\circ\circ}$ and $m_t^{MSR}$ is more consistent, with only a specific $\Omega_{1t}^{\circ\circ}$ range yielding minimal $\chi^2$ values.

A 3-D marginalisation process is needed on the $\chi^2$ distribution to enable the determination of central values and uncertainties for each parameter in relation to the others. This involves varying two parameters while fixing one, to locate the minimum $\chi^2$ value for each set of parameters. This process repeats for all variables until a minimum $\chi^2$ value is established for each bin in every parameter. The uncertainty is determined based on the parameter values that cause a unit increase in the minimal $\chi^2$ . The optimal parameter values and their corresponding uncertainties are deduced by fitting second-order polynomials to the marginalised $\chi^2$ distributions.

The overall $\chi^2$ is a combined result from the 3D parameter space across four $p_T$ bins: $750 < p_T < 1000$ GeV, $1000 < p_T < 1500$ GeV, $1500 < p_T < 2000$ GeV, and $2000 < p_T < 2500$ GeV. This combined $\chi^2$ minimisation extends over the complete phase space.

[3]Normalised to the number of degrees of freedom

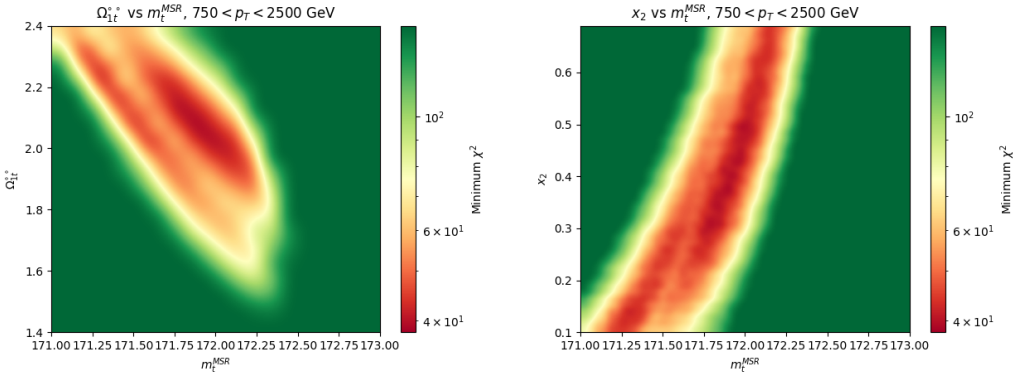


(a) (b)

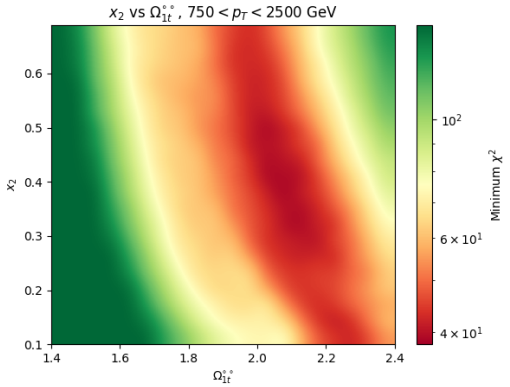


(c)

Figure 8.7: Two dimensional heatmaps comparing the $\chi^2$ for the parameters (a) $m_t^{MSR}$ and $\Omega_{1t}^{\circ\circ}$, (b) $m_t^{MSR}$ and $x_2$, and (c) $\Omega_{1t}^{\circ\circ}$ and $x_2$. The value of $\chi^2$ is represented with a colour bar, with higher values attributed to green and moving to red the lower the values reach.

In addition to theory-to-MC fits, the analysis includes theory-to-theory and MC-to-MC fits for estimating theoretical and MC-related uncertainties such as MPI modelling. These uncertainty evaluations are elaborated on in Section 8.3.

The approach for conducting theory-to-theory fits is analogous to that used in theory-to-MC fits. However, instead of comparing theory curves to MC simulations, the same theory grid is used to fit alternative theoretical jet mass curves. These alternative curves are generated by varying the scales within the theoretical calculations, which introduces different theoretical uncertainties. This method provides an estimate of the magnitude of higher order corrections that are not currently included in the calculation and, therefore, must be included as

a theoretical uncertainty in our mass relation. This procedure is conceptually similar to fitting MC simulations with grids generated under different scales but is more resource-efficient.

In the context of MC-to-MC fits, templates based on Monte Carlo simulations serve as the standard reference. Here, the mass of the MC top quark is varied against a set of MC simulations configured differently to evaluate specific uncertainties. Given that this process exclusively revolves around $m_t^{MC}$, it requires only a 1-D $\chi^2$ marginalisation process.

## 8.3 Uncertainties

The interpretation of the top quark mass parameter is affected by several uncertainties, including those related to the theory, fit uncertainties, and uncertainties relating to the lack of theoretical description of underlying event. The subsequent section focuses on methodologies to study these uncertainties, in an aim to refine the final result.

### 8.3.1 Theoretical Uncertainties

The theoretical uncertainties are based on choices of renormalisation scales specified via *profile functions* that encapsulate their jet mass dependence and provide a prescription for their variation for estimating perturbative uncertainty. The first set of scales are ones that apply to the default values used in the normalisation scale seen in Equation 8.5. Namely the hard scale variation, $\mu_N \equiv e_N Q$, the global soft variation $\mu_{gs} \equiv e_N Q_{cut}$, and mass scale variation $\mu_m \equiv e_m m_t$. Where $e_N$ and $e_m$ are defined at a value of 1 and vary to values of 0.5 and 2 for the down and up variations, respectively.

The collinear soft scale, $\mu_{cs}$, hinges on the parameter $\alpha$, which is defined within the range of $\alpha(\overset{\text{def.}}{=} 0) \in [-1, 1]$. Adding to this is the collinear-soft scale exponent, $\rho$, which lies within $\rho(\overset{\text{def.}}{=} 0) \in [-0.1, 0.1]$ and is used for examining the relations between ungroomed soft, collinear-soft, and global soft scales.

The nonperturbative transition parameter, $n_0$, situated in the $n_0(\overset{\text{def.}}{=} 0) \in [-0.1, 0.1]$ range, is key in setting the nonperturbative scale, which becomes needed when the analysis transitions into the nonperturbative region. Lastly, the bHQET jet scale variation, $e_B$, which is determined by combining the bHQET

scale with the collinear-soft scale, and is varied in the range $e_B(\overset{\text{def.}}{=} 1) \in [0.5, 2]$. This is performed while also preserving the canonical relationship between these two scales.

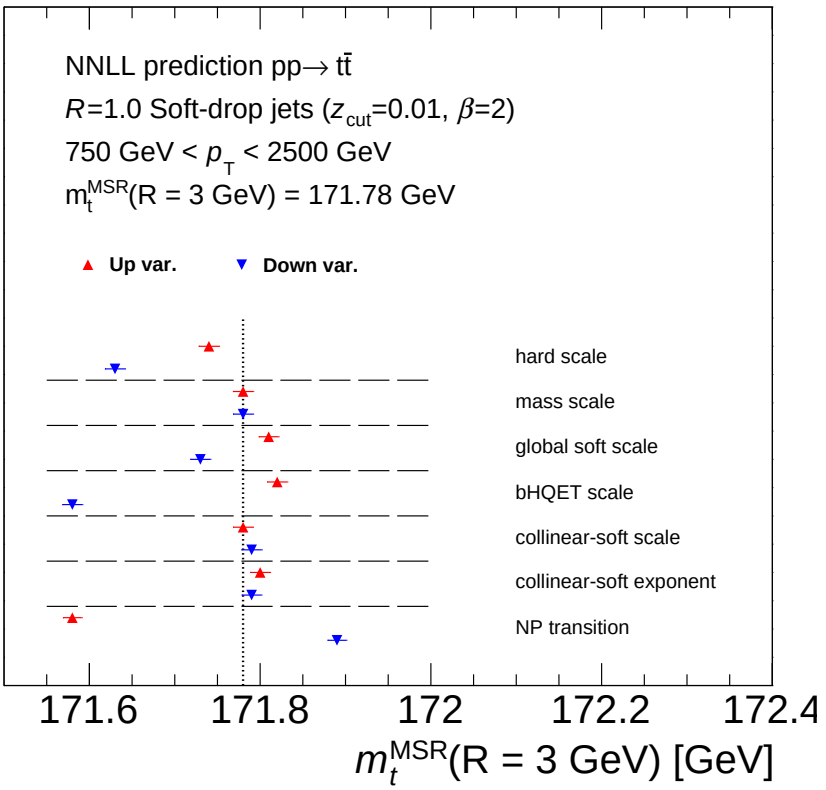


Figure 8.8: The impact of scale variations of the NNLL calculation of the top quark MSR mass. To determine the values of $m_t^{\text{MSR}}(3\text{ GeV})$, the baseline NNLL calculation is adapted to match predictions derived under various selections of the seven scales. The red (blue) triangles represent the up (down) variations of each scale variation. The horizontal lines on the points relate to the statistical uncertainty on the number of points produced in the generation of the theoretical variation jet mass distributions.

The scale variations were compared to the nominal result with a theory-to-theory fit as described in Section 8.2.3 and are illustrated in Figure 8.8. In determining the total uncertainty for the final result, we consider the range of $m_t^{MSR}(R = 3\text{ GeV})$ shifts obtained by fitting the scale-varied theoretical predictions to the nominal calculation. The largest extent of these shifts forms the envelope that defines the uncertainty assigned to the mass relation. The overall uncertainty is $^{+110}_{-200}$ MeV, and is almost two times lower than the previous result

at NLL that was determined to be $^{+230}_{-310}$ MeV in Ref. [163].

This improvement is evident in Figure 8.9, which presents a side-by-side comparison of the theory scale variation curves, normalised to the nominal curve, in the previous NLL framework and this updated framework. The decrease in uncertainty values is evident when examining the envelope over the scale variations, and the bottom panels that highlight the difference between the variations and the nominal.

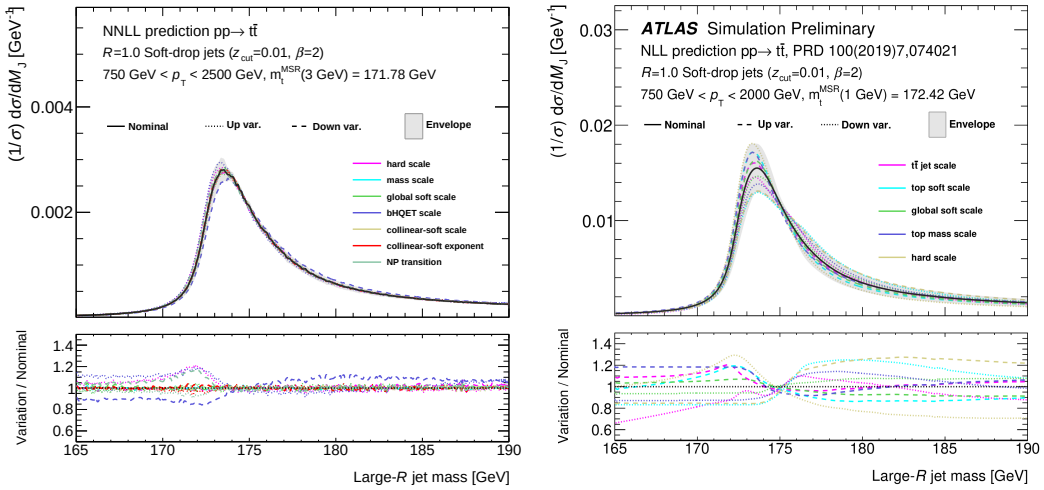


(a) (b)

Figure 8.9: The (a) NNLL and (a) NLL [223] prediction of the normalised particle-level jet mass distribution for groomed large-$R$ jets with a boosted hadronic top-quark decay (represented by a black line). The variations in the scales of the calculation are depicted by coloured lines, with the up (down) variations corresponding to dashed (dotted) line. Each curve is normalised to have the same area within the jet mass range of 172.5-180 GeV. The grey band illustrates the range covered by all scale variations.

The improvement in the theoretical uncertainty matches what is expected, as explained by the authors of Ref. [240]. This paper suggests that the scale uncertainty can be reduced by a factor of two when the theory transitions from NLL to NNLL accuracy. This uncertainty can also decrease by another factor of 2 when moving from NNLL to N$^3$LL.

### 8.3.2 Underlying Event Uncertainty

The NNLL calculation does not yet include the effects of UE, meaning that the results in this thesis are based on a comparison of the top quark jet mass to MC generators with the absence of UE. To address this, the impact of UE is studied in MC-MC comparisons with the MPI switch turned on for varied underlying event tunes. Five different variations are considered in this evaluation, with the initial variants consisting of A14 Var1 and Colour Reconnection (CR), used to gauge the UE uncertainty associated with this analysis. The remaining variants include the CMS UE, Monash, and CDF tunes, which serve to assess the influence of the underlying event across various experimental setups on the Large-$R$ jet mass within Pythia.

These findings are visually represented in Figure 8.10, which illustrates the contrast between the standard Pythia 8 distribution and those resulting from different tunes that contain different UE modelling configurations. These variations caused slight shifts in the peak of the jet mass curves, which in turn alter the calculated mass of $m_t$. We estimate the UE uncertainty as the difference between the top quark mass of the nominal sample and the top quark mass of the variation sample.

The distinct settings shown in Figure 8.10 are determined by specific parameters that influence the modelling of the jet mass distribution. Figure 8.10a illustrates the scenario where only the UE and CR parameters are adjusted in the A14 tune, with the MPI switch activated. These adjustments exclusively affect the UE simulation in Pythia, which becomes evident when contrasting these results with those in Figure 8.10b, where the MPI setting is deactivated and the deviation in mass is negligible. The most notable differences are observed in the settings depicted in Figures 8.10c and 8.10d. These variations alter parameters based on the UE modelling in different experiments, with and without MPI, respectively. In the absence of UE with the MPI setting, the variations in jet mass distributions are relatively minor, reflecting the specific tuning in each experiment. However, the inclusion of UE with the MPI setting results in more pronounced changes, as the parameter modifications predominantly reflect the UE modelling approaches unique to these experiments.

The set of parameters involved in the difference in modelling for the different tunes are based on cross-section calculations (SigmaProcess, SigmaTotal, SigmaDiffractive), parton showers as they evolve in time (TimeShower), evolution

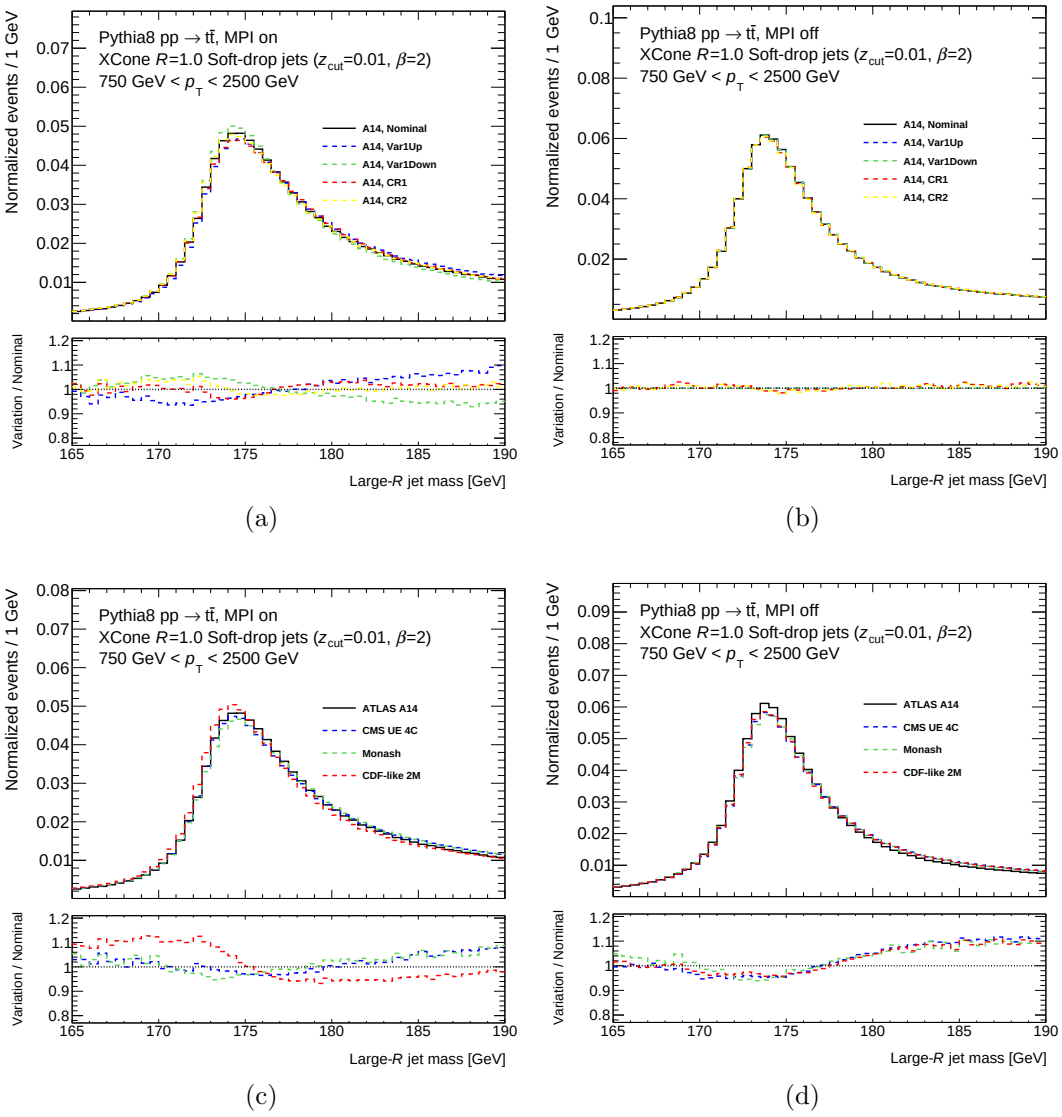


Figure 8.10: Large-$R$ jet mass distributions generated by Pythia 8. The variations between the standard A14 tuned sample and different A14 tunes affecting the UE modelling are depicted with (a) MPI on, and (b) MPI off. This is contrasted to the baseline ATLAS-based A14 tunes sample with tunes associated with various other experiments with (c) MPI on, and (d) MPI off. Each of the alternative tunes is normalised to the nominal curve.

of partons in space before the hard interaction (SpaceShower). The variables that predominantly affect the UE are those related to: interactions of multiple partons that are not part of the hard interactions, described as MPIs in Section 3 (MultipartonInteractions), the remaining partons, known as remnants, after the main interaction in order to satisfy momentum and quantum number conservation laws (BeamRemnants), and re-arrangements of the colour strings that connect quarks and gluons as they can reconnect in different ways, which can affect final state particle distributions (ColourReconnection).

The $m_t$ values shift of the different tunes depend on which specific jet $p_T$ bin we are considering. Figure 8.11 displays the values of $m_t^{MC}$ for each tune of Pythia 8 taken from MC-to-MC best fits for each of the four jet $p_T$ bins, relative to the nominal MC top quark mass which is set at 172.5 GeV. To estimate the uncertainty we take the envelope of the shifts in masses. For the majority of the tunes this will match the lowest $p_T$ bin, 750-1000 GeV, where the jets are softer and more susceptible to the influence of UE.

The first tunes of focus are the the Var1 tunes [237], which are typically used in ATLAS to determine the behaviour of UE activity. These consist of up and down variations, in which two key parameters are adjusted, ColourReconnection:range and MultipartonInteractions:alphaSvalue:

- The ColourReconnection:range parameter governs the probability of colour reconnection occurring among different parton showers or strings. Its standard value is set at 1.71, with the up (down) variation at 1.73 (1.69).
- MultipartonInteractions:alphaSvalue determines the strength of the strong coupling constant, specifically for multiparton interaction calculations. This parameter has a baseline value of 0.126, with its up (down) variation being 0.131 (0.121).

We estimate the $m_t^{MC}$ values with their related MC statistical uncertainty for the A14 Var1 variations to be 172.63±0.006 GeV for Var1Up and 172.41±0.006 GeV for Var1Down. Since the uncertainty is taken as the mass shift of the variations to the nominal, we achieve a Var1-related UE uncertainty of −90 MeV and +129 MeV.

The CR model in Pythia [241] considers where the colour flow of partons belonging to different MPI systems can be fused. The initial alternative model, CR1, is grounded in the colour rules of the QCD multiplet structure and tends to

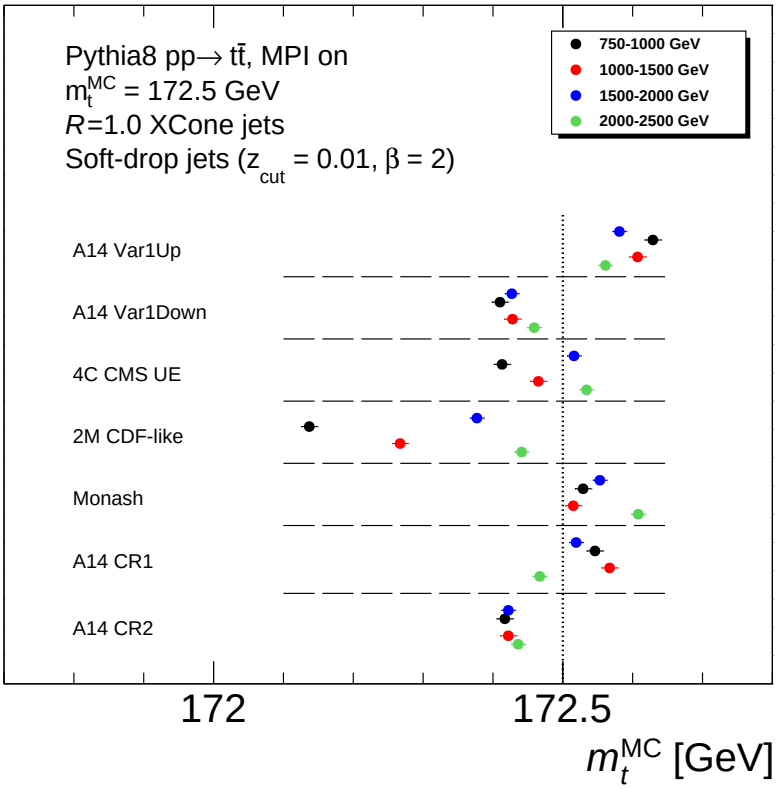


Figure 8.11: The influence of different tuning parameters on $m_t^{MC}$ across various large-$R$ jet $p_T$ bins, as simulated by Pythia 8, in comparison to the standard A14 tunes set at $m_t^{MC}$ = 172.5 GeV. This standard is indicated by a vertical black dashed line. The bins are represented by distinct coloured dots: the 750-1000 GeV $p_T$ bin is shown with a black dot, the 1000-1500 GeV $p_T$ bin with a red dot, the 1500-2000 GeV $p_T$ bin with a blue dot, and the 2000-2500 GeV $p_T$ bin with a green dot.

yield jets with greater mass as it enhances the production of baryons. In contrast, the second model, CR2, is a gluon-move model and results in a lower occurrence of massive jets as only gluons are considered for reconnection. It affects multiple Pythia parameters:

- The MultipartonInteractions:pT0Ref parameter sets a scale based on $p_T$, below which the effects MPI are suppressed. It has a nominal value of 2.09, but CR1 (CR2) is set to 1.89 (2.21).
- MultipartonInteractions:expPow influences the shape of the transverse momentum distribution for multiparton interactions and shapes how rapidly

the effective $p_T$ cutoff changes with the energy of the collision; this has a nominal value of 1.85, and for CR1 (CR2), it is 2.10 (1.63).

- Only the CR1 variation variable is affected by the ColourReconnection:m0 parameter, which detemines how how strongly colour strings between partons are reconnected during the hadronisation and has a value of 0.3 (2.17) in the nominal (CR1) tune.

- The ColourReconnection:junctionCorrection parameter affects colour reconnection adjustments for colour flow structures involved in events relating to baryons, which again only affects CR1 with a value of 9.33, with the nominal 1.20.

- The last parameters are only related to the CR2 model. The first being ColourReconnection:m2Lambda which is the equivalent of ColourReconnection:m0 for the gluon-move model, and has a nominal (CR2) value of 1.0 (6.73). The last is the ColourReconnection:fracGluon parameter which controls the fraction or probability of gluon involvement in the colour reconnection process, and has a nominal (CR2) value of 1.0 (0.93).

The $m_t^{MC}$ values measured for the colour reconnection model variations are $172.55 \pm 0.006$ GeV and $172.42 \pm 0.006$ GeV for CR1 and CR2, respectively. This leads to a CR model-related uncertainty of +46 MeV and −83 MeV.

In Figure 8.10c, the ATLAS A14 sample is compared to tunes developed by CMS (CMS 4C [242]), Peter Skands et al.(Monash [243]) and an older tune from CDF (2M [244]). The set of values for each corresponding parameter in each of the tunes can be found in Table 8.1.

The 2M tune, with the MRST PDF set, is clearly very different from the nominal sample, reflecting the large gap between the centre-of-mass energy of the Tevatron and the current study. This specific tune was evaluated in this analysis in order to verify that the change of CoM energy should have a substantial impact on the mass. We measure the $m_t^{MC}$ mass in this regime to be $172.13 \pm 0.006$ GeV, which is the largest shift from the configurations we have studied, with a mass difference of −363 MeV.

The Monash 2013 Tune for $e^+e^-$ and $pp/\bar{p}p$ processes, uses the NNPDF 2.3 LO PDF set [243]. This was developed to improve the Pythia 8 output from

| Tune Parameters | ATLAS A14 | Monash | CMS UE | 2M (CDF-like) |
|---|---|---|---|---|
| PDF Set | NNPDF 3.0 NLO | NNPDF 2.3 LO | CTEQ 6L1 | MRST LO** |
| SigmaProcess:alphaSvalue | 0.140 | 0.130 | 0.135 | 0.1265 |
| SigmaTotal:zeroAXB | on | on | on | on |
| SigmaDiffractive:dampen | on | on | on | off |
| SigmaDiffractive:maxXB | 65.0 | 65.0 | 65.0 | N/A |
| SigmaDiffractive:maxAX | 65.0 | 65.0 | 65.0 | N/A |
| SigmaDiffractive:maxXX | 65.0 | 65.0 | 65.0 | N/A |
| Diffraction:largeMassSuppress | 4.0 | 4.0 | 2.0 | 2.0 |
| TimeShower:alphaSvalue | 0.127 | N/A | N/A | N/A |
| TimeShower:dampenBeamRecoil | on | on | on | on |
| TimeShower:phiPolAsym | on | on | on | on |
| SpaceShower:alphaSvalue | 0.127 | 0.1365 | 0.137 | 0.130 |
| SpaceShower:alphaSorder | 1 | 1 | 1 | 1 |
| SpaceShower:alphaSuseCMW | off | off | off | off |
| SpaceShower:samePTasMPI | off | off | off | off |
| SpaceShower:pT0Ref | 1.56 | 2.0 | 2.0 | 2.0 |
| SpaceShower:ecmRef | 7000.0 | 7000.0 | 1800.0 | 1800.0 |
| SpaceShower:ecmPow | 0.0 | 0.0 | 0.0 | 0.0 |
| SpaceShower:pTmaxFudge | 0.91 | 1.0 | 1.0 | 1.0 |
| SpaceShower:pTdampFudge | 1.05 | 1.0 | 1.0 | 1.0 |
| SpaceShower:rapidityOrder | on | on | on | on |
| SpaceShower:rapidityOrderMPI | on | on | on | on |
| SpaceShower:phiPolAsym | on | on | on | on |
| SpaceShower:phiIntAsym | on | on | on | on |
| MultipartonInteractions:alphaSvalue | 0.126 | 0.130 | 0.135 | 0.127 |
| MultipartonInteractions:pT0Ref | 2.09 | 2.28 | 2.1006 | 2.455 |
| MultipartonInteractions:ecmRef | 7000.0 | 7000.0 | 1800.0 | 1800.0 |
| MultipartonInteractions:ecmPow | 0.215 | 0.215 | 0.2106 | 0.26 |
| MultipartonInteractions:bProfile | 3 | 3 | 3 | 3 |
| MultipartonInteractions:expPow | 1.85 | 1.85 | 1.6089 | 1.15 |
| MultipartonInteractions:a1 | 0.15 | 0.15 | 0.0 | 0.15 |
| BeamRemnants:primordialKTsoft | 0.9 | 0.9 | 0.5 | 0.5 |
| BeamRemnants:primordialKThard | 1.88 | 1.8 | 2.0 | 2.0 |
| BeamRemnants:halfScaleForKT | 1.5 | 1.5 | 1.0 | 1.0 |
| BeamRemnants:halfMassForKT | 1.0 | 1.0 | 1.0 | 1.0 |
| ColourReconnection:mode | 0 | 0 | 0 | 0 |
| ColourReconnection:range | 1.71 | 1.80 | 3.3126 | 3.0 |

Table 8.1: The variables and their related values for different $pp/p\bar{p}$ tunes in Pythia 8.

constraints imposed by LEP and SLD on hadronisation, particularly with regards to heavy-quark fragmentation and strangeness production.

The $m_t^{MC}$ values for the Monash tune are observed to be $172.53 \pm 0.01$ GeV, meaning a UE uncertainty of +29 MeV. Among all the configurations we have studied, this exhibits the lowest shift in mass with respect to the nominal A14 variation. This can be attributed to the fact that the Monash tune has served as the foundation for many other configurations developed after 2013, which includes the Pythia A14 tune.

The final tune under examination is the CMS UE tune, as referenced in [242], which employs the CTEQ 1 PDF set [245] and is specifically designed to focus on underlying event. This tune is based on the 4C tune [244], which originates

from the same Tevatron-related studies as the 2M tune. However, it further incorporates underlying event data from CMS at $\sqrt{s}$ = 7 TeV, enhancing the predictions for UE observables in $pp$ collisions at $\sqrt{s}$ = 13 TeV. Using this, $m_t^{MC}$ is measured to be $172.41 \pm 0.006$, giving an uncertainty of −87 MeV.

The uncertainty in the UE for this analysis is calculated as the quadrature sum of the Var1 and CR variation shifts. This value is determined to be $^{+137}_{-122}$ MeV. The studies involving CMS and Monash demonstrate a strong agreement with these uncertainties, suggesting that the UE modelling is under control. This is particularly relevant since Monash forms the foundation for the A14 tune. Additionally, given the similarities between CMS and ATLAS using $pp$ collision data, and the fact that the CMS UE tune is specifically developed for centre-of-mass energy measurements at 13 TeV, it provides a valuable proxy for comparison. The 2M tune is also useful in demonstrating how differences in the centre-of-mass energy influence shifts in the UE.

### 8.3.3 Methodology Uncertainty

The outcome of the fit is influenced by specific choices in the fitting method, particularly the selection of the fit and kinematic ranges. To address any potential biases in the mass relation due to these choices, uncertainties are incorporated.

The chosen fit range is between 172.5 and 180 GeV, which significantly impacts the results. The effect of varying the lower limit of the mass range in the fit is assessed by using alternative jet mass ranges starting at either 172 GeV or 173 GeV, while always extending to 180 GeV. To maintain fit stability, similar to the approach in determining theoretical uncertainty, $x_2$ is confined to the best-fit result. The MSR mass values from these alternative range fits are compared with the nominal fit, and the difference is assigned as an uncertainty, amounting to ±215 MeV.

Also, the fit must consider the $p_T$ range of the large-$R$ jet, as it influences $m_t^{MC}$. This is done by comparing fits across subsets of three $p_T$ intervals, repeating the process through all combinations of three out of four $p_T$ intervals. The maximum variations in both positive and negative directions determine the uncertainty, resulting in +63 MeV and -84 MeV.

## 8.4 Results

Finally, we reach the conclusion of the results of the chapter, which is the interpretation the MC mass of the top quark in relation to the MSR mass of the top quark. Initially, we will centre the discussion on $m_t^{MSR}(R = 1 \text{ GeV})$. Whilst it may not be the optimal renormalisation value, it serves as a standard reference point, aligning with previous studies that also used the same scale, while also offering the closest approximation to $m_t^{MC}$. The key findings are summarised as follows:

$$\begin{aligned} m_t^{MSR}(R = 1 \text{ GeV}) &= 172.07 \pm 0.02 \text{ GeV}, \\ \Omega_{1t}^{\circ\circ} &= 1.98 \pm 0.01 \text{ GeV}, \\ x_2 &= 0.36 \pm 0.03, \end{aligned} \tag{8.10}$$

where the associated uncertainty corresponds to the statistical uncertainty due to the limited MC sample.

From these results, we establish the following relation:

$$m_t^{MC} = m_t^{MSR}(R = 1 \text{ GeV}) + 430^{+285}_{-330} \text{ MeV}, \tag{8.11}$$

where the associated uncertainty values correspond to the quadrature sum of the theoretical uncertainties, methodology uncertainties, and UE uncertainties.

The most applicable analysis result to use for comparison is that of the authors in Ref. [223]. Within that analysis, which used the underlying theoretical framework described in Section 8.1.1 at NLL precision for $pp \to t\bar{t}$, the relation result, $\Delta_t^{MSR} = m_t^{MC} - m_t^{MSR}$, was measured to be $\Delta_t^{MSR} = 80^{+350}_{-400}$ MeV.

The first thing to note is the reduction in the uncertainties in our analysis, which is primarily due to enhanced precision in the theoretical framework that now includes a more accurate NNLL prescription. The comparison is shown in Figure 8.9 with the theoretical uncertainty discussion in Section 8.3.1.

The significant shift in the calculated top quark mass can be attributed to two main modifications in the analysis approach. Firstly, there's the transition from NLL to NNLL precision. Secondly, there is the addition of renormalon subtractions. The impact of these changes was evaluated through theory-to-theory comparisons, similar to the methods used for assessing theoretical uncertainties. However, instead of using distributions attributed to varied scale variations, the

theory calculation was adjusted by altering specific settings in the configuration files. These evaluations provide a rough estimate of how these adjustments influenced the jet mass distributions, though they are not as precise as the grid-based methods used in theory-to-MC fitting. Despite being less accurate, this approach is less computationally intensive, which offers us a trade-off between precision and efficiency.

The shift from NLL to NNLL precision, without any renormalon subtraction, results in an estimated 30 MeV reduction in the top quark mass. The second adjustment, which involves new settings in the underlying theory, that were described in Section 8.1.2, and the addition of renormalon subtractions, led to a further reduction of 340 MeV. Of this 340 MeV reduction, 280 MeV is attributed to the introduction of the renormalon gap subtraction. Therefore, the cumulative effect of these changes from the previous to the current analysis is approximately a 370 MeV decrease in the estimated top quark mass.

The authors of Ref.[221] perform a much more in-depth study into the effect of these changes, using boosted top quark production in $e^+e^-$ collisions. However, a direct comparison of this result with those measured in this paper is challenging due to the differing collision environments and the grooming employed here, which is not used in that analysis.

An additional check was performed to compare the different Pythia versions used for the MC templates. In this analysis Pythia 8.307 was used, while the earlier analysis employed Pythia 8.210. The difference in the resultant relations was found to be negligible within the statistical uncertainties attributed to the number of events generated in the MC samples.

Finally, we present the final result of the chapter, which interprets the MC mass of the top quark in relation to the MSR mass of the top quark at the renormalisation scale of $R = 3$ GeV, as suggested in Ref. [236]. The key findings are as follows:

$$\begin{aligned} m_t^{MSR}(R = 3 \text{ GeV}) &= 171.78 \pm 0.03 \text{ GeV}, \\ \Omega_{1t}^{\circ\circ} &= 1.96 \pm 0.01 \text{ GeV}, \\ x_2 &= 0.38 \pm 0.02, \end{aligned} \tag{8.12}$$

where the associated uncertainty corresponds to the statistical uncertainty due to the limited MC sample.

From these results, we establish the following relation:

$$m_t^{MC} = m_t^{MSR}(R = 3 \text{ GeV}) + 720^{+285}_{-330} \text{ MeV}, \tag{8.13}$$

where the associated uncertainty values correspond to the quadrature sum of the theoretical uncertainties ($^{+110}_{-200}$ MeV), methodology uncertainties ($^{+224}_{-231}$ MeV), and UE uncertainties ($^{+137}_{-122}$ MeV).

One thing to note here is the difference in the relation value between $R = 1$ GeV and $R = 3$ GeV as shown in the difference between Equation 8.11 and Equation 8.13. The value of the relation increases by 290 MeV when the renormalisation scale shifts from $1 \rightarrow 3$ GeV. When observing Figure 8.12, which illustrates the R-evolution of the mass relation, the varying values of $m_t^{MSR}$ obtained align with expectations, when using $m_t(m_t) = 162.3$ GeV. Additionally, points representing the other top quark mass calibrations discussed in this chapter are included for comparison with our results. This comparison demonstrates a strong compatibility among the points, when considering the range of statistical uncertainties.

In conclusion, we have explored the relation between the top quark mass parameter in Monte Carlo generators and the top quark mass defined in the MSR scheme. A mass relation is determined by comparing first-principle calculations for boosted large-$R$ jets with soft-drop grooming to Monte Carlo predictions. Our findings indicate that the MSR top quark mass at $R = 1$ GeV and the top quark mass parameter in Pythia 8 are compatible within the uncertainty of about 300 MeV.

Comparing to other results, we find good agreement. Notably, the analysis in Ref.[223] based on NLL calculations for the same observable reports a relation $\Delta_t^{MSR}$ of $80^{+350}_{-400}$ MeV for $pp \rightarrow t\bar{t}$ production. This result, with the considered uncertainties, aligns with our findings.

Lastly, we examine the results from $e^+e^-$ experiments, which report relations $\Delta_t^{MSR} = 200 \pm 290$ MeV [220] at NLL, $\Delta_t^{MSR} = 180 \pm 220$ MeV [220] at NNLL, and $\Delta_t^{MSR} = 30 \pm 210$ MeV [221] at NNLL+NLO precision. Again, our result is in agreement, within the margin of uncertainties, with both of these studies.

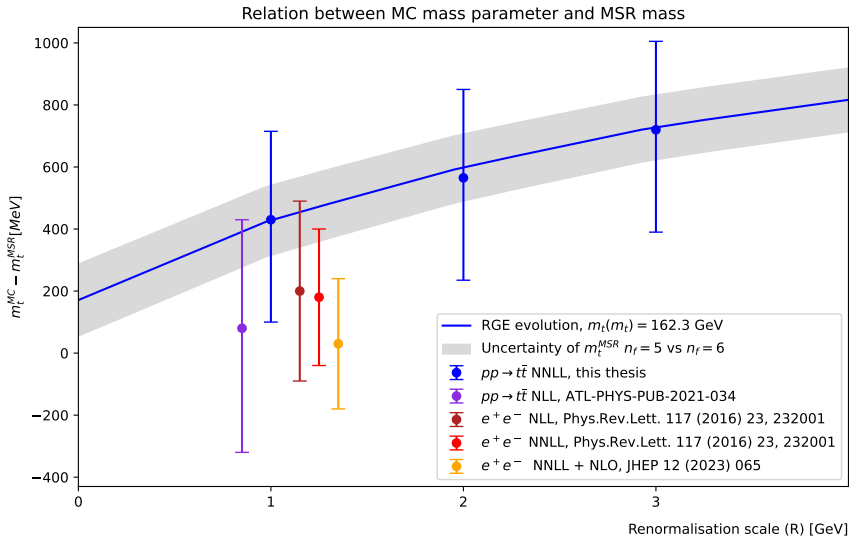


Figure 8.12: R-evolution for the mass relation $\Delta_t^{MSR} = m_t^{MC} - m_t^{MSR}(R)$, with $m_t(m_t) = 162.3$ GeV, using the REvolver software program [246]. The points represent the mass relation results and their uncertainties from the analysis of this thesis (blue points) Ref. [247], and from Ref. [223] (purple point), Ref. [220] (red points), and Ref. [221] (orange point). The leftmost blue point from this thesis is compared to results for the mass relation for $R = 1$ GeV from the literature. The grey band relates to the uncertainty applied to the R-evolution curve, when considering the difference between 5- and 6-flavour $m_t^{MSR}$ results.

## 8.5 Outlook

Precise measurements of the top quark mass have improved greatly in recent memory, notably the combined direct mass measurements detailed in Section 7.3, which have achieved an unprecedented precision of 330 MeV [211]. Because of this high level of experimental precision, the interpretation of top quark mass remains a significant challenge, introducing uncertainties that often limit the precision of these measurements. The potential of indirect measurements to validate or challenge renormalised top quark mass interpretations, like the pole mass, is used, though current uncertainties around the order of 1 GeV limit their effectiveness.

Addressing these challenges, this thesis introduces two critical advancements. The first is the MC-theory fit for establishing a more precise and reliable relation between direct mass measurements and a viable mass scheme, notably the MSR mass scheme. In addition, we have conducted an in-situ bJES calibration that is essential for enhancing precision in top quark mass measurements, considering

that the bJES is one of if not the largest uncertainty of top quark mass measurements at the LHC.

The in-situ bJES in $\gamma$+jet events, marks an initial step in demonstrating the inefficiency of inclusive JES for calibrating $b$–jets within ATLAS. However, a $b$–jet specific JES calibration chain should be implemented in order to refine the calibration of $b$–jets, which is crucial for advancing analyses within ATLAS.

The task of refining top quark mass interpretations requires further effort. Notably, the current calculation does not include the underlying event, whose MC-based estimation introduces a large uncertainty. An advanced theoretical framework that integrates the underlying event into the calculated shape function is suggested to mitigate the large uncertainty currently impacting the results. Moreover, there is ongoing development towards utilising a more aggressive SD grooming technique than the one we currently use. This new grooming approach has the potential to significantly reduce the UE's influence on jet mass, while still capturing the entirety of the top quark mass decay within the jet.

On top of this, experimental challenges such as detection inefficiencies and the effects of pile-up require thorough investigation in future studies, preferably incorporating real data to understand their impact on the sensitivity of the $m_t^{MC}$ to the dependence of MC configurations.

# Contributions and Impact

**ATLAS in-situ Development**

Within the Jet/$E^T_{\text{Miss}}$ group of the ATLAS collaboration, I collaborated with Julio Lozano Bahilo to provide the full Run 2 in-situ calibration for large-R jets in $\gamma$+jet events, as elaborated in Chapter 6.

My primary contribution to the ATLAS jet calibration effort was pioneering the in-situ calibration of the $b$-Jet Energy Scale ($b$JES) in $\gamma$+jet events. This study, detailed in Section 5.5, was a key component of the *New techniques for jet calibration with the ATLAS detector* paper, referenced in Ref. [147]. I would like to acknowledge Daniel Camarero Muñoz, without who this would not have been possible.

The dissemination of these findings extended to numerous scientific gatherings. I delivered talks at the XVIII ATLAS Hadronic Calibration Workshop, the XXX International Workshop on Deep-Inelastic Scattering and Related Subjects, and also the XXXVIII Biennial of Physics, under the sponsorship of the Spanish Royal Physics Society. Additionally, I presented these results in the poster session of The Large Hadron Collider Conference 2022.

In my role as co-organiser of the XIX ATLAS Hadronic Calibration Workshop in Valencia, I co-convened a session specifically addressing $b$-jet calibration. This session was focused on advancing a novel calibration chain for $b$-jets within the ATLAS experiment, to enhance the precision of analyses that require the use of $b$-jets.

**Top Quark Mass Relation Study**

In collaboration with my supervisors Marcel Vos and Miguel Villaplana, I conducted the top quark mass relation study, documented in Chapter 8. The theoretical underpinning of this study is owed to the contributions of Aditya Pathak and Johannes Michel. Javier Aparisi's methodological developments, stemming from his previous interpretation study referenced in Ref.[223], were also integral to our analysis. We anticipate the publication of these results in the first half of 2024, as related to Ref.[234].

I had the opportunity of representing our theory-experiment collaboration at the 15th International Workshop on Boosted Object Phenomenology, Reconstruction, Measurements, and Searches at Colliders.

# Appendix A

# MPF Results

The MPF response distributions for the in-situ JES calibration with full Run 2 data is shown for the $Z \rightarrow ee$+jet, $Z \rightarrow \mu\mu$+jet, and $\gamma$+jet processes in Figures A.1a, A.2a, and A.3a, respectively. The systematic uncertainties related to each of these responses are also displayed in Figures Figures A.1b, A.2b, and A.3b for the $Z \rightarrow ee$+jet, $Z \rightarrow \mu\mu$+jet, and $\gamma$+jet processes, respectively.

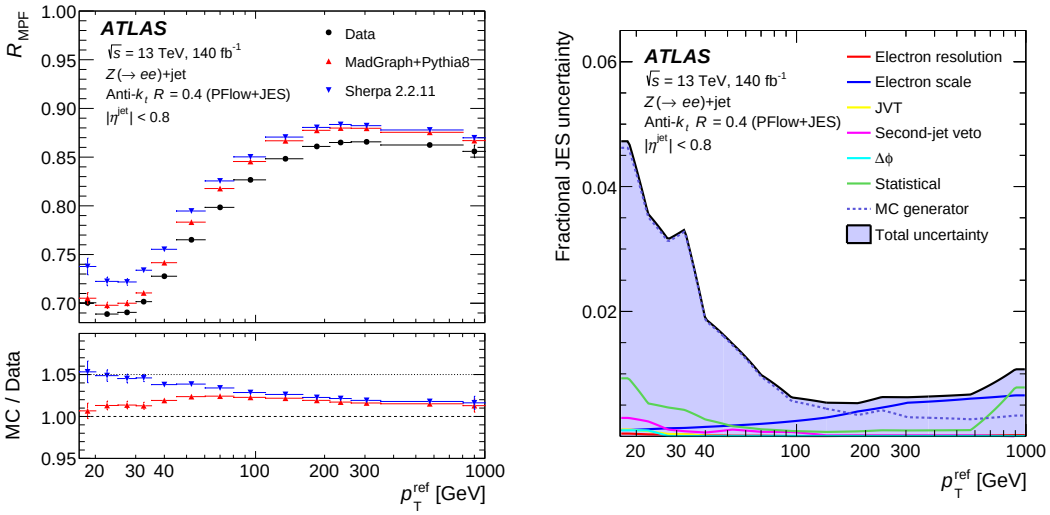


(a) (b)

Figure A.1: (a) Responses, and (b) systematic uncertainties of MPF calibrated with PFlow+JES for $Z + jet \rightarrow ee$(+jets) events as a function of $p_T^{ref}$ in the range $17 \leq p_T^{ref} \leq 1000$ GeV.

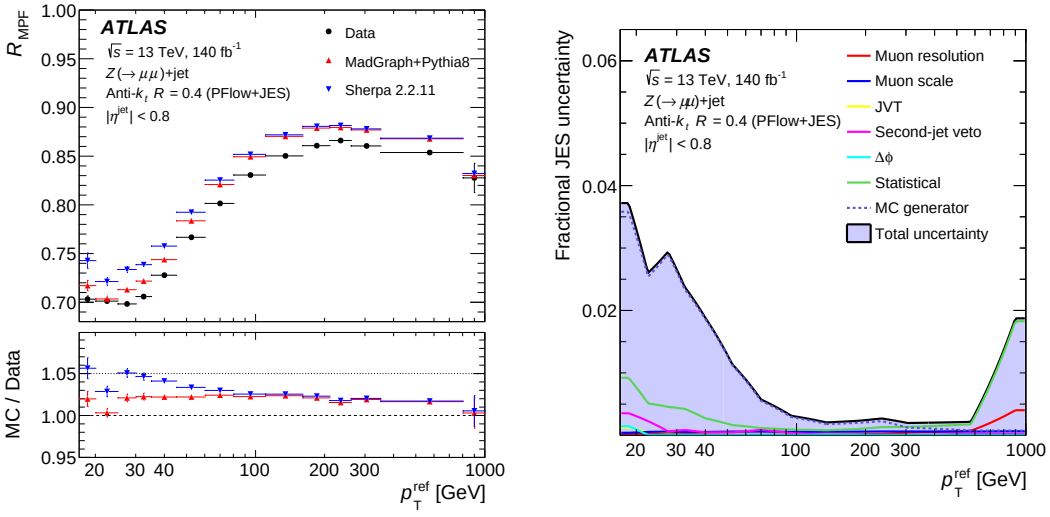


(a) (b)

Figure A.2: (a) Responses, and (b) systematic uncertainties for MPF calibrated with PFlow+JES for $Z \rightarrow \mu\mu$(+jets) events as a function of $p_T^{ref}$ in the range $17 \leq p_T^{ref} \leq 1000$ GeV.

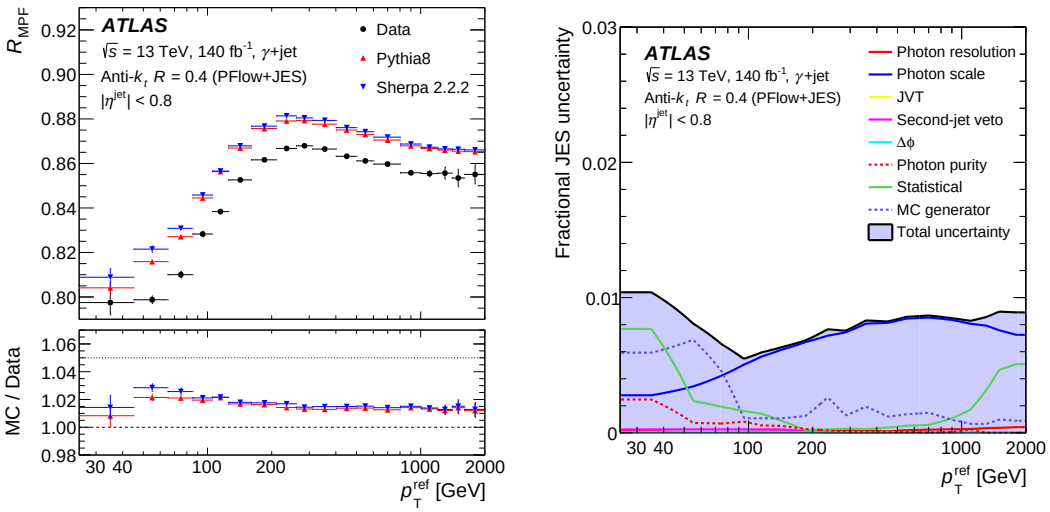


(a) (b)

Figure A.3: (a) Responses, and (b) systematic uncertainties for MPF calibrated with PFlow+JES for $\gamma$+jet events as a function of $p_T^{ref}$ in the range $17 \leq p_T^{ref} \leq 1000$ GeV.

# Appendix B

# Information of MC Generated Events

The $E_T^\gamma$ bins, cross section, filter efficiency, and number of events for the MC generators Pythia 8 and Sherpa 2.2.2 are shown in Tables B.1, B.2, and B.3 for the campaigns a, d, and e, respectively. These variables are used to normalise the MC simulations used in the bJES $\gamma$+jet study in Section 5.5. Pythia has independent samples for the treatment of prompt photons, those that come from direct and those that come from fragmentation.

| Generator (mc16a) | $E_T^\gamma$ range [GeV] | Cross Section [nb] | Filter efficiency | Number of Events |
|---|---|---|---|---|
| Pythia Direct | 17-25 | 2.0242E+03 | 8.1025E-02 | 1699000 |
| | 25-35 | 2.5465E+02 | 5.7028E-02 | 1697000 |
| | 35-70 | 8.4328E+01 | 5.4753E-02 | 2244000 |
| | 70-140 | 2.8396E+01 | 7.2863E-02 | 1796000 |
| | 140-280 | 2.6255E+00 | 7.0598E-02 | 2095000 |
| | 280-500 | 1.9839E-01 | 6.0369E-02 | 2095000 |
| | 500-800 | 1.8846E-02 | 4.4596E-02 | 2097000 |
| | 800-1000 | 2.3312E-03 | 2.4130E-02 | 258000 |
| | 1000-1500 | 7.9945E-04 | 2.3667E-02 | 260000 |
| | 1500-2000 | 5.5512E-05 | 1.9632E-02 | 259000 |
| | 2000-2500 | 5.2361E-06 | 1.6644E-02 | 100000 |
| | 2500-3000 | 5.2733E-07 | 1.4446E-02 | 100000 |
| | 3000-inf | 4.8856E-08 | 1.4371E-02 | 100000 |
| Pythia frag | 17-25 | 1.6713E+07 | 1.8154E-05 | 81470.576 |
| | 25-35 | 1.3963E+06 | 1.4053E-05 | 4343.8669 |
| | 35-70 | 3.7945E+05 | 1.4219E-05 | 2317.3629 |
| | 70-140 | 1.0618E+05 | 1.9271E-05 | 6334.0154 |
| | 140-280 | 6.7020E+03 | 2.0959E-05 | 54.262558 |
| | 280-500 | 3.4407E+02 | 2.0507E-05 | 10.397414 |
| | 500-800 | 2.3711E+01 | 1.6991E-05 | 9.1240597E-03 |
| | 800-1000 | 2.2846E+00 | 1.0123E-05 | 5.0194075E-04 |
| | 1000-1500 | 7.0119E-01 | 1.0074E-05 | 2.1069092E-04 |
| | 1500-2000 | 7.0085E-02 | 5.0238E-06 | 6.2368136E-05 |
| | 2000-inf | 1.1548E-02 | 2.4464E-06 | 2.2803637E-05 |
| SHERPA | 17-35 | 4.1548E+02 | 1 | 5114962.9 |
| | 35-70 | 4.3976E+01 | 1 | 5469197.5 |
| | 70-140 | 4.5263E-00 | 1 | 5997893.3 |
| | 140-280 | 3.7603E-01 | 1 | 6469228.4 |
| | 280-500 | 2.1864E-02 | 1 | 2002774.3 |
| | 500-1000 | 1.4637E-03 | 1 | 1373632.8 |
| | 1000-inf | 2.9864E-05 | 1 | 1052323.4 |

Table B.1: Information for MC samples used for generation of signal events in the $\gamma$+jet measurement at $\sqrt{s} = 13$ TeV using 36fb$^{-1}$ of ATLAS data.

| Generator (mc16d) | $E_T^\gamma$ range [GeV] | Cross Section [nb] | Filter efficiency | Number of Events |
|---|---|---|---|---|
| Pythia direct | 17-35 | 2.0242E+03 | 8.1025E-02 | 27917000 |
| | 35-50 | 2.5465E+02 | 5.7028E-02 | 27975000 |
| | 50-70 | 8.4328E+01 | 5.4753E-02 | 28623000 |
| | 70-140 | 2.8396E+01 | 7.2863E-02 | 28090000 |
| | 140-280 | 2.6255E+00 | 7.0598E-02 | 28427000 |
| | 280-500 | 1.9839E-01 | 6.0369E-02 | 2608000 |
| | 500-800 | 1.8846E-02 | 4.4596E-02 | 2626000 |
| | 800-1000 | 2.3312E-03 | 2.4130E-02 | 330000 |
| | 1000-1500 | 7.9945E-04 | 2.3667E-02 | 330000 |
| | 1500-2000 | 5.5512E-05 | 1.9632E-02 | 330000 |
| | 2000-2500 | 5.2361E-06 | 1.6644E-02 | 130000 |
| | 2500-3000 | 5.2733E-07 | 1.4446E-02 | 130000 |
| | 3000-inf | 4.8856E-08 | 1.4371E-02 | 130000 |
| Pythia frag | 17-35 | 1.6713E+07 | 1.8154E-05 | 108542.12 |
| | 35-70 | 1.3963E+06 | 1.4053E-05 | 30558.640 |
| | 70-140 | 3.7945E+05 | 1.4219E-05 | 14152.008 |
| | 140-280 | 1.0618E+05 | 1.9271E-05 | 15794.658 |
| | 280-500 | 6.7020E+03 | 2.0959E-05 | 189.34395 |
| | 500-1000 | 3.4407E+02 | 2.0507E-05 | 13.890877 |
| | 1000-inf | 2.3711E+01 | 1.6991E-05 | 1.1865658E-02 |
| | 800-1000 | 2.2846E+00 | 1.0123E-05 | 6.5737130E-04 |
| | 1000-1500 | 7.0119E-01 | 1.0074E-05 | 2.7557991E-04 |
| | 1500-2000 | 7.0085E-02 | 5.0238E-06 | 8.0569890E-05 |
| | 2000-inf | 1.1548E-02 | 2.4464E-06 | 2.9870902E-05 |
| SHERPA | 17-35 | 4.1548E+02 | 1 | 6394326.1 |
| | 35-70 | 4.3976E+01 | 1 | 6834301.8 |
| | 70-140 | 4.5263E-00 | 1 | 7507766.3 |
| | 140-280 | 3.7603E-01 | 1 | 8097741.0 |
| | 280-500 | 2.1864E-02 | 1 | 2508325.0 |
| | 500-1000 | 1.4629E-03 | 1 | 1706066.2 |
| | 1000-inf | 2.9864E-05 | 1 | 1309598.8 |

Table B.2: Information for MC samples used for generation of signal events in the $\gamma$+jet measurement at $\sqrt{s} = 13$ TeV using 44fb$^{-1}$ of ATLAS data.

| Generator (mc16e) | $E_T^\gamma$ range [GeV] | Cross Section [nb] | Filter efficiency | Number of Events |
|---|---|---|---|---|
| Pythia direct | 17-35 | 2.0242E+03 | 8.1025E-02 | 36804000 |
| | 35-50 | 2.5465E+02 | 5.7028E-02 | 36680400 |
| | 50-70 | 8.4328E+01 | 5.4753E-02 | 37423600 |
| | 70-140 | 2.8396E+01 | 7.2863E-02 | 36967800 |
| | 140-280 | 2.6255E+00 | 7.0598E-02 | 27464200 |
| | 280-500 | 1.9839E-01 | 6.0369E-02 | 3482000 |
| | 500-800 | 1.8846E-02 | 4.4596E-02 | 3492000 |
| | 800-1000 | 2.3312E-03 | 2.4130E-02 | 438000 |
| | 1000-1500 | 7.9945E-04 | 2.3667E-02 | 440000 |
| | 1500-2000 | 5.5512E-05 | 1.9632E-02 | 438000 |
| | 2000-2500 | 5.2361E-06 | 1.6644E-02 | 170000 |
| | 2500-3000 | 5.2733E-07 | 1.4446E-02 | 170000 |
| | 3000-inf | 4.8856E-08 | 1.4371E-02 | 169000 |
| Pythia frag | 17-35 | 1.6713E+07 | 1.8154E-05 | 135264.26 |
| | 35-70 | 1.3963E+06 | 1.4053E-05 | 43703.297 |
| | 70-140 | 3.7945E+05 | 1.4219E-05 | 18943.560 |
| | 140-280 | 1.0618E+05 | 1.9271E-05 | 18824.973 |
| | 280-500 | 6.7020E+03 | 2.0959E-05 | 244.13252 |
| | 500-1000 | 3.4407E+02 | 2.0507E-05 | 17.351569 |
| | 1000-inf | 2.3711E+01 | 1.6991E-05 | 1.5563953E-02 |
| | 800-1000 | 2.2846E+00 | 1.0123E-05 | 8.6554129E-04 |
| | 1000-1500 | 7.0119E-01 | 1.0074E-05 | 3.5778017E-04 |
| | 1500-2000 | 7.0085E-02 | 5.0238E-06 | 1.0556440E-04 |
| | 2000-inf | 1.1548E-02 | 2.4464E-06 | 3.7796911e-05 |
| SHERPA | 17-35 | 4.1548E+02 | 1 | 6215154.3 |
| | 35-70 | 4.3976E+01 | 1 | 6839968.1 |
| | 70-140 | 4.5263E-00 | 1 | 12441712 |
| | 140-280 | 3.7603E-01 | 1 | 13403140 |
| | 280-500 | 2.1864E-02 | 1 | 4154498.9 |
| | 500-1000 | 1.4629E-03 | 1 | 2574791.2 |
| | 1000-inf | 2.9864E-05 | 1 | 1907543.3 |

Table B.3: Information for MC samples used for generation of signal events in the $\gamma$+jet measurement at $\sqrt{s} = 13$ TeV using 58fb$^{-1}$ of ATLAS data.

# Appendix C

# Uncertainties of $b$–tagged direct balance

The bJES study uncertainties related to the direct balance responses for the $b$-tagged 60%, 70%, 77%, and 85% working points are displayed in Figure C.1a, C.1b, C.1c, and C.1d, respectively.

The spikes in Figures C.1a and C.1c arise due to the implementation of a rebinning function during the visualisation of uncertainties, as referenced to in Section 5.5.5. Within the context of this bootstrap rebinning function, it considers these spikes to hold statistical significance and are therefore incorporates them into the smoothing process. However, the spikes are clearly unphysical as no mechanism could yield double the uncertainty between a range of just 50 GeV.

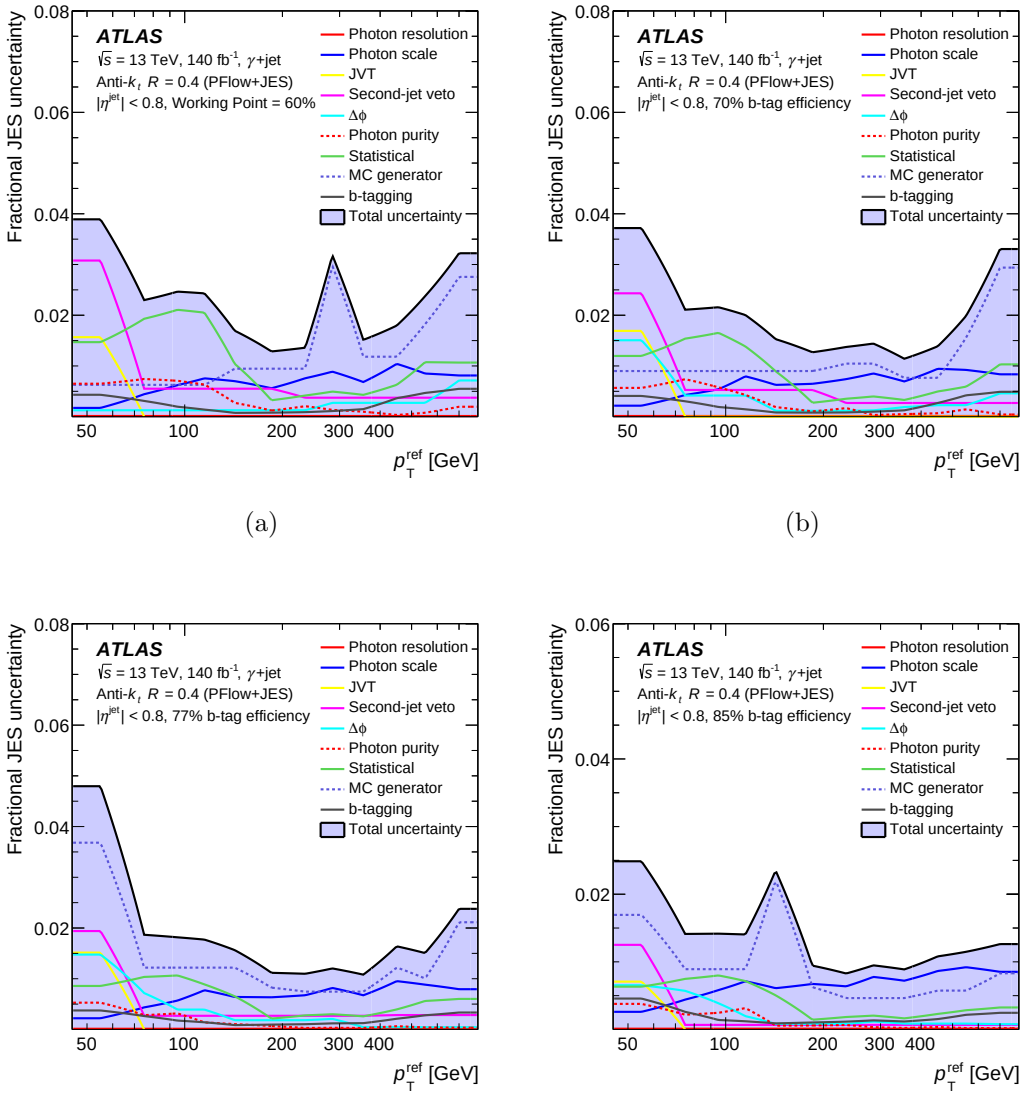


Figure C.1: Uncertainties associated with the $b$–jet direct balance JES uncertainty with PFlow+JES for $\gamma$ + jet in the range $45 \leq p_T^{ref} \leq 800$ GeV in data and MC simulation for (a) 60% and (b) 70% $b$–tagged working points and in the range $45 \leq p_T^{ref} \leq 1000$ GeV in data and MC simulation for (c) 77% and (d) 85% $b$–tagged working points.

# Appendix D

# Neutrino Effect on bJES Response

The direct balance distributions versus the number of entries between data and PYTHIA (SHERPA) between are presented in Figure D.1 (D.2). These distributions are shown for inclusive jets, and $b$–tagged jets with the 85% and 77% working points in the range $85 < p_T^{ref} < 1000$ GeV, and $b$–tagged jets with the 70% and 60% working points in the range $85 < p_T^{ref} < 800$ GeV.

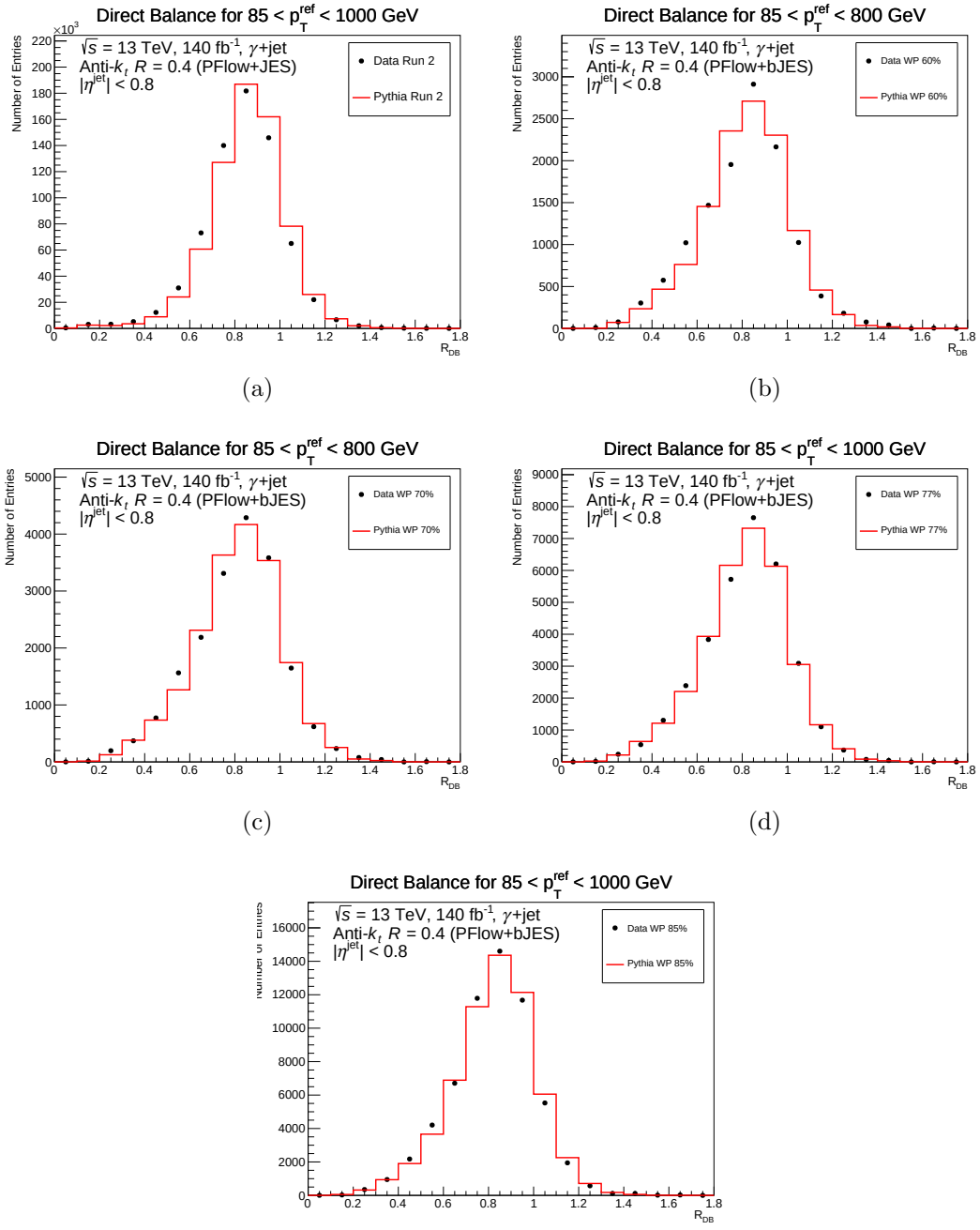


Figure D.1: The direct balance distributions of data and PYTHIA for $\gamma$+jet events in the (a) inclusive and $b$–tagged working point (b) 60%, (c) 70%, (d) 77% (e) 85% scenarios. This distribution is rebinned for all the balance response distributions in $p_T^{ref}$ bins between the range $85 < p_T^{ref} < 1000$ GeV for (a), (d), and (e), and between the range $85 < p_T^{ref} < 800$ GeV for (b), and (c),.

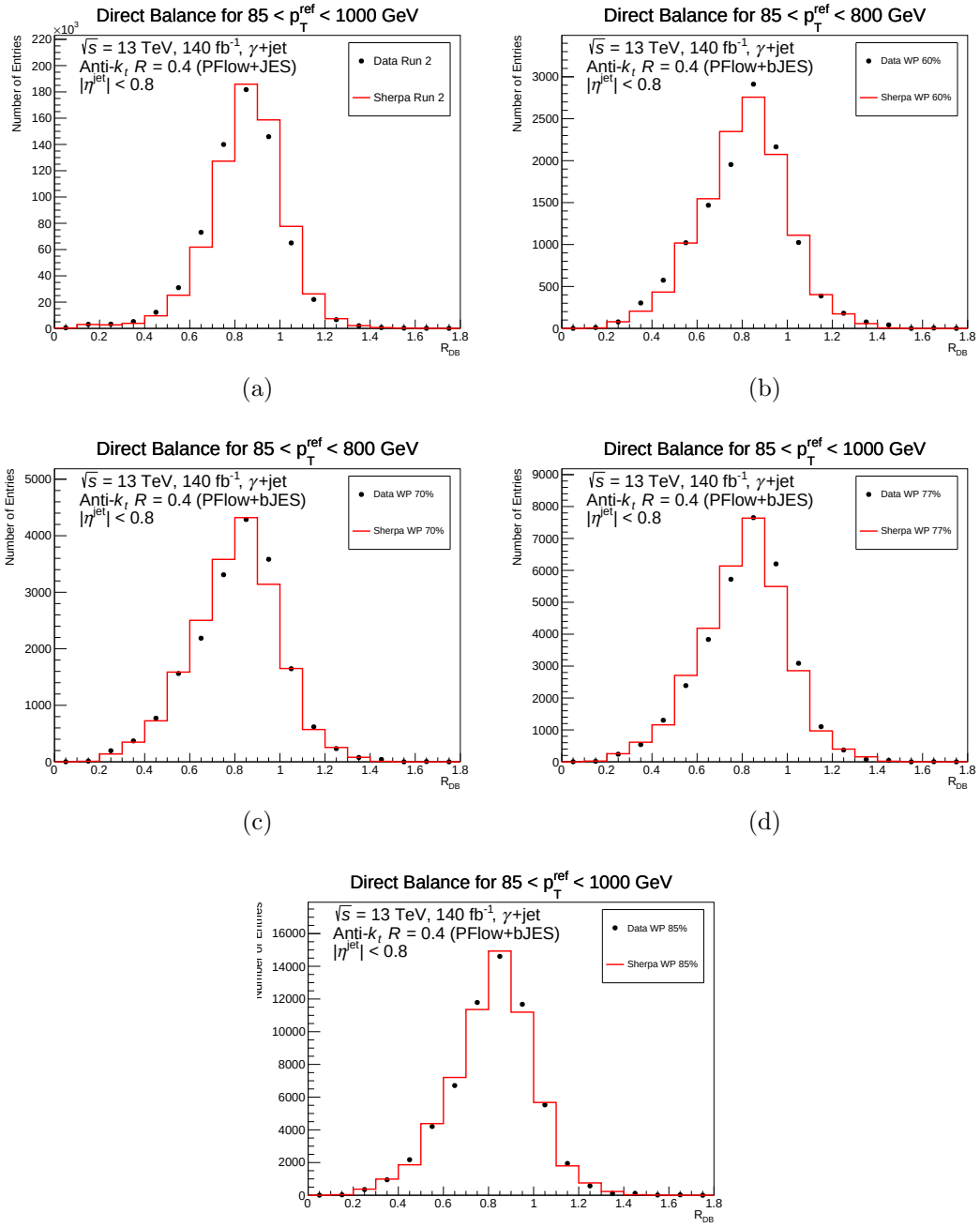


Figure D.2: The direct balance distributions of data and SHERPA for $\gamma$+jet events in the (a) inclusive and $b$–tagged working point (b) 60%, (c) 70%, (d) 77% (e) 85% scenarios. This distribution is rebinned for all the balance response distributions in $p_T^{ref}$ bins between the range $85 < p_T^{ref} < 1000$ GeV for (a), (d), and (e), and between the range $85 < p_T^{ref} < 800$ GeV for (b), and (c),.

# Resum

## El Model Estàndard

El Model Estàndard de la Física de Partícules (SM) descriu les partícules i les forces que constitueixen el nostre Univers. Les partícules en el SM es mostren en la Figura H.1 i es classifiquen en dues categories distintes: fermions i bosons. Els fermions representen la matèria de l'Univers, on interactuen amb les quatre forces fonamentals de la naturalesa: la gravetat, l'electromagnetisme (EM), la força feble i la força forta. Els bosons són els intermediaris per a la interacció entre fermions i aquestes forces. Els fermions es categoritzen en dos grups: quarks i leptons. Aquests també estan estructurats en una jerarquia de tres generacions:

- Primera Generació - quarks 'up' ($u$) i 'down' ($d$), l'electró ($e$) i el neutrí electrònic ($\nu_e$). Aquests constitueixen la matèria que forma l'Univers actualment.
- Segona Generació - quarks 'strange' ($s$) i 'charm' ($c$), el muó ($\mu$) i el neutrí muònic ($\nu_\mu$).
- Tercera Generació - quarks 'top' ($t$) i 'bottom' ($b$), el leptó tau ($\tau$) i el neutrí de tau ($\nu_\tau$).

Cadascun d'aquests quarks i leptons també tenen la seua anti-partícula que posseeix una càrrega elèctrica oposada i un nombre quàntic associat invertit. Com més alta és la generació, major és la massa de les partícules respecte al seu homòleg en la generació anterior, excepte els neutrins els quals les seues masses petites però no nul·les romanen sota determinació precisa. La partícula més pesant és el quark 'top', que és el focus principal d'aquesta tesi; conté propietats importants que poden conduir a mesuraments de més precisió del SM i a comprendre la física més enllà del Model Estàndard (BSM).

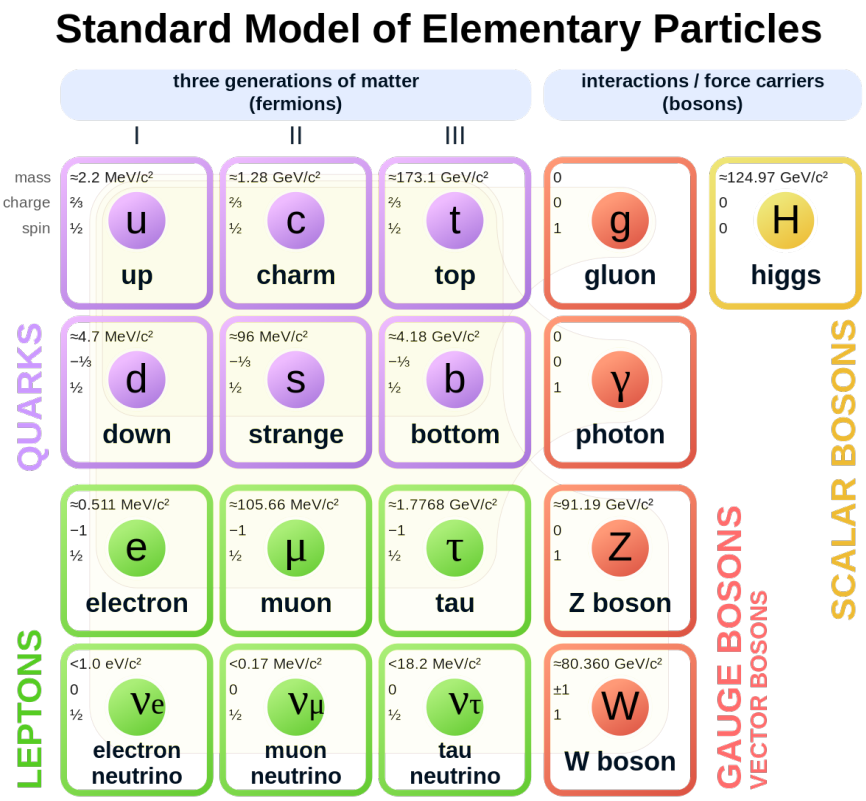


Figure H.1: Model Estàndard de Partícules Elementals [25].

Les interaccions de les partícules en el SM es descriuen a través del Lagrangià, que encapsula la dinàmica d'un sistema físic. El Lagrangià està definit com a invariable de gauge, la qual cosa significa que roman invariable sota transformacions locals. Això significa que hi ha simetries per a conservar quantitats físiques de les partícules descrites dins del Lagrangià. La base del SM es basa en el grup de simetria $SU(3)_C \otimes SU(2)_L \otimes U(1)_Y$.

Els quarks i els leptons carregats participen en interaccions electromagnètiques, que es descriuen a través d'un marc teòric conegut com a Electrodinàmica Quàntica (QED), amb fotons actuant com a bosons mediadors. Un diagrama de Feynman que representa el vèrtex QED es mostra en la Figura H.2a. Aquestes interaccions es representen pel grup de simetria $U(1)_Y$.

Tots els fermions del SM estan involucrats en interaccions febles. No obstant això, a causa de la complexitat i la naturalesa de ruptura de simetria de la força feble, aquesta ha de ser descrita en un marc més ampli conegut com la força electrodèbil (EW) que combina les forces feble i EM, representades amb el grup de simetria

$SU(2)_L \otimes U(1)_Y$. Aquesta interacció involucra els bosons massius $W^+$, $W^-$, i $Z$, juntament amb el bosó de Higgs, que és responsable d'impartir massa a les partícules. El vèrtex EW per als bosons $W$ es mostra en la Figura H.2c.

Finalment, només els quarks participen en interaccions relacionades amb la força forta. Aquestes interaccions es descriuen a través de la Cromodinàmica Quàntica (QCD), representada pel grup de simetria $SU(3)_C$, amb gluons sent els bosons responsables en aquestes interaccions. El vèrtex QCD que involucra un gluó i dos quarks s'il·lustra en la Figura H.2b. Una omissió dins del SM és la força fonamental

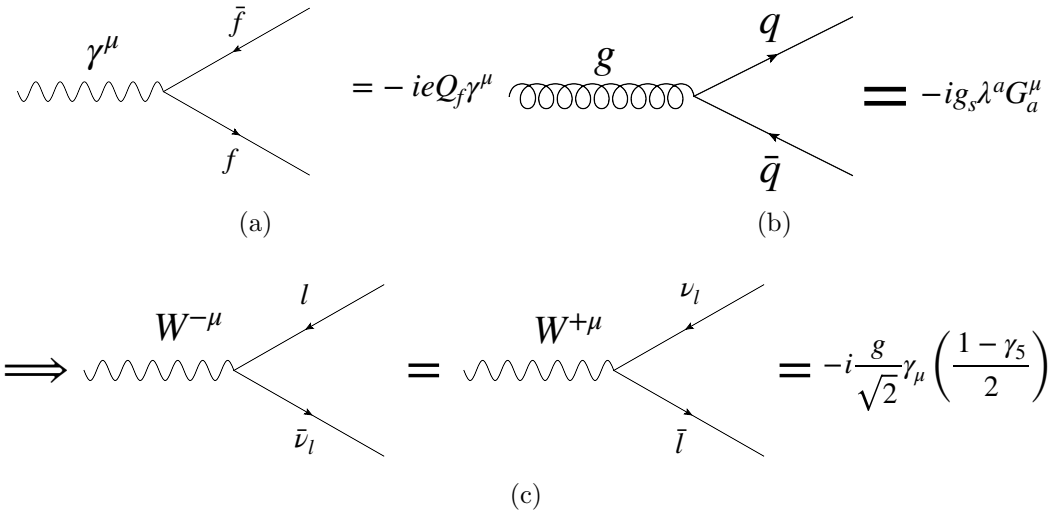


Figure H.2: Diagrames de Feynman per als vèrtexs relacionats amb les interaccions (a) QED, (b) QCD, i (c) EW.

de la gravetat a causa de la influència increïblement feble que exerceix a l'escala de la mecànica quàntica on el SM és aplicable, juntament amb la incapacitat actual de reconciliar la mecànica quàntica amb la relativitat general per a crear un marc consistent per a la gravetat quàntica.

# Acceleradors de Partícules (El LHC i ATLAS)

Un dels mètodes més efectius per a l'exploració a fons de les propietats fonamentals de les partícules i les seues interaccions és a través de l'ús d'acceleradors de partícules. Potser el més notable és el Gran Col·lisionador d'Hadrons (LHC) que destaca com el col·lisionador més potent fins a la data. El LHC està situat en un túnel circular de 26,7 quilòmetres que es troba a 100 metres sota terra, travessant

la frontera entre França i Suïssa. Dins del túnel, dos feixos de protons són corbats i accelerats a velocitats extremadament altes, ~ 99.9999991% la velocitat de la llum, amb energies que arriben fins a 6.8 TeV, usant una sèrie d'imants superconductors. Els feixos llavors són fets col·lidir en quatre punts diferents al voltant de l'anell, on es col·loquen detectors per a estudiar les partícules resultants.

La Figura H.3 il·lustra el viatge que els protons fan per a incrementar la seua energia abans d'arribar al LHC, i els subsegüents quatre punts de detecció on dipositen la seua energia. Aquesta tesi es centra principalment en el detector A Toroidal LHC ApparatuS (ATLAS), el més gran al LHC, pesant 7.000 tones i amb una longitud de 46 metres i un diàmetre de 25 metres. ATLAS és un instrument polivalent, utilitzat per a estudiar una àmplia varietat de partícules, tant hadròniques com leptòniques. Quan un detector captura l'energia d'una

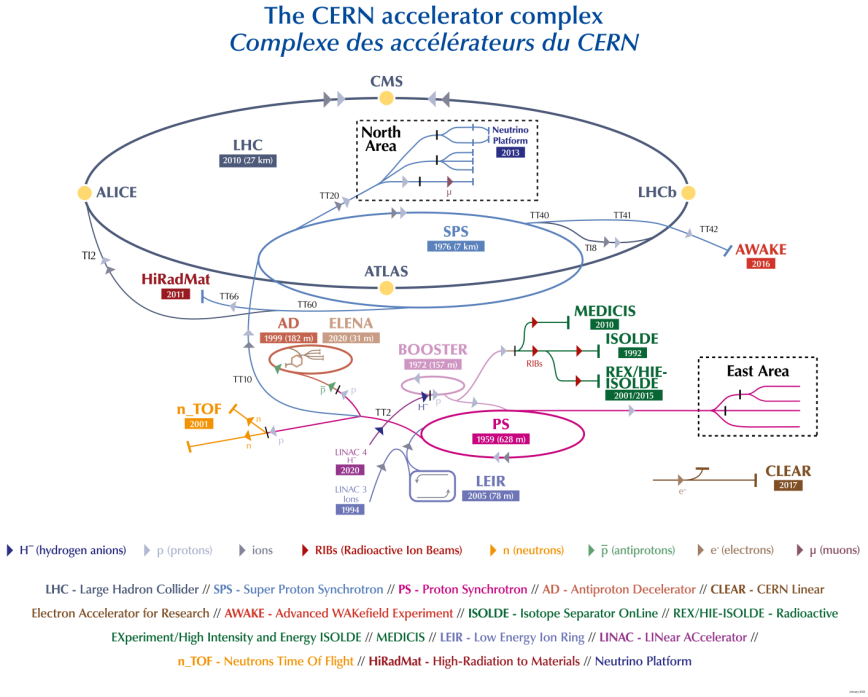


Figure H.3: Esquema del complex d'acceleradors del CERN [70].

partícula, aquesta informació es converteix en dades que els físics poden utilitzar. No obstant això, el procés d'identificació i mesura d'aquestes partícules és complex i requereix l'ús de la reconstrucció. La reconstrucció es construeix principalment a partir de signatures deixades en el detector per partícules carregades, conegudes com a trajectòries, i de punts d'interacció de les partícules, coneguts com a vèrtexs. Els neutrins no poden ser detectats en ATLAS, passant a través del detector abans

de dipositar la seua energia, però se'ls té en compte en anàlisis de física com a energia perduda, $E_T^{Miss}$.

## Simulacions Monte Carlo

Les simulacions Monte Carlo (MC) són una tècnica computacional que modela les interaccions de partícules en un col·lisionador generant un gran nombre d'esdeveniments estadísticament aleatoris. Són crucials per a corregir les mesures a un nivell on es poden comparar amb la teoria. Els generadors MC simulen cada etapa de les interaccions de partícules, com s'il·lustra en la Figura H.4. Aquestes etapes són les següents:

- Càlcul de l'Element de Matriu de Dispersió Dura: Aquesta etapa involucra càlculs pertorbatius per a determinar l'esdeveniment inicial de dispersió dura. Això és on es simula la interacció fonamental que condueix a la col·lisió o desintegració de partícules. El càlcul es basa en models teòrics i té en compte diversos factors com l'energia, el moment, i els tipus de partícules involucrades.

- Cascada de Partons, Fragmentació i Hadronització: Després de la dispersió dura inicial, la simulació procedeix a modelar les etapes subsegüents de l'esdeveniment. Això inclou la cascada de partons, on evolucionen els quarks i gluons emesos en la dispersió dura, i la fragmentació i hadronització, on aquests partons es transformen en hadrons.

- Interaccions amb el Detector (GEANT4): L'última etapa de la simulació implica modelar com les partícules generades interaccionen amb el detector. Això es realitza usant programari com GEANT4, que simula el pas de partícules a través de la matèria. Aquesta etapa té en compte diversos efectes com la pèrdua d'energia de les partícules, la dispersió, i la resolució del detector, permetent que la simulació represente acuradament com les partícules serien detectades en un experiment real.

Diversos generadors d'esdeveniments Monte Carlo estan disponibles, cadascun oferint el seu enfocament únic per simular les diverses etapes de col·lisions $pp$, des de la dispersió dura inicial fins als processos de desintegració de partícules. Aquests inclouen Pythia, que es concentra en simular les etapes de cascada de

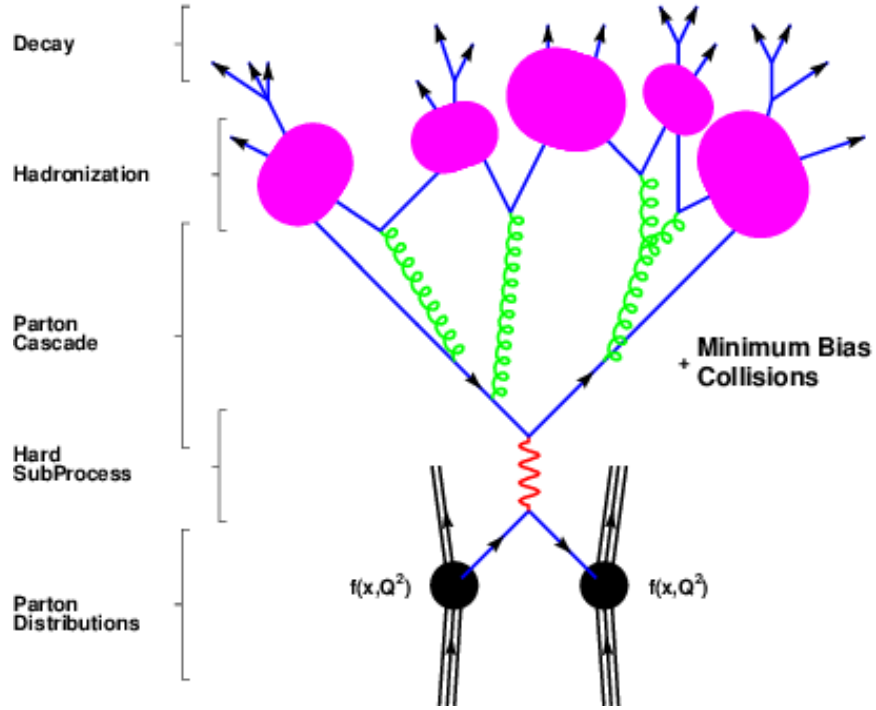


Figure H.4: L'estructura bàsica d'una col·lisió de partícules i els seus processos següents [104].

partons i hadronització amb detall, fent-lo particularment adequat per a estudis que involucren emissions més suaus i hadrons a l'estat final. Un altre és SHERPA, que és un generador d'esdeveniments MC generalitzat, que proporciona càlculs d'elements de matriu combinats amb cascades de partons.

## Calibració de jets

Dins de l'àmbit de la reconstrucció d'objectes en ATLAS, els jets juguen un paper de gran importància. Els jets es reconstrueixen a partir de l'agrupació de productes de desintegració de quarks i gluons de les interaccions *pp* inicials. Els jets s'utilitzen en la majoria de les anàlisis de dades d'ATLAS, com aquelles que se centren en mesures extremadament precises d'observables de partícules conegudes actualment, o la cerca de nous observables que encara no estan predits pel SM.

No obstant això, els jets enfronten una sèrie de problemes, com ara biaixos i degradació en el detector o senyals superposats de múltiples col·lisions *pp* que ocorren simultàniament dins de la mateixa àrea, conegut com a acumulació (pile-

up). Això requereix un procés de calibració per als jets abans que es passen a les anàlisis de física. El procés principal en ATLAS és la calibració de l'escala d'energia dels jets (JES), amb els passos individuals mostrats en la Figura H.5. Aquesta calibració s'utilitza per a determinar acuradament l'energia dels jets i corregir per les fonts d'incertesa que poden afectar les mesures amb aquests jets. Cada etapa se centra a corregir una part específica de les característiques dels

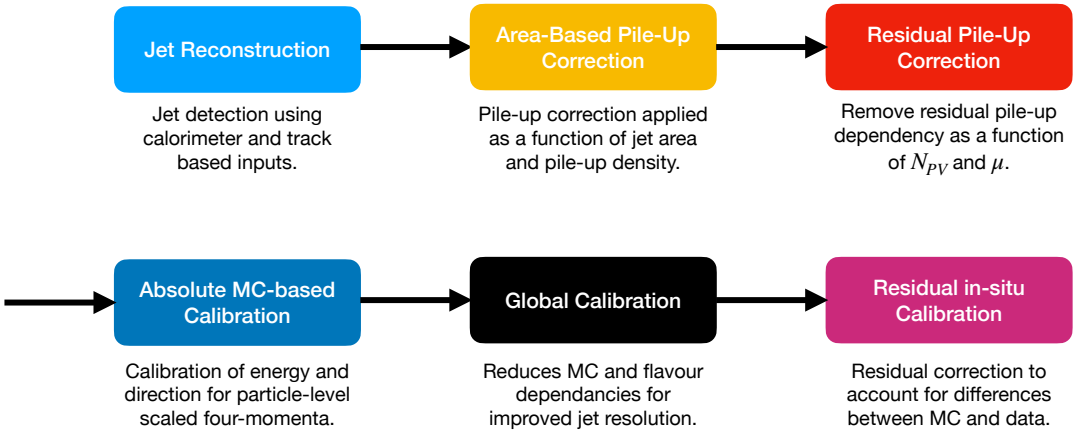


Figure H.5: Etapes de la cadena de calibració JES.

jets. Les primeres dues compten per a l'acumulació esmentada i minimitzen el seu impacte en el jet. La següent és la correcció absoluta basada en MC que ajusta el quadrimoment reconstruït d'un jet a l'escala d'energia de jets a escala de partícules calculats en simulacions MC. Això té en compte factors com les respostes del calorímetre, pèrdues d'energia en material mort en el detector, i efectes de radiació fora del con. A continuació és l'etapa de calibració global que intenta limitar la diferència en jets iniciats per gluons o quarks de diferents sabors. Això es deu al fet que els jets iniciats per quarks tenen respostes diferents depenent dels quarks involucrats i tenen respostes molt diferents dels jets iniciats per gluons.

Finalment, és la calibració residual in-situ que té en compte la diferència entre les dades i la simulació després que tots els passos previs de la cadena de calibració s'hagen realitzat. Aquestes diferències es deuen a una simulació imperfecta a causa de falles en el detector o inexactituds en modelar certs processos físics. Per a corregir això, s'ha d'aplicar una correcció basada en dades. Això es calcula a partir de mesuraments del balanç basat en $p_T$ entre un jet i un objecte de

referència ben calibrat. Les respostes de $p_T$ s'ajusten en intervals de l'objecte de referència amb una funció gaussiana i la correcció es dona com a una doble ràtio entre dades i MC:

$$\frac{1}{c} = \frac{R^{Data}_{in-situ}}{R^{MC}_{in-situ}} \tag{H.1}$$

Els processos utilitzats en la calibració in-situ són di-jets, fotó+jet, Z+jet, i multi-jet; que s'il·lustren en la Figura 5.5. Una combinació estadística de ràtios data-a-MC de les mesures de resposta s'utilitza per a aplicar una correcció exclusivament a les dades.

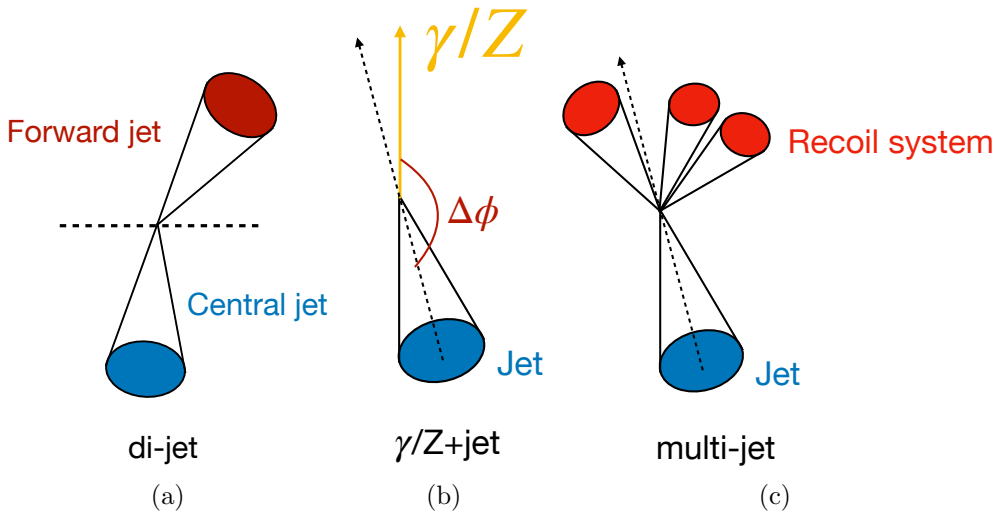


Figure H.6: Diagrames de balanç per a (a) di-jet, (b) $\gamma$/Z+jet, i (c) esdeveniments multi-jet, que s'utilitzen en la calibració residual in-situ

Una nova tècnica desenvolupada per a la part in-situ de la calibració és la inclusió de la calibració de l'escala d'energia de b-jets (bJES) amb $\gamma$+jets. Aquesta calibració compara la resposta entre fotons i jets que inclou tota la gamma d'informació de quarks disponible (que anomenarem jets inclusius) i la resposta entre fotons i $b$–jets (que anomenarem jets $b$–etiquetats). Això permet l'estudi centrar-se en els efectes del detector i simulació en $b$–jets, així com la diferència en com es desenvolupen $b$–jets i jets inclusius en MC en ATLAS.

Els quarks $b$ són una part extremadament important d'ATLAS, ja que són el canal a través del qual el quark top, $t \to Wb$, i el bosó de Higgs, $H \to bb$, es desintegren principalment. Això significa que la comprensió de $b$–jets és crucial, especialment quan s'aplica a mesures de precisió i cerques BSM.

Ja que, en dades, no podem saber exactament quins jets provenen de quarks $b$,

hi ha una tècnica d'identificació de b-jets utilitzada en ATLAS coneguda com a $b$–etiquetatge. Aquesta és un algoritme basat en xarxes neuronals multivariades que combina informació de diferents fonts per a identificar quins jets probablement provenen de la desintegració d'un quark $b$.

El $b$–etiquetatge implementa l'ús d'eficiències, que defineixen quin percentatge de jets en la mostra es consideren com a $b$–jets i la quantitat d'estadístiques que tenen. Hi ha 4 eficiències diferents, donades com a 60%, 70%, 77%, i 80%. Com més baixa és l'eficiència, major és la puresa de quark $b$ de la mostra, però menys estadístiques. Així, hi ha un equilibri a aconseguir.

La tècnica bJES pren el factor de correcció en l'Equació H.8, per a respostes de les mostres de jets $b$–etiquetats i inclusius que utilitzen mostres MC de Pythia 8 i Sherpa 2.2.2. La diferència entre la correcció JES es pren llavors com un observable anomenat $\tilde{R}_{bJES} = \frac{c_{b-tagged}}{c_{inclusive}}$. Aquest observable ens mostra la diferència entre el JES en els esdeveniments $b$–etiquetats i els esdeveniments inclusius.

La Figura H.7 mostra $\tilde{R}_{bJES}$ com a funció del moment transversal del fotó de referència per a les diferents eficiències de $b$–etiquetatge esmentades anteriorment. Hi ha un consens comú entre tots els punts en els gràfics que l'energia del $b$–jet és subestimada en comparació amb l'energia del jet inclusiu. Quan aquests valors són mitjanitzats sobre el rang de $p_T^{ref}$, es conclou que el bJES està subestimat entre un 1% i un 3.4% depenent de l'eficiència i del generador MC que s'està avaluant.

Aquests valors suggereixen que l'actual cadena de calibració JES en ATLAS no és suficientment suficient per a poder calibrar $b$–jets que seran utilitzats en anàlisis. Ja que les mesures de precisió depenen molt dels $b$–jets, si no estan ben calibrats, podria tindre un efecte en les mesures finals, com les utilitzades per a la massa del quark top. Una solució a això és una cadena de calibració JES dedicada específicament per a $b$–jets que s'aplica a anàlisis que requereixen l'ús de $b$–jets.

# El Quark Top

El quark top és el quark més pesant en el Model Estàndard. És l'únic fermió que no passa per l'hadronització, ja que la seua vida útil és inferior al temps que tarda a ocórrer l'hadronització, la qual cosa ens dona una oportunitat única per a estudiar les propietats d'un quark lliure.

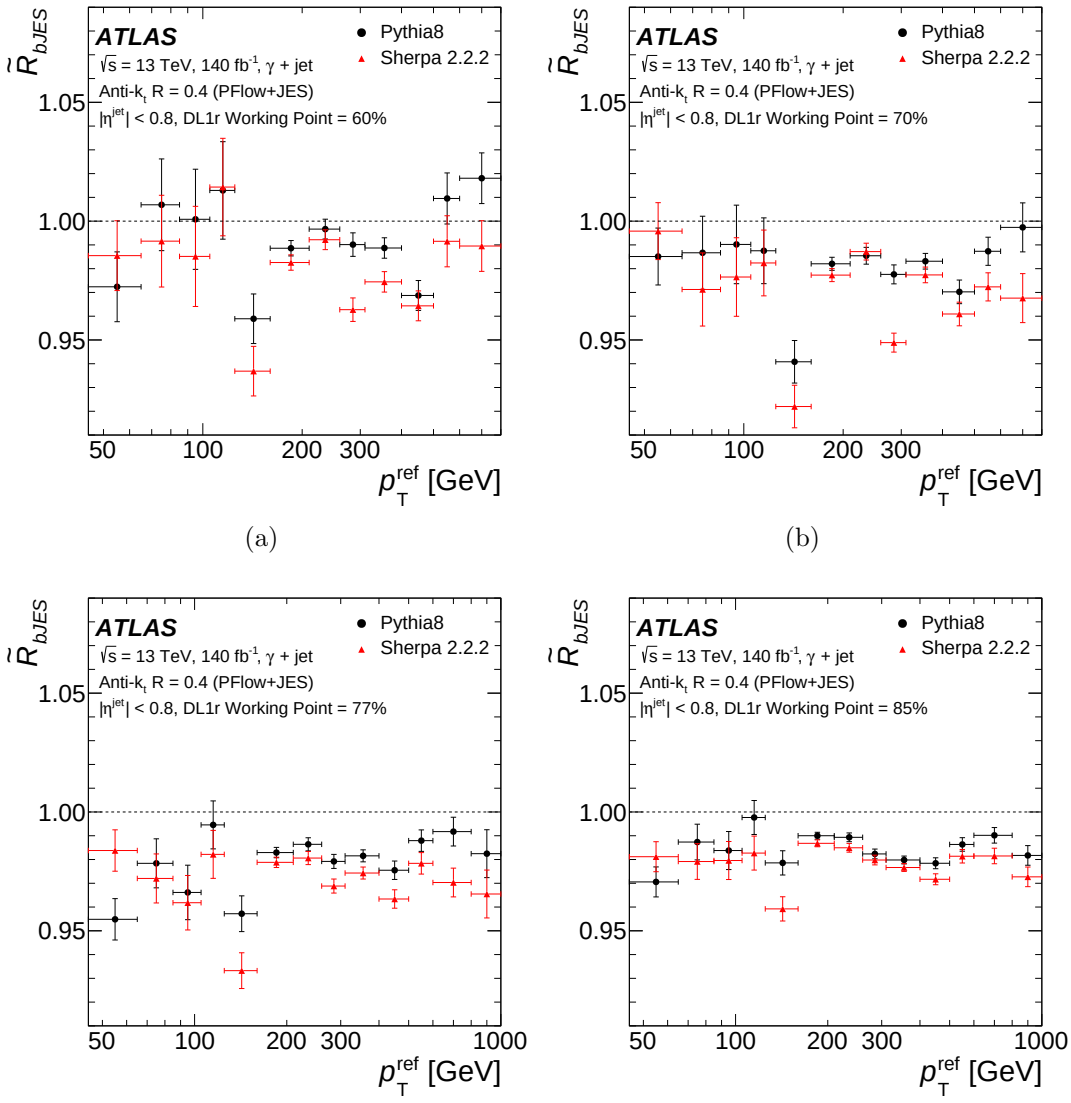


Figure H.7: $\tilde{R}_{\mathrm{bJES}}$ com a funció del moment transversal del fotó de referència determinat usant o bé Pythia 8 o Sherpa per a un punt de treball de l'algoritme de $b$–etiquetatge amb una eficiència de (a) 60%, (b) 70%, (c) 77% i (d) 85%. Les barres d'error corresponen a les incerteses estadístiques.

La probabilitat que el quark top es desintegre en partícules més lleugeres es coneix com la fracció de desintegració del quark top. La fracció de desintegració en el canal més comú, $t \to Wq$, es defineix com:

$$\mathcal{B}(t \to Wq) = \frac{\Gamma(t \to Wq)}{\Gamma_t} = \frac{|W_{tq}|^2}{|V_{tb}|^2 + |V_{ts}|^2 + |V_{td}|^2}, \tag{H.2}$$

on q són els quarks de tipus 'down' en els quals el quark top té permís per desintegració ($b$, $s$, $d$). El top es desintegra via el canal $b$ amb més freqüència, la qual cosa porta a un valor de fracció de desintegració de $\mathcal{B}(t \to Wb) = 0.957 \pm 0.034$. Això destaca la importància dels quarks $b$ i el $b$-tagging en anàlisis com les mesures de precisió del quark top.

Pel fet que el quark top es desintegra en el canal Wb gairebé el 100% del temps, l'estat final format per parells de quarks top es classifica segons els modes de desintegració dels bosons W. Això consta de tres categories: di-leptònic, semi-leptònic, i completament hadrònic. Els diagrames de Feynman per a cada mode de desintegració es mostren en la Figura H.8. Encara que el canal di-leptònic ocorre menys freqüentment a causa de la seua menor fracció de desintegració, és experimentalment el més pur a causa de la detecció directa dels leptons en l'estat final. El mode de desintegració completament hadrònic, per altra banda, té una fracció de desintegració més alta, però està fortament contaminat pel fons de multi-jets QCD. El canal semi-leptònic exhibeix característiques que estan a mig camí entre els altres dos, oferint un bon compromís entre la puresa del canal di-leptònic i les estadístiques més altes del canal completament hadrònic.

Els quarks, a causa de la força forta, experimenten un fenomen anomenat confinament de quarks quan es troben a grans distàncies l'un de l'altre, i el seu valor de l'acoblament, $\alpha_s$, és gran, fent impossible separar els quarks. No obstant això, a altes energies (distàncies més petites) $\alpha_s$ és petit i els quarks es poden tractar com a partícules lliures; això es coneix com a llibertat asimptòtica. A aquestes altes energies, s'utilitza la QCD pertorbativa, que empra una expansió en sèrie en termes de $\alpha_s$ per descriure processos de QCD quan les interaccions es debiliten a majors energies. No obstant això, en ordre superior en teoria de la pertorbació, poden sorgir infinitats a partir de bucles tancats, que porten a divergències. Mitjançant esquemes de renormalització, s'introduïxen termes a $\alpha_s$ per a combatre aquestes divergències.

Pel que fa a la massa del quark top hi ha tres esquemes de renormalització que

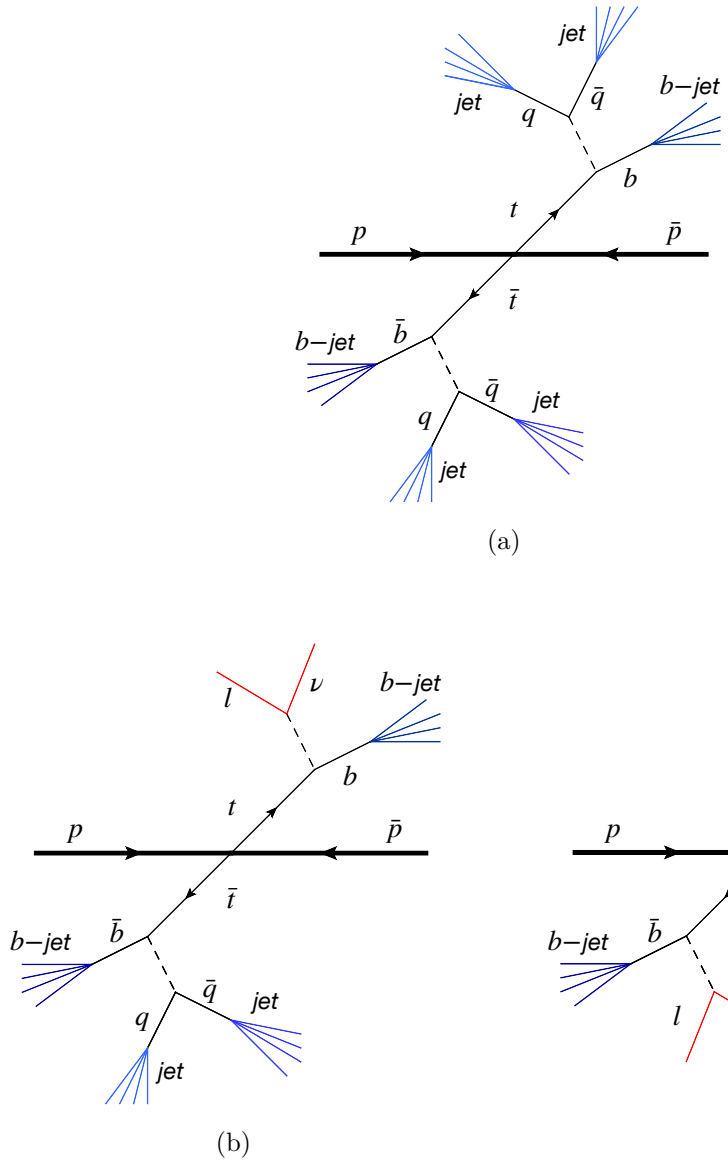


Figure H.8: Diagrames de Feynman per als processos de decaïment del quark top a través dels canals (a) completament hadrònic, (b) semi-leptònic, i (c) di-leptònic.

es discuteixen en aquesta tesi: la massa de pol $m_t^{pole}$, la massa $\overline{\text{MS}}$ $\bar{m}_t$, i la massa MSR $m_t^{MSR}$.

La massa de pol tracta la massa del quark top com una partícula lliure, corresponent a la massa del quark top tal com apareix en amplituds de dispersió a escala de partons. La massa $\overline{\text{MS}}$ és un paràmetre de massa de curta distància i dependent de l'escala. És efectiva per a processos d'alta energia on l'escala d'energia, $Q$, és més gran que $m_t$. Finalment, la massa MSR és una continuació de la massa $\overline{\text{MS}}$, en termes de ser dependent de l'escala (amb l'escala R) i de

curta distància però per a processos on $Q \leq m_t$. S'utilitza per a proporcionar una interpolació suau, com es mostra en la Figura H.9, des de $m_t(R = m_t)$ (on comença $\bar{m}_t$) fins a $m_t(R = 0)$ (on està situada la $m_t^{pole}$).

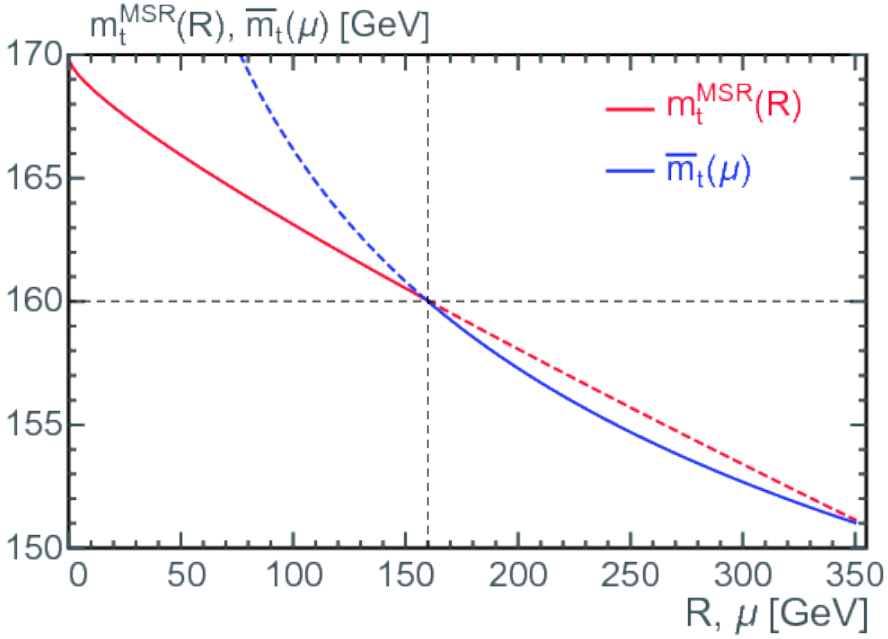


Figure H.9: Comparació de la dependència d'escala per a les masses del quark top $\overline{\text{MS}}$ i MSR com a funció de $\mu$ i $R$ en GeV, amb $m_t = 160$ GeV [206].

Quan es tracta de mesuraments de la massa del quark top, hi ha dues categories principals: directes i indirectes.

Els mesuraments directes de la massa del quark top utilitzen els productes de desintegració i els observables cinemàtiques del quark top quan es desintegra, principalment en un bosó W i un quark $b$. Aquestes desintegracions produeixen patrons de ressonància distintius i punts finals en les distribucions de massa que són inherentment sensibles a la massa del quark top. Aquests mesuraments es basen en plantilles a escala de detector creades per generadors MC, no es poden fer servir prediccions de primer principi per a aquests observables. Els mesuraments directes són més sensibles a la massa del quark top en si, però els detalls de les seues formes i la precisió de les seues ubicacions també estan modelades per la dinàmica QCD i EW subjacent a escales d'energia inferiors a la massa del quark top. D'altra banda, els mesuraments indirectes empren mesures de secció transversal inclusives i diferencials, $\sigma_{t\bar{t}}$, per a extraure la massa del quark top. Els mètodes indirectes tenen sensibilitat només del hard-scatter, la qual cosa significa

que la sensibilitat d'aquests mesuraments de massa és a escales iguals o superiors a la massa del quark top.

## Interpretació de la Massa del Quark Top

Quan es consideren els mesuraments directes de la massa del quark top, els generadors MC han aconseguit un alt nivell d'exactitud en descriure les dades, particularment en el límit d'energia suau-col·lineal, $\approx$ 1 GeV, típic per a les cascades de partons. Això suggereix que els generadors MC són prou efectius en capturar característiques importants de la QCD. No obstant això, hi ha una ambigüitat inherent en interpretar els mesuraments de massa directes dins d'un esquema de renormalització teòric de camps. Això es pot reduir a través d'estudis de 'calibració' dedicats. L'aproximació d'interpretació de la massa del quark top prova la relació entre el paràmetre de massa MC, $m_t^{MC}$, i l'esquema de massa utilitzat en aquests càlculs.

L'anàlisi principal d'aquesta tesi se centra en la interpretació de la massa del quark top MC, $m_t^{MC}$, dins del context de l'esquema MSR. La tècnica per a determinar la massa del quark top implica la reconstrucció dels productes de desintegració del quark top. Ací, l'enfocament està en quarks top impulsats, on els productes de desintegració es col·limen en un únic jet gran-R. La jerarquia cinemàtica per aquest mètode és $Qgt; gt; m_t gt; gt; \Gamma_t$. Aquest gran buit en la jerarquia estableix una clara distinció entre els processos relacionats amb la desintegració del quark top i els processos de QCD de menor energia. A més, a causa de l'estat impulsat dels quarks top, això permet una anàlisi inclusiva de la desintegració del quark top, capturant efectivament tots els productes de desintegració dins del jet gran-R.

Es requereix que el jet passe per un condicionament soft-drop (SD), per a eliminar efectivament la contaminació suau del jet sense alterar significativament les propietats del jet relacionades amb la massa del quark top.

La massa del jet gran-R impulsat i condicionat pot ser definida sumant sobre els constituents que romanen dins del jet, $\mathcal{J}_{SD}$:

$$M_J^2 = (\sum_{i \in \mathcal{J}_{SD}} p_i^\mu)^2 \cong m_t^2 + \Gamma_t m_t + ... \tag{H.3}$$

Aquesta regió de pic del jet on la sensibilitat a la massa del quark top sorgeix, significa que la posició del pic de la massa del jet pot servir com a indicador per

a deduir el valor de $m_t$.

Per a aquesta anàlisi, es generen histogrames de referència amb PYTHIA 8 en diverses bines de $p_T$ del jet, amb un nombre igual d'esdeveniments en cada interval.

Llavors són necessàries plantilles teòriques per a ajustar-se a les plantilles MC. Aquestes distribucions teòriques es caracteritzen cadascuna pels seus valors únics de paràmetres, $m_t^{MSR}$, $\Omega_1^{\circ\circ}$, i $x_2$. L'objectiu és identificar el conjunt de paràmetres que produeix una distribució de massa del jet més compatible amb el Monte Carlo observat.

En la teoria, la funció de forma no pertorbativa $F_q^{\circ\circ}$, descriu els aspectes no pertorbatius de la formació del jet. Les correccions no pertorbatives de potència principal per a la funció de forma es donen pel primer moment $\Omega_{1q}^{\circ\circ}$, i les correccions de potència d'ordre superior es donen per un paràmetre anomenat $x_2$:

$$\Omega_{1q}^{\circ\circ} = \int_0^\infty dk k^+ F_{1p}^q(k) \tag{H.4}$$

$$x_2 = \frac{\Omega_{2q}^{\circ\circ}}{(\Omega_{1q}^{\circ\circ})^2} - 1 \tag{H.5}$$

En el procediment d'ajust, $m_t^{MSR}$, $\Omega_{1q}^{\circ\circ}$, i $x_2$ s'extrauen simultàniament en una graella 3D. L'impacte dels tres paràmetres s'il·lustra en la Figura H.10. Específicament, la Figura H.10a demostra com les variacions en $m_t^{MSR}$ influencien la distribució: mentre que la forma general roman consistent, la corba experimenta un moviment corresponent al desplaçament en el pic de la massa del jet. Els efectes de $\Omega_{1q}^{\circ\circ}$ i $x_2$ es mostren en les Figures H.10b i H.10c, respectivament. Aquests paràmetres provoquen un lleuger desplaçament en el pic i variacions més pronunciades en les cues de la distribució. Notablement, $\Omega_{1q}^{\circ\circ}$ impacta predominantment tant les cues inferiors com superiors, mentre que $x_2$ afecta principalment la cua inferior. $x_2$ té una influència lleugerament menys significativa que $\Omega_{1q}^{\circ\circ}$ en les cues i té l'efecte menys significatiu en la distribució de la massa del jet dels tres paràmetres.

A més de determinar els valors per a cadascun d'aquests paràmetres, hi ha incerteses dins de l'anàlisi que cal abordar. El primer conjunt d'incerteses sorgeix de la metodologia d'ajust. L'estratègia és concentrar l'ajust al voltant del pic de la distribució de massa del jet, on la sensibilitat a la massa del quark top és més alta. Per tant, es fixen límits en la distribució de massa del jet per acomodar aquest enfocament. No obstant això, alguns processos físics subjacents

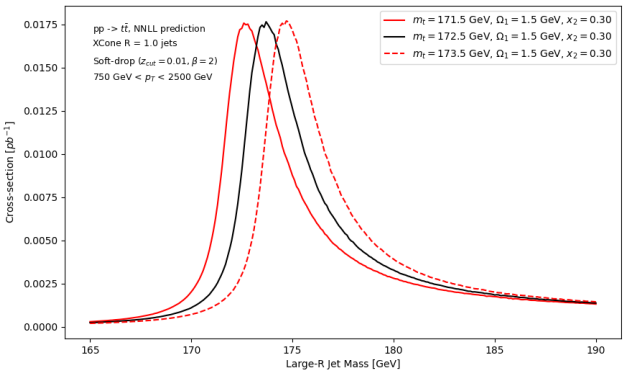


(a)

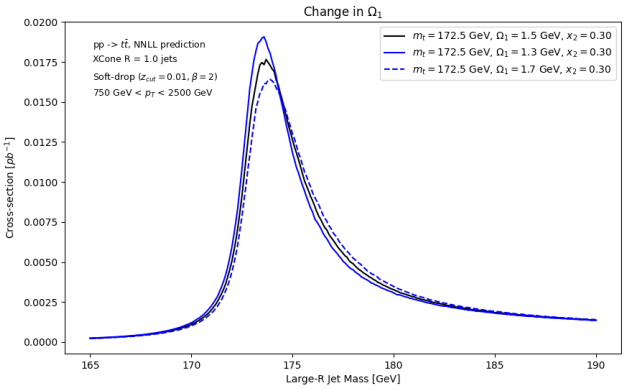


(b)

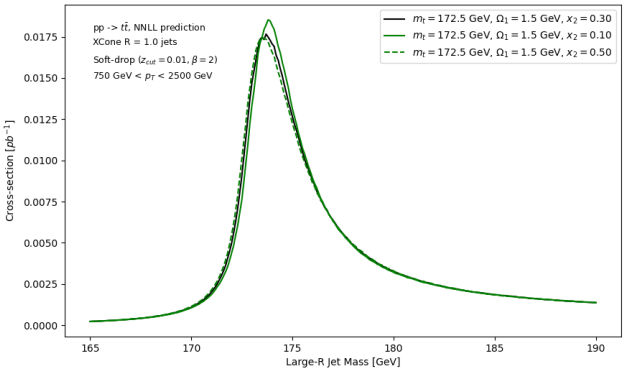


(c)

Figure H.10: Els efectes dels paràmetres (a) $m_t^{MSR}$, (b) $\Omega_1^{\circ\circ}$, i (c) $x_2$ en distribucions de massa del jet de quark top gran-R. La mostra nominal es pren amb els valors $m_t^{MSR}$ = 172.5 GeV, $\Omega_1^{\circ\circ}$ = 1.5 GeV, i $x_2$ = 0.30, com es mostra amb les corbes negres. Les variacions es consideren amb ± 1 GeVper a $m_t^{MSR}$, ± 0.2 GeVper a $\Omega_1^{\circ\circ}$, i ± 0.20 per a $x_2$.

que podrien influir en les cues inferiors de la distribució no estan inclosos en el càlcul. En conseqüència, si el límit establit es modifica, pot impactar en el resultat final. Com a resultat, s'associa una incertesa amb l'efecte que qualsevol canvi en el límit podria tindre sobre el valor de $m_t^{MSR}$.

A continuació estan les incerteses relacionades amb l'esdeveniment subjacent (UE). L'UE abasta tota l'activitat addicional que ocorre en conjunció amb processos de dispersió dura a baixa energia. Típicament, aquests processos són dispersió de gluons com $gg \to gg$. L'UE pot afectar la distribució general de la massa del jet i, encara que gran part d'això s'elimina mitjançant el condicionament SD, encara existeix certa UE en la distribució. El càlcul actualment no té en compte l'UE, així que s'estima una incertesa a través de Pythia comparant la mostra MC que utilitzem amb mostres que inclouen diferents prescripcions relacionades amb l'UE, i prenent els desplaçaments de massa de MSR d'aquesta estimació.

Finalment, hi ha incerteses teòriques que compten per a correccions d'alta precisió que no formen part de la prescripció teòrica usada en l'anàlisi. Aquestes incerteses es redueixen quan la precisió del càlcul es torna més alta. La millora de la precisió d'aquesta anàlisi és evident en la Figura 8.9, que presenta una comparació costat a costat de les corbes de variació de l'escala teòrica, normalitzades a la corba nominal. Els resultats actuals es mostren en la Figura H.11a i els resultats previs per a una anàlisi similar amb un càlcul de menor precisió es mostren en la Figura H.11b. La disminució en els valors de les incerteses és evident quan s'examina l'embolcall sobre les variacions d'escala, i els panells inferiors que ressalten la diferència entre les variacions i el nominal.

Finalment, les conclusions clau de l'anàlisi es resumixen de la següent manera:

$$\begin{aligned} m_t^{MSR}(R = 3\ \text{GeV}) &= 171.78 \pm 0.03\ \text{GeV}, \\ \Omega_1^{\circ\circ} &= 1.96 \pm 0.01\ \text{GeV}, \\ x_2 &= 0.38 \pm 0.02\ \text{GeV}, \end{aligned} \tag{H.6}$$

on la incertesa associada correspon a la incertesa estadística a causa de la mostra limitada de MC.

D'aquests resultats, establim la següent relació:

$$m_t^{MC} = m_t^{MSR}(R = 3\ \text{GeV}) + 720^{+285}_{-330}\ \text{MeV}, \tag{H.7}$$

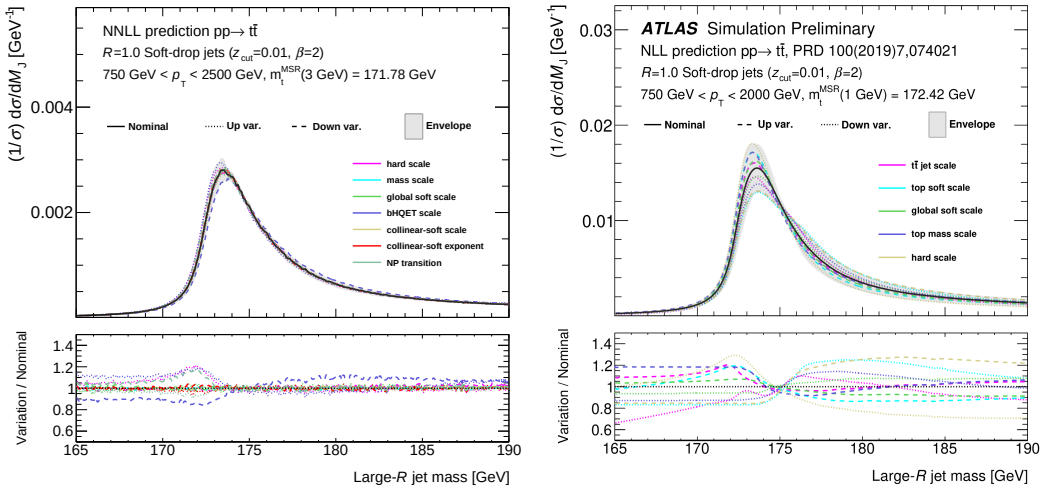


(a) (b)

Figure H.11: La (a) NNLL i (a) NLL [223] predicció de la distribució normalitzada de la massa del jet a nivell de partícules per a jets gran-R acondicionats amb una desintegració de quark top hadrònic impulsat (representat per una línia negra). Les variacions en les escales del càlcul es mostren amb línies de colors, amb les variacions cap amunt (avall) corresponents a línies de ratlla (punt). Cada corba està normalitzada per a tenir la mateixa àrea dins de l'interval de massa del jet de 172.5-180 GeV. La banda grisa il·lustra l'interval cobert per totes les variacions d'escala.

on els valors de incertesa associats corresponen a la suma en quadratura de les incerteses teòriques, incerteses de metodologia, i incerteses de l'UE.

En la Figura H.12, es mostra l'evolució de la massa MSR amb el seu valor de renormalització, R. Els punts en la corba mostren la compatibilitat d'aquesta anàlisi amb anàlisis anteriors del mateix tipus, per a diferents tipus de col·lisions i/o per a diferents nivells de precisió del càlcul. Els resultats previs només es van estudiar respecte a R = 1 GeV, així que aquesta és l'àrea de comparació. Això mostra que, dins de les incerteses dels resultats, aquesta anàlisi està en línia amb aquelles que es van trobar anteriorment.

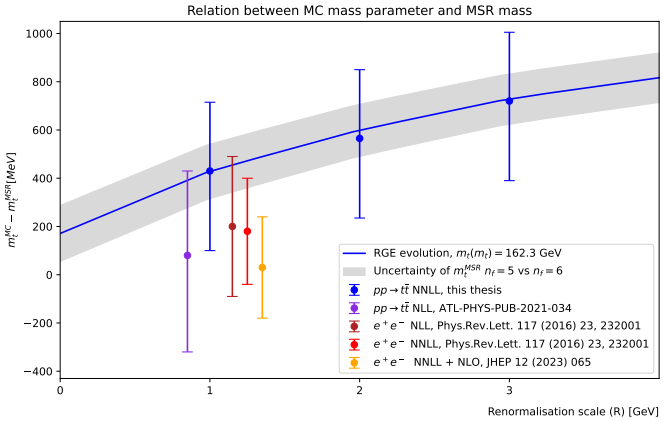


Figure H.12: Evolució de R per a la relació de massa $\Delta_t^{MSR} = m_t^{MC} - m_t^{MSR}(R)$, amb $m_t(m_t)$ = 162.3 GeV. Els punts representen els resultats de la relació de masses i les seues incerteses de l'anàlisi d'aquesta tesi (punts blaus), i de Ref. [223] (punt verd), Ref. [219] (punt morat), i Ref. [221] (punt roig). La banda grisa mostra la incertesa relacionada amb la corba d'evolució de R.

# Summary

## Standard Model

The Standard Model of Particle Physics (SM) describes the particles and the forces that make up our Universe. The particles in the SM are displayed in Figure H.1 and are classified in two distinct categories: fermions and bosons. Fermions represent the matter in the Universe, where they interact with the four fundamental forces of nature: gravity, electromagnetism (EM), the weak force, and the strong force. Bosons are the intermediaries for the interplay between fermions and these forces. Fermions are categorised in two groups: quarks and leptons. These are also structured into a hierarchy of three generations:

- First Generation - up ($u$) and down ($d$) quarks, the electron ($e$), and the electron neutrino ($\nu_e$). These constitute the matter that makes up the Universe currently.

- Second Generation - strange ($s$) and charm ($c$) quarks, the muon ($\mu$), and the muon neutrino ($\nu_\mu$).

- top ($t$) and bottom ($b$) quarks, the tau ($\tau$) lepton, and the tau neutrino ($\nu_\tau$).

Each of these quarks and leptons also have their own anti-particle that possesses an opposing electric charge and a reversed associated quantum number. The higher the generation becomes, the higher the mass of the particles to their respective counterpart in the previous generation, except neutrinos whose small yet non-zero masses remain under precise determination. The heaviest particle is the top quark, which is the main focus of this thesis; it contains important properties that can lead to greater precision measurements of the SM and to understanding physics that is beyond the Standard Model (BSM).

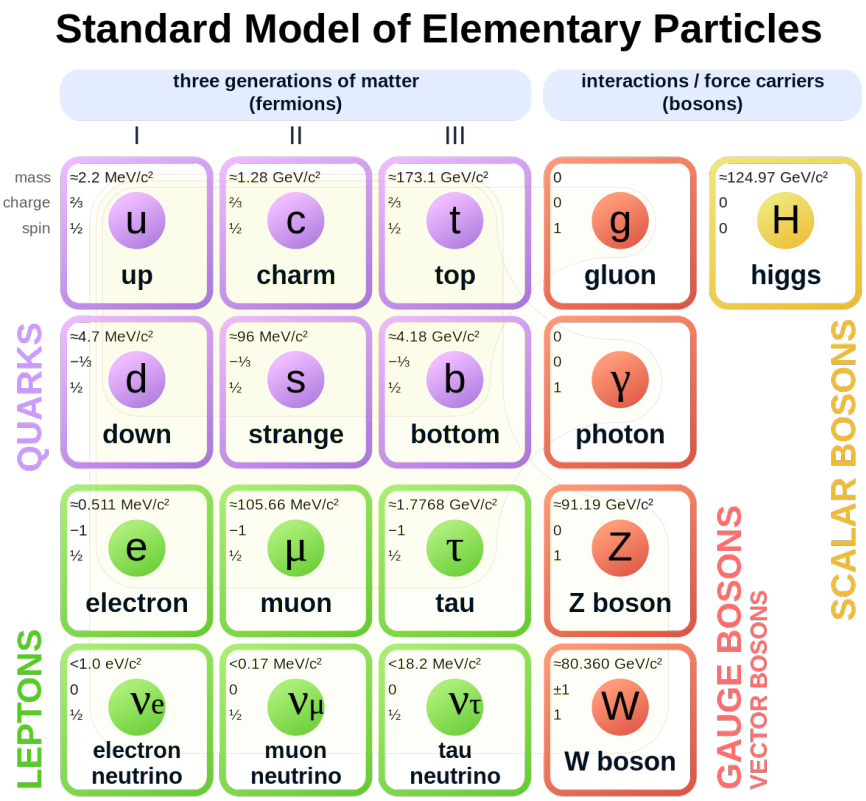


Figure H.1: Standard Model of Elementary Particles [25].

The interactions of the particles in the SM are described through the Lagrangian, which encapsulates the dynamics of a physical system. The Lagrangian is known as gauge invariant, which means it remains invariant under local transformations. This means that there are symmetries in order to conserve physical quantities of the particles described within the Lagrangian. The foundation of the SM relies on the symmetry group $SU(3)_C \otimes SU(2)_L \otimes U(1)_Y$.

Quarks and charged leptons both take part in electromagnetic interactions, which are described through a theoretical framework known as Quantum Electrodynamics (QED), with photons acting as the mediating bosons. A Feynman diagram representing the QED vertex is depicted in Figure H.2a These interactions are represented by the symmetry group $U(1)_Y$.

All the fermions of the SM are involved in weak interactions. However, due to the complexity and symmetry breaking nature of the weak force, it must be described in a broader framework known as the electroweak (EW) force that combines the weak and EM forces together, represented with the symmetry group

$SU(2)_L \otimes U(1)_Y$. This interaction involves massive $W^+$, $W^-$, and Z bosons, along with the Higgs boson, which is responsible for imparting mass to particles. The EW vertex for both the W bosons are shown in Figure H.2c.

Lastly, only quarks join in with interactions related to the strong force. These interactions are described through Quantum Chromodynamics (QCD), represented by the $SU(3)_C$ symmetry group, with gluons being the responsible bosons in these interactions. The QCD vertex involving a gluon and two quarks is illustrated in Figure H.2b. One omission within the SM is the fundamental force

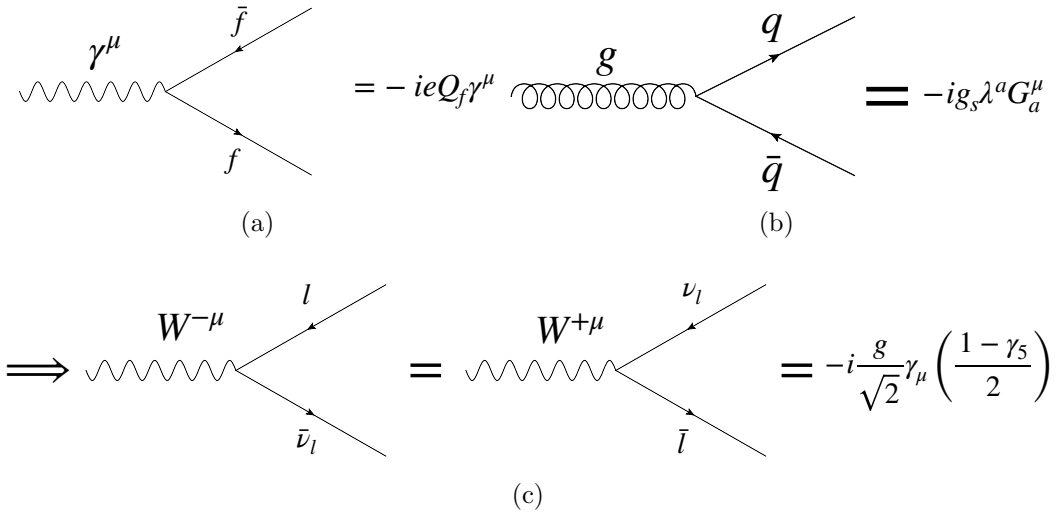


Figure H.2: Feynman diagrams for the vertices related to (a) QED, (b) QCD, and (c) EW interactions.

of gravity due to the incredibly weak influence it exerts at the quantum mechanic scale where the SM is applicable, along with the current inability to reconcile quantum mechanics with general relativity to create a consistent framework for quantum gravity.

# Particle Accelerators (The LHC and ATLAS)

One of the most effective methods for the in-depth exploration of the fundamental properties of particles and their interactions is through the use of particle accelerators. Perhaps the most notable is the Large Hadron Collider (LHC) which stands out as the most powerful collider to date. The LHC is based in a 26.7 kilometer circular tunnel that lies 100 meters underground, spanning the border

between France and Switzerland. Inside the tunnel, two beams of protons are bended and accelerated to extremely high velocities, ~ 99.9999991% the speed of light, with energies reaching to 6.8 TeV, using a series of superconducting magnets. The beams are then made to collide at four different points around the ring, where detectors are placed to study the resulting particles.

Figure H.3 illustrates the journey protons take to increase their energy before reaching the LHC, and the subsequent four detection points that they deposit their energy in. This thesis primarily focuses on the A Toroidal LHC AppartuS (ATLAS) detector, the largest at the LHC, weighing 7,000 tonnes and reaching 46 metres in length and 25 metres in diameter. ATLAS is a multi-purpose instrument, used for studying a wide variety of particles, both hadronic and leptonic. When

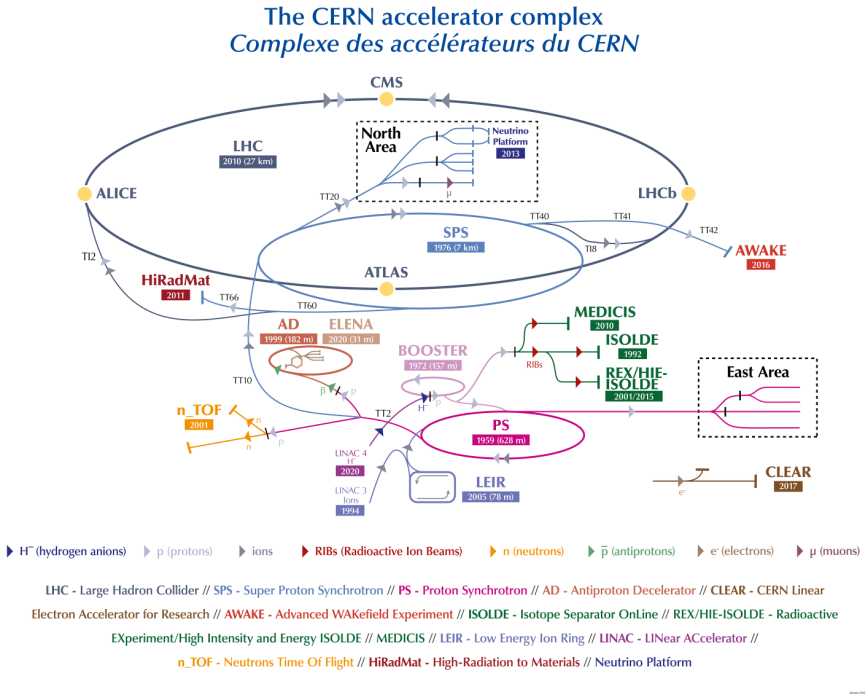


Figure H.3: Schematic of CERN accelerator complex [70].

a detector captures the energy from a particle, this information is converted into data for physicists to be able to use in physics analyses. However, the process of identification and measurement of these particles is complex and requires the use of reconstruction. The reconstruction is mainly built from signatures left in the detector from charged particles as they pass through, known as tracks and from interaction points of the particles, known as vertices. Neutrinos are not able to be detected in ATLAS, passing through the detector before depositing their energy

but they are accounted for in physics analyses as missing energy, $E_T^{Miss}$.

## Monte Carlo Simulations

Monte Carlo (MC) simulations are a computational technique that model the interactions of particles in a collider by generating a large number of statistically random events. They are crucial for correcting measurements to a level where they can be compared to theory. MC generators simulate each stage of particle interactions, as illustrated in Figure H.4. These stages are as follows:

- Hard Scatter Matrix Element Calculation: This step involves perturbative calculations to determine the initial hard scatter event. This is where the fundamental interaction that leads to the particle collision or decay is simulated. The calculation is based on theoretical models and takes into account various factors such as energy, momentum, and the types of particles involved.

- Parton Shower, Fragmentation, and Hadronisation: After the initial hard scatter, the simulation proceeds to model the subsequent stages of the event. This includes the parton shower, where the quarks and gluons emitted in the hard scatter evolve, and fragmentation and hadronisation, where these partons transform into hadrons.

- Interactions with the Detector (GEANT4): The final stage of the simulation involves modelling how the generated particles interact with the detector. This is performed using software such as GEANT4, which simulates the passage of particles through matter. This step accounts for various effects such as particle energy loss, scattering, and the detector's resolution, allowing the simulation to accurately represent how particles would be detected in a real experiment.

Several Monte Carlo event generators are available, each offering its unique approach to simulating the various stages of $pp$ collisions, from the initial hard scattering to particle decay processes. These include Pythia, which focuses on simulating the parton showering and hadronisation stages in detail, making it particularly well-suited for studies involving softer emissions and final-state

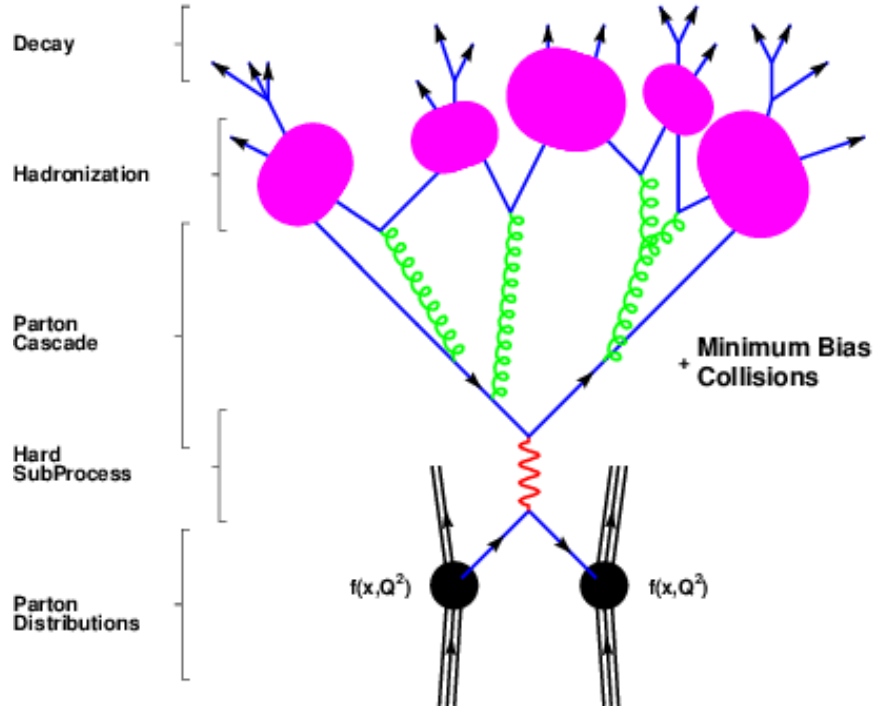


Figure H.4: The basic structure of a particle collision and its following processes [104].

hadrons. Another is SHERPA, which is a generalised MC event generator, which provides matrix element calculations combined with parton showers.

## Jet Calibration

Within the realm of object reconstruction in ATLAS, jets play a role of paramount importance. Jets are reconstructed from the clustering of decay products of quarks and gluons from the initial $pp$ interactions. Jets are used throughout a majority of ATLAS analyses such as those that focus on extremely precise measurements of currently known particle observables, or the search for new observables that are not yet predicted by the SM.

However, jets face a number of issues, such as biases and degradation in the detector or overlapping signals from multiple $pp$ collisions occurring simultaneously within the same area, known as pile-up. This requires a calibration process for the jets before they are passed onto physics analyses. The main process in ATLAS is the jet energy scale (JES) calibration, with the individual steps shown in Figure H.5. This calibration is used to accurately determine the energy of the

jets and correct for the sources of uncertainty that can affect measurements with these jets. Each stage focuses on correcting for a specific part of the characteristics

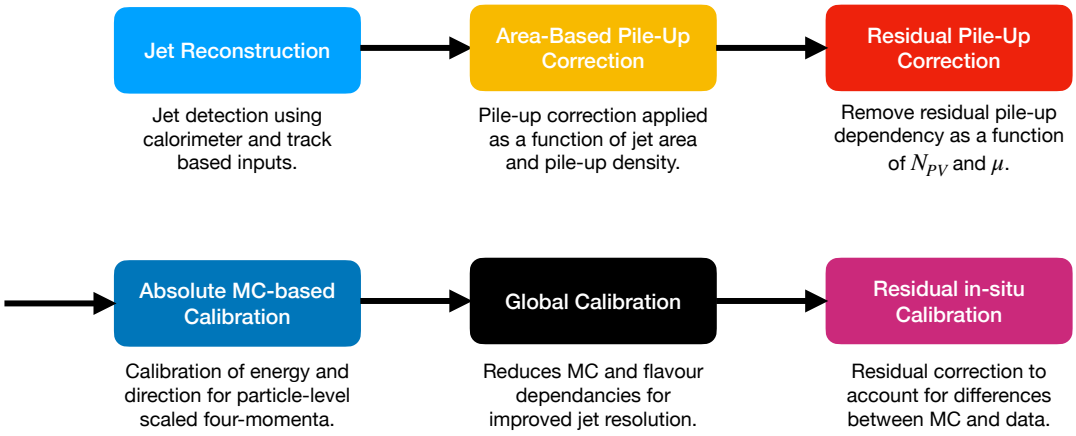


Figure H.5: JES calibration chain stages.

of jets. The first two account for the aforementioned pile-up and minimising its impact on the jet. The next is absolute MC-based correction which adjusts the reconstructed four-momentum of a jet to the energy scale of particle-level jets that are caluclated in MC simulations. This accounts for factors such as calorimeter responses, energy losses in dead material in the detector, and out-of-cone radiation effects. Next is the global calibration stage which tries to limit the difference in jets initiated from gluons or quarks of different flavours. This is due to the fact that quark-initiated jets have different responses dependent on the quarks involved and they have very different responses from gluon-initiated jets.

Lastly is the residual in-situ calibration which accounts for the difference between data and simulation after all the previous steps of the calibration chain have been carried out. These differences are due to imperfect simulation due to faults in the detector or innacuracies in modelling certain physics processes.To correct for this, a data-based correction must be applied. This is calculated from measurements of the $p_T$-based balance between a jet and a well-calibrated reference object. The $p_T$ responses are fitted in bins of the reference object with a Gaussian function and the correction is given as a double ratio between data and MC:

$$c = \frac{R_{in-situ}^{Data}}{R_{in-situ}^{MC}} \tag{H.8}$$

The processes used in the in-situ calibration are di-jets, photon+jet, Z+jet, and

multi-jet; which are illustrated in Figure 5.5. A statistical combination of data-to-MC ratios of the response measurements is used to apply a correction exclusively to the data.

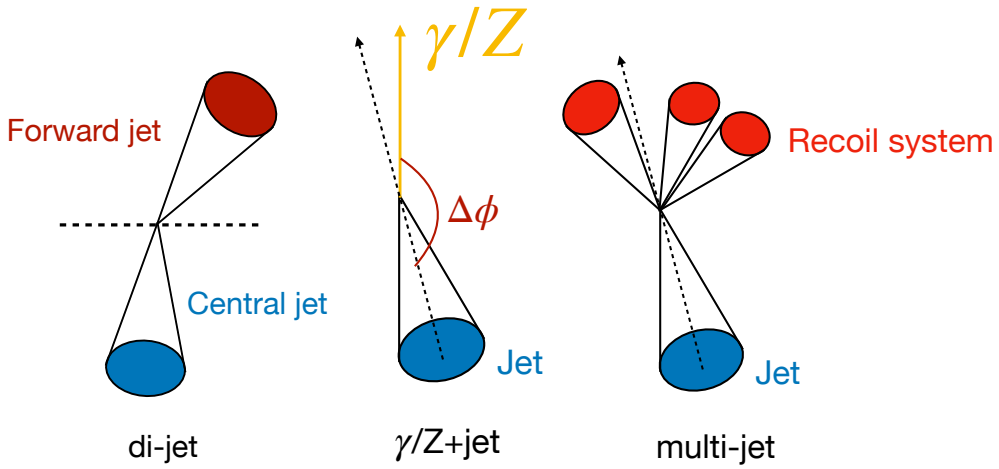


Figure H.6: Balance diagrams for (a) di-jet, (b) $\gamma$/Z+jet, and (c) multi-jet events, that are used in the residual in-situ calibration

A new technique developed for the in-situ part of the calibration is the inclusion of the b-jet energy scale (bJES) calibration with $\gamma$+jets. This calibration compares the response between photons and jets that includes the full range of available quark information (which will be called inclusive jets) and the response between photons and $b$–jets (which we will call $b$–tagged jets). This allows the study to focus on the detector and simulation effects on $b$–jets, as well as the difference in how $b$–jets and inclusive jets are developed in MC at ATLAS.

$b$ quarks are an extremely important part of ATLAS as they are the channel through which the top quark, $t \to Wb$, and the Higgs boson, $H \to bb$, mostly decay through. This means the understanding of $b$-jets is crucial, especially when being applied to precision measurements and BSM searches.

Since, in data, we can not know exactly which jets originated from $b$-quarks, there is a $b$-jet identification technique used in ATLAS known as $b$–tagging. This is a multivariate neural network-based algorithm that combines information from different sources to identify which jets are likely to have originated from the decay of a $b$-quark.

$b$–tagging consists of efficiencies, which define what percentage of jets in the

sample are considered as $b$–jets. There are 4 different efficiencies, given as 60%, 70%, 77%, and 80%. The lower the efficiency is, the higher the $b$–quark purity of the sample, however the lower the statistics. Thus, there is a balance to be made.

The bJES techniques takes the correction factor in Equation H.8, for responses of the b-tagged and inclusive jet samples which use MC samples of Pythia 8 and Sherpa 2.2.2. The difference between the JES correction is then taken as an observable called $\tilde{R}_{bJES} = \frac{c_{b-tagged}}{c_{inclusive}}$. This observable shows us how different the JES is in the $b$–tagged events and the inclusive events. Figure H.7 shows $\tilde{R}_{bJES}$ as a function of the reference photon transverse momentum for the different $b$–tagging efficiencies outlined earlier. There is a common consensus among all the points in the plots that the $b$–jet energy is underestimated compared to the inclusive jet energy. When these values are averaged out over the $p_T^{ref}$ range, it concludes that the bJES is underestimated by 1% to 3.4% depending on the efficiency and MC generator being evaluated.

These values suggest that the current JES calibration chain in ATLAS is not sufficient to be able to calibrate $b$–jets that will be used in analyses. Since precision measurements rely greatly on b-jets, if they are not calibrated well enough it could have an impactful effect on final measurements, such as those used for the top quark mass. A resolution to this is a dedicated JES calibration chain for $b$–jets specifically that is given to analyses that require the use of $b$–jets.

# The Top Quark

The top quark is the heaviest quark in the Standard Model. It is the only the only fermion that does not undergo hadronisation, as its lifetime is lower than the time it takes for hadronisation to occur, which gives us a unique opportunity to study properties of a free-quark.

The probability of the top quark decaying into lighter particles, is known as the top quark branching ratio. The branching ratio in the most common channel, $t \rightarrow Wq$, is defined as:

$$\mathcal{B}(t \rightarrow Wq) = \frac{\Gamma(t \rightarrow Wq)}{\Gamma_t} = \frac{|W_{tq}|^2}{|V_{tb}|^2 + |V_{ts}|^2 + |V_{td}|^2}, \tag{H.9}$$

where q is the down-type quarks that the top quark is permitted to decay into

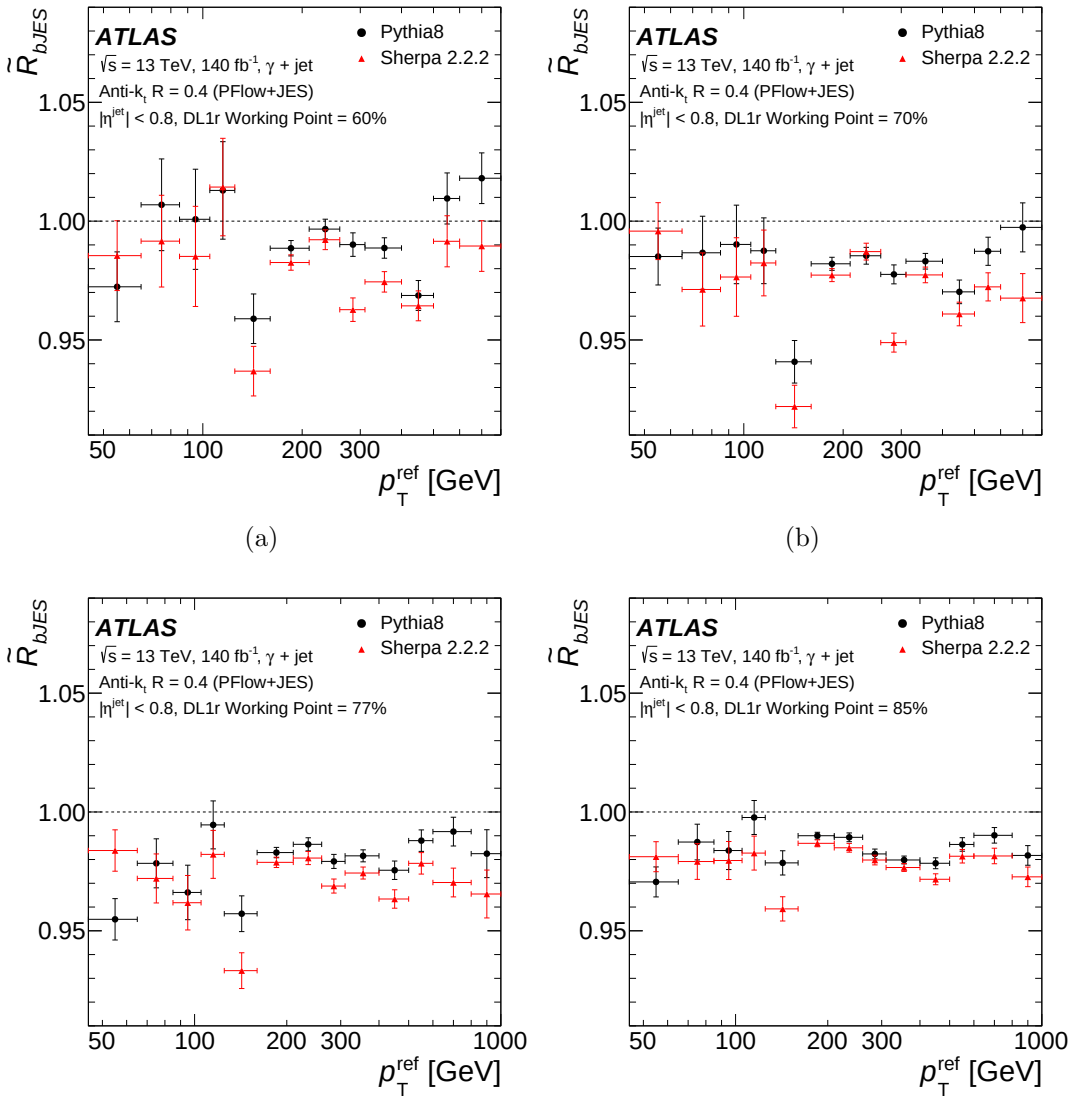


Figure H.7: $\tilde{R}_{\mathrm{bJES}}$ as a function of reference photon $p_{\mathrm{T}}$ determined using either Pythia 8 or Sherpa for $b$–tagging working point with an efficiency of (a) 60%, (b) 70%, (c) 77% and (d) 85%. The error bars correspond to the statistical uncertainties.

($b$,$s$,$d$). The top decays via the $b$ channel with the most frequency, which leads to a branching ratio value of $\mathcal{B}(t \to Wb) = 0.957 \pm 0.034$ [39]. This, highlights the importance of $b$–quarks and $b$–tagging in analyses like precision top quark measurements.

Because the top quark decays into the Wb channel almost 100% of the time, the final state formed by top quark pairs are classified according to the decay modes of the W-bosons. This consists of three categories: di-leptonic, semi-leptonic, and fully hadronic. The Feynman diagrams for each decay mode are illustrated in Figure H.8. Although the di-leptonic channel occurs less frequently due to its smaller branching fraction, it is experimentally the most pure due to the straightforward detection of the leptons in the final state. The fully hadronic decay mode, on the other hand, has a higher branching ratio but is heavily contaminated by QCD multi-jet background. The semi-leptonic decay channel exhibits characteristics that are midway between the other two, offering a good compromise between the purity of the di-leptonic channel and the higher statistics of the fully hadronic channel.

Quarks, due to the strong force, undergo a phenomenon called quark confinement at large distances from each other, when their coupling value, $\alpha_s$, is large, making it impossible for quarks to be separated. However, as high energies (smaller distances) $\alpha_s$ is small and quarks can be treated as free particles; this is asymptotic freedom. At these high energies, perturbative QCD is used, which employs a series expansion in terms of $\alpha_s$ to describe QCD processes at higher energies where the interactions become weaker. However, at higher order in perturbation theory, infinities can arise from closed loops, which lead to divergences. Through renormalisation schemes, terms are introduced to $\alpha_s$ in order to combat these divergences.

With regards to the top quark mass there are three renormalisation schemes that are discussed in this thesis: the pole mass $m_t^{pole}$, the $\overline{\text{MS}}$ mass $\bar{m}_t$, and the MSR mass $m_t^{MSR}$.

The pole mass treats the mass of the top quark as a free particle, corresponding the the mass of the top quark as it appears in parton-level scattering amplitudes. The $\overline{\text{MS}}$ mass, which is a scale-dependent, short-distance mass parameter. It is effective for high-energy processes where the energy scale, $Q$, is greater than $m_t$. Lastly, the MSR mass is a follow up of the $\overline{\text{MS}}$ mass, in terms of being scale-dependent (with the scale R) and short-distant but for processes at infrared

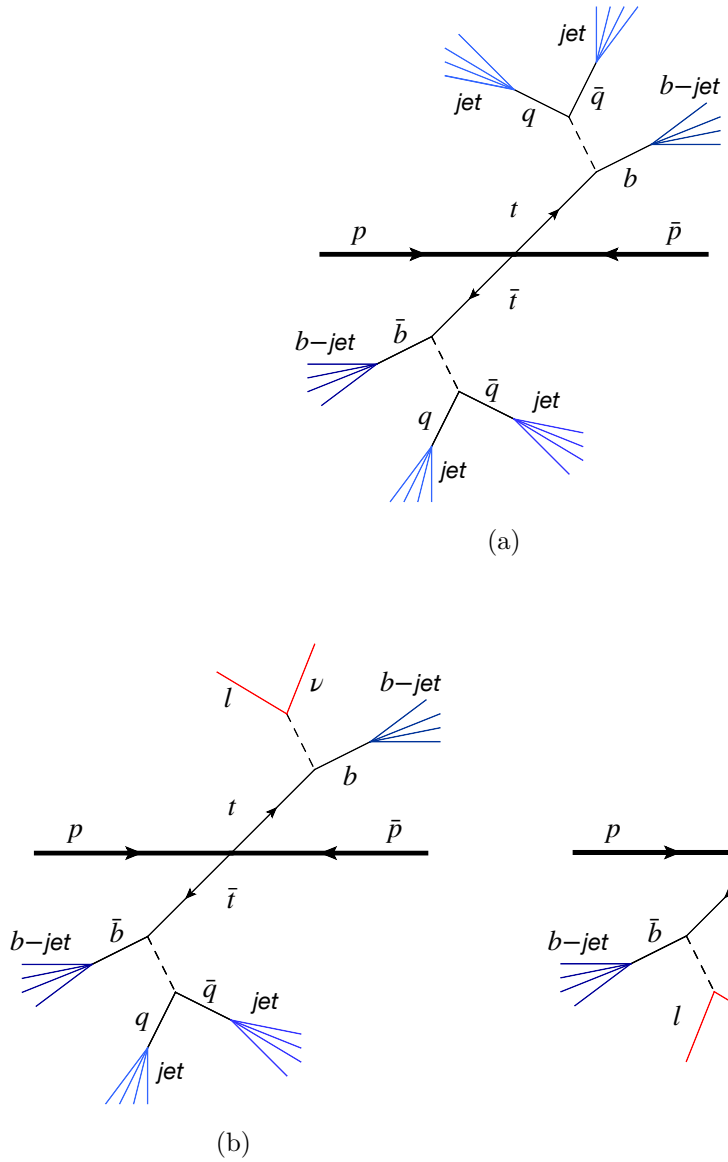


Figure H.8: Diagrames de Feynman per als processos de decaïment del quark top a través dels canals (a) completament hadrònic, (b) semi-leptònic, i (c) di-leptònic.

scales where $Q \leq m_t$. It is used to provide a smooth interpolation, as shown in Figure H.9, from $m_t(R = m_t)$ (where $\bar{m}_t$ begins) towards $m_t(R = 0)$ (where the $m_t^{pole}$ is situated).

When it comes to top quark mass measurements, there are two main categories: direct and indirect.

Direct measurements of the top quark mass use the decay products and kinematic observables of the top quark when it decays, primarily into a W

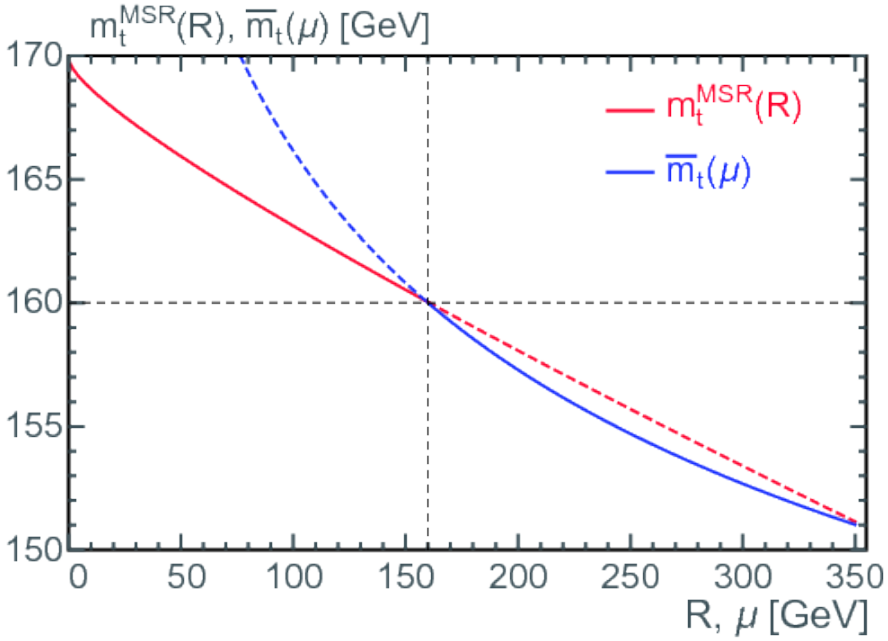


Figure H.9: Comparison of scale dependence for $\overline{\text{MS}}$ and MSR top quark masses as a function of $\mu$ and $R$ in GeV, with $m_t = 160$ GeV [206].

boson and a $b$-quark. Such decays yield distinctive resonance patterns and endpoints in mass distributions that are inherently sensitive to the top quark's mass. These measurements rely on detector-level templates created by MC generators, as first-principle predictions for these observables can not be used. Direct measurements are most sensitive to the mass of the top quark itself, yet the nuances of their shapes and the precision of their locations are also molded by the underlying QCD and EW dynamics at energy scales lower than the top quark mass. Indirect measurements, on the other hand, use inclusive and differential cross-section measurements, $\sigma_{t\bar{t}}$, to extract the top quark mass. Indirect methods have sensitivity from the hard-scatter only, meaning the sensitivity of these mass measurements is at scales of or above the top quark mass.

## Top Quark Mass Interpretation

When considering direct top quark mass measurements, MC generators have achieved a high-level of accuracy in describing data, particularly in the soft-collinear energy limit, $\approx 1$ GeV, typical for parton showers. This suggests that MC generators are effective enough at capturing important QCD features. However,

there is an inherent ambiguity in interpreting direct mass measurements within a field-theoretical renormalisation scheme. This can be reduced through dedicated 'calibration' studies. The top quarks mass interpretation approach tests the relationship between the MC mass parameter, $m_t^{MC}$, and the mass scheme used in these calculations.

The main analysis of this thesis is focused on the interpretation of the top MC quark mass, $m_t^{MC}$, within the context of the MSR scheme. The technique for determining the top quark mass involves reconstructing the decay products of the top quark. Here, the focus is on boosted top quarks, where the decay products are collimated into a single large-R jet. The kinematic hierarchy for this method is $Q >> m_t >> \Gamma_t$. This large gap in the hierarchy establishes a clear distinction between the processes related to the top quark decay and lower energy QCD processes. Additionally, due to the boosted state of the top quarks, this enables an inclusive analysis of the top quark decay, effectively capturing all the decay products within the large-R jet.

The jet is required to undergo a soft-drop (SD) grooming, to effectively remove the soft contamination from the jet without significantly altering the jet's properties related to the top quark mass.

The boosted, groomed large-R jet mass can be defined by summing over the constituents that remain within the jet, $\mathcal{J}_{SD}$:

$$M_J^2 = (\sum_{i \epsilon \mathcal{J}_{SD}} p_i^\mu)^2 \cong m_t^2 + \Gamma_t m_t + ... \tag{H.10}$$

This peak region of the jet where the sensitivity to the top quark mass arises, meaning the jet mass peak's position can serve as an indicator to deduce the value of $m_t$.

For this analysis, reference histograms are generated with Pythia 8 in several jet $p_T$ bins, with an equal number of events in each bin.

Theoretical templates are then required in order to fit to the MC templates. These theoretical distributions are each characterised by their unique parameter values, $m_t^{MSR}$, $\Omega_1^{\circ\circ}$, and $x_2$. The objective is to identify the parameter set that produces a jet mass distribution most compatible with the observed Monte Carlo.

In the theory, the nonperturbative shape function $F_q^{\circ\circ}$, describes the nonperturbative aspects of the jet formation. The leading-power nonperturbative corrections for the shape function are given by the first moment $\Omega_{1q}^{\circ\circ}$, and the

higher-order power corrections are given by a parameter denoted as $x_2$:

$$\Omega_{1q}^{\circ\circ} = \int_0^\infty dk k^+ F_{1p}^q(k) \tag{H.11}$$

$$x_2 = \frac{\Omega_{2q}^{\circ\circ}}{(\Omega_{1q}^{\circ\circ})^2} - 1 \tag{H.12}$$

For the fitting procedure, $m_t^{MSR}$, $\Omega_{1q}^{\circ\circ}$, and $x_2$ are extracted simultaneously in a 3D grid. The impact of the three parameters is illustrated in Figure H.10. Specifically, Figure H.10a demonstrates how variations in $m_t^{MSR}$ influence the distribution: while the overall shape remains consistent, the curve undergoes a movement corresponding to the shift in the jet mass peak. The effects of $\Omega_{1q}^{\circ\circ}$ and $x_2$ are depicted in Figures H.10b and H.10c, respectively. These parameters cause a slight shift in the peak and more pronounced variations in the distribution tails. Notably, $\Omega_{1q}^{\circ\circ}$ predominantly impacts both the lower and upper tails, whereas $x_2$ mainly affects the lower tail. $x_2$ has a slightly less significant influence than $\Omega_{1q}^{\circ\circ}$ on the tails and has the least effect on the jet mass distribution out of the three parameters.

As well as extracting the the values for each of these parameters, there are uncertainties within the analysis to be accounted for. The first set of uncertainties come from the fit methodology. The idea is to focus the fit within the area of the peak of the jet mass distribution, which is where the sensitivity to the top quark mass arises, so limits are placed on the jet mass distribution to account for this. However, some underlying physical processes aren't accounted for in the calculation that can affect the low tails of the distribution, thus if this set limit is changed it can affect the final result. Therefore, an uncertainty is taken with regard to the affect that a change on the limit can have on $m_t^{MSR}$.

Next are the uncertainties related to underlying event (UE). The UE encompasses all additional activity that occurs in conjunction with hard scattering processes at low energy. Typically these processes are gluon scattering such as $gg \to gg$. UE can affect the overall distribution of the jet mass and, although a lot of it is groomed away when using SD grooming, there still exists some UE in the distribution. The calculation does not currently account for UE so an uncertainty is estimated through Pythia by comparing the MC sample that we use against samples that include different prescriptions related to UE, and taking the MSR mass shifts from this estimation.

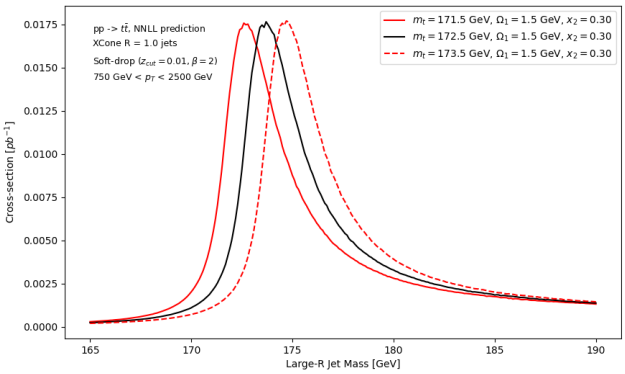


(a)

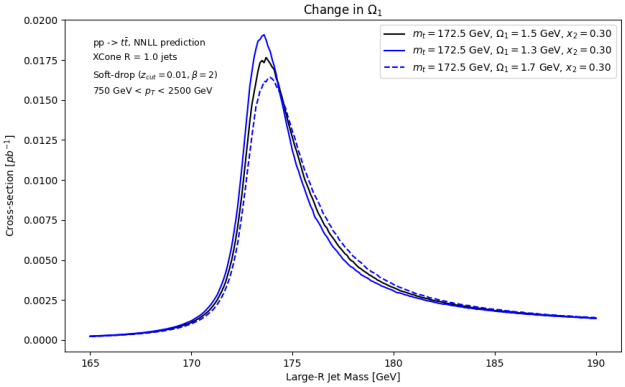


(b)

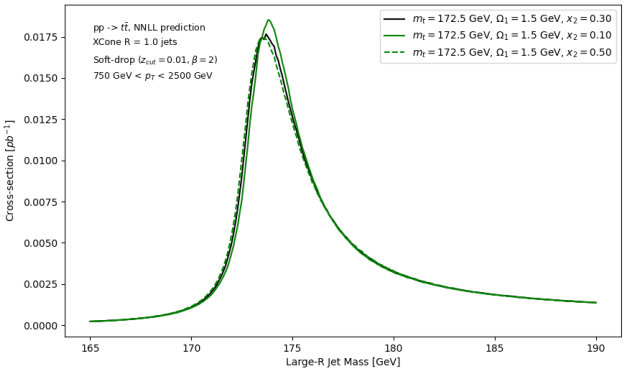


(c)

Figure H.10: The effects of the parameters (a) $m_t^{MSR}$, (b) $\Omega_1^{\circ\circ}$, and (c) $x_2$ on large-R top quark jet mass distributions . The nominal sample is taken with the values $m_t^{MSR} = 172.5$ GeV, $\Omega_1^{\circ\circ} = 1.5$ GeV, and $x_2 = 0.30$, as shown with the black curves. The variations are considered with ± 1 GeVfor $m_t^{MSR}$, ± 0.2 GeVfor $\Omega_1^{\circ\circ}$, and ± 0.20 for $x_2$.

Lastly, there are theoretical uncertainties which account for corrections at higher accuracy that are not part of the theoretical prescription used in the analysis. These uncertainties become lower when the accuracy of the calculation becomes higher. The improvement of the accuracy of this analysis is evident in Figure 8.9, which presents a side-by-side comparison of the theory scale variation curves, normalised to the nominal curve. The current results are in Figure H.11a and the previous results for a similar anlysis with a lower accuracy calculation are shown in Figure H.11b. The decrease in uncertainty values is evident when examining the envelope over the scale variations, and the bottom panels that highlight the difference between the variations and the nominal.

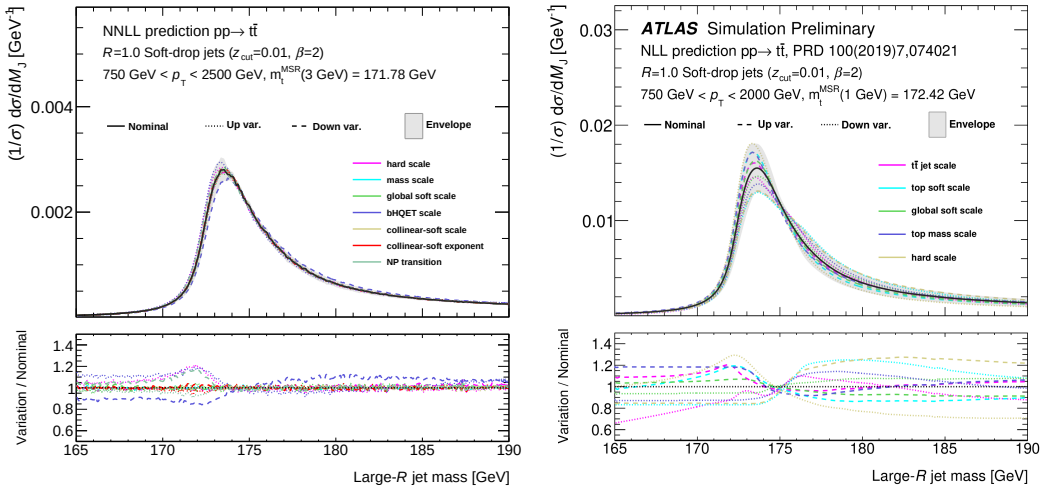


(a) (b)

Figure H.11: The (a) NNLL and (a) NLL [223] prediction of the normalised particle-level jet mass distribution for groomed large-R jets with a boosted hadronic top-quark decay (represented by a black line). The variations in the scales of the calculation are depicted by coloured lines, with the up (down) variations corresponding to dashed (dotted) line. Each curve is normalised to have the same area within the jet mass range of 172.5-180 GeV. The grey band illustrates the range covered by all scale variations.

Finally, the key findings of the analysis are summarised as follows:

$$\begin{aligned} m_t^{MSR}(R = 3\ \text{GeV}) &= 171.78 \pm 0.03\ \text{GeV}, \\ \Omega_1^{\circ\circ} &= 1.96 \pm 0.01\ \text{GeV}, \\ x_2 &= 0.38 \pm 0.02\ \text{GeV}, \end{aligned} \tag{H.13}$$

where the associated uncertainty corresponds to the statistical uncertainty due to the limited MC sample.

From these results, we establish the following relationship:

$$m_t^{MC} = m_t^{MSR}(R = 3 \text{ GeV}) + 720^{+285}_{-330} \text{ MeV}, \tag{H.14}$$

where the associated uncertainty values correspond to the quadrature sum of the theoretical uncertainties, methodology uncertainties, and UE uncertainties.

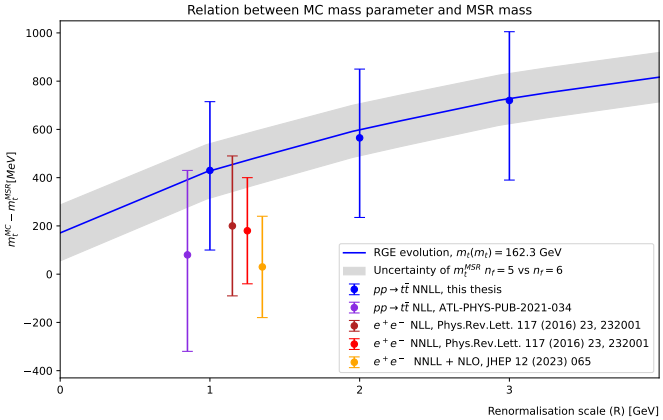


Figure H.12: R-evolution for the mass relation $\Delta_t^{MSR} = m_t^{MC} - m_t^{MSR}(R)$, with $m_t(m_t) = 162.3$ GeV. The points represent the mass relation results and their uncertainties from the analysis of this thesis (blue points), and from Ref. [223] (green point), Ref. [219] (purple point), and Ref. [221] (red point). The grey band exhibits the uncertainty related to the R-evolution curve.

In Figure H.12, the evolution of the MSR mass with its renormalisation value, R, is shown. The points on the curve show how compatible this analysis is with previous analyses of the same kind, for different types of collisions and/or for different levels of accuracy of the calculation. The previous results were only studied with respect to R = 1 GeV, so that is the area of comparison. It shows that, within the uncertainties of the results, this analysis is in line with those that were previously found.

# Acronyms

| | |
|---|---|
| **ATLAS** | **A T**oroidal **L**HC **A**pparatu**S** |
| **bHQET** | **b**oosted **H**eavy **Q**uark **E**ffective **T**heory |
| **BSM** | **B**eyond the **S**tandard **M**odel |
| **CC** | **C**harged **C**urrent |
| **CERN** | **C**onseil **E**uropeen pour la **R**eserche **N**ucleaire |
| **CKM** | **C**abibbo-**K**obayashi-**M**askawa |
| **CMS** | **C**ompact **M**uon **S**olenoid |
| **CP** | **C**harge **P**arity |
| **CR** | **C**olour **R**econnection |
| **DB** | **D**irect **B**alance |
| **DGLAP** | **D**okshitzer-**G**ribov-**L**ipatov-**A**ltarelli-**P**arisi |
| **DIS** | **D**eep-**I**nelastic **S**cattering |
| **ECAL** | **E**lectromagnetic **CAL**orimeter |
| **EFT** | **E**ffective **F**ield **T**heory |
| **EW** | **E**lectro**W**eak |
| **FCAL** | **F**orward **CAL**orimeter |
| **FCNC** | **F**lavour **C**hanging **N**eutral **C**urrent |
| **FSR** | **F**inal-**S**tate **R**adiation |
| **GNNC** | **G**lobal **N**eural **N**etwork **C**alibration |
| **GSC** | **G**lobal **S**equential **C**alibration |
| **HCAL** | **H**adronic **CAL**orimeter |
| **HL-LHC** | **H**igh-**L**uminosity **LHC** |
| **HLT** | **H**igh-**L**evel **T**rigger |
| **ID** | **I**nner **D**etector |
| **IR** | **I**nfra**R**ed |
| **IRC** | **I**nfra**R**ed and **C**ollinear |
| **ISR** | **I**nital-**S**tate **R**adiation |

| | |
|---|---|
| **JER** | **J**et **E**nergy **R**esolution |
| **JES** | **J**et **E**nergy **S**cale |
| **JMR** | **J**et **M**ass **R**esolution |
| **JMS** | **J**et **M**ass **S**cale |
| **LEP** | **L**arge **E**lectron-Positron **C**ollider |
| **LCW** | **L**ocal Hadronic **C**ell **W**eighting Scheme |
| **LHC** | **L**arge **H**adron **C**ollider |
| **LH** | **L**eft-**H**anded |
| **LL** | **L**eading **L**og |
| **LO** | **L**eading **O**rder |
| **MC** | **M**onte **C**arlo |
| **ME** | **M**atrix **E**lement |
| **MPF** | **M**issing-$E_T$ **P**rojection **F**raction |
| **MPI** | **M**ulti-**P**arton **I**nteractions |
| **ME** | **M**atrix **E**lement |
| **MEC** | **M**atrix **E**lement **C**orrection |
| **MS** | **M**uon **S**pectrometer |
| **NC** | **N**eutral **C**urrent |
| **NLL** | **N**ext-to-**L**eading **L**og |
| **NLO** | **N**ext-to-**L**eading **O**rder |
| **NN** | **N**eural **N**etwork |
| **NNLL** | **N**ext-to-**N**ext-to-**L**eading **L**og |
| **NNLO** | **N**ext-to-**N**ext-to-**L**eading **O**rder |
| **PS** | **P**arton **S**hower |
| **PDF** | **P**arton **D**ensity **F**unction |
| **QCD** | **Q**uantum **C**hromo**D**ynamics |
| **QED** | **Q**uantum **E**lectro**D**ynamics |
| **QFT** | **Q**uantum **F**ield **T**heory |
| **RGE** | **R**enormalisation **G**roup **E**quations |
| **RH** | **R**ight-**H**anded |
| **RMS** | **R**oot-**M**ean-**S**quared |
| **RS** | **R**ernormalization **S**chemes |
| **RTC** | **R**ecoil-**T**o-**C**olored |
| **SCET** | **S**oft and **C**ollinear **E**ffective field **T**heory |
| **SD** | **S**oft-**D**rop |
| **SLAC** | **S**tanford **L**inear **A**ccelerator **C**enter **SLF** |

| | |
|---|---|
| **S**ignal | |
| **L**eakage | |
| **F**ractions | |
| **SM** | **S**tandard **M**odel |
| **SMEFT** | **S**tandard **M**odel **E**ffective **F**ield **T**heory |
| **SSB** | **S**pontaneous **S**ymmetry **B**reaking |
| **SUSY** | **SU**per **SY**mmetry |
| **TDAQ** | ATLAS **T**rigger and **D**ata **Acq**uisition |
| **UC** | **U**ltra-**C**ollinear |
| **UE** | **U**nderlying **E**vent |
| **UFO** | **U**nified **F**low **O**bjects |
| **UV** | **U**ltra**V**iolet |
| **VEV** | **V**acuum**E**xpectation**V**alue |

| | |
|---|---|
| $pp$ | proton-proton |
| $p\bar{p}$ | proton-antiproton |
| $p_T$ | transverse momentum |
| $\sqrt{s}$ | centre-of-mass energy |
| $\overline{MS}$ | modified minimal subtraction renormalisation mass scheme |
| MSR | MSR renormalisation mass scheme |

# List of Figures

# List of Tables

# Bibliography


[1] Aristotle, *Metaphysics* (The Complete Works of Aristotle: The Revised Oxford Translation), J. Barnes, Ed.
Princeton: Princeton University Press, 1984 (cit. on p. I).

[2] D. Laërtius, *Lives of Eminent Philosophers*, trans. by R. Hicks.
Cambridge: Harvard University Press, 1925 (cit. on p. I).

[3] A. Lavoisier, *Traité Élémentaire de Chimie*. Paris: Cuchet, 1789
(cit. on p. I).

[4] J. Dalton, *A New System of Chemical Philosophy*.
Manchester: Bickerstaff, 1808 (cit. on p. II).

[5] D. Mendelejeff, *On the relationship of the properties of the elements to their atomic weights*, Zeitschrift für Chemie **12** 405–406 405–406, [Online]. Available:
`https://api.semanticscholar.org/CorpusID:209351400`
(cit. on p. II).

[6] H. G. J. Moseley, *Xciii. the high-frequency spectra of the elements*, Philosophical Magazine Series 1 **26** 1913 1024 1024, 1913. [Online]. Available: `https://api.semanticscholar.org/CorpusID:121000137`
(cit. on p. II).

[7] J. J. Thomson, *Cathode rays*, Phil. Mag. Ser. 5 **44** 1897 293 293, 1897
(cit. on p. II).

[8] E. Rutherford, *The scattering of alpha and beta particles by matter and the structure of the atom*, Phil. Mag. Ser. 6 **21** 1911 669 669, 1911
(cit. on p. II).

[9] N. Bohr, *On the Constitution of Atoms and Molecules*,
Phil. Mag. Ser. 6 **26** 1913 1 1, 1913 (cit. on p. II).

[10] J. S. Chadwick, *Possible existence of a neutron*,
Nature **129** 1932 312 312, 1932. [Online]. Available:
`https://api.semanticscholar.org/CorpusID:4076465` (cit. on p. III).

[11] Aristotle, *Meteorologica* (Loeb Classical Library 397),
trans. by H. D. P. Lee. Cambridge, MA: Harvard University Press, 1952
(cit. on p. III).

[12] D. René, Ed., *Discourse on Method, Optics, Geometry, Meteorology, Translated by Paul J. Olscamp*. New York: Bobbs-Merrill, 1965
(cit. on p. III).

[13] P. Gassendi, "Syntagma. logic," *The Selected Works of Pierre Gassendi*,
C. T. Brush, Ed., Johnson Reprint Corporation, 1972 (cit. on p. III).

[14] I. Newton, *Opticks*. Dover Press, 1704 (cit. on p. III).

[15] R. Hooke, *Micrographia: Or Some Physiological Descriptions of Minute Bodies Made by Magnifying Glasses*. Jo. Martyn and Ja. Allestry, 1665
(cit. on p. III).

[16] T. Young, *On the nature of light and colours*, Philosophical Transactions of the Royal Society of London **94** 1804 1 1, 1804 (cit. on p. III).

[17] M. Planck, *Über das gesetz der energieverteilung im normalspectrum*,
Annalen Phys. **309** 1901 553 553, 1901 (cit. on p. III).

[18] A. Einstein, *Über einen die erzeugung und verwandlung des lichtes betreffenden heuristischen gesichtspunkt*,
Annalen Phys. **322** 1905 132 132, 1905 (cit. on p. III).

[19] L. V. P. R. de Broglie, *Recherches sur la théorie des quanta*,
Annals Phys. **2** 1925 22 22, 1925 (cit. on p. IV).

[20] E. Schrödinger, *Quantisierung als Eigenwertproblem*,
Annalen Phys. **384** 1926 361 361, 1926 (cit. on p. IV).

[21] W. a Heisenberg, *Uber den anschaulichen Inhalt der quantentheoretischen Kinematik und Mechanik*, Z. Phys. **43** 1927 172 172, 1927 (cit. on p. IV).

[22] M. Born, *Zur Quantenmechanik der Stoßvorgänge*,
Z. Phys. **37** 1926 863 863, 1926 (cit. on p. IV).

[23] H. W. Kendall, *Deep inelastic scattering: Experiments on the proton and the observation of scaling*, Rev. Mod. Phys. **63** 1991 597 597, 1991
(cit. on p. 3).

[24] S. Weinberg, *A Model of Leptons*,
Phys. Rev. Lett. **19** 1967 1264 1264, 1967 (cit. on pp. 3, 9).

[25] A. Tarek Abouelfadl Mohamed,
"The standard model of particle physics."
Cham: Springer International Publishing, 2020 3 (cit. on pp. 5, 190, 210).

[26] ATLAS Collaboration, *Observation of a new particle in the search for the Standard Model Higgs boson with the ATLAS detector at the LHC*,
Phys. Lett. B **716** 2012 1 1, 2012. arXiv: `1207.7214 [hep-ex]`
(cit. on pp. 4, 35).

[27] P. A. M. Dirac, *Quantum theory of emission and absorption of radiation*,
Proc. Roy. Soc. Lond. A **114** 1927 243 243, 1927 (cit. on p. 7).

[28] R. P. Feynman, *Space - time approach to quantum electrodynamics*,
Phys. Rev. **76** 1949 769, L. M. Brown, Ed. 769, 1949 (cit. on p. 7).

[29] J. S. Schwinger, *Quantum electrodynamics. I A covariant formulation*,
Phys. Rev. **74** 1948 1439, K. A. Milton, Ed. 1439, 1948 (cit. on p. 7).

[30] S. Tomonaga, *On a relativistically invariant formulation of the quantum theory of wave fields*, Prog. Theor. Phys. **1** 1946 27 27, 1946 (cit. on p. 7).

[31] M. Goray and R. N. Annavarapu, *Rest mass of photon on the surface of matter*, Results in Physics **16** 2020 102866 102866, 2020 (cit. on p. 8).

[32] S. L. Glashow, *Partial Symmetries of Weak Interactions*,
Nucl. Phys. **22** 1961 579 579, 1961 (cit. on p. 9).

[33] A. Salam, *Weak and Electromagnetic Interactions*,
Conf. Proc. C **680519** 1968 367 367, 1968 (cit. on p. 9).

[34] E. Fermi, *An attempt of a theory of beta radiation. 1.*,
Z. Phys. **88** 1934 161 161, 1934 (cit. on p. 10).

[35] T. Corona, *Simulation tools for the 2km detector at the t2k experiment*,
2023, 2023 (cit. on p. 10).

[36] C. S. Wu, E. Ambler, R. W. Hayward, D. D. Hoppes, and R. P. Hudson,
*Experimental Test of Parity Conservation in $\beta$ Decay*,
Phys. Rev. **105** 1957 1413 1413, 1957 (cit. on p. 10).

[37] M. Drewes, *The Phenomenology of Right Handed Neutrinos*,
Int. J. Mod. Phys. E **22** 2013 1330019 1330019, 2013.
arXiv: `1303.6912 [hep-ph]` (cit. on p. 11).

[38] M. Kobayashi and T. Maskawa, *CP Violation in the Renormalizable Theory of Weak Interaction*, Prog. Theor. Phys. **49** 1973 652 652, 1973 (cit. on p. 17).

[39] Particle Data Group, *Review of Particle Physics*, PTEP **2022** 2022 083C01 083C01, 2022 (cit. on pp. 18, 131, 153, 219).

[40] S. L. Glashow, J. Iliopoulos, and L. Maiani, *Weak Interactions with Lepton-Hadron Symmetry*, Phys. Rev. D **2** 1970 1285 1285, 1970 (cit. on p. 18).

[41] UA1 Collaboration, *Experimental Observation of Isolated Large Transverse Energy Electrons with Associated Missing Energy at* $\sqrt{s} = 540$ *GeV*, Phys. Lett. B **122** 1983 103 103, 1983 (cit. on pp. 18, 37).

[42] UA1 Collaboration, *Experimental Observation of Events with Large Missing Transverse Energy Accompanied by a Jet Or a Photon(s) in* $p\bar{p}$ *Collisions at* $\sqrt{s} = 540GeV$, Phys. Lett. B **139** 1984 115 115, 1984 (cit. on pp. 18, 37).

[43] UA2 Collaboration, *Evidence for* $Z^0 \to e^+e^-$ *at the CERN* $\bar{p}p$ *Collider*, Phys. Lett. B **129** 1983 130 130, 1983 (cit. on pp. 18, 37).

[44] J. Goldstone, *Field Theories with Superconductor Solutions*, Nuovo Cim. **19** 1961 154 154, 1961 (cit. on p. 19).

[45] P. W. Anderson, *Plasmons, Gauge Invariance, and Mass*, Phys. Rev. **130** 1963 439, J. C. Taylor, Ed. 439, 1963 (cit. on p. 19).

[46] F. Englert and R. Brout, *Broken Symmetry and the Mass of Gauge Vector Mesons*, Phys. Rev. Lett. **13** 1964 321, J. C. Taylor, Ed. 321, 1964 (cit. on p. 19).

[47] P. W. Higgs, *Broken Symmetries and the Masses of Gauge Bosons*, Phys. Rev. Lett. **13** 1964 508, J. C. Taylor, Ed. 508, 1964 (cit. on p. 19).

[48] G. S. Guralnik, C. R. Hagen, and T. W. B. Kibble, *Global Conservation Laws and Massless Particles*, Phys. Rev. Lett. **13** 1964 585, J. C. Taylor, Ed. 585, 1964 (cit. on p. 19).

[49] O. Özdal, *The Higgs boson and right-handed neutrinos in supersymmetric models*, M.S. thesis: Izmir Inst. Tech., 2017 (cit. on p. 20).

[50] W.-S. Hou, M. Kohda, and T. Modak, *Probing for extra top Yukawa couplings in light of $t\bar{t}h(125)$ observation*,
Phys. Rev. D **98** 2018 075007 075007, 2018. arXiv: 1806.06018 [hep-ph] (cit. on p. 21).

[51] Belle Collaboration, *Observation of a narrow charmonium-like state in exclusive $B^{\pm} \to K^{\pm}\pi^{+}\pi^{-}J/\psi$ decays*,
Phys. Rev. Lett. **91** 2003 262001 262001, 2003. arXiv: hep-ex/0309032 (cit. on p. 22).

[52] LHCb Collaboration, *Observation of $J/\psi p$ Resonances Consistent with Pentaquark States in $\Lambda_b^0 \to J/\psi K^- p$ Decays*,
Phys. Rev. Lett. **115** 2015 072001 072001, 2015.
arXiv: 1507.03414 [hep-ex] (cit. on p. 22).

[53] M. Byrd, *The Geometry of SU(3)*, 1997, 1997. arXiv: physics/9708015 (cit. on p. 22).

[54] M. Carena, "Unification of couplings in the MSSM,"
*International Europhysics Conference on High-energy Physics (HEP 95)*, 1996 481. arXiv: hep-ph/9603370 (cit. on p. 25).

[55] T. Kinoshita, *The Fine structure constant*,
Rept. Prog. Phys. **59** 1996 1459 1459, 1996 (cit. on p. 24).

[56] F. Halzen and A. D. Martin,
*Quarks and Leptons: An Introductory Course in Modern Particle Physics.*
1984, ISBN: 978-0-471-88741-6 (cit. on p. 26).

[57] Particle Data Group, *Review of Particle Physics*,
PTEP **2020** 2020 083C01 083C01, 2020 (cit. on p. 27).

[58] S. Catani, M. H. Seymour, and Z. Trocsanyi, *Regularization scheme independence and unitarity in QCD cross-sections*,
Phys. Rev. D **55** 1997 6819 6819, 1997. arXiv: hep-ph/9610553 (cit. on p. 29).

[59] A. Arbey and F. Mahmoudi, *Dark matter and the early Universe: a review*, Prog. Part. Nucl. Phys. **119** 2021 103865 103865, 2021.
arXiv: 2104.11488 [hep-ph] (cit. on p. 31).

[60] Planck Collaboration, *Planck 2015 results. XIII. Cosmological parameters*, Astron. Astrophys. **594** 2016 A13 A13, 2016.
arXiv: 1502.01589 [astro-ph.CO] (cit. on pp. 31, 32).

[61] M. Felcini, "Searches for Dark Matter Particles at the LHC," *53rd Rencontres de Moriond on Cosmology*, 2018 327. arXiv: 1809.06341 [hep-ex] (cit. on p. 31).

[62] LUX-ZEPLIN (LZ) Collaboration, *First Dark Matter Search Results from the LUX-ZEPLIN (LZ) Experiment*, Phys. Rev. Lett. **131** 2023 041002 041002, 2023. arXiv: 2207.03764 [hep-ex] (cit. on p. 31).

[63] F. Pompa, *Neutrino physics with the XENONnT experiment*, Laurea thesis: Bologna U., 2019 (cit. on p. 32).

[64] Aldo Morselli on behalf of the CTA Consortium, *Search for dark matter with IACTs and the Cherenkov Telescope Array*, J. Phys. Conf. Ser. **2429** 2023 012019 012019, 2023. arXiv: 2302.11318 [astro-ph.HE] (cit. on p. 32).

[65] S. Giagu, *WIMP Dark Matter Searches With the ATLAS Detector at the LHC*, Front. in Phys. **7** 2019 75 75, 2019 (cit. on p. 32).

[66] The Supernova Cosmology Project, *Measurements of* $\Omega$ *and* $\Lambda$ *from 42 high redshift supernovae*, Astrophys. J. **517** 1999 565 565, 1999. arXiv: astro-ph/9812133 (cit. on p. 32).

[67] A. G. Riess *et al.*, *Observational evidence from supernovae for an accelerating universe and a cosmological constant*, Astron. J. **116** 1998 1009 1009, 1998. arXiv: astro-ph/9805201 (cit. on p. 32).

[68] A. Einstein, *Kosmologische Betrachtungen zur allgemeinen Relativitats theorie*, Sitzungsberichte der Kouml niglich Preussischen Akademie der Wissenschaften 1917 142 142, 1917 (cit. on p. 32).

[69] S. M. Carroll, W. H. Press, and E. L. Turner, *The Cosmological constant*, Ann. Rev. Astron. Astrophys. **30** 1992 499 499, 1992 (cit. on p. 33).

[70] E. Lopienska, *The CERN accelerator complex, layout in 2022. Complexe des accélérateurs du CERN en janvier 2022*, 2022, 2022, General Photo. [Online]. Available: https://cds.cern.ch/record/2800984 (cit. on pp. 36, 192, 212).

[71] *LHC Machine*, JINST **3** 2008 S08001, L. Evans and P. Bryant, Eds. S08001, 2008 (cit. on p. 37).

[72] M. Lamont, *The First Years of LHC Operation for Luminosity Production*, 2013 MOYAB101 MOYAB101, 2013. [Online]. Available: https://cds.cern.ch/record/2010134 (cit. on p. 37).

[73] R. Steerenberg, *Lhc report: Another run is over and ls2 has just begun...*, Last Checked Out 15/11/2023, Last Checked Out 15/11/2023. [Online]. Available: https://home.cern/news/news/accelerators/lhc-report-another-run-over-and-ls2-has-just-begun (cit. on p. 37).

[74] O. Brüning *et al.*, *The scientific potential and technological challenges of the high-luminosity large hadron collider program*, Reports on Progress in Physics **85** 2022 046201 046201, 2022. [Online]. Available: https://dx.doi.org/10.1088/1361-6633/ac5106 (cit. on p. 37).

[75] CERN, *The hl-lhc project*, Last Checked Out 15/11/2023, Last Checked Out 15/11/2023. [Online]. Available: https://hilumilhc.web.cern.ch/content/hl-lhc-project (cit. on p. 38).

[76] ALICE Collaboration, *The ALICE experiment – A journey through QCD*, 2022, 2022. arXiv: 2211.04384 [nucl-ex] (cit. on p. 38).

[77] I. Belyaev, G. Carboni, N. Harnew, C. Matteuzzi, and F. Teubert, *The history of LHCb*, Eur. Phys. J. H **46** 2021 3 3, 2021. arXiv: 2101.05331 [physics.hist-ph] (cit. on p. 38).

[78] TOTEM Collaboration, *The TOTEM experiment at the CERN Large Hadron Collider*, JINST **3** 2008 S08007 S08007, 2008 (cit. on p. 39).

[79] CERN, *Our people*, Last Checked Out 16/11/2023, Last Checked Out 16/11/2023. [Online]. Available: https://home.cern/about/who-we-are/our-people (cit. on p. 39).

[80] J. C. Collins, D. E. Soper, and G. F. Sterman, *Factorization of Hard Processes in QCD*, Adv. Ser. Direct. High Energy Phys. **5** 1989 1 1, 1989. arXiv: hep-ph/0409313 (cit. on p. 40).

[81] P. Skands, "Introduction to QCD,"
*Theoretical Advanced Study Institute in Elementary Particle Physics: Searching for New Physics at Small and Large Scales*, 2013 341.
arXiv: 1207.2389 [hep-ph] (cit. on p. 40).

[82] Y. L. Dokshitzer, *Calculation of the Structure Functions for Deep Inelastic Scattering and e+ e- Annihilation by Perturbation Theory in Quantum Chromodynamics.*, Sov. Phys. JETP **46** 1977 641 641, 1977 (cit. on p. 41).

[83] G. Altarelli and G. Parisi, *Asymptotic Freedom in Parton Language*, Nucl. Phys. B **126** 1977 298 298, 1977 (cit. on p. 41).

[84] V. N. Gribov and L. N. Lipatov, *Deep inelastic e p scattering in perturbation theory*, Sov. J. Nucl. Phys. **15** 1972 438 438, 1972 (cit. on p. 41).

[85] NNPDF Collaboration, *Parton distributions from high-precision collider data*, Eur. Phys. J. C **77** 2017 663 663, 2017.
arXiv: 1706.00428 [hep-ph] (cit. on p. 41).

[86] E. R. Nocera, R. D. Ball, S. Forte, G. Ridolfi, and J. Rojo, *A first unbiased global determination of polarized PDFs and their uncertainties*, Nucl. Phys. B **887** 2014 276 276, 2014. arXiv: 1406.5539 [hep-ph] (cit. on p. 41).

[87] J. Feltesse, "Introduction to deep inelastic scattering: Past and present," *20th International Workshop on Deep-Inelastic Scattering and Related Subjects*, 2012 3 (cit. on p. 42).

[88] S. Alekhin, K. Melnikov, and F. Petriello, *Fixed target Drell-Yan data and NNLO QCD fits of parton distribution functions*,
Phys. Rev. D **74** 2006 054033 054033, 2006. arXiv: hep-ph/0606237 (cit. on p. 42).

[89] R. D. Ball *et al.*, *Parton distributions with small-x resummation: evidence for BFKL dynamics in HERA data*,
Eur. Phys. J. C **78** 2018 321 321, 2018. arXiv: 1710.05935 [hep-ph] (cit. on pp. 42, 43).

[90] NNPDF Collaboration, *Parton distributions for the LHC Run II*,
JHEP **04** 2015 040 040, 2015. arXiv: 1410.8849 [hep-ph] (cit. on pp. 42, 153).

[91] C. AC, "Layout of ATLAS. Dessin representant le detecteur ATLAS," 1998. [Online]. Available: `https://cds.cern.ch/record/39038` (cit. on p. 44).

[92] C. Lippmann, *Particle identification*, Nucl. Instrum. Methods Phys. Res., A **666** 2011 148 148, 2011, 61 pages, 30 figures. arXiv: `1101.3276`. [Online]. Available: `http://cds.cern.ch/record/1323010` (cit. on p. 45).

[93] B. Mandelli, *The Pixel Detector of the ATLAS Experiment for the Run 2 at the Large Hadron Collider*, Nucl. Part. Phys. Proc. **273-275** 2016 1166, M Aguilar-Benítez, J Fuster, S Martí-García, and A Santamaría, Eds. 1166, 2016 (cit. on p. 46).

[94] ATLAS Collaboration, *Production and integration of the ATLAS Insertable B-Layer*, JINST **13** 2018 T05008 T05008, 2018. arXiv: `1803.00844 [physics.ins-det]` (cit. on p. 46).

[95] ATLAS Collaboration, *Operation and performance of the ATLAS semiconductor tracker in LHC Run 2*, JINST **17** 2021 P01013 P01013, 2021. arXiv: `2109.02591 [physics.ins-det]` (cit. on p. 46).

[96] D. V. Krasnopevtsev, *Tracking properties of the ATLAS Transition Radiation Tracker (TRT)*, J. Phys. Conf. Ser. **798** 2017 012150, A. Galper *et al.*, Eds. 012150, 2017 (cit. on p. 46).

[97] J. Pequenao, "Computer Generated image of the ATLAS calorimeter," 2008. [Online]. Available: `https://cds.cern.ch/record/1095927` (cit. on p. 47).

[98] J. Zang, *ATLAS LAr calorimeter commissioning for LHC Run-3*, JINST **18** 2023 C01045 C01045, 2023 (cit. on p. 48).

[99] J. Abdallah *et al.*, *Study of energy response and resolution of the ATLAS Tile Calorimeter to hadrons of energies from 16 to 30 GeV*, Eur. Phys. J. C **81** 2021 549 549, 2021. arXiv: `2102.04088 [physics.ins-det]` (cit. on p. 48).

[100] S. Palestini, *The muon spectrometer of the ATLAS experiment*, Nucl. Phys. B Proc. Suppl. **125** 2003 337, F. L. Navarria, M. Paganoni, and P. G. Pelfer, Eds. 337, 2003 (cit. on p. 48).

[101] ATLAS Collaboration, *Operation of the ATLAS trigger system in Run 2*, JINST **15** 2020 P10004 P10004, 2020. arXiv: 2007.12539 [hep-ex] (cit. on p. 50).

[102] J. Shiers, *The Worldwide LHC Computing Grid (worldwide LCG)*, Comput. Phys. Commun. **177** 2007 219 219, 2007 (cit. on p. 50).

[103] GEANT4 Collaboration, *GEANT4–a simulation toolkit*, Nucl. Instrum. Meth. A **506** 2003 250 250, 2003 (cit. on p. 54).

[104] M. Dobbs and J. B. Hansen, *The HepMC C++ Monte Carlo event record for High Energy Physics*, Comput. Phys. Commun. **134** 2001 41 41, 2001 (cit. on pp. 54, 194, 214).

[105] R. Perez Ramos, "From QCD Color Coherence to Inclusive Distributions and Correlations in Jets," *6th International Workshop on High-pT physics at LHC*, 2011. arXiv: 1106.0160 [hep-ph] (cit. on p. 57).

[106] T. Sjostrand, *The Lund Monte Carlo for Jet Fragmentation*, Comput. Phys. Commun. **27** 1982 243 243, 1982 (cit. on p. 58).

[107] J.-C. Winter, F. Krauss, and G. Soff, *A Modified cluster hadronization model*, Eur. Phys. J. C **36** 2004 381 381, 2004. arXiv: hep-ph/0311085 (cit. on p. 58).

[108] S. Dimopoulos, S. A. Raby, and F. Wilczek, *Unification of couplings*, Phys. Today **44N10** 1991 25 25, 1991 (cit. on p. 59).

[109] ALICE Collaboration, "Multiplicity and Underlying Event in ALICE: as measurements and as tools to probe QCD," *53rd Rencontres de Moriond on QCD and High Energy Interactions*, 2018 233. arXiv: 1805.05695 [nucl-ex] (cit. on p. 60).

[110] S. Höche, "Introduction to parton-shower event generators," *Theoretical Advanced Study Institute in Elementary Particle Physics: Journeys Through the Precision Frontier: Amplitudes for Colliders*, 2015 235. arXiv: 1411.4085 [hep-ph] (cit. on p. 61).

[111] J. Alwall *et al.*, *The automated computation of tree-level and next-to-leading order differential cross sections, and their matching to parton shower simulations*, JHEP **07** 2014 079 079, 2014. arXiv: 1405.0301 [hep-ph] (cit. on p. 61).

[112] N. D. Christensen and C. Duhr, *FeynRules - Feynman rules made easy*, Comput. Phys. Commun. **180** 2009 1614 1614, 2009. arXiv: 0806.4194 [hep-ph] (cit. on p. 62).

[113] J. Alwall, M. Herquet, F. Maltoni, O. Mattelaer, and T. Stelzer, *MadGraph 5 : Going Beyond*, JHEP **06** 2011 128 128, 2011. arXiv: 1106.0522 [hep-ph] (cit. on p. 62).

[114] S. Frixione, F. Stoeckli, P. Torrielli, B. R. Webber, and C. D. White, *The MCaNLO 4.0 Event Generator*, 2010, 2010. arXiv: 1010.0819 [hep-ph] (cit. on p. 62).

[115] R. Frederix *et al.*, *The automation of next-to-leading order electroweak calculations*, JHEP **07** 2018 185 185, 2018, [Erratum: JHEP 11, 085 (2021)]. arXiv: 1804.10017 [hep-ph] (cit. on p. 62).

[116] P. Nason, *A New method for combining NLO QCD with shower Monte Carlo algorithms*, JHEP **11** 2004 040 040, 2004. arXiv: hep-ph/0409146 (cit. on p. 62).

[117] S. Frixione, P. Nason, and C. Oleari, *Matching NLO QCD computations with Parton Shower simulations: the POWHEG method*, JHEP **11** 2007 070 070, 2007. arXiv: 0709.2092 [hep-ph] (cit. on p. 62).

[118] S. Alioli, P. Nason, C. Oleari, and E. Re, *A general framework for implementing NLO calculations in shower Monte Carlo programs: the POWHEG BOX*, JHEP **06** 2010 043 043, 2010. arXiv: 1002.2581 [hep-ph] (cit. on p. 62).

[119] C. Bierlich *et al.*, *A comprehensive guide to the physics and usage of PYTHIA 8.3*, 2022, 2022. arXiv: 2203.11601 [hep-ph] (cit. on pp. 62, 63, 153).

[120] M. L. Mangano, M. Moretti, F. Piccinini, and M. Treccani, *Matching matrix elements and shower evolution for top-quark production in hadronic collisions*, JHEP **01** 2007 013 013, 2007. arXiv: hep-ph/0611129 (cit. on p. 62).

[121] S. Hoeche *et al.*, "Matching parton showers and matrix elements," *HERA and the LHC: A Workshop on the Implications of HERA for LHC Physics: CERN - DESY Workshop 2004/2005 (Midterm Meeting, CERN,*

*11-13 October 2004; Final Meeting, DESY, 17-21 January 2005)*, 2005 288. arXiv: hep-ph/0602031 (cit. on pp. 63, 65).

[122] J. Bellm, S. Plätzer, P. Richardson, A. Siódmok, and S. Webster, *Reweighting Parton Showers*, Phys. Rev. D **94** 2016 034028 034028, 2016. arXiv: 1605.08256 [hep-ph] (cit. on p. 64).

[123] J. Bellm *et al.*, *Herwig 7.0/Herwig++ 3.0 release note*, Eur. Phys. J. C **76** 2016 196 196, 2016. arXiv: 1512.01178 [hep-ph] (cit. on p. 64).

[124] M. Bahr *et al.*, *Herwig++ Physics and Manual*, Eur. Phys. J. C **58** 2008 639 639, 2008. arXiv: 0803.0883 [hep-ph] (cit. on p. 64).

[125] E. Bothmann *et al.*, *Event Generation with Sherpa 2.2*, SciPost Phys. **7** 2019 034 034, 2019. arXiv: 1905.09127 [hep-ph] (cit. on p. 64).

[126] J. Alwall *et al.*, *Comparative study of various algorithms for the merging of parton showers and matrix elements in hadronic collisions*, Eur. Phys. J. C **53** 2008 473 473, 2008. arXiv: 0706.2569 [hep-ph] (cit. on p. 64).

[127] N. Lavesson and L. Lonnblad, *Merging parton showers and matrix elements: Back to basics*, JHEP **04** 2008 085 085, 2008. arXiv: 0712.2966 [hep-ph] (cit. on p. 65).

[128] S. Catani, Y. L. Dokshitzer, M. Olsson, G. Turnock, and B. R. Webber, *New clustering algorithm for multi - jet cross-sections in e+ e- annihilation*, Phys. Lett. B **269** 1991 432 432, 1991 (cit. on p. 65).

[129] S. Catani, Y. L. Dokshitzer, M. H. Seymour, and B. R. Webber, *Longitudinally invariant $K_t$ clustering algorithms for hadron hadron collisions*, Nucl. Phys. B **406** 1993 187 187, 1993 (cit. on p. 65).

[130] S Catani, Y. L. Dokshitzer, M. H. Seymour, and B. R. Webber, *Longitudinally-invariant $k_\perp$-clustering algorithms for hadron-hadron collisions*, Nucl. Phys. B **406** 1993 187 187, 1993. [Online]. Available: https://cds.cern.ch/record/246812 (cit. on p. 65).

[131] A. S. on behalf of the ATLAS Collaboration, *Optimisation of the atlas track reconstruction software for run-2*,
Journal of Physics: Conference Series **664** 2015 072042 072042, 2015.
[Online]. Available:
https://dx.doi.org/10.1088/1742-6596/664/7/072042
(cit. on p. 70).

[132] Y. Kim and H. Bang, "Introduction to kalman filter and its applications," *Introduction and Implementations of the Kalman Filter*, F. Govaers, Ed., Rijeka: IntechOpen, 2018, ch. 2.
[Online]. Available: https://doi.org/10.5772/intechopen.80600
(cit. on p. 70).

[133] I. Sanderswood,
*Development of atlas primary vertex reconstruction for lhc run 3*, 2019.
arXiv: 1910.08405 [hep-ex] (cit. on p. 71).

[134] ATLAS Collaboration, *Electron reconstruction and identification in the ATLAS experiment using the 2015 and 2016 LHC proton–proton collision data at* $\sqrt{s} = 13$ *TeV*, Eur. Phys. J. C **79** 2019 639 639, 2019.
arXiv: 1902.04655 [hep-ex] (cit. on p. 72).

[135] ATLAS Collaboration, *Electron and photon performance measurements with the ATLAS detector using the 2015–2017 LHC proton–proton collision data*, JINST **14** 2019 P12006 P12006, 2019.
arXiv: 1908.00005 [hep-ex] (cit. on pp. 72, 96).

[136] ATLAS Collaboration, *Jet reconstruction and performance using particle flow with the ATLAS Detector*, Eur. Phys. J. C **77** 2017 466 466, 2017.
arXiv: 1703.10485 [hep-ex] (cit. on p. 72).

[137] M. Cacciari, G. P. Salam, and G. Soyez, *The anti-$k_t$ jet clustering algorithm*, JHEP **04** 2008 063 063, 2008. arXiv: 0802.1189 [hep-ph]
(cit. on pp. 72, 78, 79).

[138] M. Cacciari, G. P. Salam, and G. Soyez, *FastJet User Manual*,
Eur. Phys. J. C **72** 2012 1896 1896, 2012. arXiv: 1111.6097 [hep-ph]
(cit. on pp. 72, 155).

[139] ATLAS Collaboration, *Muon reconstruction performance of the ATLAS detector in proton–proton collision data at* $\sqrt{s} = 13$ *TeV*,

Eur. Phys. J. C **76** 2016 292 292, 2016. arXiv: 1603.05598 [hep-ex] (cit. on p. 73).

[140] ATLAS Collaboration, *Performance of missing transverse momentum reconstruction with the ATLAS detector using proton–proton collisions at* $\sqrt{s} = 13\ TeV$, Eur. Phys. J. C **78** 2018 903 903, 2018. arXiv: 1802.08168 [hep-ex] (cit. on p. 73).

[141] ATLAS and CDF Collaborations, *Prompt photons at hadron colliders*, PoS **ICHEP2016** 2017 597 597, 2017 (cit. on p. 73).

[142] ATLAS Collaboration, *Measurement of the photon identification efficiencies with the ATLAS detector using LHC Run 2 data collected in 2015 and 2016*, Eur. Phys. J. C **79** 2019 205 205, 2019. arXiv: 1810.05087 [hep-ex] (cit. on p. 75).

[143] R. Atkin, *Review of jet reconstruction algorithms*, Journal of Physics: Conference Series **645** 2015 012008 012008, 2015 (cit. on p. 77).

[144] M. Cacciari, "FastJet: A Code for fast $k_t$ clustering, and more," *41st Rencontres de Moriond: QCD and Hadronic Interactions*, 2006 487. arXiv: hep-ph/0607071 (cit. on p. 78).

[145] ATLAS Collaboration, *ATLAS b-jet identification performance and efficiency measurement with* $t\bar{t}$ *events in pp collisions at* $\sqrt{s} = 13\ TeV$, Eur. Phys. J. C **79** 2019 970 970, 2019. arXiv: 1907.05120 [hep-ex] (cit. on p. 79).

[146] Yosuke Takubo on behalf of the ATLAS collaboration, *ATLAS IBL operational experience*, CERN, Tech. Rep., 2017. [Online]. Available: https://cds.cern.ch/record/2235541 (cit. on p. 80).

[147] ATLAS Collaboration, *New techniques for jet calibration with the ATLAS detector*, 2023, 2023. arXiv: 2303.17312 [hep-ex] (cit. on pp. 81, 85–88, 92, 104, 105, 110, 112, 114, 115, 175).

[148] M. Cacciari and G. P. Salam, *Pileup subtraction using jet areas*, Phys. Lett. B **659** 2008 119 119, 2008. arXiv: 0707.1378 [hep-ph] (cit. on p. 83).

[149] M. Cacciari, G. P. Salam, and G. Soyez, *The Catchment Area of Jets*, JHEP **04** 2008 005 005, 2008. arXiv: 0802.1188 [hep-ph] (cit. on p. 83).

[150] ATLAS Collaboration, *Jet global sequential corrections with the ATLAS detector in proton–proton collisions at $\sqrt{s} = 8$ TeV*, ATLAS-CONF-2015-002, 2015. [Online]. Available: https://cds.cern.ch/record/2001682 (cit. on p. 86).

[151] ATLAS Collaboration, *Jet energy scale and resolution measured in proton–proton collisions at $\sqrt{s} = 13$ TeV with the ATLAS detector*, Eur. Phys. J. C **81** 2020 689 689, 2020. arXiv: 2007.02645 [hep-ex] (cit. on p. 90).

[152] J. Pinfold *et al.*, *Performance of the ATLAS liquid argon endcap calorimeter in the pseudorapidity region 2.5 < —eta— < 4.0 in beam tests*, Nucl. Instrum. Meth. A **593** 2008 324 324, 2008 (cit. on p. 91).

[153] ATLAS Collaboration, *Electron and photon energy calibration with the ATLAS detector using LHC Run 2 data*, 2023, 2023. arXiv: 2309.05471 [hep-ex] (cit. on p. 91).

[154] ATLAS Collaboration, *Jet energy scale measurements and their systematic uncertainties in proton–proton collisions at $\sqrt{s} = 13$ TeV with the ATLAS detector*, Phys. Rev. D **96** 2017 072002 072002, 2017. arXiv: 1703.09665 [hep-ex] (cit. on p. 93).

[155] ATLAS Collaboration, *Luminosity determination in pp collisions at $\sqrt{s} = 7$ TeV using the ATLAS detector at the LHC*, Eur. Phys. J. C **71** 2011 1630 1630, 2011. arXiv: 1101.2185 [hep-ex] (cit. on p. 95).

[156] V. Lendermann *et al.*, *Combining Triggers in HEP Data Analysis*, Nucl. Instrum. Meth. A **604** 2009 707 707, 2009. arXiv: 0901.4118 [hep-ex] (cit. on p. 95).

[157] ATLAS Collaboration, *ATLAS flavour-tagging algorithms for the LHC Run 2 pp collision dataset*, 2022. arXiv: 2211.16345 [physics.data-an] (cit. on p. 96).

[158] T. Sjöstrand *et al.*, *An introduction to PYTHIA 8.2*, Computer Physics Communications **191** 2015 159 159, 2015. [Online]. Available: https://doi.org/10.1016%2Fj.cpc.2015.01.024 (cit. on p. 97).

[159] E. Bothmann *et al.*, *Event generation with sherpa 2.2*, SciPost Physics **7** 2019, 2019. [Online]. Available: https://doi.org/10.21468%2Fscipostphys.7.3.034 (cit. on p. 97).

[160] D. J. Lange, *The EvtGen particle decay simulation package*, Nucl. Instrum. Meth. A **462** 2001 152, S. Erhan, P. Schlein, and Y. Rozen, Eds. 152, 2001 (cit. on p. 97).

[161] William Buttinger, "Background estimation with the abcd method featuring the troofit toolkit," 2018 (cit. on p. 98).

[162] G. Kasieczka, B. Nachman, M. D. Schwartz, and D. Shih, *Automating the ABCD method with machine learning*, Physical Review D **103** 2021, 2021. [Online]. Available: https://doi.org/10.1103%2Fphysrevd.103.035021 (cit. on p. 98).

[163] ATLAS Collaboration, *Evaluating statistical uncertainties and correlations using the bootstrap method*, Tech. Rep., 2021. [Online]. Available: https://cds.cern.ch/record/2759945 (cit. on pp. 104, 161).

[164] ATLAS Collaboration, *Electron and photon energy calibration with the ATLAS detector using 2015–2016 LHC proton–proton collision data*, JINST **14** 2019 P03017 P03017, 2019. arXiv: 1812.03848 [hep-ex] (cit. on p. 105).

[165] ATLAS Collaboration, *Performance of b-jet identification in the ATLAS experiment*, JINST **11** 2016 P04008 P04008, 2016. arXiv: 1512.01094 [hep-ex] (cit. on p. 108).

[166] D. Habtzghi, C. Midha, and A. Das, *Modified clopper-pearson confidence interval for binomial proportion*, Journal of Statistical Theory and Applications **13** 2014 296 296, 2014 (cit. on p. 114).

[167] ATLAS Collaboration, *Jet energy measurement with the ATLAS detector in proton–proton collisions at* $\sqrt{s} = 7$ *TeV*, Eur. Phys. J. C **73** 2013 2304 2304, 2013. arXiv: 1112.6426 [hep-ex] (cit. on p. 117).

[168] ATLAS Collaboration, *Improving jet substructure performance in ATLAS using Track-CaloClusters*, ATL-PHYS-PUB-2017-015, 2017. [Online]. Available: `https://cds.cern.ch/record/2275636` (cit. on p. 117).

[169] ATLAS Collaboration, *Optimisation of large-radius jet reconstruction for the ATLAS detector in* 13 *TeV proton–proton collisions*, Eur. Phys. J. C **81** 2020 334 334, 2020. arXiv: `2009.04986 [hep-ex]` (cit. on pp. 117, 118, 122).

[170] R. Kogler *et al.*, *Jet Substructure at the Large Hadron Collider: Experimental Review*, Rev. Mod. Phys. **91** 2019 045003 045003, 2019. arXiv: `1803.06991 [hep-ex]` (cit. on pp. 117, 120).

[171] ATLAS Collaboration, *In situ calibration of large-radius jet energy and mass in* 13 *TeV proton–proton collisions with the ATLAS detector*, Eur. Phys. J. C **79** 2019 135 135, 2019. arXiv: `1807.09477 [hep-ex]` (cit. on pp. 118, 119).

[172] P. Berta, M. Spousta, D. W. Miller, and R. Leitner, *Particle-level pileup subtraction for jets and jet shapes*, JHEP **06** 2014 092 092, 2014. arXiv: `1403.3108 [hep-ex]` (cit. on p. 122).

[173] M. Cacciari, G. P. Salam, and G. Soyez, *SoftKiller, a particle-level pileup removal method*, Eur. Phys. J. C **75** 2015 59 59, 2015. arXiv: `1407.0408 [hep-ph]` (cit. on p. 122).

[174] D. Bertolini, P. Harris, M. Low, and N. Tran, *Pileup Per Particle Identification*, JHEP **10** 2014 059 059, 2014. arXiv: `1407.6013 [hep-ph]` (cit. on p. 122).

[175] ATLAS Collaboration, *Performance of jet substructure techniques for large-R jets in proton–proton collisions at* $\sqrt{s} = 7$ *TeV using the ATLAS detector*, JHEP **09** 2013 076 076, 2013. arXiv: `1306.4945 [hep-ex]` (cit. on p. 122).

[176] D. Krohn, J. Thaler, and L.-T. Wang, *Jet Trimming*, JHEP **02** 2010 084 084, 2010. arXiv: `0912.1342 [hep-ph]` (cit. on p. 123).

[177] J. M. Butterworth, A. R. Davison, M. Rubin, and G. P. Salam, *Jet substructure as a new Higgs search channel at the LHC*, Phys. Rev. Lett. **100** 2008 242001 242001, 2008. arXiv: 0802.2470 [hep-ph] (cit. on p. 123).

[178] S. D. Ellis, C. K. Vermilion, and J. R. Walsh, *Recombination Algorithms and Jet Substructure: Pruning as a Tool for Heavy Particle Searches*, Phys. Rev. D **81** 2010 094023 094023, 2010. arXiv: 0912.0033 [hep-ph] (cit. on p. 123).

[179] A. J. Larkoski, S. Marzani, G. Soyez, and J. Thaler, *Soft Drop*, JHEP **05** 2014 146 146, 2014. arXiv: 1402.2657 [hep-ph] (cit. on pp. 123, 145, 155).

[180] S. Marzani, L. Schunk, and G. Soyez, *The jet mass distribution after Soft Drop*, Eur. Phys. J. C **78** 2018 96 96, 2018. arXiv: 1712.05105 [hep-ph] (cit. on p. 124).

[181] S. Marzani, L. Schunk, and G. Soyez, *A study of jet mass distributions with grooming*, JHEP **07** 2017 132 132, 2017. arXiv: 1704.02210 [hep-ph] (cit. on p. 124).

[182] C. Frye, A. J. Larkoski, M. D. Schwartz, and K. Yan, *Factorization for groomed jet substructure beyond the next-to-leading logarithm*, JHEP **07** 2016 064 064, 2016. arXiv: 1603.09338 [hep-ph] (cit. on p. 124).

[183] F. A. Dreyer, L. Necib, G. Soyez, and J. Thaler, *Recursive Soft Drop*, JHEP **06** 2018 093 093, 2018. arXiv: 1804.03657 [hep-ph] (cit. on p. 124).

[184] Masahiro Yamatani on behalf of ATLAS collaboration, *Boosted Jets; identifying highly boosted W, Z, top, Higgs and more*, 2019, 2019. [Online]. Available: https://cds.cern.ch/record/2676523 (cit. on p. 124).

[185] I. W. Stewart, F. J. Tackmann, and W. J. Waalewijn, *N-Jettiness: An Inclusive Event Shape to Veto Jets*, Phys. Rev. Lett. **105** 2010 092002 092002, 2010. arXiv: 1004.2489 [hep-ph] (cit. on p. 124).

[186] CDF and D0 Collaborations, *Combination of Tevatron Searches for the Standard Model Higgs Boson in the $W^+W^-$ Decay Mode*, Phys. Rev. Lett. **104** 2010 061802 061802, 2010. arXiv: 1001.4162 [hep-ex] (cit. on p. 125).

[187] J. Thaler and K. Van Tilburg, *Identifying Boosted Objects with N-subjettiness*, JHEP **03** 2011 015 015, 2011. arXiv: 1011.2268 [hep-ph] (cit. on p. 126).

[188] I. W. Stewart, F. J. Tackmann, J. Thaler, C. K. Vermilion, and T. F. Wilkason, *XCone: N-jettiness as an Exclusive Cone Jet Algorithm*, JHEP **11** 2015 072 072, 2015. arXiv: 1508.01516 [hep-ph] (cit. on pp. 126, 155).

[189] ATLAS Collaboration, *Evidence for the charge asymmetry in $pp \to t\bar{t}$ production at $\sqrt{s} = 13$ TeV with the ATLAS detector*, 2022, 2022. arXiv: 2208.12095 [hep-ex] (cit. on p. 126).

[190] CMS Collaboration, *Measurement of the top quark mass using events with a single reconstructed top quark in pp collisions at $\sqrt{s} = 13$ TeV*, JHEP **12** 2021 161 161, 2021. arXiv: 2108.10407 [hep-ex] (cit. on p. 126).

[191] CDF Collaboration, *Observation of top quark production in $\bar{p}p$ collisions*, Phys. Rev. Lett. **74** 1995 2626 2626, 1995. arXiv: hep-ex/9503002 (cit. on p. 129).

[192] D0 Collaboration, *Observation of the top quark*, Phys. Rev. Lett. **74** 1995 2632 2632, 1995. arXiv: hep-ex/9503003 (cit. on p. 129).

[193] CDF and D0 collaborations, *Combination of CDF and D0 results on the mass of the top quark using up* 9.7fb$^{-1}$ *at the Tevatron*, 2016, 2016. arXiv: 1608.01881 [hep-ex] (cit. on p. 129).

[194] ATLAS Collaboration, *Direct top-quark decay width measurement in the $t\bar{t}$ lepton+jets channel at $\sqrt{s} = 8$ TeV with the ATLAS experiment*, Eur. Phys. J. C **78** 2018 129 129, 2018. arXiv: 1709.04207 [hep-ex] (cit. on p. 131).

[195] CMS Collaboration, *Measurement of the ratio $\mathcal{B}(t \to Wb)/\mathcal{B}(t \to Wq)$ in pp collisions at $\sqrt{s} = 8$ TeV*, Phys. Lett. B **736** 2014 33 33, 2014. arXiv: 1404.2292 [hep-ex] (cit. on p. 131).

[196] D0 Collaboration, *An Improved determination of the width of the top quark*, Phys. Rev. D **85** 2012 091104 091104, 2012. arXiv: 1201.4156 [hep-ex] (cit. on p. 131).

[197] C. Herwig, T. Ježo, and B. Nachman, *Extracting the Top-Quark Width from Nonresonant Production*, Phys. Rev. Lett. **122** 2019 231803 231803, 2019. arXiv: 1903.10519 [hep-ex] (cit. on p. 131).

[198] J. C. Lagarias, *Euler's constant: Euler's work and modern developments*, Bulletin of the American Mathematical Society **50** 2013 527 527, 2013. [Online]. Available: https://api.semanticscholar.org/CorpusID:119612431 (cit. on p. 133).

[199] R. Tarrach, *The Pole Mass in Perturbative QCD*, Nucl. Phys. B **183** 1981 384 384, 1981 (cit. on pp. 134, 135).

[200] M. C. Smith and S. S. Willenbrock, *Top quark pole mass*, Phys. Rev. Lett. **79** 1997 3825 3825, 1997. arXiv: hep-ph/9612329 (cit. on p. 134).

[201] M. Beneke, *Renormalons*, Phys. Rept. **317** 1999 1 1, 1999. arXiv: hep-ph/9807443 (cit. on p. 135).

[202] P. Nason, *Theory Summary*, PoS **TOP2015** 2016 056, L. Lista, F. Margaroli, and F. Tramontano, Eds. 056, 2016. arXiv: 1602.00443 [hep-ph] (cit. on p. 135).

[203] A. H. Hoang, C. Lepenik, and M. Preisser, *On the Light Massive Flavor Dependence of the Large Order Asymptotic Behavior and the Ambiguity of the Pole Mass*, JHEP **09** 2017 099 099, 2017. arXiv: 1706.08526 [hep-ph] (cit. on p. 135).

[204] W. A. Bardeen, A. J. Buras, D. W. Duke, and T. Muta, *Deep Inelastic Scattering Beyond the Leading Order in Asymptotically Free Gauge Theories*, Phys. Rev. D **18** 1978 3998 3998, 1978 (cit. on p. 135).

[205] M. Beneke, P. Marquard, P. Nason, and M. Steinhauser, *On the ultimate uncertainty of the top quark pole mass*, Phys. Lett. B **775** 2017 63 63, 2017. arXiv: 1605.03609 [hep-ph] (cit. on p. 135).

[206] A. H. Hoang *et al.*, *The MSR mass and the $\mathcal{O}(\Lambda_{\mathrm{QCD}})$ renormalon sum rule*, JHEP **04** 2018 003 003, 2018. arXiv: 1704.01580 [hep-ph] (cit. on pp. 136, 137, 201, 221).

[207] A. H. Hoang, A. Jain, I. Scimemi, and I. W. Stewart, *Infrared Renormalization Group Flow for Heavy Quark Masses*, Phys. Rev. Lett. **101** 2008 151602 151602, 2008. arXiv: 0803.4214 [hep-ph] (cit. on p. 136).

[208] M. B. Voloshin, *'Optical' sum rule for form-factors of heavy mesons*, Phys. Rev. D **46** 1992 3062 3062, 1992 (cit. on p. 136).

[209] I. I. Y. Bigi, M. A. Shifman, and N. Uraltsev, *Aspects of heavy quark theory*, Ann. Rev. Nucl. Part. Sci. **47** 1997 591 591, 1997. arXiv: hep-ph/9703290 (cit. on p. 136).

[210] CMS Collaboration, *Measurement of the top quark mass using a profile likelihood approach with the lepton+jets final states in proton–proton collisions at $\sqrt{s} = 13$ TeV*, 2023, 2023. arXiv: 2302.01967 [hep-ex] (cit. on p. 137).

[211] ATLAS and C. Collaborations, *Combination of measurements of the top quark mass from data collected by the ATLAS and CMS experiments at $\sqrt{s} = 7$ and* 8 TeV, 2023, 2023. arXiv: 2402.08713 [hep-ex] (cit. on pp. 138–140, 172).

[212] ATLAS Collaboration, *Measurement of the top-quark mass in $t\bar{t} + 1$-jet events collected with the ATLAS detector in pp collisions at $\sqrt{s} = 8$ TeV*, JHEP **11** 2019 150 150, 2019. arXiv: 1905.02302 [hep-ex] (cit. on pp. 139, 141).

[213] A. H. Hoang, *What is the Top Quark Mass?* Ann. Rev. Nucl. Part. Sci. **70** 2020 225 225, 2020. arXiv: 2004.12915 [hep-ph] (cit. on p. 139).

[214] A. H. Hoang, "The Top Mass: Interpretation and Theoretical Uncertainties," *7th International Workshop on Top Quark Physics*, 2014. arXiv: 1412.3649 [hep-ph] (cit. on pp. 139, 142).

[215] M. Czakon and A. Mitov, *Top++: A Program for the Calculation of the Top-Pair Cross-Section at Hadron Colliders*,
Comput. Phys. Commun. **185** 2014 2930 2930, 2014.
arXiv: 1112.5675 [hep-ph] (cit. on p. 141).

[216] L. T. W. Group, *Top quark (indirect) mass measurements*,
Last Checked Out 10/11/2023, Last Checked Out 10/11/2023.
[Online]. Available: https://twiki.cern.ch/twiki/bin/view/LHCPhysics/LHCTopWGSummaryPlots (cit. on p. 141).

[217] ATLAS and CMS Collaborations, *Combination of inclusive top-quark pair production cross-section measurements using ATLAS and CMS data at* $\sqrt{s} = 7$ *and* $8\ TeV$, 2022, 2022. arXiv: 2205.13830 [hep-ex] (cit. on p. 141).

[218] CMS Collaboration, *Measurement of the top quark pole mass using* $t\bar{t}$*+jet events in the dilepton final state in proton–proton collisions at* $\sqrt{s} = 13\ TeV$, 2022, 2022. arXiv: 2207.02270 [hep-ex] (cit. on p. 141).

[219] J. Kieseler, K. Lipka, and S.-O. Moch, *Calibration of the top-quark monte carlo mass*, Phys. Rev. Lett. **116** 16 2016 162001 162001, 16 2016.
[Online]. Available:
https://link.aps.org/doi/10.1103/PhysRevLett.116.162001
(cit. on pp. 143, 207, 226).

[220] M. Butenschoen *et al.*, *Top Quark Mass Calibration for Monte Carlo Event Generators*, Phys. Rev. Lett. **117** 2016 232001 232001, 2016.
arXiv: 1608.01318 [hep-ph] (cit. on pp. 143, 171, 172).

[221] B. Dehnadi, A. H. Hoang, O. L. Jin, and V. Mateu, *Top Quark Mass Calibration for Monte Carlo Event Generators – An Update*, 2023, 2023.
arXiv: 2309.00547 [hep-ph] (cit. on pp. 143, 170–172, 207, 226).

[222] A. H. Hoang, S. Mantry, A. Pathak, and I. W. Stewart, *Extracting a Short Distance Top Mass with Light Grooming*,
Phys. Rev. D **100** 2019 074021 074021, 2019.
arXiv: 1708.02586 [hep-ph] (cit. on pp. 144, 145, 147, 151).

[223] ATLAS Collaboration, *A precise interpretation for the top quark mass parameter in ATLAS Monte Carlo simulation*,
ATL-PHYS-PUB-2021-034, 2021.

[Online]. Available: https://cds.cern.ch/record/2777332
(cit. on pp. 144, 150, 161, 169, 171, 172, 175, 206, 207, 225, 226).

[224] S. Fleming, A. H. Hoang, S. Mantry, and I. W. Stewart, *Jets from massive unstable particles: Top-mass determination*,
Phys. Rev. D **77** 2008 074010 074010, 2008. arXiv: hep-ph/0703207
(cit. on p. 146).

[225] S. Fleming, A. H. Hoang, S. Mantry, and I. W. Stewart, *Top Jets in the Peak Region: Factorization Analysis with NLL Resummation*,
Phys. Rev. D **77** 2008 114003 114003, 2008. arXiv: 0711.2079 [hep-ph]
(cit. on p. 146).

[226] C. W. Bauer, S. Fleming, and M. E. Luke, *Summing Sudakov logarithms in $B \to X_s\gamma$in effective field theory.*,
Phys. Rev. D **63** 2000 014006 014006, 2000. arXiv: hep-ph/0005275
(cit. on p. 146).

[227] C. W. Bauer, S. Fleming, D. Pirjol, and I. W. Stewart, *An Effective field theory for collinear and soft gluons: Heavy to light decays*,
Phys. Rev. D **63** 2001 114020 114020, 2001. arXiv: hep-ph/0011336
(cit. on p. 146).

[228] C. W. Bauer and I. W. Stewart, *Invariant operators in collinear effective theory*, Phys. Lett. B **516** 2001 134 134, 2001. arXiv: hep-ph/0107001
(cit. on p. 146).

[229] C. W. Bauer, D. Pirjol, and I. W. Stewart, *Soft collinear factorization in effective field theory*, Phys. Rev. D **65** 2002 054022 054022, 2002.
arXiv: hep-ph/0109045 (cit. on p. 146).

[230] M. Beneke, A. P. Chapovsky, M. Diehl, and T. Feldmann, *Soft collinear effective theory and heavy to light currents beyond leading power*,
Nucl. Phys. B **643** 2002 431 431, 2002. arXiv: hep-ph/0206152
(cit. on p. 146).

[231] M. Beneke and T. Feldmann, *Multipole expanded soft collinear effective theory with non-Abelian gauge symmetry*,
Phys. Lett. B **553** 2003 267 267, 2003. arXiv: hep-ph/0211358
(cit. on p. 146).

[232] R. J. Hill and M. Neubert, *Spectator interactions in soft collinear effective theory*, Nucl. Phys. B **657** 2003 229 229, 2003. arXiv: `hep-ph/0211018` (cit. on p. 146).

[233] A. V. Manohar and M. B. Wise, *Heavy quark physics*. 2000, vol. 10, ISBN: 978-0-521-03757-0 (cit. on p. 146).

[234] J. Michel, A. Pathak, and I. W. Stewart, *Hadron-level lightly groomed boosted top jets at NNLL*, 2024, 2024, Publication forthcoming (cit. on pp. 150, 175).

[235] T. Mäkelä, A. H. Hoang, K. Lipka, and S.-O. Moch, *Investigation of the scale dependence in the MSR and $\overline{MS}$ top quark mass schemes for the $t\bar{t}$ invariant mass differential cross section using LHC data*, JHEP **09** 2023 037 037, 2023. arXiv: `2301.03546 [hep-ph]` (cit. on p. 152).

[236] M. V. Garzelli, L. Kemmler, S. Moch, and O. Zenaiev, *Heavy-flavor hadro-production with heavy-quark masses renormalized in the $\overline{\mathrm{MS}}$, MSR and on-shell schemes*, JHEP **04** 2021 043 043, 2021. arXiv: `2009.07763 [hep-ph]` (cit. on pp. 152, 170).

[237] A. Buckley, "ATLAS Pythia 8 tunes to 7 TeV data," *6th International Workshop on Multiple Partonic Interactions at the LHC*, 2014 29 (cit. on pp. 153, 164).

[238] M. A. Ebert, J. K. L. Michel, F. J. Tackmann, *et al.*, *SCETlib: A C++ Package for Numerical Calculations in QCD and Soft-Collinear Effective Theory*, DESY-17-099 2018, 2018, webpage: `http://scetlib.desy.de` (cit. on p. 155).

[239] S. G. de la Hoz et al. on behalf of the ATLAS Collaboration, *Computing activities at the Spanish Tier-1 and Tier-2s for the ATLAS experiment towards the LHC Run3 and High-Luminosity periods*, EPJ Web Conf. **245** 2020 07027 07027, 2020 (cit. on p. 156).

[240] B. Bachu, A. H. Hoang, V. Mateu, A. Pathak, and I. W. Stewart, *Boosted top quarks in the peak region with N3LL resummation*, Phys. Rev. D **104** 2021 014026 014026, 2021. arXiv: `2012.12304 [hep-ph]` (cit. on p. 161).

[241] ATLAS Collaboration, *A study of different colour reconnection settings for Pythia8 generator using underlying event observables*, 2017, 2017. [Online]. Available: `https://cds.cern.ch/record/2262253` (cit. on p. 164).

[242] CMS Collaboration, *Event generator tunes obtained from underlying event and multiparton scattering measurements*, Eur. Phys. J. C **76** 2016 155 155, 2016. arXiv: `1512.00815 [hep-ex]` (cit. on pp. 166, 167).

[243] P. Skands, S. Carrazza, and J. Rojo, *Tuning PYTHIA 8.1: the Monash 2013 Tune*, Eur. Phys. J. C **74** 2014 3024 3024, 2014. arXiv: `1404.5630 [hep-ph]` (cit. on p. 166).

[244] R. Corke and T. Sjostrand, *Interleaved Parton Showers and Tuning Prospects*, JHEP **03** 2011 032 032, 2011. arXiv: `1011.1759 [hep-ph]` (cit. on pp. 166, 167).

[245] J. Pumplin *et al.*, *New generation of parton distributions with uncertainties from global QCD analysis*, JHEP **07** 2002 012 012, 2002. arXiv: `hep-ph/0201195` (cit. on p. 167).

[246] A. H. Hoang, C. Lepenik, and V. Mateu, *REvolver: Automated running and matching of couplings and masses in QCD*, Comput. Phys. Commun. **270** 2022 108145 108145, 2022. arXiv: `2102.01085 [hep-ph]` (cit. on p. 172).

[247] N. Bouchhar *et al.*, *Interpreting the direct Monte Carlo top mass parameter using the groomed jet mass.*, 2024, 2024, Publication forthcoming (cit. on p. 172).